Doctoral Dissertation

Influence of Short Period Xallarap Effect on Binary Lens Parameters in the Analysis of OGLE-2019-BLG-0825

Yuki Satoh

Department of Earth and Space Science,

Graduate School of Science, Osaka University

October 25, 2023

Yuki Satoh

Abstract

We present an analysis of microlensing event OGLE-2019-BLG-0825. This event was identified as a planetary candidate by preliminary modeling. We find that significant residuals from the best-fit static binary-lens model exist and a xallarap effect can fit the residuals very well and significantly improves χ^2 values. On the other hand, by including the xallarap effect in our models, we find that binary-lens parameters like mass-ratio, q, and separation, s, cannot be constrained well. However, the parameters of the source, such as orbital period and semi-major axis, are consistent across models with different lens system parameters. We therefore constrain the properties of the source system better than the properties of the lens system. The source system consists of a host of G-type main-sequence star orbited by a brown dwarf with a period of $P \sim 5$ days. This analysis is the first to demonstrate that the xallarap effect with short periods can affect binary-lens parameters in planetary events. The contents of Chapters 3 and 4 in this dissertation are published as Satoh et al. (2023).

Table of Contents

List of Figures

List of Tables

Chapter 1

Introduction

The question of how many planetary systems exist in the universe and whether there are other planets like our own, "Are we alone in the universe?" is one of the universal questions of humanity. Identifying planets outside our solar system, or exoplanets, and understanding their characteristics, provides one interpretation of the question. Exoplanets were first found on 51 Pegasi in 1995 (Mayor & Queloz, 1995). The planet is a Jupiter-mass object orbiting closer to Mercury, a type of hot Jupiter that does not exist in our solar system. A year later, Butler & Marcy (1996) discovered a not-so-hot Jupiter-like planet with a lower mass limit of 47Umab, $m_{\rm p} \sin i \sim 2.4$ Jupiter mass, orbital period $P \sim 3$ years, and orbital length radius $\sim$2 au. Exoplanets orbiting binary stars such as Keplar-16b (Doyle et al., 2011) have also been confirmed. More than 5,000 planets have been identified so far, extending the human worldview (Figure 1.1).

Brown dwarfs are objects with masses between those of stars and planets. These objects are classified based on the mass at which hydrogen fusion occurs. A star would need a mass of about $0.08 M_\odot$ (about $80 M_{\rm Jup}$) to have stable light hydrogen fusion in its interior. Even for objects lighter than this mass, if they are heavier than about $0.01 M_\odot$ (about $13 M_{\rm Jup}$), nuclear burning of deuterium will occur. Objects with masses in this $0.01 - 0.08 M_\odot$ (i.e., $13 - 80 M_{\rm Jup}$) range are called brown dwarfs. On the other hand, some researchers call objects formed in protoplanetary disks "planets" even if they are in the $13 - 80 M_{\rm Jup}$ range, and only $13 - 80 M_{\rm Jup}$ objects formed by the fragmentation of molecular cloud cores are called "brown dwarfs". However, it is difficult to

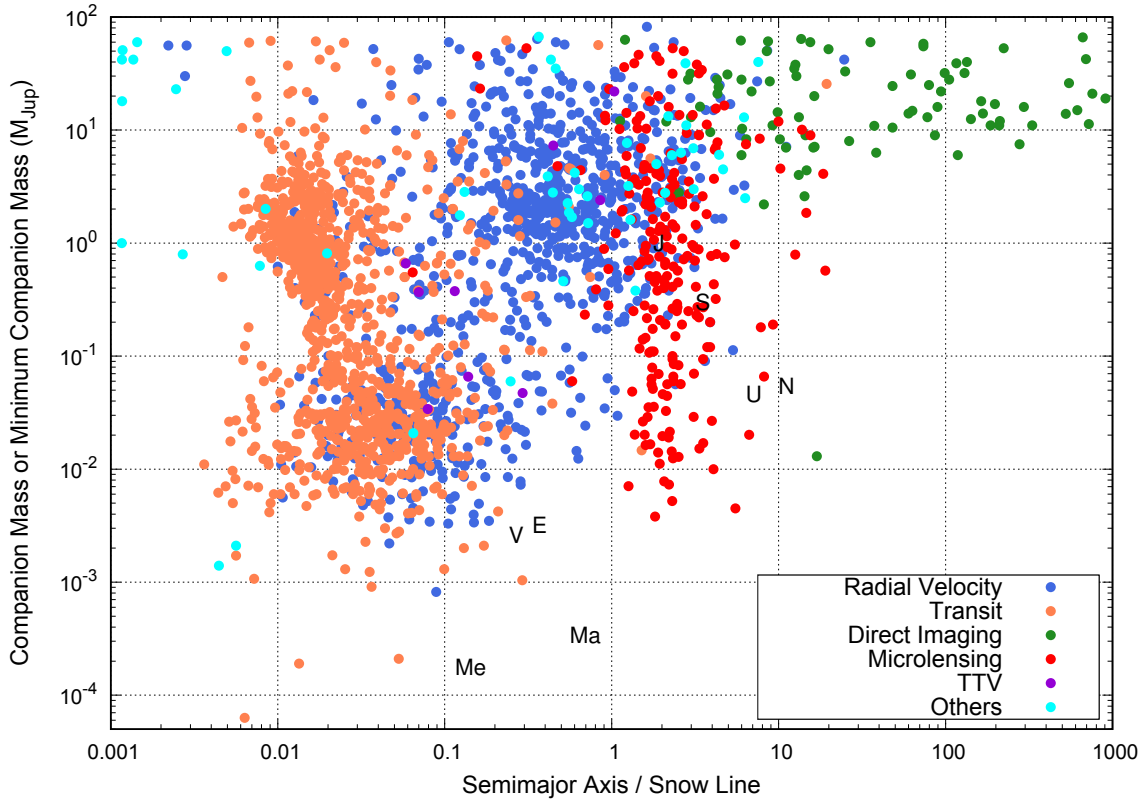

Figure 1.1: The distribution of masses and orbits of planets and brown dwarfs. Different colors indicate planet and brown dwarf discovery methods: blue is the radial velocity method, orange is the transit method, green is the direct imaging method, red is the microlensing method, purple is the TTV (Transit Timing Variations) method, and cyan is other planet-finding methods. Each is described in Section 1.2. The planets of the solar system are indicated by letters. The horizontal axis is the orbit length radius normalized by the snow line assuming $2.7\,\mathrm{au} \times (M_*/M_\odot)$, where M_* is the host star mass and $M_\odot$ is the mass of the Sun. The vertical axis is the mass or minimum mass of the planet or brown dwarf. The snow line is the distance from the central star at which H_2O becomes solid. The area near the snow line is considered important for planet and brown dwarf because of the increase in solid materials that can be used as materials for planet and brown dwarf formation.

determine the formation process with certainty from current observations. In this dissertation, we simply define brown dwarfs as objects in the $13-80M_{\rm Jup}$ range. Relatively heavy brown dwarfs are thought to have physical and chemical properties similar to those of late M-type stars because they undergo deuterium fusion in their youth and have temperatures similar to those of late M-type stars. Furthermore, after the nuclear burning of deuterium is complete, the temperature of the atmosphere cools, which is thought to have properties similar to those of a giant planet. Thus, brown dwarfs are objects with both stellar and planetary characteristics. The first brown dwarf candidate was GD165B orbiting the white dwarf GD165 (Kumar, 1963). However, due to large uncertainties in mass estimation, it was not confirmed as a brown dwarf at the time. The first reliable brown dwarf Gl229B was discovered by Nakajima et al. (1995); Oppenheimer et al. (1995). The near-infrared spectrum of Gl229B has an absorption band of $\rm CH_4$, which does not exist in objects with higher temperatures like stars, and this is why it was confirmed as a brown dwarf. Since the discovery of Gl229B, about 1,300 brown dwarfs have been discovered to date.

1.1 Formation of Planets and Brown Dwarfs

Planets are thought to form in protoplanetary disks around stars during the star formation process. Brown dwarfs as companions are thought to follow a formation path similar to that of giant planets or, like binary stars, by fragmentation of molecular cloud core or circumstellar disks. This section describes models of planetary and brown dwarf formation theories.

1.1.1 Core Accretion Model

The core accretion model is a common planetary formation model that is currently being considered, and is also called the cold start model. Safronov (1972) developed a comprehensive theoretical model of terrestrial planets, and Hayashi et al. (1985) developed the Kyoto Model, which unifies the formation of terrestrial planets, giant gas planets, and ice planets. Together, the Kyoto model and the Safronov model are referred to as the standard model of core accretion. The core accretion model suggests that it takes $\sim 10^7$ years from the contraction of the interstellar molecular

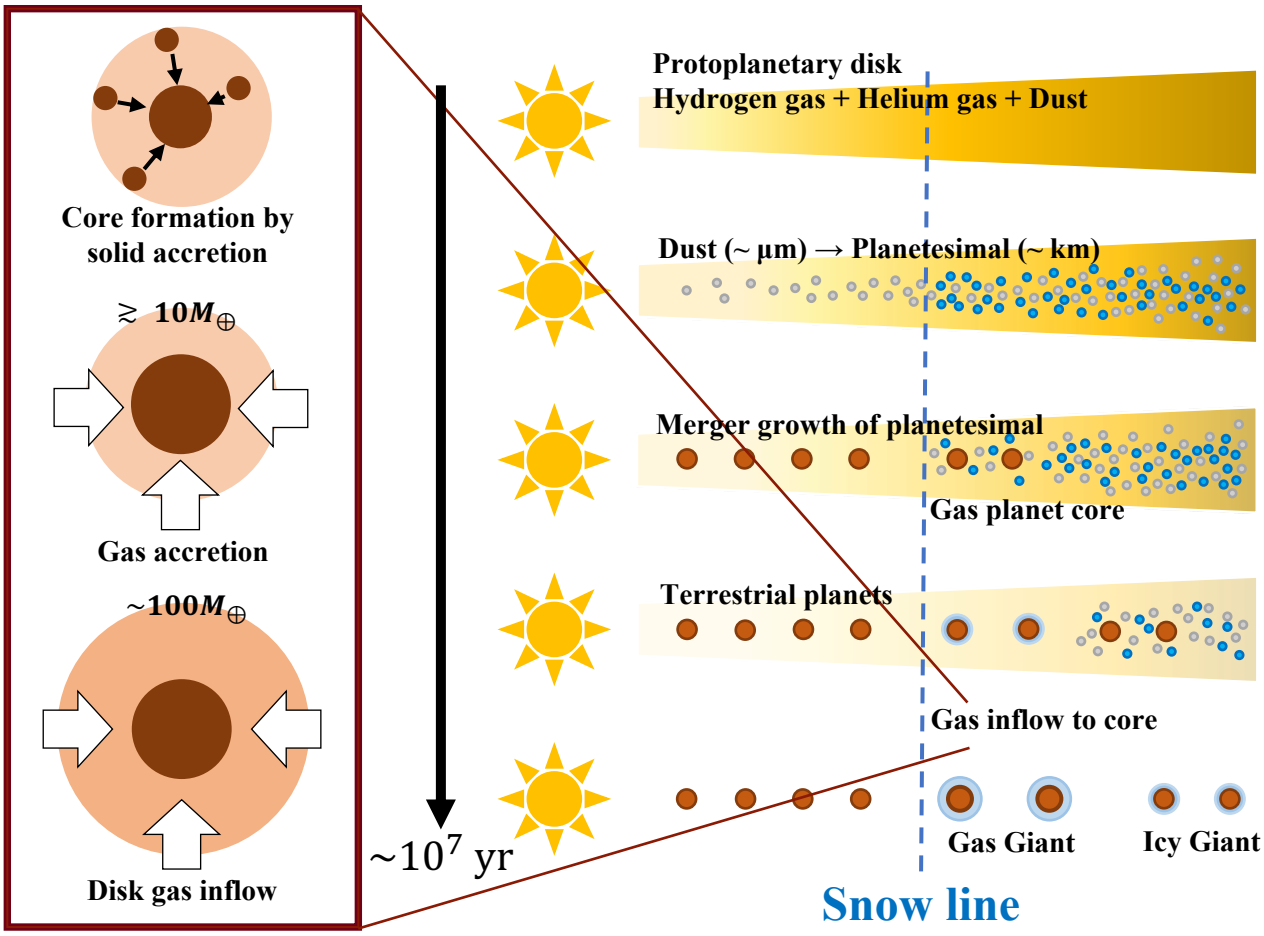

Figure 1.2: Schematic of the core accretion model. The progression is from top to bottom. The time scale of the core accumulation model is on the order of 10^7 years.

cloud, the origin of star and planet formation, to the end of star and planet formation (Pollack et al., 1996). Figure 1.2 shows a schematic diagram of the core accretion model. In the core accretion model, planet formation follows the following five steps

1. A molecular cloud several light-years in size shrinks and star formation occurs. Around the same time, a protoplanetary disk composed primarily of hydrogen and helium gases is formed. The radius of a protoplanetary disk may reach up to 100 au. In the protoplanetary disk, dust with a size of less than μm condenses. In the solar system, silicate dust and iron dust condensed beyond ~0.05 au, and ice dust condensed beyond the snow line (~2.7 au).

2. Dust collides one after another to form planetesimal of 1 km to 10 km in diameter. After formation, the asteroids grow at a rate of several cm per year.

3. Planetesimal merge and grow into protoplanets. Outside the snow line, solid material accretion proceeds. The size of protoplanets is about 0.1 Earth mass in the terrestrial planet region (about $0.4 - 1.5$ au for the solar system), several times the Earth mass near Jupiter's orbit (about the same as the estimated Jupiter core), and about 10 Earth mass near Uranus' and Neptune's orbit.

4. When the core mass exceeds $5 - 10$ Earth mass, the influx of disk gas forms a giant gas planet that exceeds 100 times the Earth mass (this runaway growth was not a concept in the Kyoto model or the Safronov model, but has been proposed as an extension of the analysis of these models).

5. The solar wind blows all the gas and dust from the protoplanetary disk into space and the planet stops growing. The ice planet formed after the gas is blown away will not acquire gas and will finish growing. Protoplanets in the inner region begin to collide with each other after the disappearance of disk gas, and terrestrial planets are formed.

1.1.2 Gravitational Instability Model

In the gravitational instability model, the protoplanetary disk splits due to its own gravitational instability, and planets and companion stars are formed directly. The initial temperature is high and is called the hot mode. Planet formation by the gravitational instability model is shorter than the core accretion model, on the order of 10^6 years (Spiegel & Burrows, 2012). The conditions under which the disk becomes unstable are given by,

$$Q \equiv \frac{v_{\rm s}\kappa}{\pi G\Sigma} < 1, \tag{1.1}$$

where $v_{\rm s}$ is the speed of sound, Σ is the areal density, and κ is the epicyclic frequency. The parameter Q is called Toomre Q value (Toomre, 1964). Stars and gas in the circumstellar disk

are moving in a nearly circular motion, but with small oscillations in the plane of rotation and in the vertical direction. The oscillation in the plane of rotation is called epicyclic motion, and the angular velocity of this oscillation is called the epicyclic frequency. The further away from the central star, the lower the temperature, the smaller the sound velocity $v_{\rm s}$. Also, the epicyclic frequency becomes smaller. Therefore, the further away from the central star, the more likely it is to become gravitationally unstable.

1.1.3 Nice Model and Grand Tack Hypothesis

The Nice model (Gomes et al., 2005; Morbidelli et al., 2005; Tsiganis et al., 2005) is a theoretical model in which Uranus and Neptune experience large-scale orbital changes due to the gravitational interaction of Jupiter, Saturn, Uranus, and Neptune in a narrow orbital alignment after planet formation. The Solar system is thought to have experienced a period known as the Late Heavy Bombardment about 3.8 billion years ago. During that period, about 700 million years after their formation, Mercury, Venus, and Earth-Mars and Earth's moons are also thought to have experienced celestial collisions with many small bodies. One piece of evidence for the Late Heavy Bombardment Period is a crater chronology estimate that most of the craters on the Moon were formed by meteorite impacts around 3.8 billion years ago. The Nice model can explain the events that caused this Late Heavy Bombardment.

In the Nice model, immediately after the planets formed, Jupiter and Saturn were at approximately the same positions as they are today, and Uranus and Neptune were located inside their present positions. Four planets in close orbital arrangements oscillate with each other due to gravitational perturbations. Eventually, when Jupiter and Saturn are in a $2:1$ mean orbital resonance position, the system becomes dynamically unstable. As a result, Uranus and Neptune, which have less mass than Jupiter and Saturn, are bounced outward. This migration brings asteroids and planetesimal that were located around Jupiter, Saturn, Uranus, and Neptune immediately after formation, or beyond Neptune, or in the asteroid belt to Earth's orbit, resulting in Late Heavy Bombardment. Older theoretical models that did not consider planetary migration had the problem that the gas in the protoplanetary disk dissipated before Uranus and Neptune acquired their

current atmospheres, but based on the Nice model, the formation of Uranus and Neptune can be explained. The timescale for the dissipation of the disk gas is on the order of 10^6 years. It can also explain the orbital distribution of trans-Neptunian objects (TNOs) and the orbital relationship between Neptune and Pluto.

It is the Grand Tack hypothesis (Walsh et al., 2011) that provided one explanation for how the Jupiter-Saturn-Uranus-Neptune alignment in a narrow orbit could be achieved in the first place. In the Grand Tack hypothesis, Jupiter slowly shortens its orbital distance toward the Sun, but is caught midway by a similarly falling Saturn, which pulls it back to near its current position. At this time, Uranus and Neptune continue to grow on the outside, resulting in four giant planets in a narrow orbital interval. As the planet grows and its mass becomes about the same as Jupiter's, the planet's gravity causes the gas near the planet's orbit to be blown away, forming a ring-shaped gap in the protoplanetary disk. The planet that created the gap is trapped in the gap by the reaction from the inner and outer disks, and falls slowly into the host star along with the disk gas. The timescale is millions of years, and this migration is referred to as a Type Ⅱ migration. The lighter planet falls into the host star without opening a gap in the gas disk. For example, Earth at 1 au and Jupiter's core ice protoplanet at 5 au will fall to the main star in about 100,000 years. This migration is referred to as a Type Ⅰ migration. Saturn is unable to fully gap its gas disk and migrates with a velocity intermediate between Type Ⅰ and Type Ⅱ migration. This migration is referred to as a Type Ⅲ migration. The reason Saturn is able to catch up to Jupiter under the Grand Tack hypothesis is that Jupiter performs Type Ⅱ migration, while Saturn performs Type Ⅲ migration which is faster. Saturn catches up with Jupiter and becomes a $3:2$ mean motion resonance, which means that the gap in the gas disk created by Jupiter overlaps the gap created by Saturn. The balance of gravitational torque from the gas disk is then broken, exerting an outward force on the Jupiter-Saturn pair, pulling them back into outer orbits. Whether or not a Grand Tack really occurred has yet to be determined, and the results of more detailed fluid calculations are awaited.

1.1.4 Formation of Companion Brown Dwarfs

Ma & Ge (2014) found that brown dwarf companions with $M_{\rm p} \sin i < 42.5\ M_{\rm Jup}$ have an eccentricity distribution consistent with that of massive planets, and brown dwarfs with $M_{\rm p} \sin i > 42.5$ $M_{\rm Jup}$ have an eccentricity distribution consistent with that of binary stars. They also found that the host star of the companion brown dwarf is metal-poor and has a significantly different metal abundance distribution than the host star of the giant planets. They conclude that brown dwarfs with $M_{\rm p} \sin i < 42.5\ M_{\rm Jup}$ are formed by gravitational disk instabilities in protoplanetary disks, that their eccentricities are likely excited by scattering, and brown dwarfs with $M_{\rm p} \sin i > 42.5$ $M_{\rm Jup}$ are formed by molecular cloud fragmentation, just like stars. Tokovinin & Moe (2020) explain brown dwarf deserts by using simulations of disc fragmentation to show that it is difficult for a companion star to move to $P < 100$ days without undergoing accretion that would cause it to grow above 0.08 solar mass.

1.2 Exoplanets and Brown Dwarfs Discovery Methods

The discovery of exoplanets and brown dwarfs and their diversity provides feedback to existing theories of planet and brown dwarf formation. “Hot Jupiters” in which the first planet discovered, 51 Pegasi, is classified; “eccentric planets” with an eccentricity $e > 0.1$; “super-Earth” with a size or mass between Earth and Neptune; and “wide-orbit giant planets” whose semi-major axis is larger than that of Neptune, are planets not found in our solar system. In response to the observation results of exoplanets, discussions are progressing on theoretical studies such as the orbital evolution of planets, which are difficult to explain with classical planet formation theory. The characteristics of the resulting planets vary depending on the method used to observe exoplanets. This section describes typical methods for the discovery of exoplanets and brown dwarfs.

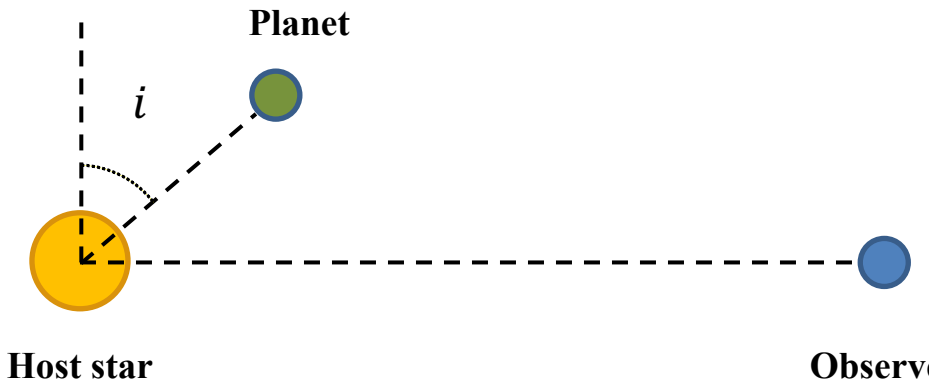

Figure 1.3: Schematic diagram of orbital inclination angle. The angle between the planet's orbital plane and the direction perpendicular to the line of sight is i.

1.2.1 Radial Velocity Method

The Radial velocity (hereafter, RV) method detects a planet by capturing the oscillations of the host star (spectral lines of the planet) due to the planet's gravity. The velocity amplitude K is described by the following equation.

$$\begin{aligned} K &= M_{\rm p} \sin i \sqrt{\frac{G}{(M_* + M_{\rm p})a}} = \left(\frac{2\pi G}{P}\right)^{1/3} \frac{1}{\sqrt{1-e^2}} \frac{M_{\rm p} \sin i}{(M_* + M_{\rm p})^{2/3}} \\ &\sim 0.09 \left(\frac{M_{\rm p} \sin i}{M_\oplus}\right) \sqrt{\frac{1}{M_*/M_\odot}} \sqrt{\frac{1}{a/1\ {\rm au}}}\ {\rm m/s} \\ &\sim 12.5 \left(\frac{M_{\rm p} \sin i}{M_{\rm Jup}}\right) \sqrt{\frac{1}{M_*/M_\odot}} \sqrt{\frac{1}{a/5.2\ {\rm au}}}\ {\rm m/s}, \end{aligned} \tag{1.2}$$

where the parameter $M_{\rm p}$ is the planetary mass, the parameter M_* is the host star mass, the parameter P is the orbital period, the parameter a is the orbital radius, and G is constant of gravitation. As shown in Figure 1.3, the parameter i is the orbital inclination angle of the planet, which is the angle between the planet's orbital plane and the direction perpendicular to the line of sight. $M_{\rm planet,obs}$, which can be derived by the RV method, is described by the following equation,

$$M_{\rm planet,obs} = M_{\rm planet,true} \times \sin i. \tag{1.3}$$

Therefore, the observed mass $M_{\rm planet,obs}$ is the minimum mass of true planetary mass $M_{\rm planet,true}$. The expected value of $\sin i$ is based on the following,

$$\langle \sin i \rangle = \frac{\int_0^{\pi/2} P(i) \sin i di}{\int_0^{\pi/2} P(i) di} = \frac{\int_0^{\pi/2} 2\pi \sin i \times \sin i di}{\int_0^{\pi/2} 2\pi \sin i di} = \frac{\pi}{4}, \tag{1.4}$$

where $P(i)$ is the probability that the planet takes orbital inclination i. Thus, statistically, $M_{\rm planet,true}$ can be interpreted as follows:

$$M_{\rm planet,true} = \frac{4}{\pi} \times M_{\rm planet,obs} \sim 1.273 \times M_{\rm planet,obs}. \tag{1.5}$$

Current measurement accuracy is $K \sim 1\ {\rm m\ s^{-1}}$. The velocity amplitudes of Jupiter and Earth to the Sun are $K_{\rm Earth\ to\ Sun} \sim 9\ {\rm cm\ s^{-1}}$, $K_{\rm Jupiter\ to\ Sun} \sim 12.5\ {\rm m\ s^{-1}}$, respectively. Therefore, RV searches for Earth-like planets around Sun-like stars will be buried by noise and the vibrations of the star itself. However, the RV method can detect planets with small semi-major axis a that orbit M-type stars ($0.08 M_\odot \lesssim M_* \lesssim 1.5 M_\odot$). More than 1,000 planets have been confirmed to date, including 51 Peg b, the first planet confirmed, and Proxima b (Anglada-Escudé et al., 2016), the closest exoplanet to our solar system. High-precision near-infrared instruments such as the IRD (InfraRed Doppler for the Subaru telescope: Tamura et al., 2012; Kotani et al., 2014) on the Subaru 8.2 m telescope are making RV observations of nearby M-type stars.

1.2.2 Transit Method

The transit method detects a planet based on periodic changes in luminosity due to eclipses of the primary star that occur during the planet's orbit. The planetary radius can be estimated from the eclipse amplitude. The photometric amplitude is described by the following equation,

$$\begin{aligned} \frac{\Delta B}{B} &\sim 0.01 \times \left(\frac{R_{\rm p}}{R_\oplus}\right)^2 \left(\frac{R_*}{R_\odot}\right)^{-2} \% \\ &\sim 1 \times \left(\frac{R_{\rm p}}{R_{\rm Jup}}\right)^2 \left(\frac{R_*}{R_\odot}\right)^{-2} \%, \end{aligned} \tag{1.6}$$

where $\Delta B/B$ is the change in relative luminosity, $R_{\rm p}$ is the radius of the planet, and R_* is the radius of the host star. Detecting Jupiter-like and Earth-like planets around a Sun-like star, respectively, requires photometric accuracy of less than 1% for Jupiter and 0.01 $\%$ (10 ppm) for Earth.

The conditions under which transit occurs can be expressed as follows.

$$a\cos i \leq R_* + R_{\rm p}, \tag{1.7}$$

where a is the orbital radius, i is the orbital inclination, R_* is the host star radius, and $R_{\rm p}$ is the planetary radius. Therefore, transit occurring probability $P_{\rm transit}$ can be expressed as,

$$P_{\rm transit} = \int_0^{R_*+R_{\rm p}/a} d\cos i = (R_* + R_{\rm p}/a). \tag{1.8}$$

The transit probability of a planet in Earth orbit around the Sun is $P_\oplus = 5 \times 10^{-3}$ and that of a planet in Jupiter orbit around the Sun is $P_{\rm Jup} = 9 \times 10^{-4}$. Thus, as with the RV, there is an observational bias toward planets closer to the host star.

The Transit method has the potential for false positives, such as eclipsing a companion star, transiting red or brown dwarfs, or blending of a companion star. Therefore, additional observations are required. Since the detection of Hot Jupiter HD 209458 (e.g., Charbonneau et al., 2000) in 2000, this method has so far confirmed about 4000 planets. Characterization of planetary atmospheres is also possible by comparing the direct light from the host star with the transit light from the planetary atmosphere. By detecting changes in luminosity due to secondary eclipses, which are eclipses when a planet passes behind its host star, the orbital eccentricity can also be estimated by knowing the time interval between primary and secondary eclipses.

Transit planetary systems show periodic host star dimming. If there is an undetected planet in this planetary system, the timing of the transit planet's transit may change due to gravitational interactions with the undetected planet. This change is called the Transit timing variations, and the method of using it to search for planets is called the TTV (Transit Timing Variations) method. Since the planetary mass can be constrained from the TTV method, the planetary density can be estimated by combining it with the planetary radius information from the transit method.

By comparing the spectrum of the host star while the planet is in transit with the spectrum of the host star when the planet is not in transit, we can obtain the spectrum of the planetary atmosphere. This is called transit spectroscopy. In 2019, Benneke et al. (2019) and Tsiaras et al. (2019) confirmed the presence of H_2O in the atmosphere of super-earth K2-18b using this technique. Secondary eclipses are useful for estimating atmospheric composition and planetary temperatures because they allow us to observe planetary albedo and the thermal radiation of the planet.

The Kepler telescope (Borucki et al., 2010), launched in March 2009 to search for planets using the Transit method, has taken photometry of more than 500,000 stars in 9.5 years of observations. Kepler detected about 4600 transiting planet candidates, of which about 2300 were confirmed. Many of the planets identified by Kepler are at distances that are difficult to characterize. Launched in April 2018, TESS (Transiting Exoplanet Survey Satellite: Ricker et al., 2015) conducts transit exploration with the goal of discovering many small planets orbiting stars at close distances from Earth.

1.2.3 Direct Imaging Method

The direct imaging method detects planets by masking the light of the primary star, which is several orders of magnitude brighter than the planet, and photometrically measuring the light of the planet. RV and Transit methods are only suitable for searching for planets around host stars with low stellar activity whereas the direct imaging method can be applied to both young and old stars. The colour, luminosity, and spectrum of the planet itself can be measured, and the mass can be estimated from the luminosity, temperature, and composition information. Furthermore, it is possible to dynamically derive mass from the motion of objects.

Direct imaging methods require (a) High Resolution, (b) High Sensitivity, and (c) High Contrast, all of which are necessary. In the visible near-infrared, the reflected flux can be measured primarily, with little contribution from radiation. The reflection contrast $c_{\rm ref}$ is given by

$$
\begin{aligned}
c_{\rm ref} \equiv \frac{f_{\rm p}^{\rm ref}}{f_*} &= \frac{2\phi(\beta)}{3} A \left(\frac{R_{\rm p}}{a}\right) \\
&\sim 10^{-10} \left(\frac{A}{0.3}\right) \left(\frac{R_{\rm p}}{R_\oplus}\right)^2 \left(\frac{a}{1\,{\rm au}}\right)^{-2} \\
&\sim 10^{-8} \left(\frac{A}{0.3}\right) \left(\frac{R_{\rm p}}{R_{\rm Jup}}\right)^2 \left(\frac{a}{1\,{\rm au}}\right)^{-2},
\end{aligned}
\tag{1.9}
$$

where f_* is the luminosity of the host star, $f_{\rm ref}$ is the reflected luminosity of the planet, $R_{\rm p}$ is the planetary radius, a is the orbital radius, and A is the albedo of the planet. $\phi(\beta)$ is called the Lambert phase function and is a function of the phase angle $\beta = \angle({\rm host} - {\rm planet} - {\rm observer})$, given by

$$
\phi(\beta) \equiv [\sin\beta - (\pi - \beta)\cos\beta]/\pi. \tag{1.10}
$$

At mid-infrared wavelengths longer than 10 μm or even longer, the radiation flux is observable and the contribution of reflection is almost negligible. The contrast of radiation as a function of wavelength λ, $c_{\rm rad}(\lambda)$ is given by

$$
c_{\rm rad}(\lambda) = \frac{R_{\rm p}^2}{R_*^2} \frac{\exp\left[\frac{hc}{\lambda k_{\rm B} T_*}\right] - 1}{\exp\left[\frac{hc}{\lambda k_{\rm B} T_{\rm p}}\right] - 1}, \tag{1.11}
$$

where R_* is the primary star radius, T_* is the primary star temperature, and $T_{\rm p}$ is the planetary temperature. For the Earth around the Sun, it is 10^6 in the long wavelength limit as shown in the following equation,

$$
c_{\rm rad} = \frac{R_{\rm p}^2 T_{\rm p}}{R_*^2 T_*} = 4 \times 10^{-6} \left(\frac{R_{\rm p}}{R_\oplus}\right)^2 \left(\frac{R_*}{R_\odot}\right)^{-2} \left(\frac{T_{\rm p}}{293{\rm K}}\right) \left(\frac{T_*}{5778{\rm K}}\right)^{-1}. \tag{1.12}
$$

Observing the solar system at a distance of 10 pc, (a) the distance between the Sun and the Earth is $0''.1$, (b) the apparent brightness of the Earth is 30 magnitudes of the star, and (c) the reflection contrast between the Sun and the Earth is 10^{-10}. While resolution and sensitivity are achievable, contrast is beyond the capabilities of current visible infrared telescopes. Therefore, the main target of the direct imaging method is currently a relatively young ($< 10^9$ years old), low-contrast, self-luminous giant planet around its host star. Direct imaging of an Earth-size planet

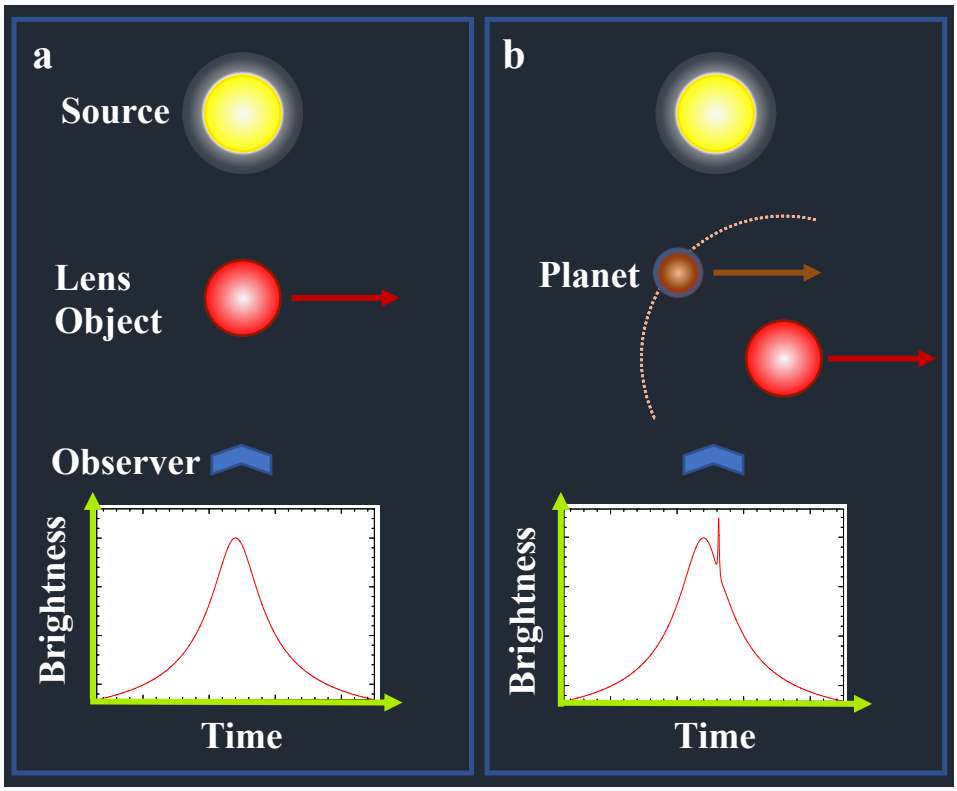

Figure 1.4: Schematic diagram of gravitational microlensing. (Left panel) When a lens object (gravitational source) passes in front of a light source star, the light of the source star is bent by gravity like a lens and its brightness changes over time. (Right panel) If a planet is associated with the lens object, a secondary perturbation to the light curve may occur.

around a nearby M-type star requires observing a high contrast of 10^{-8} at less than $0''.1$. Ground-based observations of these planets require next-generation large telescopes such as the Extremely Large Telescope (ELT), Thirty Meter Telescope (TMT), and Giant Magellan Telescope (GMT). Direct imaging of super-Earths around nearby G-type stars requires observations with contrasts as high as 10^9 at $0''.1$ or less. The Nancy Grace Roman Space Telescope (Spergel et al., 2015, previously named WFIRST, hereafter Roman) coronagraph will achieve a contrast of $\sim 5 \times 10^8$.

1.2.4 Gravitational Microlensing Method

The gravitational microlensing method is a planetary discovery technique that utilizes the phenomenon of light being bent by gravity, a phenomenon known from the theory of relativity. As

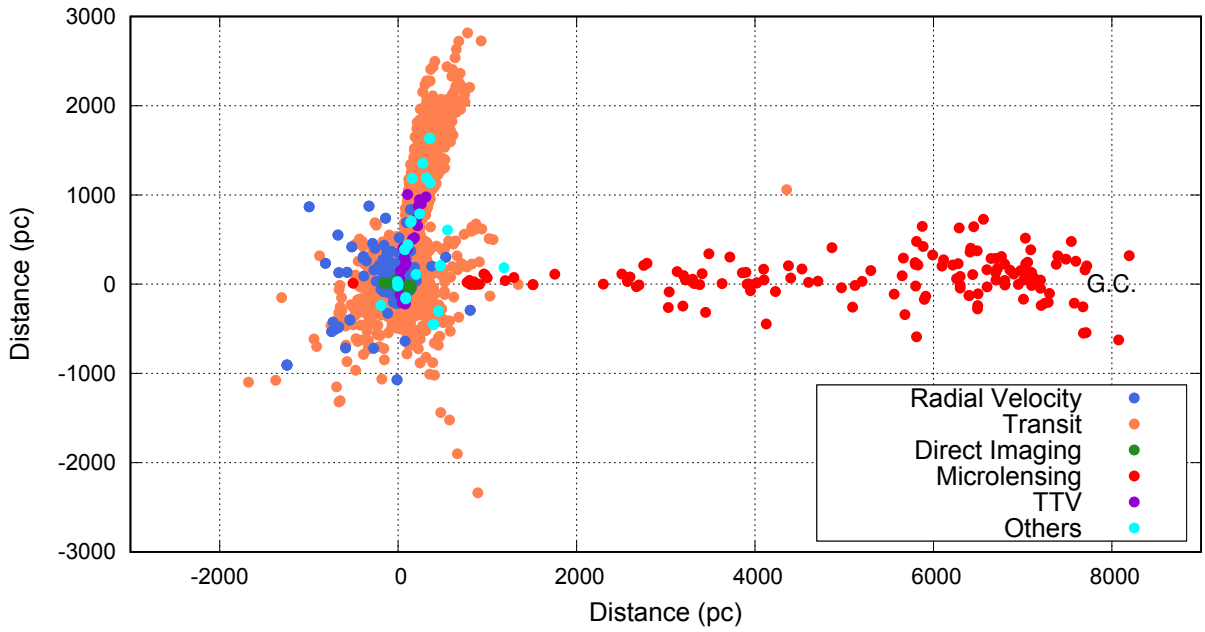

Figure 1.5: Distribution of exoplanet distances. The difference in colour is the planet discovery method: blue is the radial velocity method, orange is the transit method, green is the direct imaging method, red is the microlensing method, purple is the TTV method, and cyan is other planet discovery methods. The horizontal axis is the distance from the earth to the Galactic center in the positive direction, and the vertical axis is the Galactic longitude $l = 90°$ in the positive direction. The Galactic center is assumed to be 8 kpc from the earth and is denoted as "G.C.". Most of the planets beyond 3 kpc from Earth have been confirmed by the microlensing method.

shown in the right panel of the Figure 1.4, the brightness of the source changes with time as the lensing object, the gravitational source, passes in front of the source. In the case of binary and planetary systems, secondary brightening is caused by the companion star, as shown in the left panel. From this secondary intensification, microlensing planets can be identified. The gravity microlensing method has the following characteristics.

1. Sensitivity at distances beyond the snow line of $1-4$ au (Tsapras et al., 2016). As described in Section 1.2, snow line is the distance from the central star that is sufficient for volatiles such as water and methane to condense and become solid. For the solar system, the water snow line is located at 2.7 au, in the main belt between Mars and Jupiter. The temperature at which water sublimates is about 170 K. Inside the snow line, water becomes gaseous vapor, while outside the snow line it becomes solid ice. These solid materials that exist outside the snow line provide the material for planet formation. Protoplanets outside the snow line grow to more than 10 Earth mass, enough mass to acquire hydrogen and helium gases by accretion. The snow line can be thought of as a boundary separating the rocky planets from the icy and gaseous planets. Thus, the snow line is an important area for studying planetary formation. Figure 1.1 shows the distribution of planets identified so far, with the orbit length radius normalized by the snow line on the horizontal axis and the planet mass on the vertical axis. The difference in colour is the difference in planetary discovery methods. The letters represent the planets of the solar system. Due to the problem of photometric accuracy in the RV method and the problem of transit probability in the transit method, planetary exploration near the snow line is difficult, and the gravitational microlensing method is complementary to these methods. The direct imaging method is sensitive to planets beyond the snow line, but the gravitational microlensing method has the ability to detect lower-mass planets.

2. The ability to detect planets orbiting a faint (distant from Earth) host star because the brightness of the lens star is not used. Figure 1.5 shows the distribution of distances for the confirmed planets. The horizontal axis is the distance from the earth to the Galactic center in the positive direction, and the vertical axis is the Galactic longitude $l = 90^\circ$ in the positive direction. Figure 1.5 shows that most of the planets farther than 3 kpc from Earth were identified by microlensing. As described in Section 1.3, the formation of planets is related to the amount of metals and other factors, and it has been suggested that the appearance of planets may differ depending on their environments even within the Galaxy. Once we know the distribution of planets far from Earth, we can compare it with the local planetary distribution to study the influence of the Galactic environment on planet formation. The sensitivity of the

microlensing method is maximum at a lens position of approximately half the distance to the source.

3. The ability to detect the host star with almost no bias with respect to its characteristics (e.g., spectral type and activity) because it does not use the brightness of the lens star. This means that planets and their primary stars can be detected in proportion to their true abundance in the Galactic disk. Furthermore, this method can detect free-floating planets, planetary-mass objects that do not orbit a particular primary star.

4. Sensitivity to planets as light as the Earth's mass. The detectability of a planet is governed by the cadences of observations and the finite size of the source. The perturbation time that a lens object gives to the light from the source is proportional to the square root of the mass of the lens object. The perturbation of the light curve for a planet of a Earth mass is ~ 4 hours. For a Jupiter-mass planet, it is ~ 4 days. Therefore, observations at cadences shorter than these times will allow analysis of the features. Note, however, that if the source is too large, as described in Section 2.3.1, the perturbation by the planetary lens will be buried.

1.3 Occurrence and Characteristics

Two parameters exist for the occurrence rate of a planet. One is the fraction of stars with planets per all stars, $F_{\rm h}$. This is an indicator of the number of planetary systems. The other is the average number of planets per all stars $\bar{n}_{\rm p}$. This is an indicator of the number of planets. The results of the Kepler mission have made it possible to statistically study short-period planets in the inner part of the system. According to Howard et al. (2012), the occurrence rate of planets per star $\bar{n}_{\rm p}$ with an orbital period of less than 50 days is 0.130 ± 0.008 for $2R_\oplus \lesssim R_{\rm p} \lesssim 4R_\oplus$, 0.023 ± 0.003 for $4R_\oplus \lesssim R_{\rm p} \lesssim 8R_\oplus$, 0.013 ± 0.002 for $8R_\oplus \lesssim R_{\rm p} \lesssim 32R_\oplus$, and 0.165 ± 0.008 for $2R_\oplus \lesssim R_{\rm p} \lesssim 32R_\oplus$. The radii of Neptune and Jupiter are $R_{\rm Nep} \sim 4R_\oplus$, $R_{\rm Jup} \sim 11R_\oplus$. The occurrence of small planets is relatively high. If observations can be made using both the RV and Transit methods, the orbital inclination can be constrained to be $i \sim 90^\circ$. Furthermore, from the radius and mass of the planet, the density of the planet can be derived. Not only can it distinguish between rocky and gaseous

planets, but it can also distinguish between terrestrial-like rocky planets with thin atmospheres and rocky planets with thick atmospheres. Most planets with radii less than $1.5R_{\oplus}$ have been suggested to have rocky compositions (e.g., Weiss & Marcy, 2014). Fulton et al. (2017) showed from the size distribution of 2025 Kepler planets that the occurrence rate of $R_{\rm p} = 1.5 - 2R_{\oplus}$ planets between super-Earth and sub-Neptune is more than twice deficient at orbital periods $P < 100$ days, and small planets which are close to the host star are divided into two groups, $R_{\rm p} < 1.5R_{\oplus}$ and $R_{\rm p} = 2 - 3R_{\oplus}$. Bashi et al. (2020) using RV data from the High Accuracy Radial velocity Planet Searcher (HARPS: e.g., Mayor et al., 2003) spectrograph with orbital periods of $P = 2 - 100$ days and masses of $1M_{\oplus} \leq M_{\rm p} \sin i \leq 20M_{\oplus}$, showed that the occurrence rate of planetary systems per star $F_{\rm p}$ is $0.23^{+0.04}_{-0.03}$ and the occurrence rate of planets per star $\bar{n}_{\rm p}$ is 0.36 ± 0.05. Neptune's mass is $M_{\rm Neptune} \sim 17M_{\oplus}$.

The occurrence rate of Earth-sized planets in the Habitable Zone (e.g., Petigura et al., 2013; Kopparapu, 2013) is still under debate, although it is estimated to be about 10% for Sun-like (G-type) and 50% for M-type stars. The Habitable Zone (HZ) is located at ~ 1 au around a G-type star and $\gtrsim$0.1 au around an M-type star. The HZ can be further defined by two types of habitable zones: conservative and optimistic (Kopparapu et al., 2013, 2014; Chandler et al., 2016). The inside of the Conservative Habitable Zone (CHZ) is limited by a runaway greenhouse effect and the outside by a maximum greenhouse, and the CHZ of the solar system has an orbital radius of $0.95 - 1.67$ au and a planetary surface temperature of 228-294 K for the solar system. The inner limit of the Optimistic Habitable Zone (OHZ) assumes "recent Venus", the outer limit assumes "early Mars", and the OHZ of the solar system has an orbital radius of $0.5 - 2$ au and a planetary surface temperature of $203 - 405$ K.

Galactic environments may also influence planet formation (Gonzalez et al., 2001; Lineweaver et al., 2004; Spinelli et al., 2021). In fact, radial velocity surveys in the 25 pc region near the Sun reported that the occurrence rate of hot Jupiters is about $\sim 2\%$ (Hirsch et al., 2021), whereas Kepler transit surveys report that the occurrence rate of hot Jupiters around G-type and K-type stars near Cygnus is about $\sim 0.5\%$ (Howard et al., 2012; Santerne et al., 2012, 2016; Fressin et al., 2013).

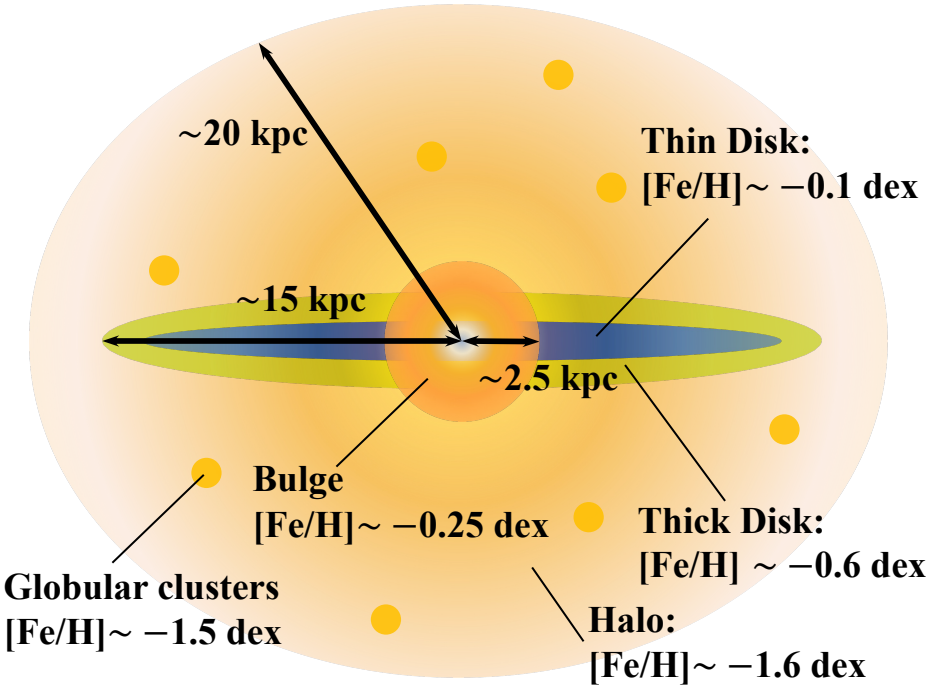

Figure 1.6: Schematic of the Galaxy as seen from the edge-on. The Galaxy consists of the bulge, disk, and halo, with globular clusters inside the halo. The disk is further divided into thick disk and thin disk. These component stars have different metallicity for each population.

Santos et al. (2017) showed that rocky and water planets with significantly different mass fractions of iron and silicate form in different Galactic environments.

The Milky Way consists of an ellipsoid bulge at the center, disk, and halo surrounding the bulge and disk, with globular clusters inside the halo. Figure 1.6 is a schematic of the Milky Way galaxy as seen from the edge-on, showing the metallicity of the bulge, thick disk, thin disk, and halo. Figure 1.7 shows the relationship between distance from the center and metal abundance in the thin disk. In astronomy, elements heavier than helium are called metals, and their abundances are called metallicity. Elemental synthesis in the Big Bang in the early universe produces hydrogen (^{1}H, deuterium D $=^2$ H, and tritium ^{3}H), helium (^{3}He, ^{4}He), trace amounts of lithium (^{7}Li) and beryllium (^{7}Be). Subsequently, the radioactive elements triple hydrogen ^{3}H (half-life 12.3 years) and beryllium ^{7}Be (half-life 53 days) decay radioactively to ^{3}He and lithium ^{7}Li respectively, leaving ^{1}H, D $=^2$ H, ^{3}He, ^{4}He, ^{7}Li remain. The abundance ratios of these elements calculated following the Big Bang theory are consistent with observations and provide an important basis for Big Bang cos-

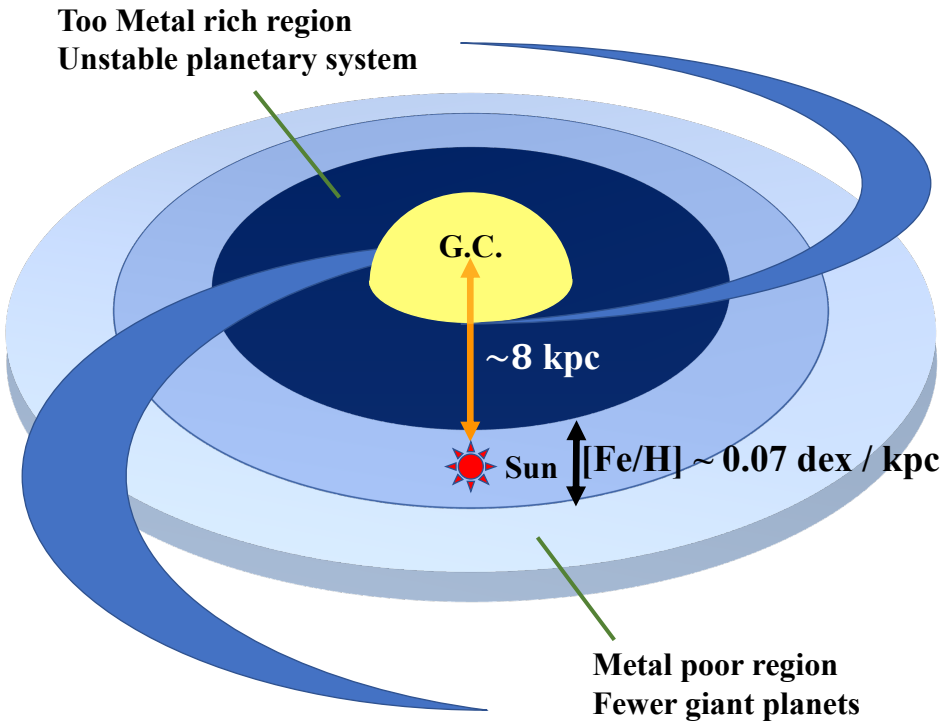

Figure 1.7: Relationship between distance from the Galactic center and metal abundance in the Galaxy's thin disk. The Galactic center is denoted as G.C. In the solar neighborhood, [Fe/H] increases by 0.07 per kpc from the outer to the Galactic center (Gummersbach et al., 1998). From the viewpoints of the occurrence rate and the stability of planetary systems, the Galactic Habitable Zone is expected to be the torus region from the Galactic center including the Sun.

mology. Elements heavier than these elements are produced by elemental synthesis inside the star and subsequent supernova explosions and neutron mergers (Tsujimoto & Shigeyama, 2014). Elements scattered into space by supernovae are reduced to interstellar gas, and stars born from that interstellar gas become more metallicity. This cycle repeats itself, increasing the amount of heavy elements in the galaxy over time. Therefore, metal abundances are important for understanding the star formation history of that stellar population.

The majority of stars comprising the Galactic bulge are older, with few O-, B-, A-, or F-type stars. Metal abundances are $-1.29 \lesssim [\mathrm{Fe/H}] \lesssim +0.51$ with an average value of -0.25 (Fulbright et al., 2006). In the Galactic halo, stars are often older and low-matalicity, with $[\mathrm{Fe/H}] \sim -1.6$ dex (Ryan & Norris, 1991). The Galactic disk of about 15 kpc radius can be classified into a

thin disk with a scale height of 0.3 kpc from the Galactic plane and a thick disk of 1 kpc, with an estimated metallicity of $[\mathrm{Fe/H}] \sim -0.6$ dex for the thick disk (Wyse & Gilmore, 1995). The metallicity of the stars in the thin disk is roughly $[\mathrm{Fe/H}] = -0.1$ (Vickers et al., 2021). In thin disks, the metal content (e.g., [Fe/H]) is higher in the Galactic center and lower in the outer regions because star formation is more active in the Galactic center and Type II SNe occur. In the solar neighborhood (about 8 kpc from the center), $[\mathrm{Fe/H}]$ and $[\mathrm{O/H}]$ drop by about $-0.07 \ \mathrm{dex} \ \mathrm{kpc}^{-1}$ from the Galactic center outward (Gummersbach et al., 1998). For extrasolar galaxies, Large Magellanic Cloud metallicity is estimated to be about 40% of the Galactic mass (Choudhury et al., 2016) and Small Magellanic Cloud metallicity about 10% of the Galactic mass (Choudhury et al., 2018). Giant planets tend to be found around stars with high metallicity (e.g., Santos et al., 2004; Fischer & Valenti, 2005; Sousa et al., 2019). Zhu (2019) shows that giant planets with $R_{\mathrm{p}} > 4R_{\oplus}$ are more likely to occur in stars with metal-rich, that there is no difference in the metallicity of stars with planets of radius $R_{\mathrm{p}} < 4R_{\oplus}$, and that stars with planets have higher metallicity than those without, regardless of the planet mass. Adibekyan et al. (2021) show that there is a correlation between the chemical composition of planets and that of their hosts. Furthermore, the abundance of alpha elements has also been suggested to influence planet formation (Haywood, 2008, 2009; Adibekyan et al., 2012a,b; Bashi et al., 2020). Bashi et al. (2020) studied the occurrence rate of small planets ($1M_{\oplus} \leq M_{\mathrm{p}} \sin i \leq 20M_{\oplus}$) per star for metal-poor stars ($-1 < [\mathrm{Fe/H}] < -0.25$) and showed that stars with large $[\alpha/\mathrm{Fe}]$ had $F_{\mathrm{h}} = 0.30^{+0.09}_{-0.08}$, while stars with smaller $[\alpha/\mathrm{Fe}]$ have $F_{\mathrm{h}} < 0.11$, indicating that $[\alpha/\mathrm{Fe}]$ affects the occurrence rate of small planets. Stars in the thick disk generally have higher $[\alpha/\mathrm{Fe}]$ than stars in the thin disk (e.g., Haywood et al., 2013). In other elemental ratios, Adibekyan et al. (2015) showed that stars with low-mass planets ($< 30M_{\oplus}$) have higher $\mathrm{Mg/Si}$ than stars with giant planets ($> 30M_{\oplus}$).

As for the relationship between planetary system stability and metallicity, Zhu (2019) found that the number of planetary systems simply increases as $[\mathrm{Fe/H}]$ increases, whereas the number of planets plateaus or begins to decrease at $[\mathrm{Fe/H}] = 0$. This may be due to the fact that multi-planet systems are prone to planetary scattering due to their high density and may not be stable (e.g., Matsumura et al., 2013). Furthermore, giant planets around metal-poor stars tend to have low eccen-

tricity (Dawson & Murray-Clay, 2013). Buchhave et al. (2018) showed that Cool Jupiters ($a > 1$ au) with low eccentricity ($e < 0.25$) orbit metal-poor stars on average. Beaugé & Nesvorný (2013) showed that small planets orbiting metal-poor stars ($R_{\rm p} < 4R_{\oplus}$) have longer periods ($P > 5$ days) than small planets orbiting metal-rich stars. Petigura et al. (2018) found that Sup-Neptune with orbital period $P > 10$ days increases the occurrence rate with longer orbital period for $[{\rm Fe/H}] < 0$, whereas the occurrence rate decreases with longer orbital period for $[{\rm Fe/H}] > 0$. This suggests a dynamical influence by a distant orbiting giant planet at $P > 10$ days. In other words, while high metallicities tend to produce giant planets, they also tend to cause planetary scattering. As mentioned above, the relationship between the Galactic environment and metal abundance, and between metal abundance and planet formation, is one important factor in studying the Galactic Habitable Zone (GHZ; Gonzalez et al., 2001; Lineweaver et al., 2004; Spinelli et al., 2021), the area in our Galaxy where life is possible.

1.4 Brown Dwarfs

1.4.1 Properties of Brown Dwarfs

Substellar objects that have sufficient mass for deuterium (D $=^2$ H) nuclear burning but not for light hydrogen (^{1}H) nuclear burning are called brown dwarfs. The mass range of the brown dwarf is about $13 - 80\ M_{\rm Jup}$ (i.e. about $0.012 - 0.08\ M_{\odot}$). After nuclear burning of deuterium, it is cooled by radiation. Brown dwarfs are in fully convection and are composed primarily of metallic hydrogen. The pressure in the brown dwarf's core is 10^5 Mbar and the temperature is $10^4 - 10^6$ K. The atmospheric pressure of a brown dwarf is $1 - 10$ bar and the temperature is below 3000 K. The effective temperatures $T_{\rm eff}$ of brown dwarfs classified by spectra as L-, T-, and Y-type are $T_{\rm eff} = 1400 - 2500$ K, $T_{\rm eff} = 500 - 1400$ K, and $T_{\rm eff} < 500$ K, respectively. Brown dwarfs are degenerate in age and mass, so an old heavy brown dwarf and a light young brown dwarf have the same temperature and luminosity. In general, the radius of a brown dwarf $R_{\rm BD}$ is $R_{\rm BD} \sim 1 R_{\rm Jup}$. The first reliable discovery of brown dwarfs was made by Nakajima et al. (1995) and Oppenheimer et al. (1995). Those two papers were successful not only in direct imaging but also in spectroscopic

observations. This first brown dwarf discovered was Glise 229B, the companion of the M-type star Glise 229, which is about 6 pc from Earth.

1.4.2 Brown Dwarfs as Companions

The majority of brown dwarfs are isolated objects, but about 5% have been detected as wide-orbital companions orbiting main-sequence hosts (Gizis et al., 2001, 2002). Stassun et al. (2006) reported a binary system of brown dwarfs with orbital periods of about 9.78 days, 0.054 ± 0.005 $M_{\odot}$ and 0.034 ± 0.003 $M_{\odot}$. One of the characteristics of brown dwarfs as companions is their low occurrence rate at distances $a < 3 - 4$ au from the host star. This is known as a brown dwarf desert (Marcy & Butler, 2000). Brown dwarf deserts are particularly prominent in the solar-type host stars (Duchêne & Kraus, 2013). Marcy & Butler (2000) show that only less than 0.5% of FGK dwarfs have brown dwarf companions at orbital radii $0 - 3$ au. At orbital distances greater than 50 au, the occurrence rate is 6 ± 4 $\%$ (Neuhäuser & Guenther, 2004). At orbital radii beyond 1000 au, the occurrence rate of brown dwarf companions is the same as that of stellar companions, about 18 $\%$ (Perryman, 2018). In sun-like stars, fewer than 100 brown dwarf companions are known (e.g., Ma & Ge, 2014; Grieves et al., 2017). Grether & Lineweaver (2006) show that brown dwarf companions with orbital periods $P < 5$ years around sun-like stars have an occupancy rate of less than 1 $\%$. Sahlmann et al. (2011) estimated an upper limit of 0.6 $\%$ for the occurrence rate of a close brown dwarf companion around a sun-like star. There are particularly dry regions at $P < 100$ days (e.g., Kiefer et al., 2019, 2021).

Focusing on the mass of brown dwarfs, Grether & Lineweaver (2006) and Ma & Ge (2014) showed that few brown dwarf companion stars have masses of $30 - 55$ $M_{\rm Jup}$ ($0.029 - 0.053$ $M_{\odot}$). Borgniet et al. (2017) derived the occurrence rate of brown dwarfs around A- and F-type stars. The occurrence rate of brown dwarfs with orbital period $P = 1 - 1000$ day is 2Note that the occurrence rate of Jupiter-mass ($1 - 13$ $M_{\rm Jup}$) objects with orbital periods $P = 1 - 1000$ days around $M_{*} = 1.1 - 1.5$ $M_{\odot}$ and $1.5 - 3$ $M_{\odot}$ is 4 $\%$ and 6 $\%$, respectively (Perryman, 2018). The population of brown dwarfs around more massive host stars may be relatively high (Guillot et al., 2014; Troup et al., 2016).

There is still no clear explanation for the origin of brown dwarfs. Some theories attribute this to the inward movement of the brown dwarf's orbit and the resulting merger with the host star (Armitage & Bonnell, 2002), while others attribute it to differences in the formation processes of planets and brown dwarfs (Matzner & Levin, 2005). Duchêne & Kraus (2013) showed that tidal interactions with the host star may be forming brown dwarf deserts.

Most detections of brown dwarf companions are based on RV methods or direct imaging, and few brown dwarf companions have been found in regions far from Earth, such as the Galactic bulge region. As described further in Chapters 3 and 4, if brown dwarf companions in the center of the galaxy are discovered by gravitational microlensing and other methods, and if we can determine the occurrence rate of brown dwarf companions in environments different from those in the neighborhood, we may be able to study the effect of the Galactic environment on brown dwarf formation by comparing it with the frequency of brown dwarfs in the neighborhood.

Chapter 2

Gravitational Microlensing

About 150 planets and brown dwarfs have been confirmed so far by the gravitational microlensing method. This method can approach parameters such as planetary mass and orbital radius. As described in Section 1.2.4, the gravitational microlensing method has complementary capabilities to other methods, such as sensitivity to planets far from the Earth and beyond the snow line. Since it does not use light from lens objects, it can also detect free-floating planets. This chapter describes the details of the gravity microlensing method. Section 2.1 describes a brief history. Section 2.2 describes the principles. Section 2.3 describes higher-order effects. Section 2.4 describes extended methods.

2.1 Brief History

Einstein (1936) reported the theory that light is bent by gravity. If the mass of the gravitational source is on the scale of a galaxy or galaxy cluster, the image of the background object will be split or distorted. When the mass of the gravitational source is on the stellar scale, the order of the separation angle of the image of the background star is about 1 mas, well below the resolution of typical ground-based instruments. The term microlens was introduced by Paczynski (1986a). The motivation for the first microlensing survey was to look for evidence of dark matter in the Galactic haloes (Gott, 1981; Paczynski, 1986b). Since 1993, the EROS (Expérience de Recherche d'OBjet

Sombres: Aubourg et al., 1993), OGLE (Optical Gravitational Microlensing: Udalski et al., 1993), MACHO (Massive Compact Halo Objects: Alcock et al., 1993), DUO (Disk Unseen Objects: Alard, 1996), MOA (Microlensing Observations in Astrophysics: Muraki et al., 1999) conducted large-scale microlensing projects surveying millions of stars.

Observations by the MACHO group toward the Large Magellanic Cloud (LMC) suggested that about 20% of the dark matter in the Galaxy is stellar-mass objects (Alcock et al., 2000). On the other hand, results from the EROS group suggested that much of the excess microlensing may be due to stars within the LMC itself (Tisserand et al., 2007).

With most of the constraints on dark matter resolved, the focus of observations then turned to exoplanets. Mao & Paczynski (1991) and Gould & Loeb (1992) studied the theory of gravitational microlensing effects when one or more planets orbit the main lens and showed that even low-mass planets can be detected. In addition, Gould & Loeb (1992) found that perturbations from lensing planets are detected about 17% of the time for Jupiter-type planets (about 5 au from the host star) and about 3% of the time for Saturn-type planets. These probabilities occur especially when the planet is between about $0.6 - 1.6\ R_{\rm E}$. where $R_{\rm E}$ is the Einstein radius. Subsequently, determined detection probabilities (Bolatto & Falco, 1994), extended to Earth-mass planets including the effect of finite source sizes (Bennett & Rhie, 1996; Wambsganss, 1997), determined physical parameters (Gaudi & Gould, 1997), determined realistic observation detection rates in programs (Peale, 1997; Gaudi & Sackett, 2000), distinguishing between binary sources and planetary perturbations (Gaudi, 1998; Jung et al., 2017), simulating high-magnitude events (Rattenbury et al., 2002), the effects of wide-orbit planets (Han & Kang, 2003; Han et al., 2005), the effects of multiple planets (Han, 2005), and other theoretical issues and simulations were studied. The first reliable microlensing planet OGLE-2003-BLG-235Lb/MOA-2003-BLG-53Lb was confirmed by the MOA and OGLE groups in 2003 (Bond et al., 2004). Subsequently, (Gaudi et al., 2008) reported the first multi-planet microlens event OGLE-2006-BLG-109. The first gravitational microlensing habitable planet candidate MOA-2011-BLG-293Lb was detected in 2011 (Yee et al., 2012; Batista et al., 2014). Bennett et al. (2014) reported a system of sub-Earth Mass satellites orbiting around a 4 Jupiter-mass free-floating planetary candidate. Bennett et al. (2016) confirmed

the first circumstellar microlensing planet OGLE-2007-BLG-349(AB)b. Scheduled for launch in May 2027, Roman is NASA's flagship mission selected for the 2010 astronomy and astrophysics decadal survey. Microlensing observations of the Galactic center region will be performed for approximately 1.2 years. As a result, it is estimated that about 1,400 microlensing planets will be discovered, of which about 200 are expected to be $3M_{\oplus}$ or less (Penny et al., 2019). Sajadian (2021) predicted that 35 planets whose projected orbital distance are in the Optimistic Habitable Zone (see 1.3) were detected by Roman, of which about one is below $10M_{\oplus}$.

2.2 Principles

2.2.1 Single Lens Equation

The analytical formula for gravitational microlensing was derived by Refsdal (1964). Consider the arrangement shown in Figure 2.1. The light from the source passes a distance r away from the lensing object, is bent by the gravity of the lens object, and reaches the observer. In this state, the deflection angle $\alpha_{\rm GR}$ of the bent ray can be written as follows (e.g., Will, 1993):

$$\alpha_{\rm GR} = \frac{4{\rm G}M_{\rm L}}{{\rm c}^2{\rm r}} = \frac{2R_{\rm S}}{r}, \tag{2.1}$$

where $M_{\rm L}$ is the mass of the lens object, G is the gravitational constant, and c is the speed of light, $R_{\rm S}$ is the Schwarzschild radius and $R_{\rm S} \ll r$. The Schwarzschild radius $R_{\rm S}$ can be expressed as follows:

$$R_{\rm S} = \frac{2{\rm G}M_{\rm L}}{{\rm c}^2}. \tag{2.2}$$

As shown in Figure 1.4, $D_{\rm L}$ and $D_{\rm S}$ are the distance from the observer to the lens object and the distance from the observer to the source object, respectively. The value $D_{\rm LS}$ is the distance between the lens and the source, $D_{\rm LS} = D_{\rm S} - D_{\rm L}$. The angle $\theta_{\rm S}$ is the separation angle between the lens and the source, and $\theta_{\rm I}$ is the separation angle between the lens and Image [+]. Both are small angles

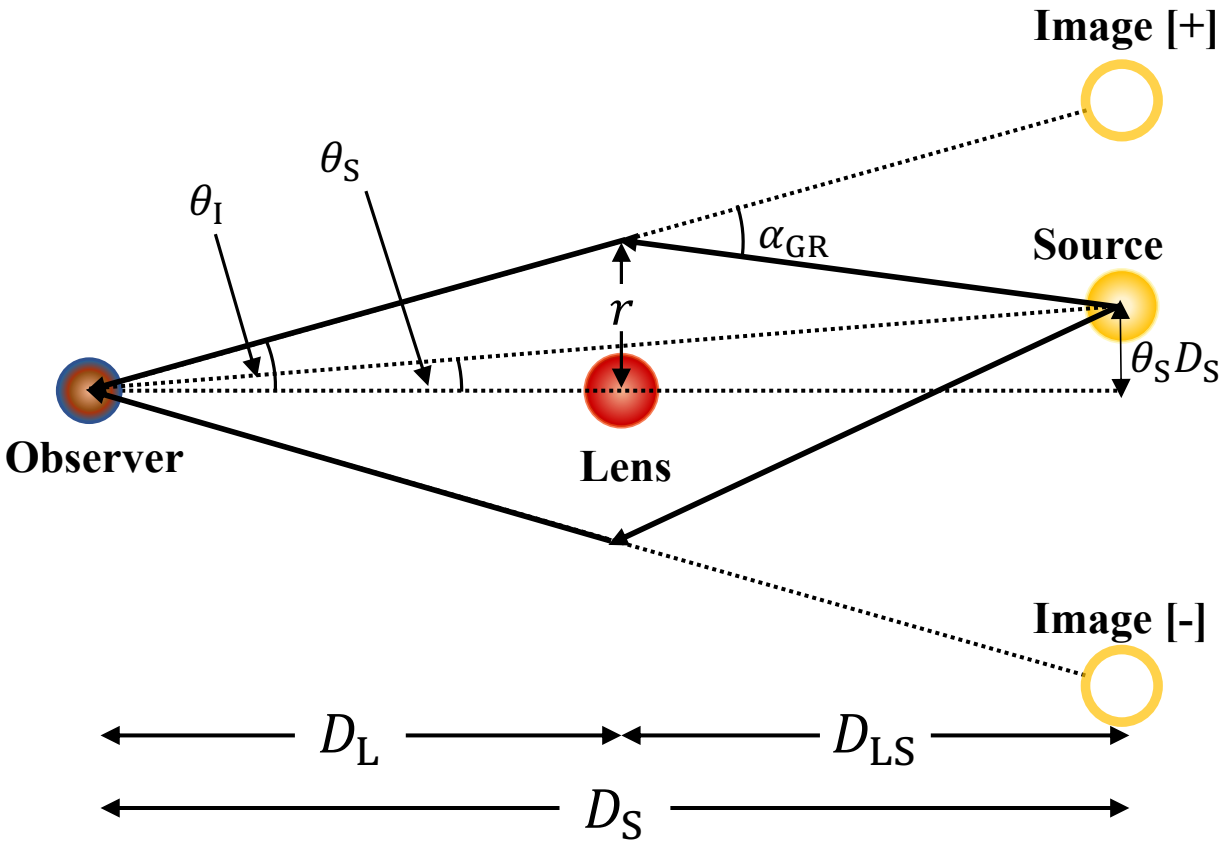

Figure 2.1: Schematic diagram of microlensing events. The distance from the observer to the lensing object is $D_{\rm L}$ and the distance from the observer to the source object is $D_{\rm S}$. The distance between the lens and the light source is $D_{\rm LS}$, where $D_{\rm LS} = D_{\rm S} - D_{\rm L}$. The light from the source is bent by an angle $\alpha_{\rm GR}$ due to the gravity of the lens object and reaches the observer. The separation angle between the lens source and the source is $\theta_{\rm S}$, and the separation angle between the lens source and the image is $\theta_{\rm I}$.

because the lens and the source are far away from the observer. Thus, it can be approximated as follows:

$$\sin\theta_{\rm S} \sim \theta_{\rm S}, \tag{2.3}$$

$$\sin\theta_{\rm I} \sim \theta_{\rm I}, \tag{2.4}$$

$$\theta_{\rm S} D_{\rm S} = \frac{D_{\rm S}}{D_{\rm L}} r - \alpha_{\rm GR} D_{\rm LS} = \frac{D_{\rm S}}{D_{\rm L}} r - \frac{2R_{\rm S}}{r} D_{\rm LS}. \tag{2.5}$$

By dividing both sides of Equation 2.5 by $D_{\rm S}$ and substituting $\theta_{\rm I} = r/D_{\rm L}$, $\theta_{\rm S}$ can be expressed as,

$$\theta_{\rm S} = \theta_{\rm I} - 2R_{\rm S} \frac{D_{\rm LS}}{D_{\rm L} D_{\rm S}} \frac{1}{\theta_{\rm I}}. \tag{2.6}$$

Equation 2.6 is the lens equation and is quadratic in $\theta_{\rm I}$, which means that there are two images (solutions). By relativity, the Einstein radius $R_{\rm E}$, the radius of the Einstein ring, and its angular radius $\theta_{\rm E}$ can be expressed as follows:

$$\theta_{\rm E} = \left[2R_{\rm S} \frac{D_{\rm LS}}{D_{\rm L} D_{\rm S}} \right]^{\frac{1}{2}} = \left[\frac{4{\rm G}M_{\rm L}}{{\rm c}^2} \frac{D_{\rm LS}}{D_{\rm L} D_{\rm S}} \right]^{\frac{1}{2}}, \tag{2.7}$$

$$r_{\rm E} = \theta_{\rm E} D_{\rm L} = \left[2R_{\rm S} \frac{D_{\rm L} D_{\rm S}}{D_{\rm LS}} \right]^{\frac{1}{2}}, \tag{2.8}$$

where Equation 2.2 is used. Substituting typical values for Equations 2.7 and 2.8 yields the following,

$$\begin{aligned} \theta_{\rm E} &\sim 1.0 \left(\frac{M_{\rm L}}{M_\odot} \right)^{\frac{1}{2}} \left(\frac{D_{\rm L}}{4{\rm kpc}} \right)^{-\frac{1}{2}} \left(\frac{D_{\rm S}}{8{\rm kpc}} \right)^{-\frac{1}{2}} \left(\frac{D_{\rm LS}}{8{\rm kpc}} \right)^{\frac{1}{2}} {\rm mas} \\ &\sim 0.3 \left(\frac{M_{\rm L}}{0.3M_\odot} \right)^{\frac{1}{2}} \left(\frac{D_{\rm L}}{6{\rm kpc}} \right)^{-\frac{1}{2}} \left(\frac{D_{\rm S}}{8{\rm kpc}} \right)^{-\frac{1}{2}} \left(\frac{D_{\rm LS}}{2{\rm kpc}} \right)^{\frac{1}{2}} {\rm mas}, \end{aligned} \tag{2.9}$$

$$\begin{aligned} r_{\rm E} &\sim 4.1 \left(\frac{M_{\rm L}}{M_\odot} \right)^{\frac{1}{2}} \left(\frac{D_{\rm L}}{4{\rm kpc}} \right)^{\frac{1}{2}} \left(\frac{D_{\rm S}}{8{\rm kpc}} \right)^{-\frac{1}{2}} \left(\frac{D_{\rm LS}}{8{\rm kpc}} \right)^{\frac{1}{2}} {\rm au} \\ &\sim 2.3 \left(\frac{M_{\rm L}}{0.3M_\odot} \right)^{\frac{1}{2}} \left(\frac{D_{\rm L}}{6{\rm kpc}} \right)^{\frac{1}{2}} \left(\frac{D_{\rm S}}{8{\rm kpc}} \right)^{-\frac{1}{2}} \left(\frac{D_{\rm LS}}{2{\rm kpc}} \right)^{\frac{1}{2}} {\rm au}. \end{aligned} \tag{2.10}$$

From Equations 2.6, 2.7, and 2.8, the lens equation can be expressed as follows:

$$\theta_{\mathrm{I}}^2 - \theta_{\mathrm{S}}\theta_{\mathrm{I}} - \theta_{\mathrm{E}}^2 = 0. \tag{2.11}$$

Thus, the two solutions of the image are as follows:

$$\theta_{+,-} = \frac{1}{2}\left(\theta_{\mathrm{S}} \pm \sqrt{{\theta_{\mathrm{S}}}^2 + 4{\theta_{\mathrm{E}}}^2}\right). \tag{2.12}$$

From Equation 2.12, the separation angle $\Delta\theta$ between the two images can be expressed as,

$$\Delta\theta \equiv \theta_+ - \theta_- = \sqrt{{\theta_{\mathrm{S}}}^2 + 4{\theta_{\mathrm{E}}}^2}. \tag{2.13}$$

If the observer, lens source and source object are aligned ($\theta_{\mathrm{S}} = 0$), the two images merge to form an Einstein ring with angular radius θ_{E}. As described in Section 2.1, a typical Einstein angular radius of ~ 1 mas or less is far below the angular resolution of current telescopes, making it impossible to resolve the two images.

The plane perpendicular to the line of sight that includes the lens object is called the lens plane, and the plane that includes the source is called the source plane. Figure 2.2 shows the source and source image in the lens plane. Magnification is defined as the ratio of the solid angle of the image to the solid angle of the source. Defining the solid angle of the source as $d\Omega$, the solid angle of the Image [+] as $d\Omega_+$, and the solid angle of the Image [-] as $d\Omega_-$, the magnification rate $A_\pm$ can be expressed as follows:

$$A_\pm = \left|\frac{d\Omega_\pm}{d\Omega}\right| = \left|\frac{u_\pm d\theta du_\pm}{u d\theta du}\right| = \left|\frac{u_\pm du_\pm}{u du}\right|. \tag{2.14}$$

The separation angle between the lens and the source θ_{S}, and between the lens and the source image $\theta_\pm$, are expressed in units of Einstein radius as follows:

$$u \equiv \frac{\theta_{\mathrm{S}}}{\theta_{\mathrm{E}}}. \tag{2.15}$$

$$u_\pm \equiv \frac{\theta_\pm}{\theta_{\mathrm{E}}}. \tag{2.16}$$

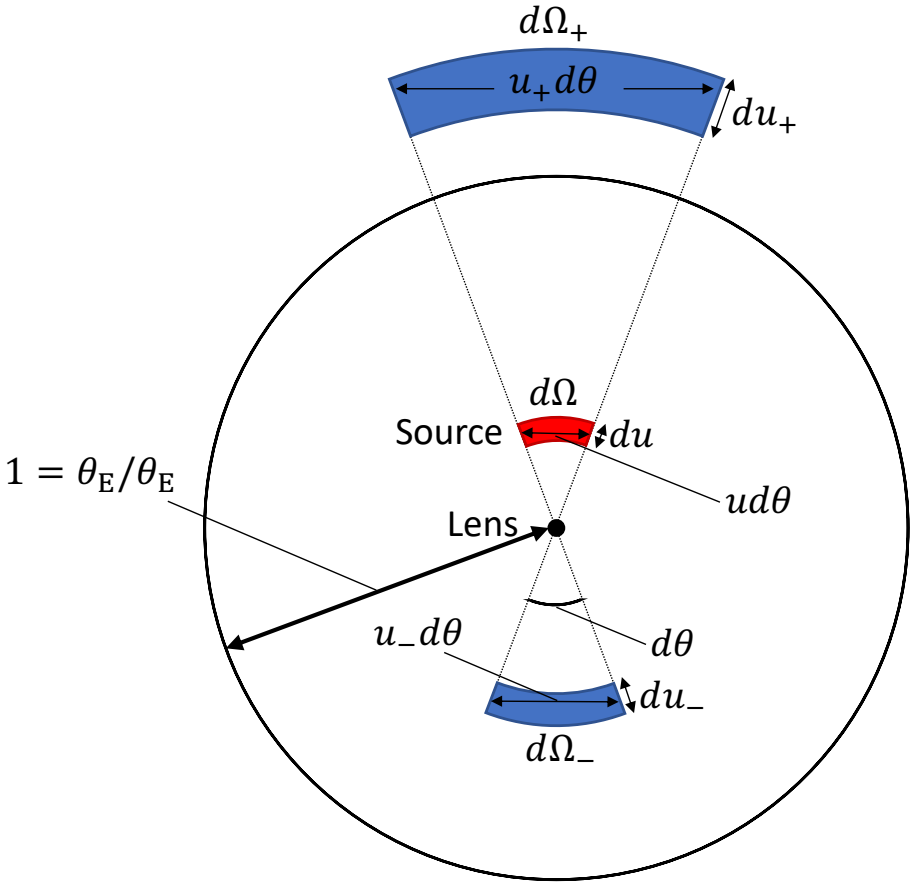

Figure 2.2: Schematic diagram for source and source image in the lens plane. The separation angle from the lens to the source is defined as u normalized by the Einstein angle radius. The red area shows the solid angle of the source and the blue area shows the solid angle of the source image.

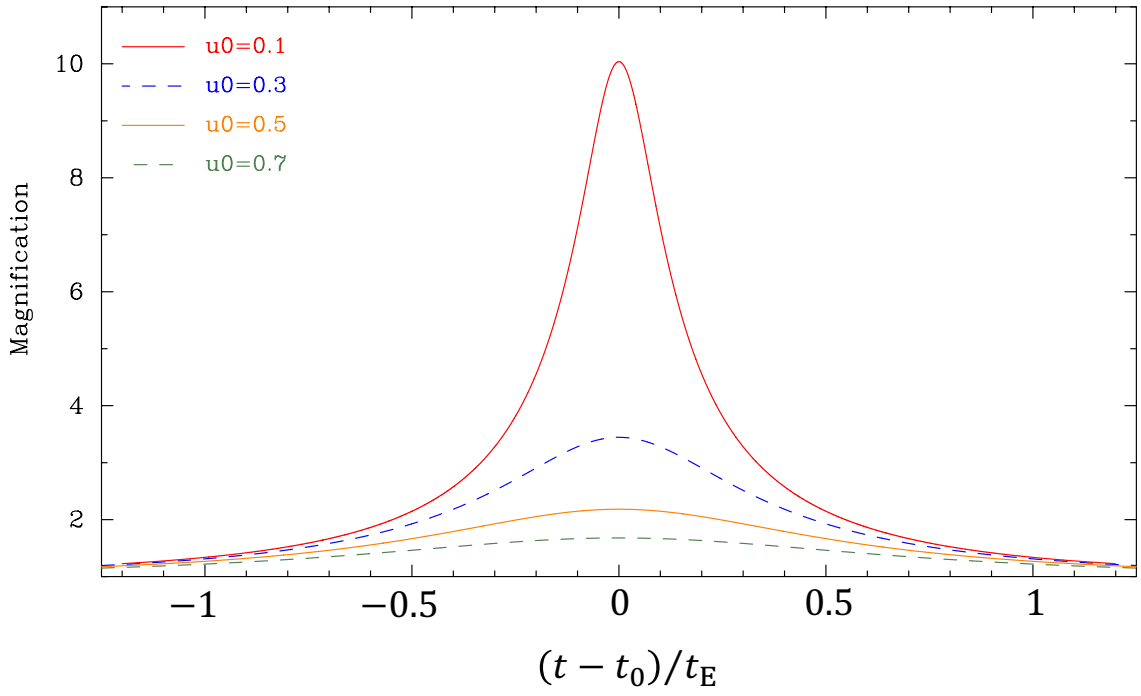

Figure 2.3: Relationship between u and magnification. Horizontal axis is time and vertical axis is magnification rate. The difference between the lines is the difference in u_0: $u_0 = 0.1$ for the red solid line, $u_0 = 0.3$ for the blue dashed line, $u_0 = 0.5$ for the yellow solid line, and $u_0 = 0.7$ for the green dashed line, respectively. The smaller u_0 is, the higher the magnification.

From, Equations 2.12, 2.14, 2.15 and 2.16, the following equation is derived,

$$\frac{u_\pm}{u} = \frac{1}{2}\left(1 \pm \frac{1}{u}\sqrt{u^2+4}\right), \tag{2.17}$$

$$\frac{du_\pm}{du} = \frac{1}{2}\left(1 \pm \frac{u}{\sqrt{u^2+4}}\right), \tag{2.18}$$

$$A_\pm = \frac{1}{2}\left(\frac{u^2+2}{u\sqrt{u^2+4}} \pm 1\right), \tag{2.19}$$

$$A \equiv A_+ + A_- = \frac{u^2+2}{u\sqrt{u^2+4}}. \tag{2.20}$$

Figure 2.3 shows the relationship between u and magnification. The horizontal axis is time, normalized by the time t_E that the relative velocity $v_\perp$ of the lens and the source crosses the

Einstein radius. t_0 is the time at which u is at its minimum. Figure 2.3 plots the model curves for $u_0 = 0.1,\ 0.3,\ 0.5,\ 0.7$. The red solid line is $u_0 = 0.1$, the blue dashed line is $u_0 = 0.3$, the yellow solid line is $u_0 = 0.3$, the green dashed line is $u_0 = 0.7$. As can be seen from Figure Figure 2.3, when u_0 is small (i.e., when the source passes close to the lens in the lens plane), the magnification increases. The magnification at $u = 1$ ($A \sim 1.34$) is considered the threshold to be a microlensing event. If the observer, lens, and source are almost aligned in a straight line, $u \to 0$ and the following is obtained,

$$\frac{u^2+2}{u\sqrt{u^2+4}} \to \frac{1}{u} \,(\text{as } u \to 0). \tag{2.21}$$

If the solid angle of the source is infinitesimal, the magnification rate $A = \infty$ for $u = 0$. Also, $u \to \infty$ is as follows:

$$\lim_{u\to\infty} \frac{u^2+2}{u\sqrt{u^2+4}} = \frac{1+4(\frac{1}{u^2})+(\frac{1}{u^2})}{1+4(\frac{1}{u^2})} \sim 1. \tag{2.22}$$

If the source is not a point but has a finite size, as described in Section 2.3.1, even if one small area of the source has $u = 0$, the other small areas have $u \neq 0$, thus $d\Omega$ is also not $d\Omega = 0$. Therefore, if the source has a finite magnitude, the magnification factor will have a finite magnitude even if $u \to 0$. The observed flux $f(t)$ of microlensing lensing events can be expressed as in Equation 3.2 using the magnification rate A, the flux f_s of the source, and the unmagnified flux f_b on the line of sight. Figure 2.4, u can be expressed as follows using the Einstein radius crossing time $t_{\rm E}$, the minimum separation u_0 between the source and the lens center of mass, and the time t_0 at which u becomes u_0,

$$u(t) = \left(\left[\frac{t-t_0}{t_{\rm E}} \right]^2 + u_0^2 \right)^{\frac{1}{2}}, \tag{2.23}$$

where $t_{\rm E}$ is called the event timescale. The event timescale $t_{\rm E}$ can be expressed as follows from relationship between Einstein's radius $r_{\rm E}$ and the relative velocity of the lens and source perpendicular to the line of sight $v_\perp$, or from the relationship between $\theta_{\rm E}$ and the relative angular velocity of the lens and source perpendicular to the line of sight $\mu_{\rm rel}$,

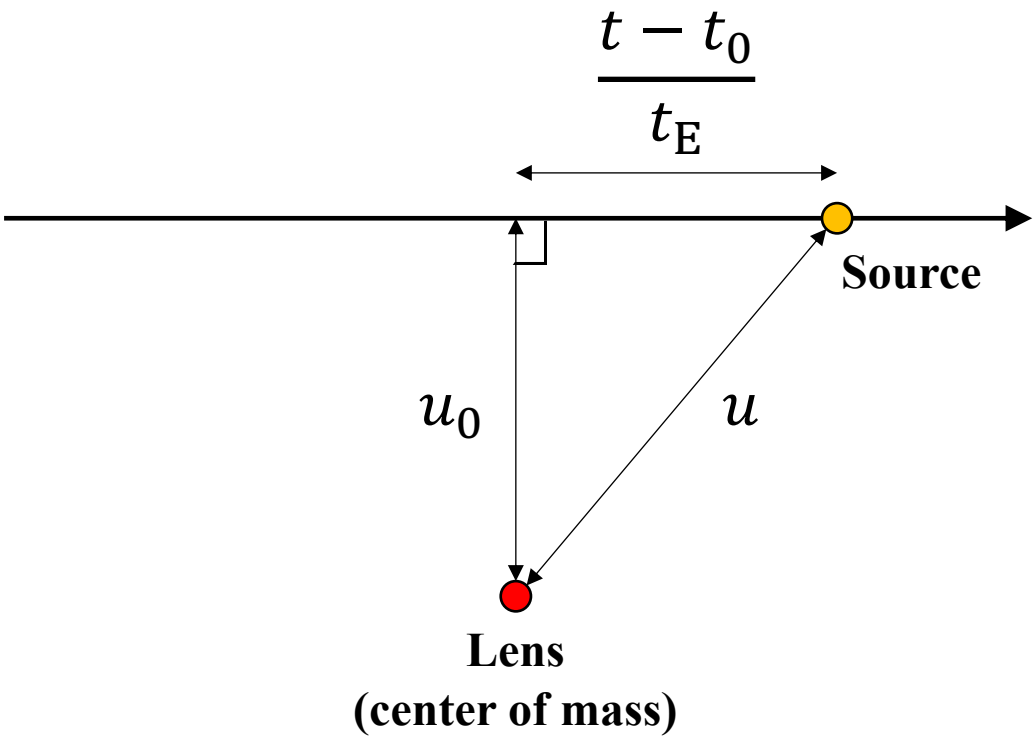

Figure 2.4: Schematic diagram of u_0 and u. Due to the relative proper motion of the lens and the source, u varies with time. The minimum separation angle between the source and lens normalized by the Einstein angle radius is u_0, the time at which the separation angle between the source and the lens is minimized is t_0, and the time it takes for the source to cross the Einstein radius is $t_{\rm E}$.

$$\begin{aligned} t_{\rm E} &= \frac{r_{\rm E}}{v_\perp} = \frac{\theta_{\rm E}}{\mu_{\rm rel}} \\ &\sim 35 \left(\frac{M_{\rm L}}{M_\odot}\right)^{\frac{1}{2}} \left(\frac{D_{\rm L}}{4\ {\rm kpc}}\right)^{\frac{1}{2}} \left(\frac{D_{\rm S}}{8\ {\rm kpc}}\right)^{-\frac{1}{2}} \left(\frac{D_{\rm LS}}{4\ {\rm kpc}}\right)^{\frac{1}{2}} \left(\frac{v_\perp}{200\ {\rm km\ s^{-1}}}\right)^{-1} {\rm days}, \end{aligned} \tag{2.24}$$

where Equation 2.2 is used to transform the equation. Equation 2.24 shows that $t_{\rm E}$ is proportional to the square root of the lens mass. Under conditions where the source is 8 kpc away from the bulge center, 4 kpc from the Earth to the lens, and the lens mass is 1 solar mass, $t_{\rm E}$ is about 35 days.

2.2.2 Binary Lens Equation

Gravitational microlensing events in which the lens is a binary or planetary system are called binary lens events. The basic properties of binary lenses were studied by Schneider & Weiss (1986), and the first example of a binary lens light curve was given by Mao & Paczynski (1991). For binary lenses, three parameters are added to the parameters $(t_{\rm E}, t_0, u_0)$ in the single lens equation. These are: the ratio of the lens companion mass $M_{\rm C}$ to the lens host mass $M_{\rm H}$, $q = M_{\rm C}/M_{\rm H}$; the separation between the lens host and lens companion $a_\perp$ projected onto a plane perpendicular to the observer and normalized by the Einstein radius $r_{\rm E}$, $s = a_\perp/r_{\rm E}$; and the angle of incidence of the source relative to the line connecting the lens components, α. These three parameters make the light curve of a binary lens diverse. As can be seen from Euation 2.24, the event time scale $t_{\rm E}$ is scaled by $q^{1/2}$. Typically, perturbations due to planetary lensing appear in the light curves for about 4 days for Jupiter masses and 4 hours for Earth masses.

Figure 2.5 shows the configuration of a binary lens event. For binary lens events, the light from the source is affected by the gravity of the two lens objects. Considering the refraction angle $\alpha_{\rm GR}$ of a light ray as a composite of the effects of bending in the direction of each mass point, it can be expressed as follows:

$$\overrightarrow{\alpha_{\rm GR}} = \sum_{i=1}^{2} \frac{4GM_i}{c^2|\overrightarrow{r_i}|^2}\overrightarrow{r_i}, \tag{2.25}$$

where $\overrightarrow{r_i}$ is the position of the image if bent only by the gravity of lens i and M_i is the mass of lens i. When a source that should be visible at $\overrightarrow{r_0}$ is shifted by $D_{\rm LS}\overrightarrow{\alpha_{\rm GR}}$ due to the gravity of two lenses and appears as an image at $\overrightarrow{r} = \overrightarrow{r_i} + \overrightarrow{a_i}$, the following equation can be expressed from Figure 2.5,

$$\begin{aligned}
\overrightarrow{r} - \overrightarrow{r_0} &= \frac{D_{\rm L}D_{\rm LS}}{D_{\rm S}}\overrightarrow{\alpha_{\rm GR}} \\
&= \frac{4G}{c^2}\frac{D_{\rm L}D_{\rm LS}}{D_{\rm S}}\sum_{i=1}^{2} M_i\frac{\overrightarrow{r} - \overrightarrow{a_i}}{|\overrightarrow{r} - \overrightarrow{a_i}|^2} \\
&= R_{\rm E}^2\sum_{i=1}^{2}\frac{M_i}{M_{\rm L}}\frac{\overrightarrow{r} - \overrightarrow{a_i}}{|\overrightarrow{r} - \overrightarrow{a_i}|^2},
\end{aligned} \tag{2.26}$$

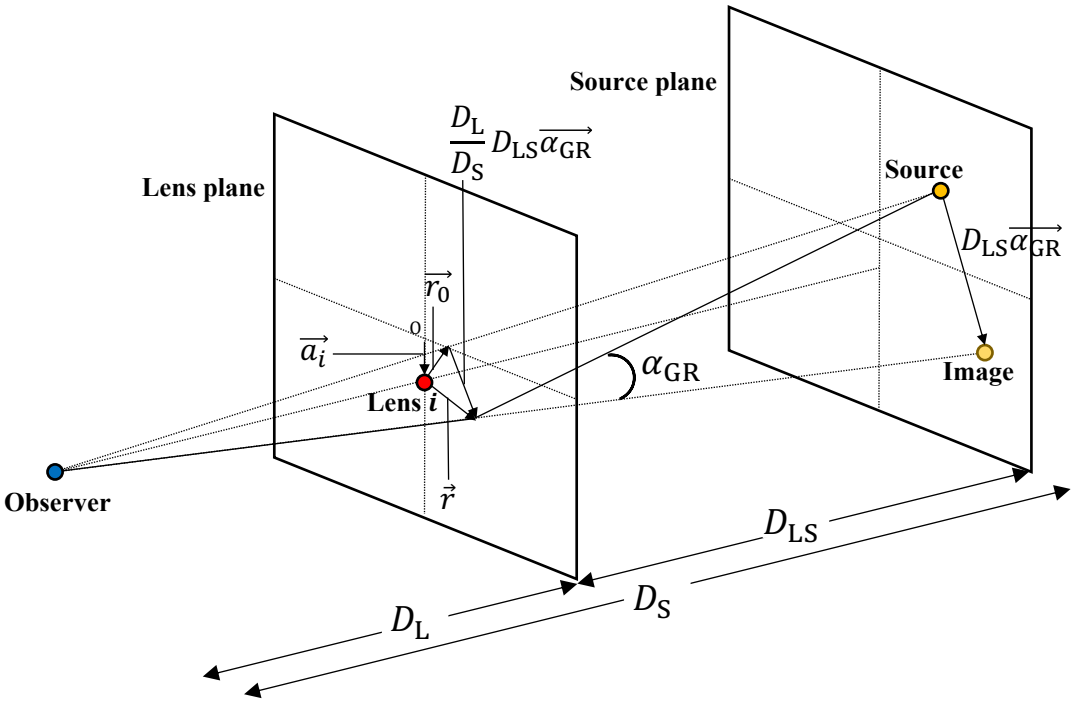

Figure 2.5: Schematic diagram of a binary lens. Of the planes perpendicular to the observer, the plane containing the lens object is called the lens plane, and the plane containing the source object is called the source plane. Although there are two lens objects in the binary lens event, one of them is omitted for the sake of clarity in the figure. A source that should be observed at $\overrightarrow{r_0}$ is shifted by $D_{\rm LS}\overrightarrow{\alpha_{\rm GR}}$ due to the gravity of two lenses and appears as an image at $\overrightarrow{r}$. The position vector of lens i is $\overrightarrow{a_i}$.

where Equations 2.2 and 2.8 are used. The value $M_{\rm L}$ is the total lens mass. Further introducing $\boldsymbol{y} = \overrightarrow{r}/r_{\rm E}$, $\boldsymbol{u} = \overrightarrow{r_0}/r_{\rm E}$, $\boldsymbol{y_i} = \overrightarrow{a_i}/r_{\rm E}$, and the ratio of the mass M_i of each lens component in the total lens mass $M_{\rm L}$, $\epsilon_i = M_i/M_{\rm L}$, the following equation can be expressed,

$$\boldsymbol{y} - \boldsymbol{u} = \sum_{i=1}^{2} \epsilon_i \frac{\boldsymbol{y} - \boldsymbol{y_i}}{|\boldsymbol{y} - \boldsymbol{y_i}|^2}, \tag{2.27}$$

$$\boldsymbol{u} = \boldsymbol{y} - \sum_{i=1}^{2} \epsilon_i \frac{\boldsymbol{y} - \boldsymbol{y_i}}{|\boldsymbol{y} - \boldsymbol{y_i}|^2}, \tag{2.28}$$

Solving Equation 2.28 for $\boldsymbol{y}$ allows us to compute the position of the source image from the position of the source. If the lens component N_{L} is two, $\boldsymbol{y}$ in Equation 2.28 has five solutions (i.e., it is a fifth-order equation), so at most five images appear. For $N_{\mathrm{L}} \geq 2$, a number no greater than $5(N_{\mathrm{L}} - 1)$ (and generally less) is the number of true solutions to the lens equation (Gaudi, 2012). In general analysis, vectors are converted to complex numbers so that they can be treated as scalar quantities, and the position of the image is calculated numerically. Equation 2.28 in complex coordinates, the lens equation can be expressed as,

$$\begin{aligned} \xi &= z - \sum_{i=1}^{2} \epsilon_i \frac{z - z_i}{|z - z_i|^2} \\ &= z - \sum_{i=1}^{2} \epsilon_i \frac{1}{\bar{z} - \bar{z_i}}, \end{aligned} \tag{2.29}$$

where $\xi = (u_1,\ u_2)$ is the source position, $z = (y_1,\ y_2)$ is the image position, and $\bar{z}$ and $\bar{z_i}$ are the complex coefficients of z and z_i, respectively. Considering that Eqquation 2.29 is the mapping $(z \to \xi(z))$ from the small area element of the image to the small area element of the source, from Witt (1990), the Jacobian J of this mapping and its determinant $\det J$ are as follows:

$$J = \begin{bmatrix} \frac{\partial \xi}{\partial z} & \frac{\partial \xi}{\partial \bar{z}} \\ \frac{\partial \bar{\xi}}{\partial z} & \frac{\partial \bar{\xi}}{\partial \bar{z}} \end{bmatrix}, \tag{2.30}$$

$$\det J = \left(\frac{\partial \xi}{\partial z}\right)^2 - \frac{\partial \xi}{\partial \bar{z}} \frac{\partial \bar{\xi}}{\partial \bar{z}}. \tag{2.31}$$

From Equations 2.29 and 2.31, the following equation is obtained,

$$\det J = 1 - \left| \sum_{i=1}^{2} \frac{\epsilon_i}{(\bar{z} - \bar{z_i})^2} \right|^2 \tag{2.32}$$

Since J was the Jacobian of the mapping from the small area element to the small area element of the source, $\det J$ is the area of the source divided by the area of the image. The magnification is the area of the image divided by the area of the source. Therefore, it can be shown by the following equation,

$$A = \frac{1}{|\det J|}. \tag{2.33}$$

For a multiple lenses event with $N_{\rm L}$ lenses, Equations 2.28, 2.29, and 2.32 are as follows:

$$\boldsymbol{u} = \boldsymbol{y} - \sum_{i=1}^{N_{\rm L}} \epsilon_i \frac{\boldsymbol{y} - \boldsymbol{y_i}}{|\boldsymbol{y} - \boldsymbol{y_i}|^2}, \tag{2.34}$$

$$\xi = z - \sum_{i=1}^{N_{\rm L}} \epsilon_i \frac{1}{\bar{z} - \bar{z_i}}, \tag{2.35}$$

$$\det J = 1 - \left| \sum_{i=1}^{N_{\rm L}} \frac{\epsilon_i}{(\bar{z} - \bar{z_i})^2} \right|^2. \tag{2.36}$$

The properties and degeneracies of the system with three lenses are studied in detail in Song et al. (2014).

2.2.3 Caustic and Critical Curve

From the Equation 2.33, $\det J \to 0$ and diverges to $A \to \infty$. For a single lens, $u = 0$ (i.e., when observer-lens-source is aligned in a straight line), $\det J = 0$. For binary lenses, the following equation is obtained for $\det J = 0$ from Equation 2.32,

$$\left| \sum_{i=1}^{N_{\rm L}} \frac{\epsilon_i}{(\bar{z} - \bar{z_i})^2} \right|^2 = 1. \tag{2.37}$$

In other words, considering a circle of radius 1 in the complex plane, it can be expressed as follows using Euler's formula,

$$e^{i\phi} = \sum_{i=1}^{N_{\rm L}} \frac{\epsilon_i}{(\bar{z} - \bar{z_i})^2}. \tag{2.38}$$

By integrating Equation 2.38 with $0 < \phi < 2\pi$, the position z of the source image where $\det J = 0$ is a closed curve. A closed curve consisting of a series of source image positions z where $\det J = 0$ is called a critical curve. For a single lens, the critical curve coincides with the Einstein ring. The closed curve with a series of source positions ξ corresponding to the critical curve is called caustic.

That is, if the point source is on caustic, the magnification rate A diverges infinitely. The caustic curve of a binary lens consists of cusps and folds, which are concave sections connected on the cusp.

Figures 2.6 shows the magnification maps of the binary lens system for different q which is the mass ratio of the companion to host, and s which is the distance between the host and the companion projected in a plane perpendicular to the line of sight normalized by the Einstein radius. Each (q, s) is shown in the upper left corner of each panel. The primary lens (host) is shown at the origin and the planet are shown on the positive side of the x-axis. The black filled circle at $(x, y) = (0, 0)$ in each panel is the primary star of the lens system, the black filled circles at $(x, y) = (0.8, 0)$ (upper panel), $(x, y) = (1, 0)$ (middle panel) and $(x, y) = (1.3, 0)$ (lower panel) are the companion stars of the lens system, the black curve is critical curve and the red curve is caustic. The shading of the colour bar indicates the magnification rate. The shape and size of the caustics depend on q and s. As can be seen from the Figure (caustic and critical curve), the magnification rate is higher around the caustic. As the source crosses or approaches the caustic, a sudden change in magnification rate occurs, appearing as a spike-like perturbation on the light curve. This feature, called anomaly, is important in the interpretation of the light curves of binary lens events because it allows for the estimation of the shape of the caustics (i.e., lens parameters q and s) and the angle of incidence α.

For binary lens events, two of the solutions to the (complex) fifth-order lens equation in Equation 2.35 are pseudo, and the caustics indicate the boundaries of the region in the source plane where three or five images exist. When the source is inside the caustic, five images appear. When the source is outside the caustic, three images appear. The thresholds value of q, s that determines the form of the caustics is given by Dominik (1999) as follows:

$$s_{\rm c} = \left\{ \frac{\left[(1+q)^2 - s_{\rm c}^4\right]^3}{27q} \right\}^{1/8}, \tag{2.39}$$

$$s_{\rm w} = \left(1 + q^{1/3}\right)^{3/2}. \tag{2.40}$$

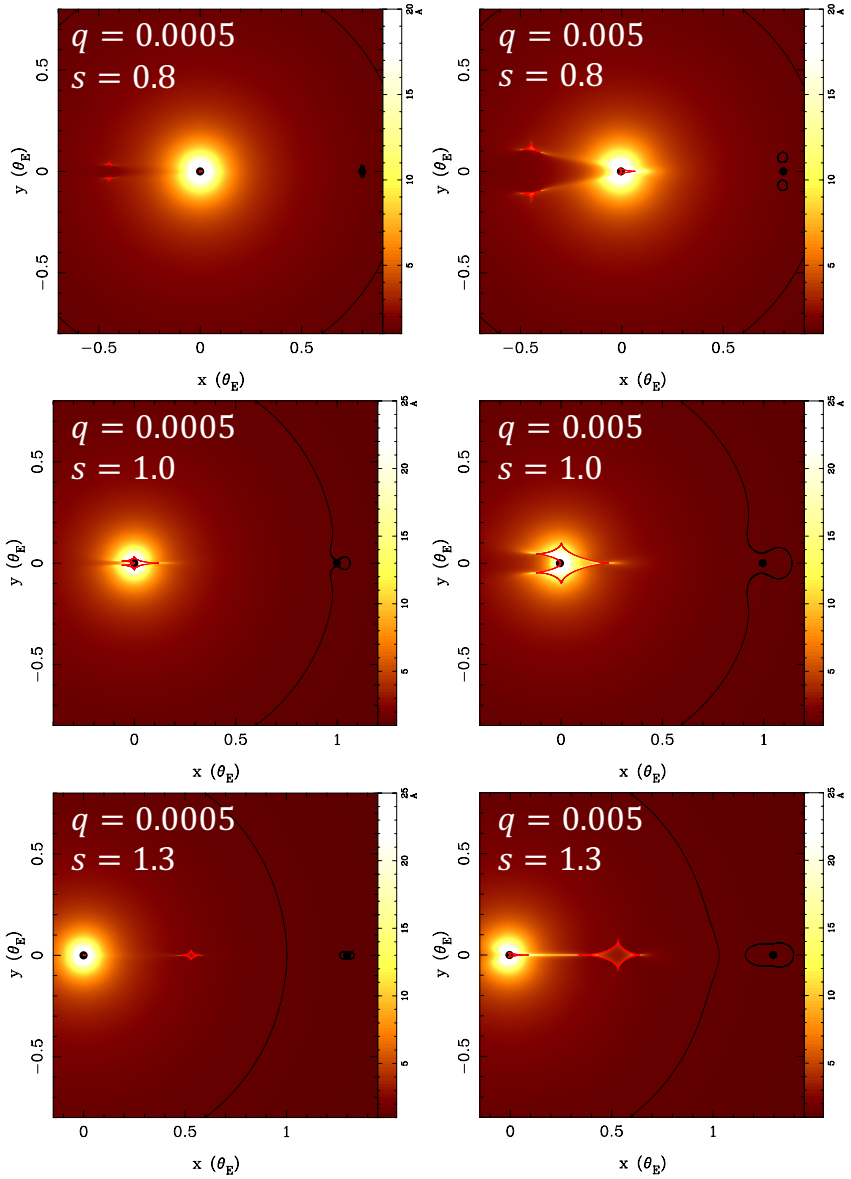

Figure 2.6: The magnification maps of the binary lens system for different q which is the mass ratio of the companion to host, and s which is the distance between the host and the companion projected in a plane perpendicular to the line of sight normalized by the Einstein radius. Each (q, s) is shown in the upper left corner of each panel. The primary lens (host) is shown at the origin and the planet are shown on the positive side of the x-axis. The black filled circle at $(x, y) = (0, 0)$ in each panel is the primary star of the lens system, the black filled circles at $(x, y) = (0.8, 0)$ (upper panel), $(x, y) = (1, 0)$ (middle panel) and $(x, y) = (1.3, 0)$ (lower panel) are the companion stars of the lens system, the black curve is critical curve and the red curve is caustic. The shading of the colour bar indicates the magnification rate. The shape and size of the caustics depend on (q, s).

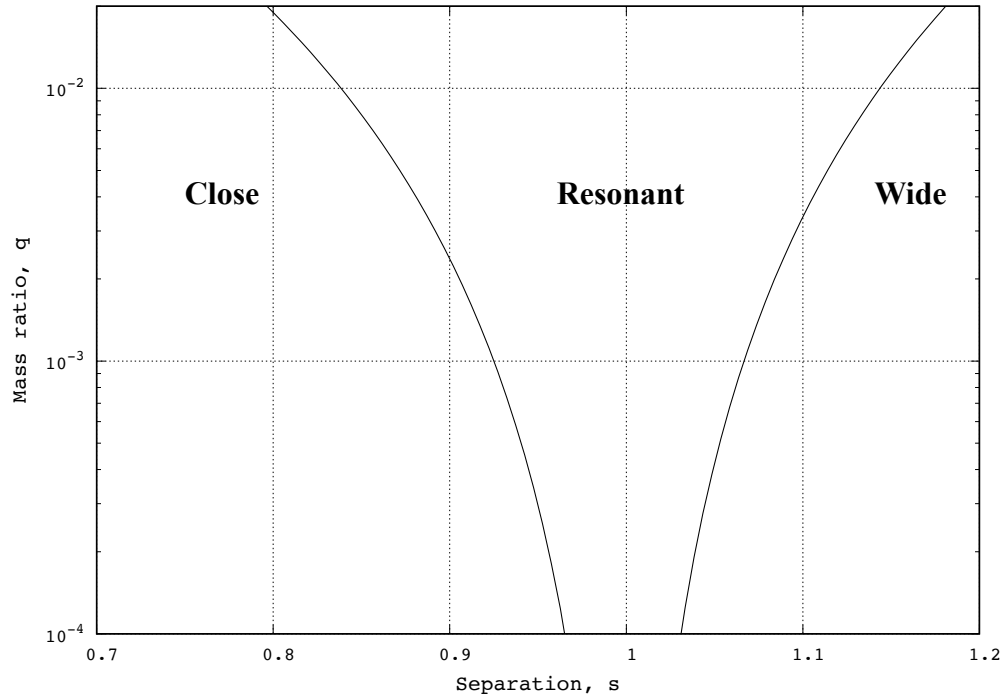

Figure 2.7: Relationship between the caustic topologies and q, s. In the region where $q << 1$, the resonant caustic appears only at $s \sim 1$.

For $q \ll 1$, Equations 2.39 and 2.40 can be approximated as follows: (Dominik, 1999; Cassan, 2008; Gaudi, 2012),

$$s_{\rm c} \sim 1 - \frac{3}{4} q^{1/3}, \tag{2.41}$$

$$s_{\rm w} = 1 + \frac{3}{2} q^{3/2}. \tag{2.42}$$

As shown in Figure 2.7, these critical values define the regions of the topology that are close ($s < s_{\rm c}$), intermediate ($s_{\rm c} < s < s_{\rm w}$), and wide ($s > s_{\rm w}$). The shape and number of caustics vary with each region, as shown in Figure 2.6. The shape and number of caustics in each region are as follows:

1. In the close topology, three caustics appear. They are the central caustics and two triangle caustics on the opposite sides of the host-planet axis (called planetary caustics).

2. In the wide topology, two caustics appear. The central caustics and the two caustics with four cusps on the same side of the host-planet axis (also called planetary caustics).

3. In the intermediate topology, the central caustic and the planetary caustic merge into one large caustic. This caustic is called the resonance caustic (Chung, 2009; Gaudi, 2012).

The majority of planetary microlensing events occur in ${s_{\rm c}}^3 \leq s \leq {s_{\rm w}}^{1.8}$ (Yee et al., 2021).

As shown in Figure 2.6, if the x-axis is the axis connecting the lens primary star and the companion star, and the companion star is in the positive direction of the x-axis, the planetary caustic position $x_{\rm p}$ can be expressed as follows: (Griest & Safizadeh, 1998),

$$x_{\rm p} \sim (s^2 - 1)/s. \tag{2.43}$$

2.3 Higher-Order Effects

2.3.1 Finite Source

The source star should always have a size, but it is not always detectable in all events, and its size is often detectable in high magnification events. As the source passes through the caustics and the surrounding region of high light intensification, various small areas within the source are magnified at various times, revealing the source size.

When considering finite source effect, the value ρ, which is the angular radius of the source θ_* normalized by the Einstein angular radius $\theta_{\rm E}$, is added to the fitting parameter. Therefore, ρ can be expressed as follows,

$$\rho \equiv \frac{\theta_*}{\theta_{\rm E}}. \tag{2.44}$$

The angular radius of the source, θ_* can be derived by the corrected colour and magnitude of the source for extinction and reddening, to the empirical formula for colour and magnitude. From Equation 2.7, the following equation can be derived,

$$M_{\rm L} = \frac{c^2 {\theta_{\rm E}}^2}{4G} \frac{D_{\rm S} D_{\rm L}}{D_{\rm LS}}. \tag{2.45}$$

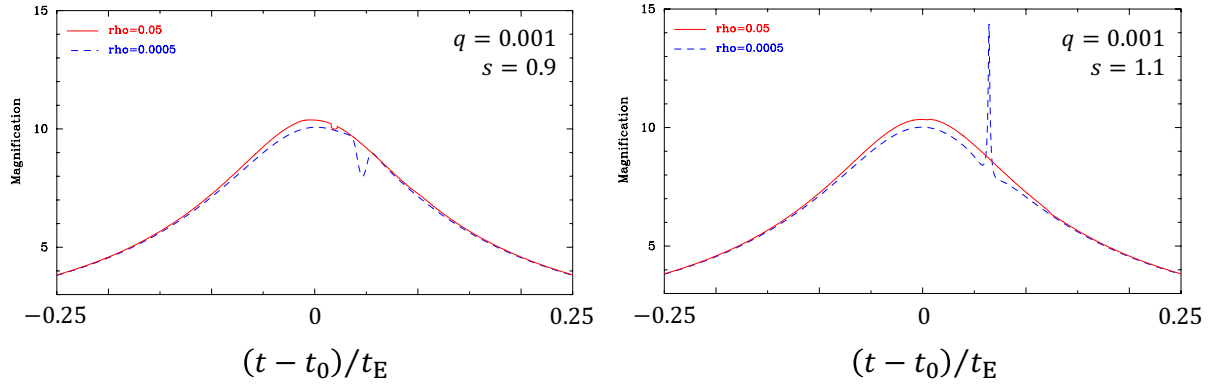

Figure 2.8: Microlensing light curves for different values of ρ, the value at which the angular radius θ_* of the source is normalized by the Einstein angular radius $\theta_{\rm E}$. The left panel is a lens system with (q, s)=(0.0001, 0.9) and the right panel is a lens system with (q, s)=(0.0001, 1.1). In each panel, the solid red line indicates $\rho = 0.05$ and the dashed blue line indicates $\rho = 0.0005$. The perturbation to the light curve by the planet, which can be seen at $\rho = 0.0005$, almost disappears at $\rho = 0.05$.

Thus, if ρ can be detected, the $M_{\rm L}$ corresponding to $D_{\rm L}$ can be calculated by assuming $D_{\rm S}$. From Equation 2.24, $\mu_{\rm rel} = \theta_{\rm E}/t_{\rm E}$. Therefore, once $\theta_{\rm E}$ is known, the relative velocity $\mu_{\rm rel}$ between the source and the lens normalized by the Einstein radius can be obtained.

On the other hand, the perturbation to the light curve by the planet becomes less significant for smaller ρ (smaller θ_*) and generally reaches the detection limit at $\rho \sim 0.03$. Figure 2.8 shows the light curves for different ρ sizes. If the star with radius $R_\odot$ is the source, microlensing planets with $M_{\rm p} \sim 0.02 M_\oplus \sim 2 M_{\rm Moon}$ will not be detected. In the case of a source with a red clamp on the bulge, a lens planet with $M_p \lesssim 5 M_\oplus$ will be impossible to detect due to finite source effects (Perryman, 2018).

When considering finite source effects, the magnification is derived by dividing the magnification due to each small area of the source by the entire source and averaging. As shown in Figure 2.3, the source is u away from the lens. Considering a small element located $\overrightarrow{u'}$ from the

center of the source and its position vector $\overrightarrow{U} = (u + u'\cos\varphi, u'\sin\varphi)$, the magnification of the entire source image $A(u|\rho)$ can be shown as follows:

$$\begin{aligned} A(u|\rho) &= \frac{\int A(U)u'du'd\varphi}{\int udu'd\varphi} \\ &= \frac{1}{\pi\rho^2}\int_{u'=0}^{u'=\rho}\int_{\varphi=0}^{\varphi=2\pi} A\left(\sqrt{u^2+u'^2+2uu'\cos\varphi}\right)u'du'd\varphi, \end{aligned} \tag{2.46}$$

where the coordinate axis is perpendicular to the position vector u of the source object, $U = |\overrightarrow{U}| = \sqrt{u^2+u'^2+2uu'\cos\varphi}$. And the range of u' is $0 \leq u \leq \rho$. For a single lens with $u \to 0$, the following equation can be expressed, from $A(u) \sim 1/u$ in $u \ll 1$,

$$\lim_{u\to 0} A(u|\rho) = \frac{2}{\rho}. \tag{2.47}$$

If the finite source effect is sufficiently weak, a multipole approximation can greatly reduce the computation time of the exact finite source effect (Pejcha & Heyrovský, 2009). The commonly used quadrupole or hexadecapole approximation uses a resolution of 9 or 13 point sources.

2.3.2 Parallax

When considering the orbit of the Earth, the relative motion of the lens and the source deviates from linear motion and is affected by microlensing parallax. Note that Equation 2.23 assumes simple constant velocity linear motion of the lens and the source relative to the observer. Figure 2.9 is a schematic of the parallax effect. $\pi_{\rm rel}$ is defined as the relative parallax between the lens and the source as follows:

$$\pi_{\rm rel} = \pi_{\rm L} - \pi_{\rm S} = {\rm au}\left(\frac{1}{D_{\rm L}} - \frac{1}{D_{\rm S}}\right) = {\rm au}\left(\frac{D_{\rm LS}}{D_{\rm L}D_{\rm S}}\right), \tag{2.48}$$

where au is the astronomical unit. $\boldsymbol{\pi_E} = (\pi_{\rm E,N}, \pi_{\rm E,E})$ is obtained as the observed quantity of gravitational microlensing events. where $\pi_{\rm E,N}$ and $\pi_{\rm E,E}$ represent the north and east components of $\pi_{\rm E}$ projected onto the sky plane in equatorial coordinates. The scalar quantity of microlensing parallax $|\pi_{\rm E}|$ is defined as the relative parallax $\pi_{\rm rel}$ between lens and source normalized by the Einstein radius $\theta_{\rm E}$ as follows (Gould, 1992, 2004):

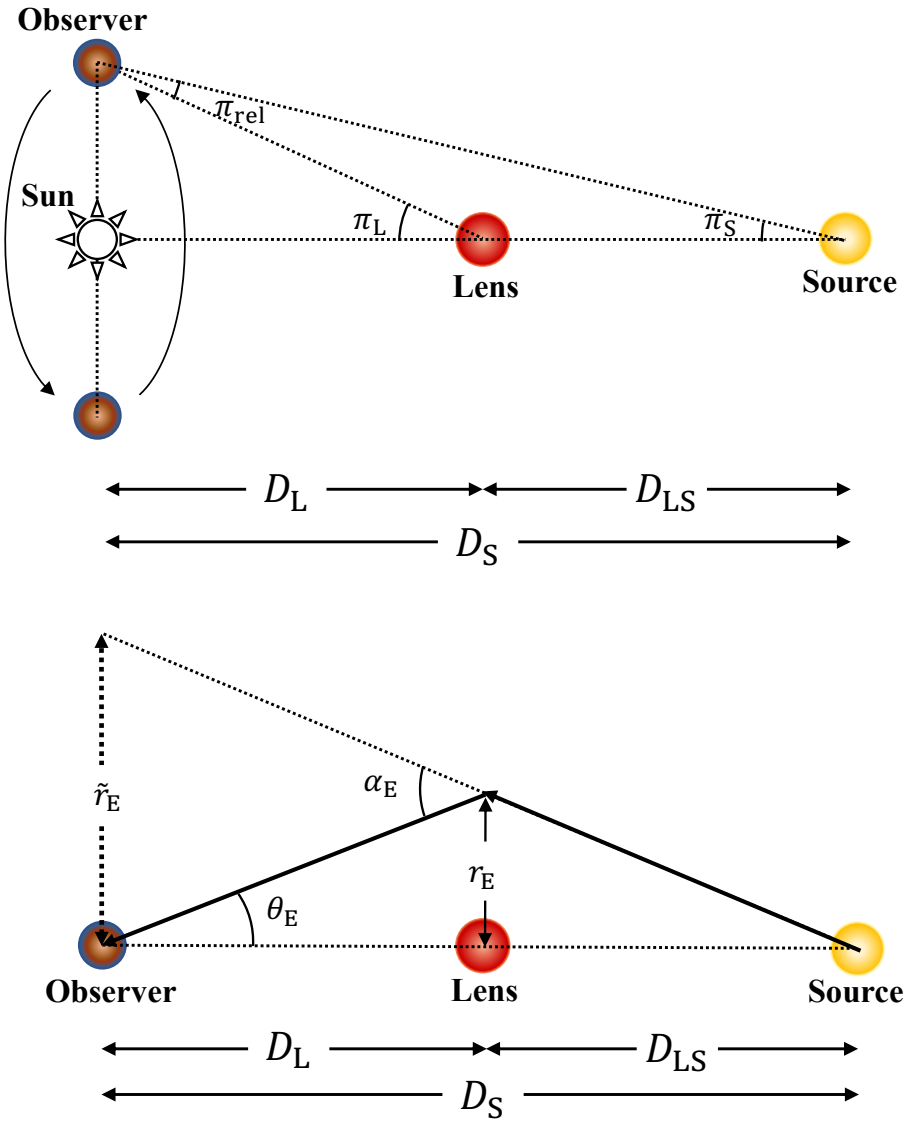

Figure 2.9: (Top Panel): Schematic of the parallax effect. Microlensing parallax $\boldsymbol{\pi_{\rm E}}$ can be expressed as $|\boldsymbol{\pi_{\rm E}}| = \pi_{\rm rel}/\theta_{\rm E}$ using the Einstein radius $\theta_{\rm E}$, and relative parallax $\pi_{\rm rel}$ between lens and source. (Bottom Panel): Schematic of $\tilde{r}_{\rm E}$. The Einstein radius $r_{\rm E}$ is projected onto the solar system scaled value $\tilde{r}_{\rm E}$. Microlensing parallax can be obtained by measuring the light curve from a distance in the observer plane.

$$\pi_{\rm E} = \frac{\pi_{\rm rel}}{\theta_{\rm E}}. \tag{2.49}$$

Since $D_{\rm L}$ and $D_{\rm S}$ in Figure 2.9 are very long, the small angle approximation can be applied to $\alpha_{\rm E}$ and $\theta_{\rm E}$, thus $\tilde{r}_{\rm E} = \alpha_{\rm E} D_{\rm L}$ and $r_{\rm E} = \theta_{\rm E} D_{\rm L}$. Furthermore, substituting $r = r_{\rm E}$ and $\alpha_{\rm GR} = \alpha_{\rm E}$ in Equation 2.1, the following equation can be shown,

$$\alpha_{\rm E} r_{\rm E} = \theta_{\rm E} \tilde{r}_{\rm E} = \frac{4GM_{\rm L}}{c^2}. \tag{2.50}$$

Also, since $r_{\rm E} = \tilde{r}_{\rm E} D_{\rm LS}/D_{\rm S}$ from Figure 2.9, the following equation can be expressed,

$$\theta_{\rm E} = \frac{r_{\rm E}}{D_{\rm L}} = \frac{D_{\rm LS}}{D_{\rm L} D_{\rm S}} \tilde{r}_{\rm E} = \frac{\pi_{\rm rel}}{\rm au} \tilde{r}_{\rm E}, \tag{2.51}$$

where Equation 2.49 is used. From Equations 2.49 and 2.51, $\pi_{\rm E}$ can be expressed as,

$$\pi_{\rm E} = \frac{\rm au}{\tilde{r}_{\rm E}}. \tag{2.52}$$

From Equations 2.44, 2.48, 2.50, 2.51 and 2.52 the following equation is derived,

$$M_{\rm L} = \frac{\theta_{\rm E}}{\kappa \pi_{\rm E}} = \frac{\theta_*}{\rho} \frac{1}{\kappa \pi_{\rm E}}, \tag{2.53}$$

$$D_{\rm L} = \frac{\rm au}{\pi_{\rm E} \theta_{\rm E} + {\rm au}/D_{\rm S}} = \frac{\rm au}{\pi_{\rm E}(\theta_*/\rho) + {\rm au}/D_{\rm S}}, \tag{2.54}$$

where $\kappa = 4G/(c^2 {\rm au}) \sim 8.144$ [mas $M_\odot^{-1}$]. θ_* can be obtained from the empirical formula for the color and radius of nearby stars. Therefore, when the finite source effect (i.e. ρ) and the parallax effect (i.e. $\pi_{\rm E}$) are detected, assuming a distance $D_{\rm S}$ to the source, the distance and mass to the lens source can be derived.

In addition, The host mass of the lens system $M_{\rm L,H}$ and companion mass $M_{\rm L,C}$ of the lens system and their projection semi-major distance to the lens plane $a_{\rm L,\perp}$ can be expressed by the following equations, respectively,

$$M_{\rm L,H} = \frac{M_{\rm L}}{1+q}, \tag{2.55}$$

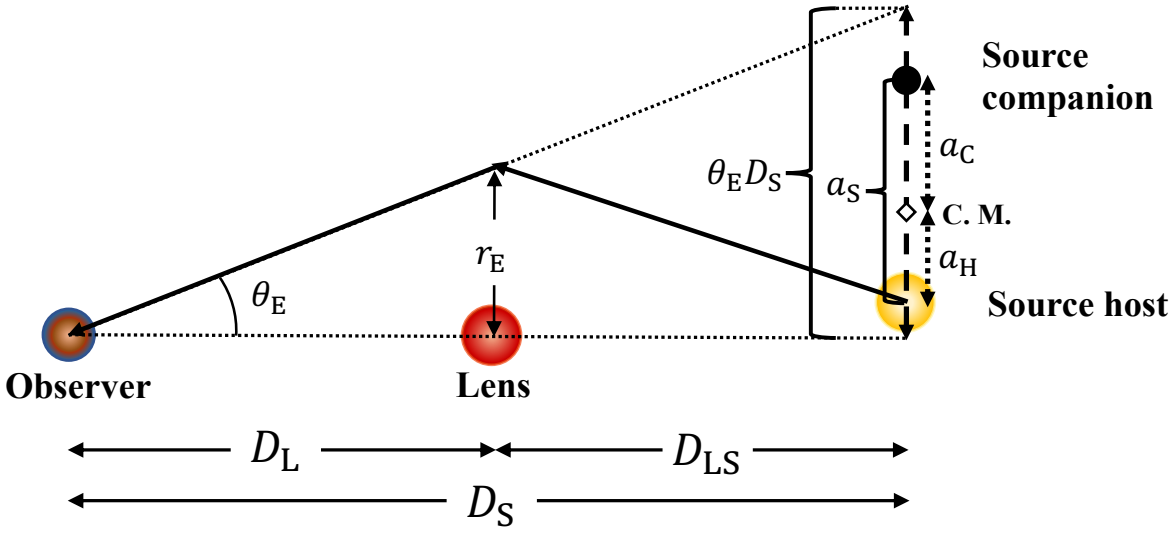

Figure 2.10: Schematic of the xallarap effect. The scalar quantity of the xallarap vector $\xi_{\rm E}$ is defined as the distance as between the source system host and the source system center of mass $a_{\rm H}$, normalized by the Einstein radius projected onto the source plane $\theta_{\rm E} D_{\rm S}$, $\xi_E = a_{\rm H}/\theta_{\rm E} D_{\rm S}$. The center of mass is denoted as C.M.

$$M_{\rm L,C} = \frac{q M_{\rm L}}{1+q}, \tag{2.56}$$

$$a_{\rm L,\perp} = s \theta_{\rm E} D_{\rm L}. \tag{2.57}$$

The expected value of the semi-major distance of lens companion in three dimensions can be expressed by,

$$a_{\rm L,exp} = \sqrt{\frac{3}{2}} a_{\rm L,\perp}. \tag{2.58}$$

As shown above, if $M_{\rm L}$ and $D_{\rm L}$ can be solved, important parameters such as $M_{\rm L,H}$, $M_{\rm L,C}$, $a_{\rm L,\perp}$, and $a_{\rm L,exp}$ can be solved, which can provide information on the characteristics of the lens system.

2.3.3 Xallarap

If the source has a companion star, the source is in orbital motion. Thus, similar to the parallax effect, the relative motion of the source and lens as seen by the observer deviates from uniform linear motion. While the parallax effect is motion in the observer plane, this case is motion in the source plane. This effect is called the xallarap effect (Bennett, 1998; Goldman, 1998), a reversed spelling of parallax. Smith et al. (2003) and Poindexter et al. (2005) show that the xallarap effect mimics the parallax effect. An early study of the effect of the xallarap (i.e. binary source motion) effect on the light curve of microlensing events was done by Griest & Hu (1992); Han & Gould (1997); Paczynski (1997). Note that the xallarap effect only considers the motion of the source primary, which is different from the source companion magnification (Section 2.3.5).

The xallarap effect can be described by the following seven parameters; the direction toward the solar system relative to the orbital plane of the source system, RA_ξ and decl_ξ; the source orbital period, P_ξ; the source orbital eccentricity e_ξ; the perihelion $T_{\rm peri}$; the xallarap vector, $\boldsymbol{\xi_{\rm E}} = (\xi_{\rm E,N}, \xi_{\rm E,E})$. Figure 2.10 is the schematic of the xallarap effect. The scalar quantity of the xallarap vector, $|\boldsymbol{\xi_{\rm E}}| = \xi_{\rm E}$, is defined as the distance between the center of mass of the source system and the source host, $a_{\rm H}$, normalized by the Einstein radius mapped to the source plane $(r_{\rm E}/D_{\rm L})D_{\rm S} = \theta_{\rm E} D_{\rm S}$, and can be expressed as follows:

$$\xi_{\rm E} \equiv \frac{a_{\rm H}}{\theta_{\rm E} D_{\rm S}}. \tag{2.59}$$

The distance between the source primary and the source companion, $a_{\rm S}$, can be expressed as follows using $a_{\rm H}$ and the distance between source companion and the center of mass of the source system, $a_{\rm C}$,

$$a_{\rm S} = a_{\rm H} + a_{\rm C}. \tag{2.60}$$

Furthermore, $a_{\rm S}$, $a_{\rm H}$, and $a_{\rm C}$ have the following relationship from Newton's third law,

$$\frac{a_{\rm S}}{M_{\rm S,H} + M_{\rm S,C}} = \frac{a_{\rm H}}{M_{\rm S,C}} = \frac{a_{\rm C}}{M_{\rm S,H}}, \tag{2.61}$$

where $M_{\rm S,H}$ is the source host the mass and $M_{\rm S,C}$ is the source companion mass. Thus, Equation 2.59 can be restated as follows:

$$\xi_{\rm E} = \frac{a_{\rm S}}{\theta_{\rm E} D_{\rm S}} \frac{M_{\rm S,C}}{M_{\rm S,H} + M_{\rm S,C}}. \tag{2.62}$$

Considering Kepler's third law with $a_{\rm S}$ as the semi-major axis, Equation 2.62 further reduces to Equation 3.17.

Chapter 3 will discuss the xallarap effect in more detail.

2.3.4 Lens Orbital Motion

The light curve can be also affected by the orbital motion of the lens planet around the host star. It is known that the parallax and lens orbital motion effects are degenerate (Batista et al., 2011; Skowron et al., 2011; Bachelet et al., 2012; Park et al., 2013). Therefore, when considering lens orbital motion, the parallax effect should be considered simultaneously. Simplified lens orbital motion effects can be modeled by adding the rate of change of the distance between lens components projected onto the lens plane at t_0, ds/dt ; and the angular velocity relative to the source orbit, $d\psi/dt$ (Batista et al., 2011; Skowron et al., 2011). The ratio of kinetic energy to potential energy projected onto the lensing plane of the lens companion can be written as follows (Dong et al., 2009; Skowron et al., 2011):

$$\left| \frac{\rm KE}{\rm PE} \right|_{\perp} = \frac{(a_{\rm L,\perp}/{\rm au})^3}{8\pi^2 (M_{\rm L}/M_{\odot})} \left[\left(\frac{1}{s} \frac{ds}{dt} \right)^2 + \frac{d\psi}{dt} \right], \tag{2.63}$$

where $M_{\rm L}$ is the total mass of the lensing system, and $a_{\perp}$ is the semi-major axis of the lens companion projected onto the lens plane. In general, the analysis is performed under the condition that the lens companion is gravitationally bound to the lens primary star, $|{\rm KE/PE}|_{\perp} < 1$ (or less).

2.3.5 Binary Source

In this case, source flux magnification can be considered and is described by the following equation,

$$A(t,\boldsymbol{x})f_s = \frac{A_1(t,\boldsymbol{x})f_{s,1} + A_2(t,\boldsymbol{x})f_{s,2}}{f_{s,1}+f_{s,2}} = \frac{A_1(t,\boldsymbol{x}) + q_{F,j}A_2(t,\boldsymbol{x})}{1+q_{F,j}}, \tag{2.64}$$

where $A_i(t,\boldsymbol{x})$ and $f_{s,i}$ are the magnification and source flux of the i-th source. The flux ratio of the two sources $q_{F,j} = f_{s,2}/f_{s,1}$ differs depending on the j-th passband. Considering the effect of two sources, the time of the second source closest to the center of mass, $t_{0,2}$; the impact parameter of the second source normalized by the Einstein radius, $r_{\rm E}$, $u_{0,2}$; and the second source angular radius in units of $\theta_{\rm E}$, ρ_2; the flux ratio of the two sources $q_{F,j}$ on the j-th band are added. ρ_2 is usually well constrained at caustic crossings.

2.4 Extended Method

2.4.1 Astrometric Microlensing

The light centroid of an unresolved source may not be constant as the solid angle ratio of each microlensing image changes over time. This is called an astrometric microlensing (e.g., Hog et al., 1995; Miyamoto & Yoshii, 1995). The light centroid typically changes in 10^{-4} seconds. From Equations 2.12, 2.19, and 2.20, the astrometric deflection angle of the light centroid $\delta\theta$ can be expressed as follows:

$$\begin{aligned}
\delta\theta &= \frac{A_+\theta_+ + A_-\theta_-}{A_+ + A_-} - \theta_{\rm S} \\
&= \frac{1}{4}\left[\left(\frac{u^2+2}{u\sqrt{u^2+4}}+1\right)\left(\theta_{\rm S}+\sqrt{\theta_{\rm S}^2+4\theta_{\rm E}^2}\right) + \left(\frac{u^2+2}{u\sqrt{u^2+4}}-1\right)\left(\theta_{\rm S}+\sqrt{\theta_{\rm S}^2-4\theta_{\rm E}^2}\right)\right] \\
&\qquad\qquad \times \frac{u\sqrt{u^2+4}}{u^2+2} - \theta_{\rm S} \\
&= \frac{1}{2}\left[\frac{(u^2+2)}{\sqrt{u^2+4}}\theta_{\rm E} - \sqrt{(u\theta_{\rm E})^2+4\theta_{\rm E}^2}\right]\frac{u\sqrt{u^2+4}}{u^2+2} - u\theta_{\rm E} = \frac{u\theta_{\rm E}}{u^2+2}.
\end{aligned} \tag{2.65}$$

The derivative of Equation 2.65 is as follows:

$$\dot{\delta\theta} = -\frac{(u+\sqrt{2})(u-\sqrt{2})}{(u^2+2)^2} \tag{2.66}$$

From Equation 2.66, the maximum astrometric deflection angle of the light centroid is reached at $u = \sqrt{2}$. Considering the case of lens in the Galactic bulge ($\theta_{\rm E} \sim 300$ μas), $\delta\theta \sim 0.1$ mas.

Although there are still no reports of planetary mass object discoveries by astrometric microlenses, research has been conducted (e.g., Mao & Paczynski, 1991; Dominik & Sahu, 2000; Han & Lee, 2002; Zakharov, 2015; Nucita et al., 2017). If the lens system has a companion of about Jupiter mass, the time when the astrometric deflection angle is $\delta\theta > 10$ μas lasts for a few days (Perryman, 2018).

Sahu et al. (2022) and Lam et al. (2022) published their analysis of the astrometric microlensing event OGLE-2011-BLG-0462 at the same time in July 2022. The astrometric shift for OGLE-2011-BLG-0462 is estimated to be over 1 mas. Sahu et al. (2022) combined astrometric data from the Hubble Space Telescope, ground-based light curves and parallax for their analysis. The results show that the lensing object of OGLE-2011-BLG-0462 (OGLE-2011-BLG-0462L) has $7.1 \pm 1.3 M_{\odot}$ and an Earth to lens distance of 1.58 ± 0.18 kpc. Since the lens does not emit light, they conclude that OGLE-2011-BLG-0462L is a black hole, making this study the first mass measurement of an isolated black hole. Lam et al. (2022) also combined astrometric data from the Hubble Space Telescope with light curves and parallaxes from high-density ground-based sampling to show that the OGLE-2011-BLG-0462L is a $1.6 - 4.4 M_{\odot}$ black hole or neutron star located at $0.7 - 1.9$ kpc from Earth. In October 2022 Mróz et al. (2022) showed that the discrepancy was due to a systematic error and that OGLE-2011-BLG-0462L is a $7.9 \pm 0.8 M_{\odot}$ black hole located at 1.49 ± 0.12 kpc from Earth. Mróz et al. (2022) describes low-level blending by the source companion as a challenge for astrometric black hole mass measurements.

2.4.2 Transit Microlensing

In transit surveys (Section 1.2.2), gravitational lens effects of foreground planets are usually negligible. However, if the gravitational deflection angle is comparable to the angular size of the transit object, both lensing and occultation can occur. For brown dwarfs orbiting a few au, lensing effects can reach several percent of transit depth. Furthermore, if the object passing in the foreground is a remnant object, the lensing effect can be larger than the transits signal (Perryman, 2018). In this

case, the transit light curve is slightly brighter near the entrance and exit of the transit than before occultation.

Kepler Object of Interest 256 (KOI-256) is a binary system with an orbital period of 1.37865 ± 0.00001 days, consisting of a cold white dwarf ($M_* = 0.59 \pm 0.09\ M_\odot$, $R_* = 0.013 \pm 0.001\ R_\odot$, $T_{\rm eff} = 7100 \pm 700$ K) and an active M dwarf ($M_* = 0.51 \pm 0.16\ M_\odot$, $R_* = 0.540 \pm 0.014\ R_\odot$, $T_{\rm eff} = 3450 \pm 50$ K), where $T_{\rm eff}$ is the effective temperature of the star. The Einstein ring size of the white dwarf is $r_{\rm E} = 0.005 \pm 0.001 R_\odot$, and the lensing effect makes the transit depth shallower than expected from the normal transit geometry (Muirhead et al., 2013). This effect is useful for constraining the size ratio of the lens to the source, the limb-darkening of the source, and the surface gravity of the lens.

2.4.3 Quaser Microlensing

Quaser microlensing has the role of a tool to spatially study the accretion disk structure of quasars (e.g., Pooley et al., 2007). Furthermore, the density distribution of quality points in galaxies and galaxy clusters can be studied from emission line shifts and double lines in the accretion disk structure of quasars (e.g., Morgan et al., 2008; Dai & Guerras, 2018; Bhatiani et al., 2019). In Quaser microlensing, light from the background quasar is split into multiple images due to strong gravitational lensing effects (Walsh et al., 1979) caused by a lensing galaxy or galaxy cluster in the foreground. It is also secondarily magnified by stars and free-floating planets near the lens galaxy region and reaches the observer. Because the accretion disk of a quasar is rotating at high speed, the emission lines emitted from it are red-shifted in the region moving away from the observer and blueshifted in the region approaching. When these emission lines cross the caustics, they are magnified and observed as energy shifts or double lines. This energy shift or double line does not correlate between the respective images resulting from the strong gravitational lensing effect. Chartas et al. (2017) considered the possibility that this emission line shift was due to radiation from hot spots or patches inhomogeneous disk or absorption and shielding of the continuum, but concluded that it was due to gravitational microlensing.

Dai & Guerras (2018) studied the point mass distribution in the lens giant elliptical galaxy at redshift $z = 0.295$ which is generating the quadruple image of source quasar RXJ1131-1231 at $z = 0.658$. The results of Dai & Guerras (2018) show that the density of caustics satisfying line-shift frequencies cannot be explained by the number of stellar-mass objects alone. Furthermore, Dai & Guerras (2018) suggested that planetary-mass objects from the Moon to about Jupiter mass exist at a ratio of $\sim 10^{-4}$ to total lens mass. This implies that there are approximately 2,000 planetary-mass objects per main-sequence star. Bhatiani et al. (2019) studied the point mass distribution in the galaxy of lensed quasar QJ0158-4325 with the lens at $z = 0.317$ and in the galaxy cluster of lensed quasar SDSS J1004 + 4112 with the lens at $z = 0.68$. The results of Bhatiani et al. (2019) results show that the fraction of objects with Moon ($10^{-8}\ M_{\odot}$) to Jupiter ($10^{-3}\ M_{\odot}$) masses in the total halo mass is $\sim\ 3 \times 10^{-4}$ for QJ0158-4325 and $\sim\ 1 \times 10^{-4}$ for SDSS J1004 + 4112. Thus, planetary-mass objects that are not bound by stellar gravity are universal, and they may be free-floating planets or primordial black holes.

Chapter 3

OGLE-2019-BLG-0825

3.1 Introduction

As detailed in Chapter 2, the gravitational microlensing method is a method for detecting exoplanets that utilizes the phenomenon that light is deflected by gravity (Liebes, 1964; Paczynski, 1991) and is sensitive to planets beyond the snow line (Gould & Loeb, 1992; Bennett & Rhie, 1996). Giant planets are thought to form near and beyond the snow line (Ida & Lin, 2004; Laughlin et al., 2004; Kennedy et al., 2006). In gravitational microlensing, when a lensing object crosses in front of a source star, the brightness of the source star changes with time owing to the gravitational effect of the lensing object. Furthermore, if this lensing object is accompanied by a planetary or binary-star companion, the gravity of this companion will cause a secondary magnification. The gravitational microlensing method does not use the light from the lensing object, but only the time-dependent variations arising form the gravitational effect of the lensing object or objects on the light from the source. Therefore, the gravitational microlensing method has the advantage over other planet detection methods of being able to detect planets around faint stars at distances far from Earth (Gaudi, 2012). By comparing the occurrence rates of planets in the distant region detected by the gravitational microlensing method with the frequency of planets in the local region, we can investigate the influence of the Galactic environment on planet formation.

The detection of distant planets and brown dwarfs allows us to consider the influence of the Galactic environment on planet and brown dwarf formation. It has been thought that different Galactic environments have different planetary occurrence rates (Gonzalez et al., 2001; Lineweaver et al., 2004; Spinelli et al., 2021). In fact, radial velocity surveys in the 25 pc region near the Sun reported that the occurrence rate of hot Jupiters is about $\sim 2\%$ (Hirsch et al., 2021), whereas Kepler transit surveys report that the occurrence rate of hot Jupiters around G- K- type stars near Cygnus is about $\sim 0.5\%$ (Howard et al., 2012; Santerne et al., 2012, 2016; Fressin et al., 2013). Although Koshimoto et al. (2021) recently found that planetary frequencies do not depend significantly on the Galactocentric distance based on their 28 planet sample, their result is still too uncertain to discuss environmental effects precisely.

In the analysis of gravitational microlensing events, it is sometimes difficult to distinguish perturbations given by the lens secondary to the light curve from those given by higher-order effects (Griest & Hu, 1992; Rota et al., 2021). One of the higher-order effects, the parallax effect, is the effect of the acceleration of the Earth's orbital motion on the light curve. The xallarap effect is a higher-order effect on the light curve when the source is binary (Griest & Hu, 1992; Han & Gould, 1997; Paczynski, 1997; Poindexter et al., 2005). Binary stars are common in the Universe, with binary systems of two or more stars accounting for about 30% of all stellar systems (Lada, 2006; Badenes et al., 2018). When a source is accompanied by a companion star, the companion is not necessarily magnified, but the light curve is affected by the orbital motion of the source primary (Rota et al., 2021). Although most of the binary stars are too wide between their primary and companion stars to reliably detect a xallarap effect, a systematic survey of 22 long-term events in the bulge shows that 23% of them are indeed affected by xallarap (Poindexter et al., 2005). The effect of xallarap on lensing planet detection efficiency has not been fully investigated but is known to exist (Zhu et al., 2017).

We present in this paper an analysis of OGLE-2019-BLG-0825 and report that the xallarap effect was detected and that the lensing system parameters changed before and after the xallarap effect was included. Section 3.2 describes the data for event OGLE-2019-BLG-0825. Section 3.3 describes our data reduction. Section 3.4 describes our modeling in detail. Section 3.5 derives the

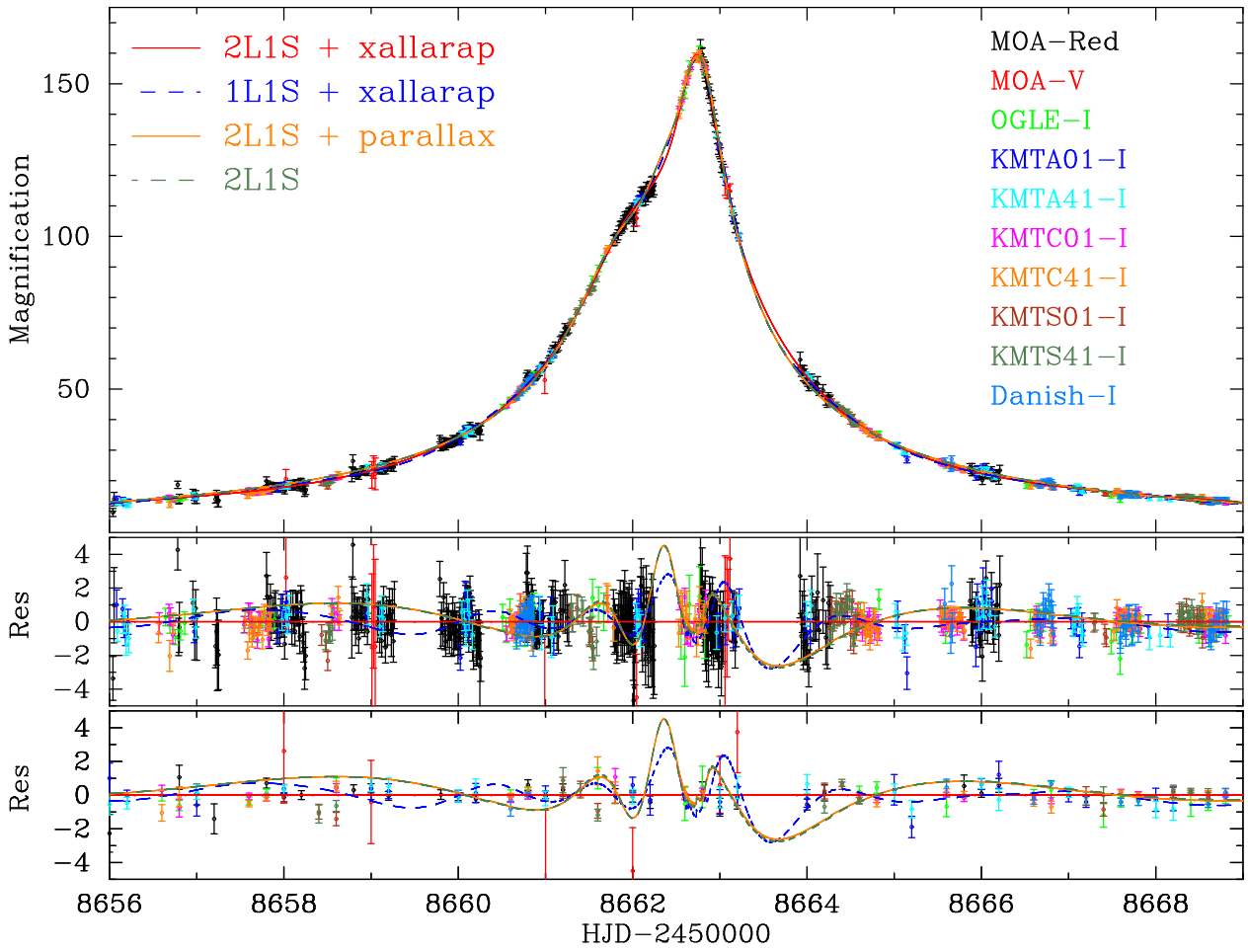

Figure 3.1: (Top panel) Light curve for OGLE-2019-BLG-0825. Error bars are renormalized according to Equation (3.1). The red solid, blue dashed, orange solid, and green dashed lines are the best 2L1S + xallarap model, the best 1L1S + xallarap model, the best 2L1S + parallax model and the best standard 2L1S model described in Section 3.4, respectively. (Middle panel) Residuals from the best 2L1S + xallarap model. (Bottom panel) Residuals from the best 2L1S + xallarap model binned by 0.2 days.

color and magnitude of the source and calculates the physical parameters of the source system from the color and magnitude of the source and the fitting parameters of the microlensing. Section 3.6 describes the estimation of the physical parameters of the lens system by Bayesian analysis.

Table 3.1: Data Sets for OGLE-2019-BLG-0825

Telescope	Collaboration	Label	Filter	$N_{\rm use}$	k[1]	$e_{\rm min}$[1]
MOA-II 1.8m	MOA	MOA	MOA-Red	3949	1.330	0.009
			V	86	0.835	0
Warsaw 1.3m	OGLE	OGLE	I	1535	1.453	0.007
KMTNet Australia 1.6m	KMTNet	KMTA01[2]	I	704	1.649	0
		KMTA41[3]	I	719	1.613	0
KMTNet Chile 1.6m		KMTC01[2]	I	952	0.761	0.004
		KMTC41[1]	I	954	1.436	0
KMTNet South Africa 1.6m		KMTS01[2]	I	881	1.490	0
		KMTS41[3]	I	887	1.416	0
Danish 1.54m	MiNDSTEp	Danish	I	76	0.706	0

[1] Parameters for the error normalization.
[2] Data observed in BLG01 in the overlapped area.
[3] Data observed in BLG41 in the overlapped area.

3.2 Observation

Microlensing event OGLE-2019-BLG-0825 was first discovered on June 3, 2019 ($\mathrm{HJD}' \sim 8638$)[2] at J2000 equatorial coordinates $(\mathrm{R.A.}, \mathrm{decl.}) = (17^h52^m21^s.62, -30^\circ48'13''.2)$ corresponding to Galactic coordinates $(l, b) = (-0.849, -2.214)$, by the Optical Gravitational Lensing Experiment (OGLE; Udalski, 2003) collaboration. OGLE conducts a microlensing survey using the 1.3m Warsaw Telescope with a 1.4 deg^2 field-of-view (FOV) CCD camera at Las Campanas Observatory in Chile and distributes alerts of the discovery of microlensing events by their OGLE-IV Early Warning System (Udalski et al., 1994; Udalski, 2003; Udalski et al., 2015). The event is located in the OGLE-IV field BLG534, which is observed on Cousins I-band with an hourly cadence (Mróz et al., 2019).

The Microlensing Observations in Astrophysics (MOA; Bond et al., 2001; Sumi et al., 2003) collaboration also independently discovered this event on June 23, 2019, and identified it as MOA-2019-BLG-273 using the MOA alert system (Bond et al., 2001). The MOA collaboration conducts a microlensing exoplanet survey toward the Galactic bulge using the 1.8m MOA-II telescope with a 2.2 deg^2 wide FOV CCD camera, MOA-cam3 (Sako et al., 2008), at the University of Canterbury's

[2] $\mathrm{HJD}' \equiv \mathrm{HJD} - 2450000$

Mount John Observatory in New Zealand. The MOA survey uses a custom wide band filter referred to as $R_{\rm MOA}$ corresponding to the sum of the Cousins R and I bands. In addition, a Johnson V-band filter is used primarily for measuring the color of the source. The event is located in the MOA field gb4, which is observed with high cadence once every 15 minutes. As a member of the MOA collaboration, I participated in the observation of this event from September 4 ($\mathrm{HJD}' \sim 8730$) to September 30 ($\mathrm{HJD}' \sim 8756$).

The Korea Microlensing Telescope Network (KMTNet; Kim et al., 2016) collaboration conducts a microlensing survey using three 1.6m telescopes each with a 4.0 deg^2 FOV CCD camera. The telescopes are located at the Cerro Tololo Inter-American Observatory (CTIO) in Chile, the South African Astronomical Observatory (SAAO) in South Africa, and Siding Spring Observatory (SSO) in Australia. This event is located in an overlapping region with two KMTNet observed fields (KMTNet BLG01 and BLG41), which are observed with high cadence once every 15 minutes and was discovered by the KMTNet EventFinder (Kim et al., 2018) as KMT-2019-BLG-1389 on June 28, 2019.

The Danish telescope of MiNDSTEp (Microlensing Network for the Detection of Small Terrestrial Exoplanets) made follow-up observations in I-band. MiNDSTEp uses the 1.54m Danish Telescope at the European Southern Observatory at La Silla Observatory in Chile (Dominik et al., 2010). Data from the Spitzer space telescope (Yee et al., 2015) were also available, but these show no detectable signal and so are not used. A summary of all datasets used in the analysis of OGLE-2019-BLG-0825 is shown in Table 3.1.

The above data sets are used in our light curve analysis. To reduce long-term systematics on the baseline, we used approximately 2 years of data over $8100 \leq \mathrm{HJD}' \leq 8800$. Figure 3.1 shows the light curve of OGLE-2019-BLG-0825 and the standard binary lens single source model (hereafter, standard 2L1S), the binary lens single source with parallax effect model (hereafter, 2L1S + parallax), the single lens single source with xallarap effct model (hereafter 1L1S + xallarap), and the best-fit model (binary lens single source with xallarap effect model, hearafter 2L1S + xallarap), described in Section 3.4, respectively. As will be discussed in detail in Section 3.5, the xallarap

model analysis assumes that the magnified flux of the second source is too weak to be detected, so it is denoted 1S.

3.3 Data Reduction

The OGLE data were reduced with the OGLE Difference Image Analysis (DIA) (Wozniak, 2000) photometry pipeline (Udalski, 2003; Udalski et al., 2015) which uses the DIA technique (Tomaney & Crotts, 1996; Alard & Lupton, 1998; Alard, 2000). The MOA data were reduced with MOA's implementation of the DIA photometry pipeline (Bond et al., 2001). The KMTNet data were reduced with their PySIS photometry pipeline (Albrow et al., 2009). The MiNDSTEp data were reduced using DanDIA (Bramich, 2008; Bramich et al., 2013).

It is known that the nominal error bars calculated by the pipelines are incorrectly estimated in such crowded stellar fields. We follow a standard empirical error bar normalization process (Yee et al., 2012) intended to estimate proper uncertainties for the lensing parameters in the light curve modeling. This process, described below, hardly affects the best-fit parameters (Ranc et al., 2019). We renormalize the photometric error bars using the formula

$$\sigma_i' = k\sqrt{\sigma_i^2 + e_{\rm min}^2}, \tag{3.1}$$

in which σ_i' is the renormalized uncertainty in magnitude, while σ_i is an uncertainty of the i-th original data point obtained from the photometric pipeline. The variables k and $e_{\rm min}$ are renormalizing parameters. For preliminary modeling, we search for the best-fit lensing parameters using σ_i. We then construct a cumulative χ^2 distribution as a function of lensing magnification. The $e_{\rm min}$ value is chosen so that the slope of the distribution is uniform (Yee et al., 2012). The k value is chosen so that $\chi^2/\text{d.o.f.}^3 \simeq 1$. In Table 3.1, we list the calculated error bar renormalization parameters.

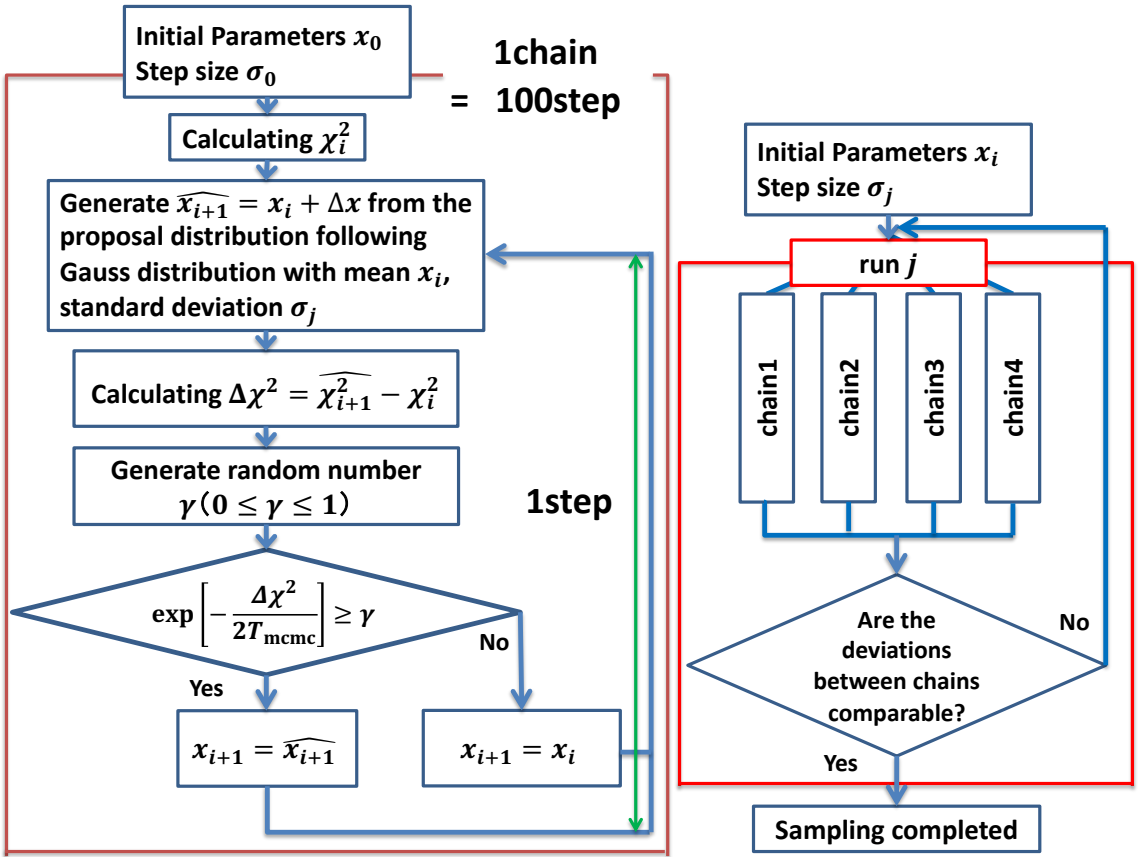

Figure 3.2: Metropolis-Hastings Markov Chain Monte Carlo algorithm used for light-curve fitting in this analysis.

3.4 Light Curve Modeling

The model flux for a microlensing event is given by the following equation,

$$f(t) = A(t, \boldsymbol{x}) f_s + f_b, \tag{3.2}$$

where $A(t, \boldsymbol{x})$ is the source flux magnification, f_s is the flux of the source star, and f_b is the blend flux. In the 1L1S model, $\boldsymbol{x}$ is described by four parameters (Paczynski, 1986b): the time of the source closest to the center of mass, t_0; the Einstein radius crossing time, t_{E}; the impact parameter, u_0, and the source angular radius, ρ. Both u_0 and ρ are in units of the angular Einstein radius, θ_{E}.

[3]Degrees of freedom.

For modeling the light curve, we used the Metropolis-Hastings Markov chain Monte Carlo method. The finite source effect, an effect in which the source has a finite angular size, was calculated using the image-centered inverse-ray shooting method (Bennett & Rhie, 1996; Bennett, 2010) as implemented by Sumi et al. (2010). Figure 3.2 shows the Metropolis-Hastings Markov chain Monte Carlo algorithm used in this study. In the 1L1S analysis, initial values and step sizes were set to $t_0 = 2458662$ days, $\sigma_{t_0} = 10$ days, $t_{\rm E} = 10$ days, $\sigma_{t_{\rm E}} = 10$ days, $u_0 = 0.005$, $\sigma_{u_0} = 0.005$, respectively. In the 1L1S analysis with finite source effects added, the initial value of ρ is 0 and the step size of rho is 0.02. Varying these initial values and step sizes hardly changes the optimal solution obtained. As described in Section 3.4.1, the 2L1S analysis divides (q, s, α) into $34,440$ different grids and uses combinations of these grids as initial values. Initial values for parameters other than (q, s, α) were generated using random numbers, and the step sizes were $\sigma_{t_0} = 10$ days, $\sigma_{t_{\rm E}} = 10$ days, and $\sigma_{u_0} = 0.005$ days. The algorithm first computes χ^2 using the initial value $\boldsymbol{x_i}$. Next, a Gaussian distribution with mean $\boldsymbol{x_i}$ and standard deviation σ_j is generated using the initial value $\boldsymbol{x_i}$ and step size σ_j. where i means the number of the step to be described later and j means the number of the run to be described later. Then $\hat{\boldsymbol{x}}_{\boldsymbol{i}}$ is proposed from that Gaussian distribution, and with some probability accept or reject that $\hat{\boldsymbol{x}}_{\boldsymbol{i+1}}$. If accepted, the process proceeds as $\boldsymbol{x_{i+1}} = \hat{\boldsymbol{x}}_{\boldsymbol{i}}$, if rejected, $\boldsymbol{x_{i+1}} = \boldsymbol{x_i}$. Note that if χ^2 with $\hat{\boldsymbol{x}}_{\boldsymbol{i+1}}$ is better than χ^2 with $\boldsymbol{x_i}$, the sampling is certainly accepted. In this paper, this series of processes is called 1step, and 100 steps is called one chain. Furthermore, four chains are calculated in parallel and are called run. In other words, 400 steps are calculated in one run. If the deviation between the steps in a chain is larger than the deviation between the four chains, sampling is terminated, assuming that sampling is sufficient to determine the posterior distribution of the probability density. The algorithm can be set to not terminate sampling until an arbitrary number of runs for reliability, and in this analysis, sampling is not terminated when run < 20, so the minimum number of runs is 20. The parameter $T_{\rm mcmc}$ in Figure 3.2 is a parameter that adjusts the probability of accepting the proposed $\hat{x}_{i+1}$. Except in the early stages of the analysis, such as grid search, $T_{\rm mcmc} = 1$ was usually used. In the early stages of the analysis, the sample acceptance decision is calculated with 400 steps = 1 run as the smallest unit and $T_{\rm mcmc} = 100$ in order to explore a wide parameter

space. Also, if χ^2 using the optimal solution in the $j+1$-th run is better than χ^2 using the optimal solution in the j-th run, the calculation is also performed for the $j+2$-th run with $T_{\mathrm{mcmc}} = 100$. If a solution better than the optimal solution for the j-th run cannot be obtained for the $j+1$-th run, the acceptance decision is calculated with $T_{\mathrm{mcmc}} = 1$ for the $j+2$-th and subsequent runs. The posterior probability distribution used for the final parameter estimation is based only on the sample when $T_{\mathrm{mcmc}} = 1$. In addition, the standard deviation of the proposal distribution is updated up to 11 times. The first update is performed at the end of the run when the number of accepted samples reaches 21 (let's say the j-th run), and the information on the optimal solution and variance in the sampling performed in the first through the j-th runs is carried over as the initial values and step size for the $j+1$-th run. From there until the $j+7$-th run, at the end of each run, the optimal solution and standard deviation of the sampling of the previous run are taken over as the initial values and step size for the next run. The eighth update of the proposal distribution is made at the end of the run in which the 100th sample has been sampled in total since the first sampling in the first run. The ninth update is performed at the end of the run in which the 200th sampling from the first sampling was performed in the first run. The tenth update is performed at the end of the run in which the 300th sampling from the first sampling was performed in the first run. The eleventh update is performed at the end of the run in which the 400th sampling from the first sampling was performed in the first run. Thereafter, samples are proposed from the same proposal distribution until the end of the algorithm. The optimal solution is estimated using a posterior distribution with samples generated from the same proposal distribution that generated the optimal solution. The reason for this is that the detailed balancing condition, one of the four basic conditions (Markov chain: the probability $T(\{\boldsymbol{x_i}\} \to \{\boldsymbol{x_{i+1}}\})$ of transition from $\boldsymbol{x_i}$ to $\boldsymbol{x_{i+1}}$ is determined only by $\boldsymbol{x_i}$, independent of the past history $\boldsymbol{x_0}$, $\boldsymbol{x_1}$, ... , $\boldsymbol{x_{i-1}}$; Irreducible: any variable combination $\{\boldsymbol{x}\}$, $\{\boldsymbol{x'}\}$ can be transitioned in a finite number of steps; Aperiodic: all $\boldsymbol{x}$ satisfy that the greatest common divisor of the number of steps required to get from $\boldsymbol{x}$ to $\boldsymbol{x}$ and back is 1; Detailed balancing condition; transition probability T satisfies $P(\{\boldsymbol{x}\})\cdot T(\{\boldsymbol{x}\} \to \{\boldsymbol{x'}\}) = P(\{\boldsymbol{x'}\})\cdot T(\{\boldsymbol{x'}\} \to \{\boldsymbol{x}\})$ of the Markov chain Monte Carlo method for any variable combination $\{\boldsymbol{x}\}, \{\boldsymbol{x'}\}$), is no longer satisfied before and after the proposal distribution is updated. In addition, if the Markov chain

Monte Carlo method chooses initial values that deviate significantly from the correct values, the correlation of the initial values remains in the sampling for several steps from the start. In other words, if we use sampling of the steps to arrive at a value that is independent of the initial value, the effect of the initial value remains on the estimated value unless the number of samples is extremely large. Therefore, samples before equilibrium is reached should not be used to derive the posterior distribution. The algorithm addresses this problem by discarding samples prior to the eleventh update of the proposal distribution, based on the idea that the algorithm has arrived at a value independent of the initial value by the eleventh update of the proposal distribution.

Note that f_s and f_b parameters are obtained from a linear-fit using the method of Rhie et al. (1999). We adopt the following linear limb-darkening law for source brightness:

$$S_\lambda(\vartheta) = S_\lambda(0)\left[1 - u_\lambda(1 - \cos(\vartheta))\right], \tag{3.3}$$

where ϑ represents the angle between the line of sight and the normal to the surface of the source star. $S_\lambda(\vartheta)$ is a limb-darkening surface brightness of ϑ at wavelength λ. We estimated the effective temperature of the source star in Section 3.5 to be $T_{\rm eff} = 5425 \pm 359$ K (González Hernández & Bonifacio, 2009). In this analysis, we assume the source star's metallicity $[{\rm M/H}] = 0$, surface gravity $\log g = 4.5$, and microturbulent velocity $v = 1$ km/s. We use the limb-darkening coffi-cients $u_V = 0.685$, $u_R = 0.604$ and $u_I = 0.518$, which are taken from the ATLAS model with $T_{\rm eff} = 5500$ K (Claret & Bloemen, 2011). Since $R_{\rm MOA}$ covers both R- and I-band wavelengths, we adopted the average value $u_{R_{\rm MOA}} = (u_R + u_I)/2 = 0.561$. In addition, as will be discussed in more detail in Chapter 4, we assume that the source of this event is a main-sequence star.

As the result of 1L1S model analysis, we found that $(t_0, t_{\rm E}, u_0, \rho) = (8662.6, 47.6, 1.2 \times 10^{-2}, 4.8 \times 10^{-3})$ is the best solution. This 1L1S best model is $\Delta\chi^2 = 21400$ worse than the best standard 2L1S model.

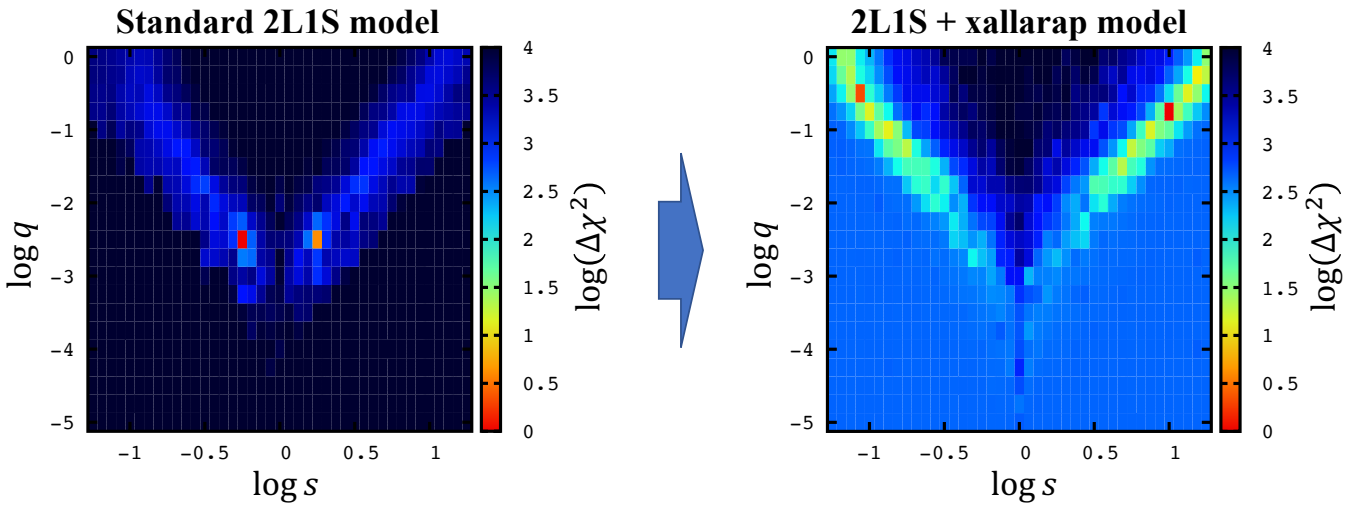

Figure 3.3: Map of $\Delta\chi^2$ in each s–q grid from the (q, s, α) grid search for the standard 2L1S model (Left) and for the 2L1S + xallarap model (Right). The best fit α is chosen for each grid location, respectively. In the map of the standard 2L1S model, we found the best solution at $q \sim 10^{-3}$. However, for the 2L1S + xallarap map, best solutions at two other local minima appear at $q > 0.1$.

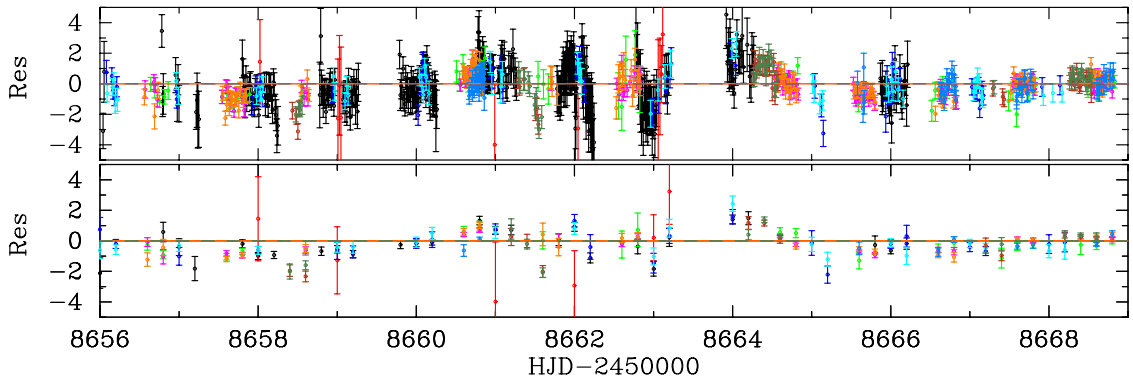

Figure 3.4: Residuals based on the best model of 2L1S (i.e. close 1). The lower panel is binned by 0.2 days.

3.4.1 Standard Binary Lens

In the standard 2L1S model, three additional parameters are required; the mass ratio of a lens companion relative to the host, q; the projected separation normalized by Einstein radius between binary components, s; the angle between the binary-lens axis and the source trajectory direction, α.

Because the χ^2 surface of the microlensing parameter has a very complicated shape, 34440 values of (q, s, α), which have a particularly large impact on the shape of the light curve were initially fixed in the fitting process. Here we uniformly take 21 values between $-5 \leq \log q \leq 0$, 41 values between $-1.25 \leq \log s \leq 1.25$, 40 values in $0 \leq \alpha \leq 2\pi$, respectively. For the top 1000 combinations which gave good fits, we performed the fitting again with q, s, and α free. This process minimizes the chance that we miss local solutions even in a large and complex microlensing parameter space. The left panel of Figure 3.3 shows the results of the grid search analysis for the standard 2L1S model.

As a result of the analysis, the best fit standard 2L1S model is $(q, s) = (3.3 \times 10^{-3}, 0.57)$ (close1). Hereafter, we call solutions with $s < 1$ and $s > 1$ as "close" and "wide", respectively. We call the best standard 2L1S as close1. We also found local minima at $(q, s) = (3.4 \times 10^{-3}, 1.75)$ (wide1) with $\Delta\chi^2 \sim 0.4$, $(q, s) = (2.1 \times 10^{-2}, 0.28)$ (close2) with $\Delta\chi^2 \sim 20.4$ and $(q, s) = (2.1 \times 10^{-2}, 3.78)$ (wide2) with $\Delta\chi^2 \sim 23.3$. Detailed parameters of the standard binary models are shown in Table 3.2. However, we observed systematic residuals around the peak of $8657 < \mathrm{HJD}' < 8667$ in these models, as depicted by the green dashed line in Figure 3.1. In Figure 3.4 shows the residuals based on the best model of 2L1S (i.e., close 1). The lower panel is binned by 0.2 days. The other three models also have similar residuals. We therefore proceed to model the light curve with higher order effects.

Table 3.2: Parameters of the standard 2L1S models

Model	close1	close2	wide1	wide2
t_0(HJD-2458660)	2.474 ± 0.001	2.483 ± 0.001	2.473 ± 0.001	2.489 ± 0.001
$t_{\rm E}$ (days)	74.7 ± 2.0	75.7 ± 2.0	72.8 ± 1.8	77.3 ± 2.0
u_0 (10^{-3})	7.30 ± 0.21	7.11 ± 0.19	7.53 ± 0.19	6.91 ± 0.19
q (10^{-3})	3.30 ± 0.11	20.71 ± 9.84	3.39 ± 0.10	21.33 ± 1.15
s	0.569 ± 0.004	0.207 ± 0.038	1.747 ± 0.011	3.776 ± 0.063
α (radian)	5.034 ± 0.002	2.766 ± 0.002	5.036 ± 0.003	2.767 ± 0.002
ρ (10^{-3})	2.95 ± 0.09	0.48 ± 0.28	3.02 ± 0.09	0.47 ± 0.14
χ^2	11744.7	11765.1	11745.1	11768.0
$\Delta\chi^2$	-	20.4	0.4	23.3

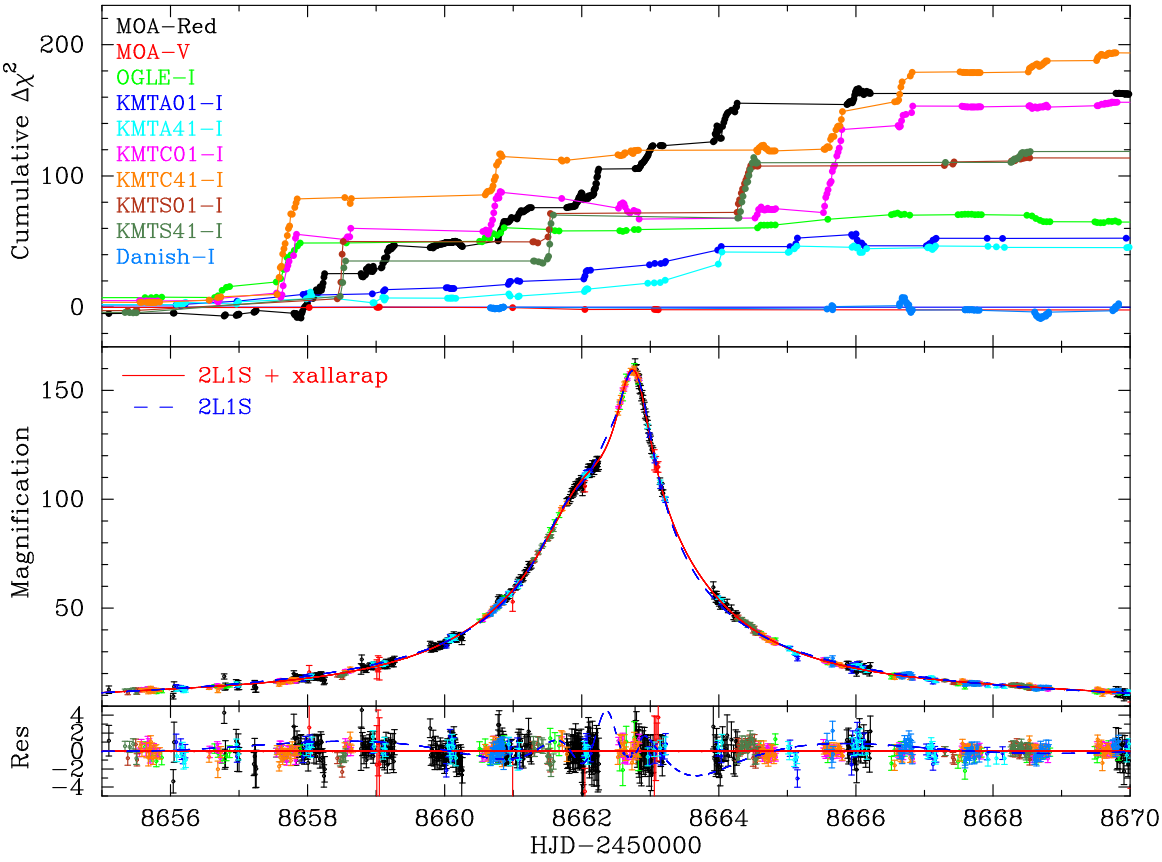

Figure 3.5: (Top panel) Cumulative $\Delta\chi^2$ for the xallarap model compared to the standard binary lens model. Each color corresponds to each instrument listed the left side of the axes. (Middle panel) The light curve of the best 2L1S + xallarap model (solid red line), and the light curve of the standard 2L1S best model (blue dashed line). (Bottom panel) Residuals of the light curves from the 2L1S + xallarap model.

Table 3.3: Parameters of the 2L1S + xallarap models, 1L1S + xallarap model, and 1L1S + xallarap + parallax model

Model	XLclose1	XLclose2	XLwide1	XLwide2	1LXL	1LXLPL
range of q	$q \leq 0.1$	$0.1 < q \leq 1$	$q \leq 0.1$	$0.1 < q \leq 1$	-	-
t_0(HJD-2458660)	2.576 ± 0.005	2.573 ± 0.007	2.572 ± 0.004	2.575 ± 0.006	2.744 ± 0.001	2.744 ± 0.001
$t_{\rm E}$ (days)	97.7 ± 2.6	93.8 ± 3.1	100.7 ± 3.4	133.3 ± 11.5	67.2 ± 2.0	73.5 ± 1.5
u_0 (10^{-3})	-7.16 ± 0.22	-6.98 ± 0.21	7.06 ± 0.21	4.91 ± 0.35	6.93 ± 0.20	6.31 ± 0.14
q	0.09 ± 0.01	0.44 ± 0.11	0.10 ± 0.01	0.94 ± 0.37	-	-
s	0.141 ± 0.004	0.085 ± 0.004	7.403 ± 0.438	18.040 ± 1.263	-	-
α (radian)	0.429 ± 0.008	1.937 ± 0.010	5.846 ± 0.008	4.350 ± 0.009	-	-
ρ (10^{-3})	2.56 ± 0.13	2.15 ± 0.12	2.41 ± 0.11	1.44 ± 0.16	7.04 ± 0.20	6.41 ± 0.14
${\rm RA}_\xi$ (degree)	81.6 ± 11.7	153.2 ± 10.5	75.9 ± 14.5	155.4 ± 8.5	31.3 ± 0.5	32.1 ± 0.5
${\rm decl}_\xi$ (degree)	54.5 ± 10.5	36.9 ± 16.4	-79.4 ± 12.8	-40.7 ± 14.1	9.9 ± 0.2	9.9 ± 0.3
P_ξ (days)	5.42 ± 0.04	5.53 ± 0.05	5.43 ± 0.04	5.54 ± 0.05	2.91 ± 0.02	2.9 ± 0.02
$\xi_{\rm E,N}$ (10^{-3})	1.82 ± 0.15	-0.36 ± 0.36	-1.65 ± 0.11	0.34 ± 0.20	-3.59 ± 0.11	-3.23 ± 0.08
$\xi_{\rm E,E}$ (10^{-3})	0.69 ± 0.34	1.53 ± 0.12	0.42 ± 0.41	1.07 ± 0.10	2.86 ± 0.09	2.58 ± 0.07
$\pi_{\rm E,N}$	-	-	-	-	-	0.09 ± 0.05
$\pi_{\rm E,E}$	-	-	-	-	-	0.26 ± 0.14
χ^2	10856.4	10840.9	10861.2	10842.7		
$\Delta\chi^2$	15.5	-	20.3	1.8		

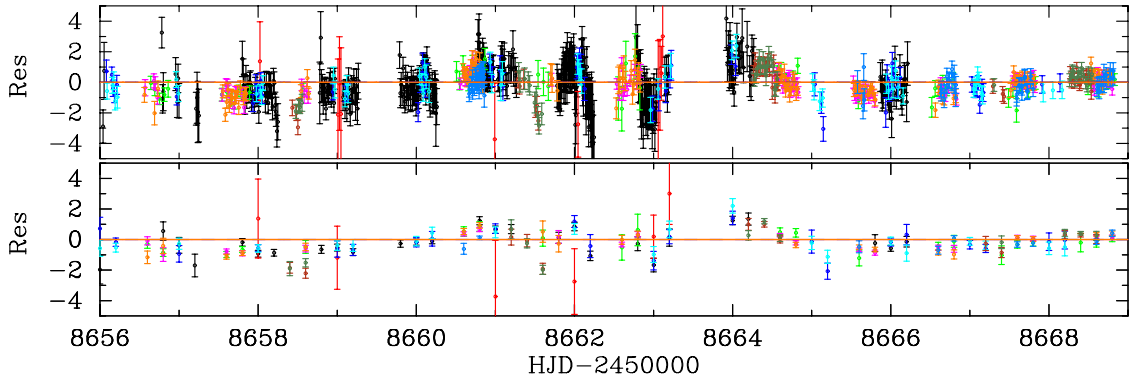

Figure 3.6: Residuals based on the best model of 2L1S + parallax. The bottom panel is binned by 0.2 days.

3.4.2 Parallax

It is known that the acceleration of Earth orbital motion affects the light curve of microlensing events (Gould, 1992, 2004; Smith et al., 2003; Dong et al., 2009). This parallax effect can be described by the microlensing parallax vector $\boldsymbol{\pi_{\rm E}} = (\pi_{\rm E,N}, \pi_{\rm E,E})$ where $\pi_{\rm E,N}$ and $\pi_{\rm E,E}$ represents respectively the north and east components of $\boldsymbol{\pi_{\rm E}}$ projected onto the sky plane in equatorial coordinates. The direction of $\boldsymbol{\pi_{\rm E}}$ is defined to coincide with the direction of the geocentric lens-source relative proper motion projected onto the sky plane at the reference time $t_{\rm fix}$, and the amplitude of $\boldsymbol{\pi_{\rm E}}$ is $\pi_{\rm E} = {\rm au}/\tilde{r}_{\rm E}$ ($\tilde{r}_{\rm E}$ is the Einstein radius projected inversely to the observation plane) (Gould, 2000).

As a result of modeling by adding two parameters of $\pi_{\rm E,N}$ and $\pi_{\rm E,E}$, we found two degenerate models with $(q, s) = (3.5 \times 10^{-3}, 0.57)$ and $(q, s) = (3.4 \times 10^{-3}, 1.74)$, that are better than the standard 2L1S model by $\Delta\chi^2 = 68.3$. However, the cumulative $\Delta\chi^2$ improvement for parallax model relative to standard 2L1S model is not consistent between the data sets. Furthermore, we still found systematic residuals around the peak of $8657 < {\rm HJD}' < 8667$ in these models, as seen in the standard 2L1S model shown by the orange solid line in Figure 3.6.

3.4.3 Xallarap

We next consider the possibility that the short term residuals in $8657 < \mathrm{HJD}' < 8667$ are caused by a short period binary source system, i.e., they arise owing to the xallarap effect.

The xallarap effect can be described by the following seven parameters; the direction toward the solar system relative to the orbital plane of the source system, RA_ξ and decl_ξ; the source orbital period, P_ξ; the source orbital eccentricity e_ξ; the perihelion $T_{\rm peri}$; the xallarap vector, $\boldsymbol{\xi_{\rm E}} = (\xi_{\rm E,N}, \xi_{\rm E,E})$. Note that this effect does not include the magnifying effect of the source companion star; only the source host contributes to the magnification. We denote this model of the microlensing event as the 2L1S + xallarap model rather than as the 2L2S model to distinguish it from a model including secondary source magnification. As discussed in detail in Section 3.5, the flux ratio of the source companion to the host star in the I-band in the best 2L1S + xallarap model is $\sim 10^{-7}$. Therefore, we assume that the brightening of the source companion star is negligible.

We first fit using 78,960 values of xallarap parameters $(\mathrm{RA}_\xi, \mathrm{decl}_\xi, P_\xi)$ with the four best standard 2L1S models (close1, wide1, close2, and wide2) as initial values. We used 20 evenly spaced values for $0 \leq \mathrm{RA}_\xi < 360$, 21 values for $-90 \leq \mathrm{decl}_\xi < 90$, 19 and 99 values for $1 < P_\xi$ [days] < 19 and $20 < P_\xi$ [days] < 1000, respectively. After that, we fit again with $(\mathrm{RA}_\xi, \mathrm{decl}_\xi, P_\xi)$ as free parameters. As a result, we found the best solutions with $P_\xi \sim 5$ days independently from the initial values of close1, wide1, close2, and wide2. We also found that the final q and s values are quite different from their initial values, and did not converge. Therefore, we next set $P_\xi \sim 5$ days as the initial value, RA_ξ and decl_ξ to random values, and performed model fitting with 34,440 values of (q, s, α) using the same procedure as the standard 2L1S modeling described in Section 3.4.1. Short-period binary stars orbiting in $P_\xi \sim 5$ days are affected by orbital circularization due to tidal friction (Fabrycky & Tremaine, 2007). The tidal circularization time is discussed in Chapter 4, but it is reasonable to assume that at the age of the stars in the Galactic bulge (Sit & Ness, 2020), the orbit is fully circularized. Therefore, we fixed the eccentricity at $e_\xi = 0$. When $e_\xi = 0$, $T_{\rm peri}$ can be eliminated as a fitting parameter. The results are shown in the right panel of Figure 3.3.

The figure shows that there are degenerate solutions for various combinations of (q, s) values in the range of $\Delta\chi^2 \lesssim 20$. Table 3.3 shows the best fit model parameters for the wide and close

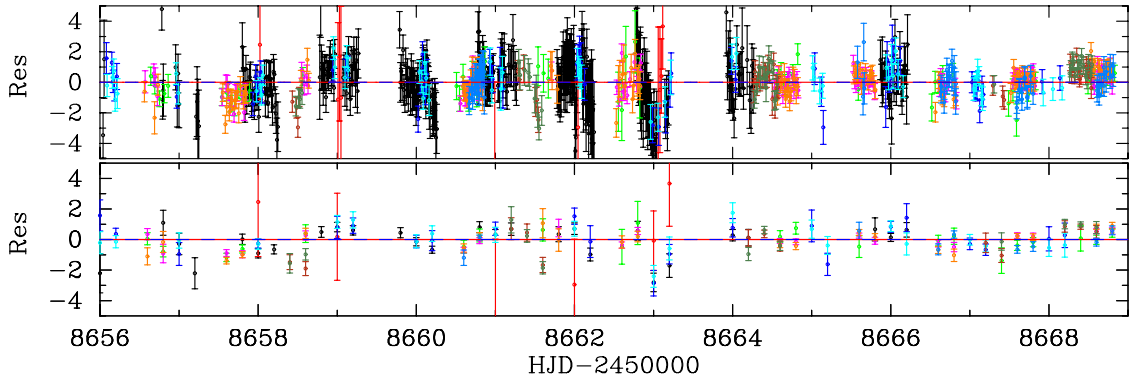

Figure 3.7: Residuals based on the best model of 1L1S + xallarap. The lower panel is binned by 0.2 days.

solutions. The reason for the slight difference in $\Delta\chi^2$ between Figure 3.3 and Table 3.3 is that the models in Table 3.3 were fitted with q, s, and α set free. We label the best models of the mass ratio range in the 2L1S + xallarap close model, respectively: the best with $q \leq 0.1$ is XLclose1, the best with $0.1 < q \leq 1$ is XLclose2. Similarly, in the wide model of 2L1S + xallarap, we label the best with $q \leq 0.1$ as XLwide1, the best with $0.1 < q \leq 1$ as XLwide2. Figure 3.1 shows the best 2L1S + xallarap model (i.e. XLclose2). The xallarap models fit the light curves better than the standard 2L1S models.

Figure 3.5 shows the cumulative $\Delta\chi^2$ of the best 2L1S + xallarap model relative to the best standard 2L1S model. One can see that the 2L1S + xallarap model improves χ^2 around the peak of $8657 < \mathrm{HJD}' < 8667$. The 2L1S + xallarap model improved χ^2 by 903.7 from the standard 2L1S model and by 835.5 from the 2L1S + parallax model. Figure 3.8 shows the geometry of the primary lens, source trajectory, caustics on the magnification map for the best 2L1S + xallarap model. The short orbital period of the source star with $P_\xi \sim 5$ days make the source's trajectory a wavy line.

We applied the same procedure for 1L1S and found the best 1L1S + xallarap model has $\Delta\chi^2 = 470.6$ worse than the best 2L1S + xallarap model. However, asymmetric maps similar to Figure 3.8 can be created by binary lenses of various parameters, which led to the emergence of various

degenerate 2L1S + xallarap models. We label the best 1L1S + xallarap model as 1LXL. Even the 1L1S + xallarap + parallax model was $\Delta\chi^2 = 444.8$ worse than the best 2L1S + xallarap model. We label the best 1L1S + xallarap + parallax model as 1LXLPL. The parameters of each of the best models are listed in Table 3.4. The number of data points used in the calculation of χ^2 is 10743, which is the total number of data points shown in Table 3.1. The value $\Delta\chi^2$ takes the difference from the best model, 2L1S + xallarap. The value Reduced-χ^2 is χ^2 divided by the degrees of freedom = (data points) - (number of parameters). The value χ^2 calculated using only data points in the range shown in Figure 3.1 ($8656 \leq \mathrm{HJD}' \leq 8669$) is defined as χ^2_{peak}, and its $\Delta\chi^2_{\mathrm{peak}}$ and Reduced-χ^2_{peak} are also included in the table. The number of data points for $8656 \leq \mathrm{HJD}' \leq 8669$ is 894. We considered other higher order effects and combinations of them such as 2L1S + xallarap + parallax, 2L1S + xallarap + parallax + lens orbital motion, and 1L2S, but could not detect them significantly. For comparison with the 2L1S + xallarap model, we also fitted the 2L1S model with a variable source. In this case, the amplitude of the variation, γ; the period of the variation, T_{v}; and the initial phase, β are additional parameters. We fixed the other parameters at those of the best standard 2L1S model (i.e., close1). However, the χ^2 improvement from the best standard 2L1S model was only 139.1, $\Delta\chi^2 = 764.6$ worse than the best 2L1S + xallarap model. To confirm, we performed 2L1S + xallarap fitting analysis with $\xi_{\mathrm{E,N}}$, $\xi_{\mathrm{E,E}}$, RA_ξ, decl_ξ, and P_ξ set free and the other parameters fixed to the best standard 2L1S model. As a result, the χ^2 was improved by 594.5 over the best standard 2L1S model. This is only $\Delta\chi^2 = 309.3$ worse than the best 2L1S + xallarap model. That is, for two models (2L1S + xallarap and 2L1S + variable source) with the same fixed lens parameters, the 2L1S + xallarap model has 455.3 better χ^2 than the 2L1S + variable source model. Finally, we conclude that the best model in this analysis is XLclose2. In addition, the xallarap signal is consistent, and considering additional higher order effects on 2L1S + xallarap has little influence on our conclusions.

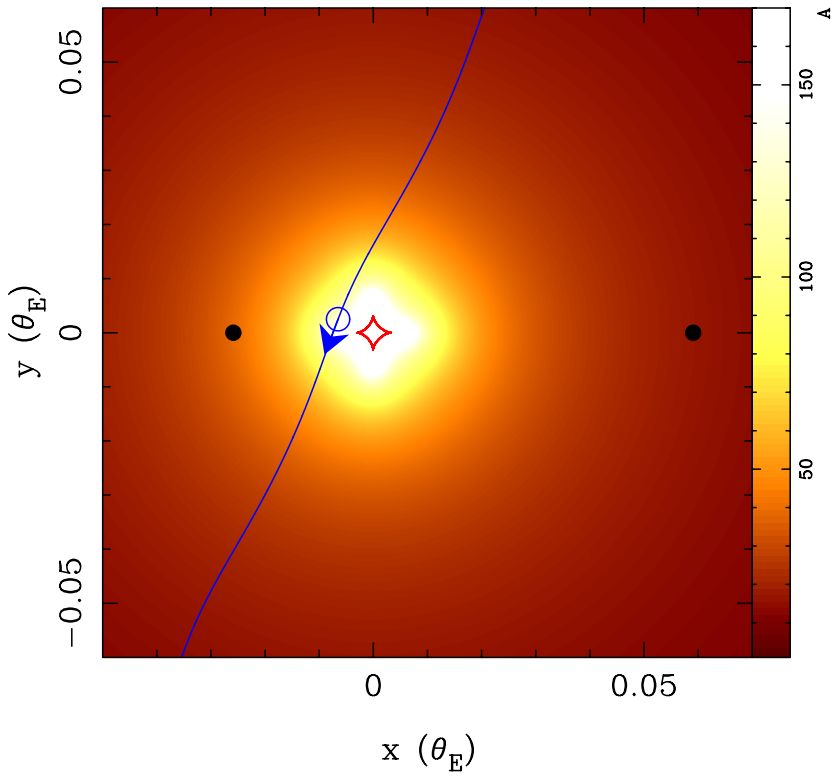

Figure 3.8: The geometry of the primary lens, source trajectory, caustics on the magnification map for the best 2L1S + xallarap model. The black filled circle on the left indicates the primary lens. The black filled circle on the right indicates the lens companion. The blue line with arrow represents the source trajectory. The blue circles represent the source size and position at t_0. The red closed curve represents the caustic. The colored contours represent the magnification map.

Table 3.4: Comparison of χ^2 between each microlensing models

Model	$N_{\rm param}$	χ^2	$\Delta\chi^2$	reduced-χ^2	$\chi^2_{\rm peak}{}^*$	$\Delta\chi^2_{\rm peak}{}^*$	reduced-$\chi^2_{\rm peak}{}^*$
1L1S	4	33144.7	22303.8	3.09	21118.1	20256.1	24.16
1L1S + xallarap	9[1]	11311.5	470.6	1.06	1255.2	393.2	1.45
standard 2L1S	7	11744.7	903.7	1.10	1590.0	728.0	1.83
2L1S + parallax	9	11676.5	835.5	1.09	1578.6	716.6	1.82
2L1S + xallarap	12**	10840.9	-	1.01	862.0	-	1.00

* The value χ^2 calculated using only the data points near the magnification peak ($8656 \leq {\rm HJD}' \leq 8669$ (894 data points)) is defined as $\chi^2_{\rm peak}$.

** The source orbital eccentricity is fixed at $e_\xi = 0$. When $e_\xi = 0$, $T_{\rm peri}$ can be eliminated as a chain parameter.

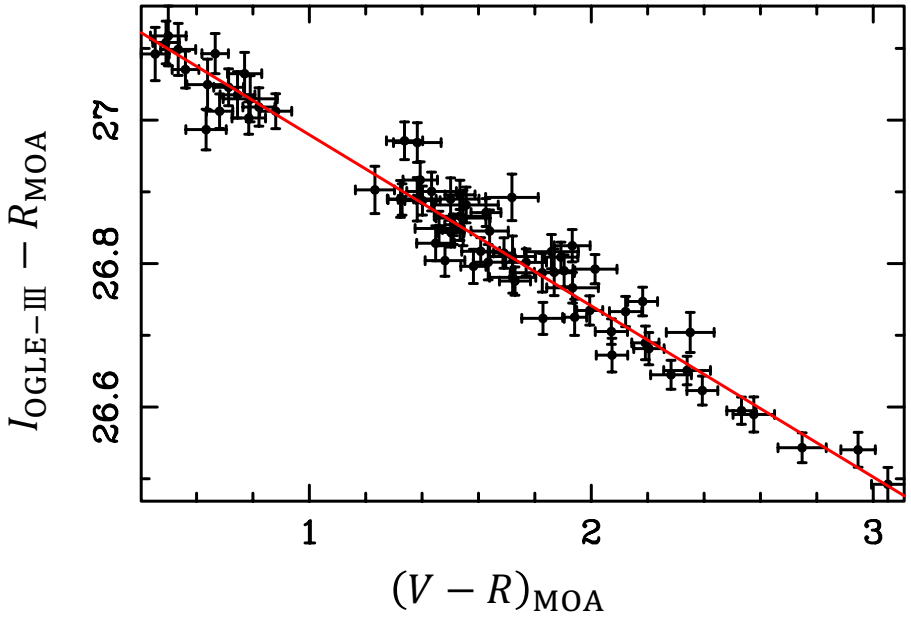

Figure 3.9: Relationship between $I_{\mathrm{OGLE-III}} - R_{\mathrm{MOA}}$ and $(V-R)_{\mathrm{MOA}}$. The red line indicates the regression line shown in Equation 3.4, and the black dots indicate the color of the object used to derive the regression line.

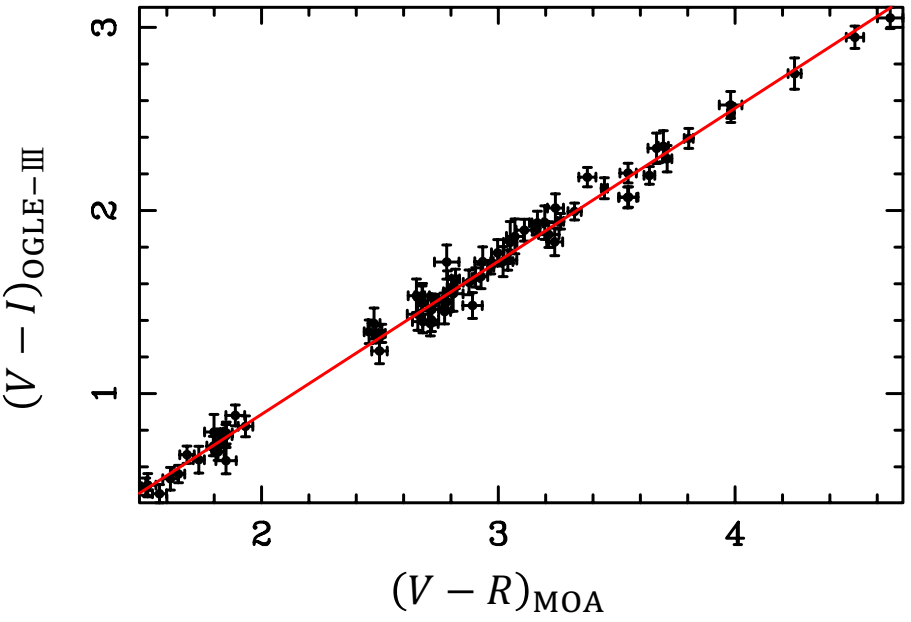

Figure 3.10: Relationship between $(V-I)_{\mathrm{OGLE-III}}$ and $(V-R)_{\mathrm{MOA}}$. The red line indicates the regression line shown in Equation 3.5, and the black dots indicate the color of the object used to derive the regression line.

3.5 Source System Properties

We estimated the angular source radius, θ_*, from the color and magnitude of the source. The best fit instrumental source magnitudes of $R_{\rm MOA}$ and $V_{\rm MOA}$ are calibrated to the Cousins I-band and Johnson $V-$band magnitude scales by cross-referencing to the stars in the OGLE-III photometry map (Szymański et al., 2011) within $0''.7$ of the event.

For reliability, we restricted stars to $16 \leq V_{\rm OGLE-III}$ [mag] ≤ 19, and performed 5σ clipping in the linear regressions of $V_{\rm MOA}$ vs. $V_{\rm OGLE-III}$ and $(I_{\rm OGLE-III} - R_{\rm MOA})$ vs. $(V-R)_{\rm MOA}$ and $(V-I)_{\rm OGLE-III}$ vs. $(V-R)_{\rm MOA}$, respectively. From the final 73 remaining objects, the following conversion equations from $R_{\rm MOA}$ and $(V-R)_{\rm MOA}$ to $I_{\rm OGLE-III}$ and $(V-I)_{\rm OGLE-III}$ were obtained by linear regression,

$$I_{\rm OGLE-III} = R_{\rm MOA} - (0.24 \pm 0.01) \times (V-R)_{\rm MOA} + (27.22 \pm 0.01), \tag{3.4}$$

$$(V-I)_{\rm OGLE-III} = (1.20 \pm 0.01) \times (V-R)_{\rm MOA} + (0.94 \pm 0.02). \tag{3.5}$$

The regression lines from $R_{\rm MOA}$ and $(V-R)_{\rm MOA}$ to $I_{\rm OGLE-III}$ and $(V-I)_{\rm OGLE-III}$ and the objects used to derive the regression lines are shown in Figures 3.9 and 3.10. As a result, the color and magnitude with the extinction of the source star for the best-fit 2L1S + xallarap model were $(V-I, I)_{\rm S} = (2.527 \pm 0.031, 21.035 \pm 0.015)$.

Next, the red clump giant (RCG) centroid was estimated by performing $N(I)dI$ fitting on the I-band magnitude distribution of stars within $2'$ of the star. where $N(I)$ is the number density of I-band magnitudes of stars in the Red Giant Branch and $N(I)dI$ is the number of stars in the I-band magnitude range dI. A color-magnitude diagram of the stars within $2'$ around OGLE-2019-BLG-0825 is shown in Figure 3.11. The following equation from (Nataf et al., 2013a) was used for fitting,

$$\begin{aligned} N(I)dI =& A\exp[B(I-I_{\rm RCG})] + \frac{N_{\rm RCG}}{\sqrt{2\pi}\sigma_{\rm RCG}} \exp\left[-\frac{(I-I_{\rm RCG})^2}{2\sigma_{\rm RCG}^2}\right] \\ &+ \frac{N_{\rm RGBB}}{\sqrt{2\pi}\sigma_{\rm RGBB}} \exp\left[-\frac{(I-I_{\rm RGBB})^2}{2\sigma_{\rm RGBB}^2}\right] + \frac{N_{\rm AGBB}}{\sqrt{2\pi}\sigma_{\rm AGBB}} \exp\left[-\frac{(I-I_{\rm AGBB})^2}{2\sigma_{\rm AGBB}^2}\right], \end{aligned} \tag{3.6}$$

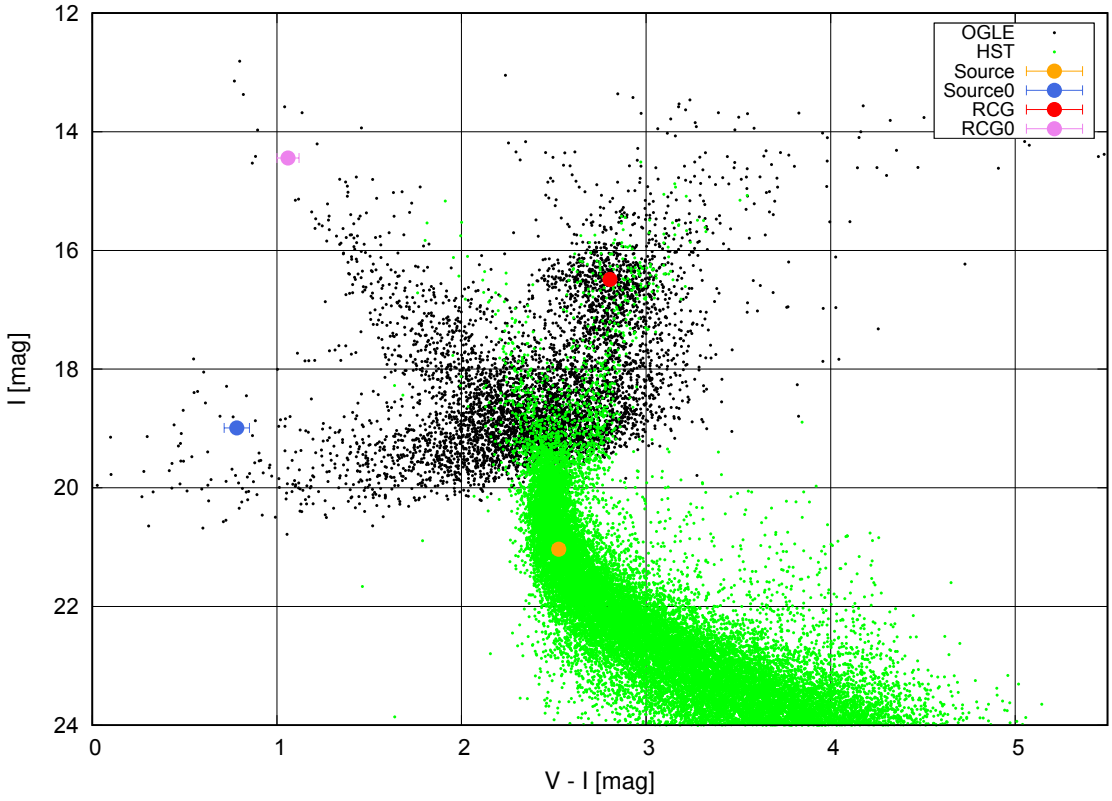

Figure 3.11: Color Magnitude Diagram (CMD, black dots) of the OGLE-III stars within $2'$ around OGLE-2019-BLG-0825. The green dots are stars in Baade's window based on Hubble Space Telescope observations (Holtzman et al., 1998), color- and magnitude-matched at the RCG position. The orange dot marked "Source" in the legend represents the position of the source with extinction, blue dot marked "Source0" in the legend represents the position of the source without extinction, red dot marked "RCG" in the legend represents the position of RCG centroid with extinction within $2'$ around OGLE-2019-BLG-0825, and pink dot marked "RCG0" in the legend represents the position of RCG centroid without extinction within $2'$ around OGLE-2019-BLG-0825.

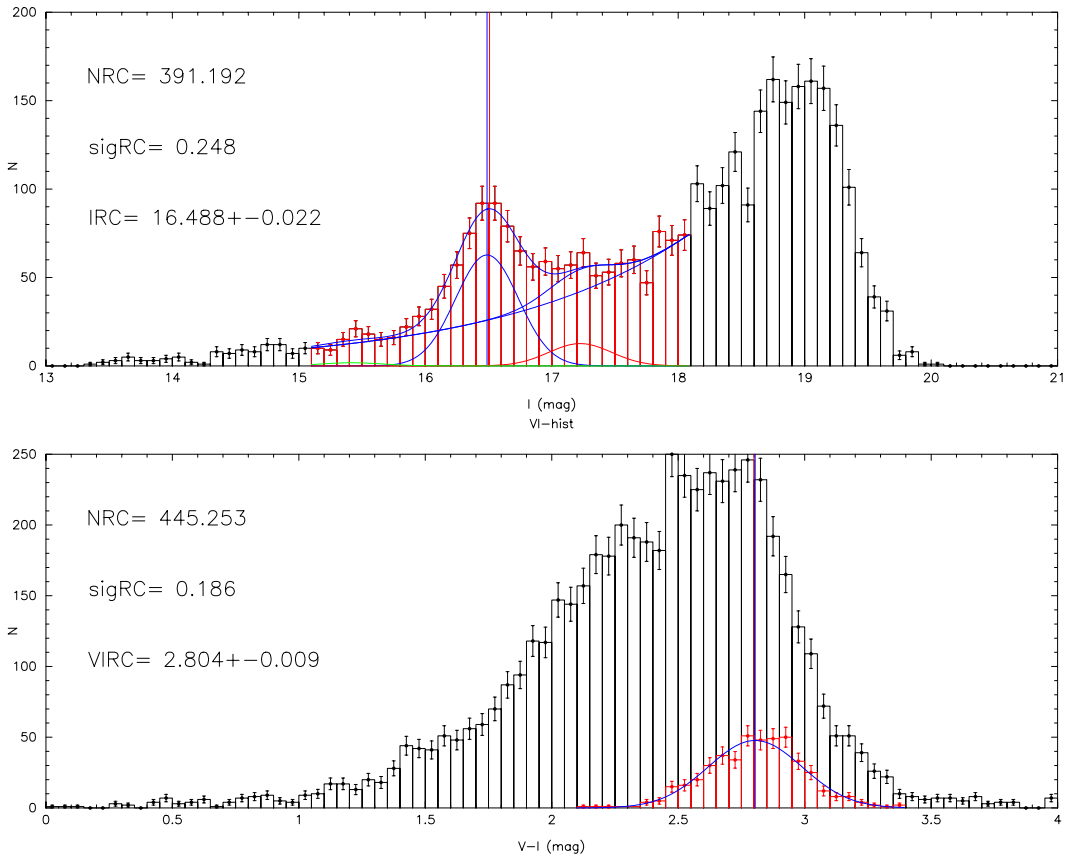

Figure 3.12: (Top panel) Histogram of I-band magnitudes of OGLE-III stars within $2'$ of OGLE-2019-BLG-0825. The blue vertical line is $I_{\rm RCG}$, the median magnitude of the I-band for the RCG. The magenta vertical line is $I_{\rm RCG,mean}$, the mean magnitude of the I-band for the RCG. The magenta, blue, red, and green curves show $LF_{\rm RG}(I)$, $LF_{\rm RCG}(I)$, $LF_{\rm RGBB}(I)$, and $LF_{\rm AGBB}(I)$ obtained by fitting. The color differences between the red and black histograms are those used and not used for fitting, respectively, and the stars in the red histogram are $|I - I_{\rm RCG,mean}| < 1.5$. The fitting results of $N_{\rm RCG}$, $\sigma_{\rm RCG}$, and $I_{\rm RCG}$ are shown on the left side as NRC, sigRC, and IRC, respectively. (Bottom panel) Histogram of $V-I$ color of OGLE-III stars within $2'$ of OGLE-2019-BLG-0825. The blue vertical line is $(V-I)_{\rm RCG}$, the median $V-I$ color for the RCG. The magenta vertical line is $I_{\rm RCG,mean}$, the mean $V-I$ color for the RCG. The blue curve shows the best-fitted Gaussian function. The color differences between the red and black histograms are those used and not used for fitting, respectively, and the stars in the red histogram are $|I - I_{\rm RCG}| < 0.3$ and $|(V-I) - (V-I)_{\rm RCG,mean}| < 0.7$. The fitting results of $N_{\rm RCG}$, $\sigma_{\rm RCG}$, and $(V-I)_{\rm RCG}$ are shown on the left side as NRC, sigRC, and VIRC, respectively.

where "RGBB" and "AGBB" mean "Red Giant Branch Bump" and "Asymptotic Giant Branch Bump" and "Asymptotic Giant Branch Bump", respectively. $N_{\rm RGBB}$ and $N_{\rm AGBB}$ are the number of RGBB and AGBB, respectively; $I_{\rm RGBB}$ and $I_{\rm AGBB}$ are the I-band magnitudes of RGBB and AGBB, respectively; and $\sigma_{\rm RGBB}$ and $\sigma_{\rm AGBB}$ are the standard deviation of I-band magnitudes of RGBB and AGBB, respectively. Each term in Equation 3.6 is defined as follows:

$$LF_{\rm RG}(I) = A\exp[B(I - I_{\rm RCG})], \tag{3.7}$$

$$LF_{\rm RCG}(I) = \frac{N_{\rm RCG}}{\sqrt{2\pi}\sigma_{\rm RCG}}\exp\left[-\frac{(I - I_{\rm RCG})^2}{2\sigma^2_{\rm RCG}}\right], \tag{3.8}$$

$$LF_{\rm RGBB}(I) = \frac{N_{\rm RGBB}}{\sqrt{2\pi}\sigma_{\rm RGBB}}\exp\left[-\frac{(I - I_{\rm RGBB})^2}{2\sigma^2_{\rm RGBB}}\right], \tag{3.9}$$

$$LF_{\rm AGBB}(I) = \frac{N_{\rm AGBB}}{\sqrt{2\pi}\sigma_{\rm AGBB}}\exp\left[-\frac{(I - I_{\rm AGBB})^2}{2\sigma^2_{\rm AGBB}}\right]. \tag{3.10}$$

In this analysis, the RGBB and AGBB parameters were fixed at the following mean values (Nataf et al., 2013b) to minimize the systematic influence of additional parameters on the fit,

$$N_{\rm RGBB} = 0.201 \times N_{\rm RCG}, \tag{3.11}$$

$$N_{\rm AGBB} = 0.028 \times N_{\rm RCG}, \tag{3.12}$$

$$I_{\rm RGBB} = I_{\rm RCG} + 0.737, \tag{3.13}$$

$$I_{\rm AGBB} = I_{\rm RCG} - 1.07, \tag{3.14}$$

$$\sigma_{\rm RGBB} = \sigma_{\rm AGBB} = \sigma_{\rm RCG}. \tag{3.15}$$

Therefore, the four parameters $I_{\rm RCG}$, $\sigma_{\rm RCG}$, B, and $N_{\rm RCG}/A$ are free. Then, a histogram of $V - I$ magnitudes was created for stars with magnitudes $|I - I_{\rm RCG}| \leq 0.7$ and fitted with a Gaussian function to obtain the $V - I$ magnitude of the RCG. Figure 3.12 shows histograms of the I-band magnitudes and $V - I$ colors, respectively, of the stars in the OGLE-III photometric map. As a result, we estimate that the centroid of the color and magnitude with extinction of the RCG within $2'$ around star OGLE-2019-BLG-0825 is $(V - I, I)_{\rm RCG} = (2.804 \pm 0.009, 16.488 \pm 0.022)$. The intrinsic color and magnitude of the RCG stars are $(V - I, I)_{\rm RCG,0} = (1.060 \pm 0.060, 14.443 \pm 0.040)$ (Bensby et al., 2013; Nataf et al., 2013a). Then, we calculated $(E(V-I), A(I)) = (1.744\pm$

0.061, 2.045 ± 0.046). Finally, we have the intrinsic color and magnitude of the source star $(V - I, I)_{\rm S,0} = (0.783 \pm 0.068,\ 18.990 \pm 0.048)$ for the best 2L1S + xallarap model. Also, Figure 3.11 shows that the source is a main-sequence star and unlikely to be a variable star. Table 3.5 shows that the values for $(V - I, I)_{\rm S,0}$ for the other models are almost the same.

We estimated the angular source radius of $\theta_* = 0.538 \pm 0.039$ μas from the relation,

$$\log(2\theta_*) = 0.50 + 0.42(V - I)_0 - 0.2I_0, \tag{3.16}$$

where the accuracy of the relational equation is better than 2% (Fukui et al., 2015). This relation is based on Boyajian et al. (2014), but derived by limiting to FGK stars with $3900 < T_{\rm eff}$ [K] < 7000 (Boyajian, 2014, Private Communication). Then, we calculated the lens's Einstein radius of $\theta_{\rm E} = \rho\theta_* = 0.25 \pm 0.02$ mas and the lens-source relative proper motion of $\mu_{\rm rel} = \theta_{\rm E}/t_{\rm E} = 0.97 \pm 0.10$ mas yr^{-1}.

The amplitude of the xallarap vector, $\xi_{\rm E}$ is described as follows,

$$\xi_{\rm E} \equiv \Big(\frac{\theta_{\rm E} D_{\rm S}}{1\ {\rm au}}\Big)^{-1} \Big(\frac{P_\xi}{1\ {\rm yr}}\Big)^{2/3} \Big(\frac{M_{\rm S,C}}{M_\odot}\Big) \Big(\frac{M_{\rm S,H} + M_{\rm S,C}}{M_\odot}\Big)^{-2/3}, \tag{3.17}$$

where $M_{\rm S,H}$ and $M_{\rm S,C}$ are the masses of host and companion of the source system, respectively. $M_{\rm S,H}$ is estimated by using isochrones (PARSEC; Bressan et al., 2012) and the absolute magnitude of the host source star $M(I_{\rm S}) = I_{\rm S,0} + 5\log_{10} D_{\rm S}[{\rm pc}] + 5 = 4.48 \pm 0.38$ mag assuming $D_{\rm S} = 8.0 \pm 1.4$ kpc. Then, $M_{\rm S,C}$ can be solved from Equation (3.17). Also, using Kepler's third law,

$$\Big(\frac{a_{\rm S}}{1\ {\rm au}}\Big)^3 \Big(\frac{P_\xi}{1\ {\rm yr}}\Big)^{-2} = \Big[\frac{M_{\rm S,H} + M_{\rm S,C}}{M_\odot}\Big], \tag{3.18}$$

we can solve $a_{\rm S}$ which is the semi-major axis of the source system. In addition, we calculated $L_{\rm S,C}/L_{\rm S,H}$, the luminosity ratio in the I-band of the source companion $L_{\rm S,C}$ to the source host $L_{\rm S,H}$. For this we used the mass-luminosity empirical relation of Bennett et al. (2015), which combines Henry & McCarthy (1993) and Delfosse et al. (2000), and the isochrone model of Baraffe et al. (2003). We used the Henry & McCarthy (1993) relation for $M > 0.66\ M_\odot$, the Delfosse et al. (2000) relation for $0.12\ M_\odot < M < 0.54\ M_\odot$. For low-mass stars ($M < 0.10\ M_\odot$) we used

the isochrone model of Baraffe et al. (2003) for sub-stellar objects at an age of 10 Gyr. At the boundary of these mass ranges, we interpolated linearly between the two relations. Table 3.5 shows our calculated properties of the source system for the 2L1S + xallarap models in Table 3.3. The source host in the best 2L1S + xallarap model is a G-type main-sequence star and the source companion is a brown dwarf with a semi major axis of $a_{\rm S} = 0.0594 \pm 0.0005$ au. The luminosity ratio at the I-band of the source companion $L_{\rm S,C}$ is small, $L_{\rm S,C}/L_{\rm S,H} = (1.0 \pm 0.3) \times 10^{-7}$, and does not conflict with our assumption the magnified flux of the second source is too weak to be detected.

Table 3.5: Source system properties of the 2L1S + xallarap models

Model	XLclose1	XLclose2	XLwide1	XLwide2
range of q	$q \leq 0.1$	$0.1 < q \leq 1$	$q \leq 0.1$	$0.1 < q \leq 1$
$V_{\rm S}$ (mag)	23.58 ± 0.03	23.56 ± 0.03	23.55 ± 0.03	23.56 ± 0.03
$I_{\rm S}$ (mag)	21.06 ± 0.01	21.04 ± 0.01	21.02 ± 0.01	21.06 ± 0.01
$H_{\rm S}$ (mag)	18.54 ± 0.30	18.52 ± 0.48	18.51 ± 0.48	18.54 ± 0.48
$K_{\rm S}$ (mag)	18.31 ± 0.48	18.29 ± 0.48	18.28 ± 0.48	18.31 ± 0.48
$(V-I)_{\rm S}$ (mag)	2.52 ± 0.03	2.53 ± 0.03	2.52 ± 0.03	2.53 ± 0.03
$I_{\rm S,0}$ (mag)	19.01 ± 0.05	18.99 ± 0.05	19.00 ± 0.05	19.01 ± 0.05
$(V-I)_{\rm S,0}$ (mag)	0.78 ± 0.07	0.78 ± 0.07	0.78 ± 0.07	0.78 ± 0.07
$\theta_{\rm E}$ (mas)	0.53 ± 0.04	0.25 ± 0.02	0.22 ± 0.02	0.37 ± 0.05
$\mu_{\rm rel}$ (mas yr^{-1})	0.78 ± 0.07	0.97 ± 0.10	0.81 ± 0.07	1.01 ± 0.16
$M_{\rm S,H}$ ($M_\odot$)	0.865 ± 0.045	0.867 ± 0.045	0.869 ± 0.045	0.865 ± 0.045
$M_{\rm S,C}$ ($M_\odot$)	0.050 ± 0.005	0.048 ± 0.004	0.047 ± 0.004	0.051 ± 0.006
$a_{\rm S}$ (10^{-2} au)	5.86 ± 0.04	5.94 ± 0.05	5.87 ± 0.03	5.95 ± 0.05
$L_{\rm S,C}/L_{\rm S,H}$ (10^{-7})	1.15 ± 0.34	1.02 ± 0.26	0.95 ± 0.23	1.21 ± 0.47
χ^2	10856.4	10840.9	10861.2	10842.7
$\Delta\chi^2$	15.5	-	20.3	1.8

We estimated $M_{\rm S,H}$, $M_{\rm S,C}$, $a_{\rm S}$, and $L_{\rm S,C}/L_{\rm S,H}$ in Table 3.5 assuming that the source star is 10 Gyr old and has the same metallicity as the Sun (i.e., $[{\rm M/H}] = 0$). We have calculated the properties of the XLclose2 source star system in isochrone models of different ages and metallicities to clarify the uncertainty caused by this assumption. We compared stellar ages at 5×10^9 years and 10^{10} years, and stellar metallicity at $[{\rm M/H}] = -0.5$, 0, and $+0.5$. Table 3.6 shows the properties of the source system for the XLclose2 in its different isochrone models. Using the isochrones with a stellar age of 5 Gyr, the masses of the host and companion stars are slightly higher than when using

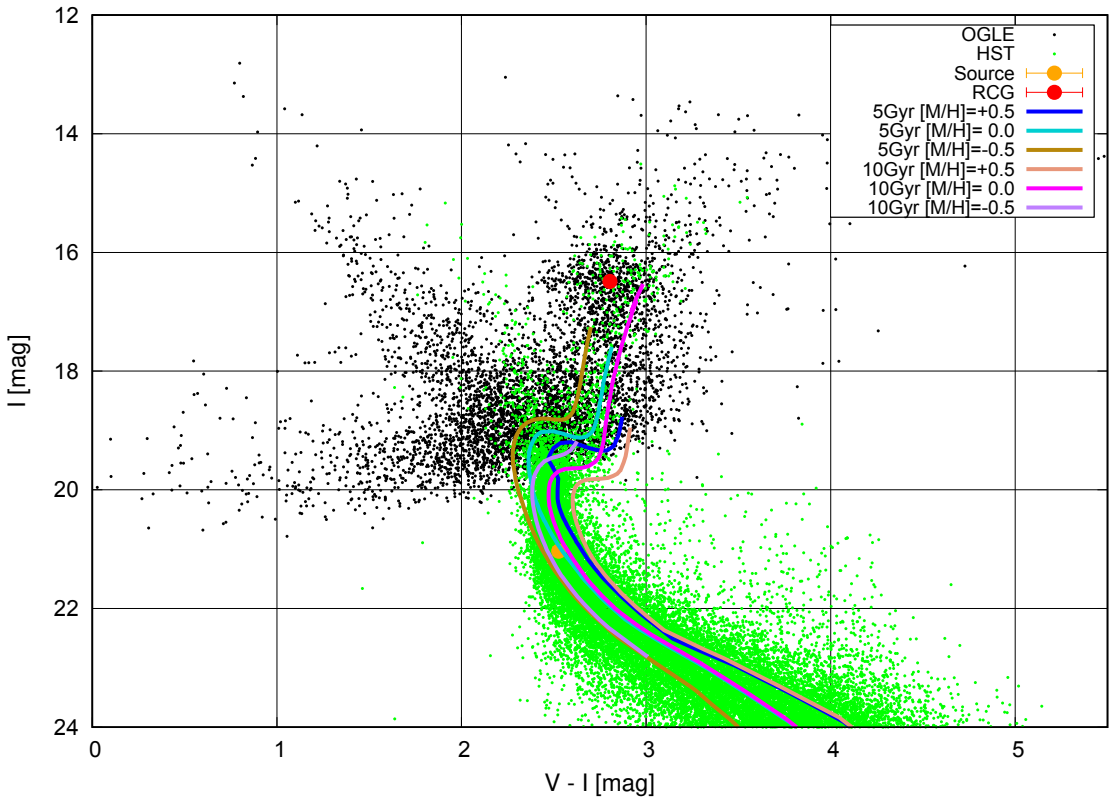

Figure 3.13: Same CMD as in Figure 3.11, but plots isochrones of various stellar ages and metallicities. The isochrones are shifted by the amount of reddning and extinction $(E(V-I), A(I)) = (1.744 \pm 0.061, 2.045 \pm 0.046)$ from the intrinsic color and absolute magnitude, respectively, after considering the distance modulus. The blue curve is the isochrone for a stellar age of 5 Gyr and $[\mathrm{M/H}] = -0.5$. The turquoise curve is the isochrone for a stellar age of 5 Gyr and $[\mathrm{M/H}] = 0$. The golden curve is the isochrone for a stellar age of 5 Gyr and $[\mathrm{M/H}] = +0.5$. The salmon pink curve is the isochrone for a stellar age of 10 Gyr and $[\mathrm{M/H}] = -0.5$. The magenta curve is the isochrone for a stellar age of 10 Gyr and $[\mathrm{M/H}] = 0$ and was used for the calculations in Table 3.5. The purple pink curve is the isochrone for a stellar age of 10 Gyr and $[\mathrm{M/H}] = +0.5$.

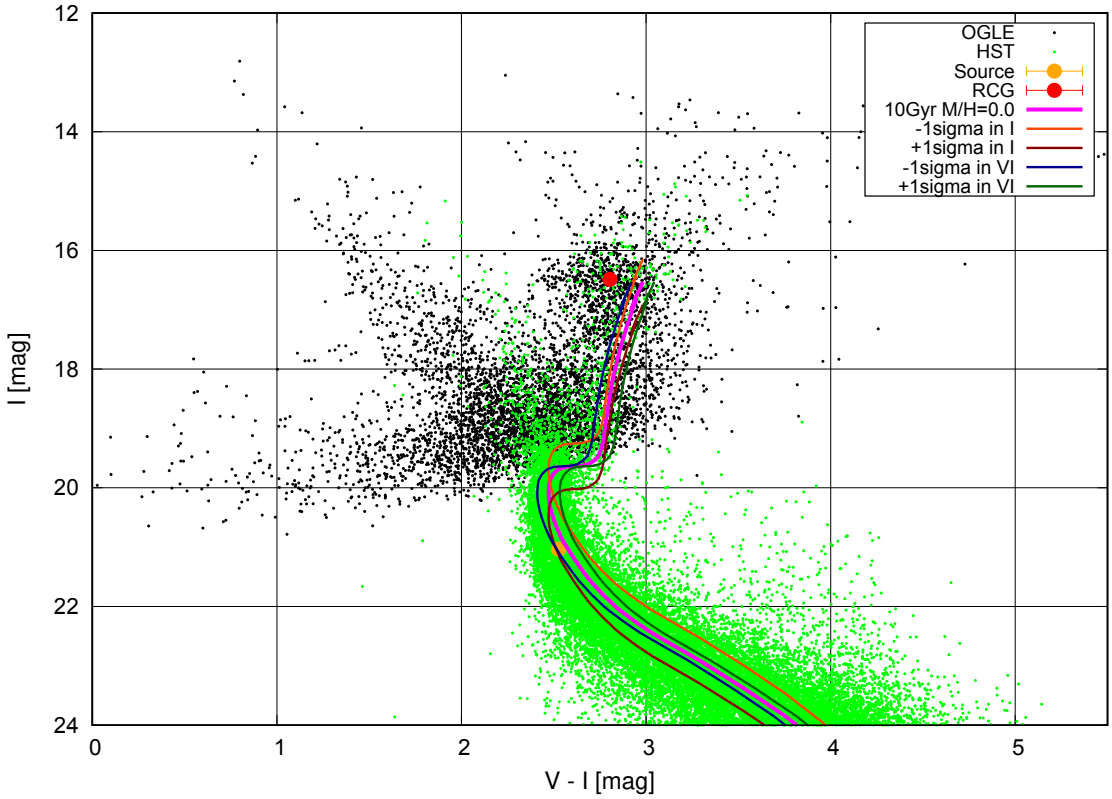

Figure 3.14: Same CMD as in Figure 3.11, but the isochrones used in the calculations in Table 3.5 are plotted, as well as the isochrones shifted by the error in the I-band magnitude extinction and distance of the source and by the error in the $V - I$ color reddening of source. The magenta curve is the isochrone for a stellar age of 10 Gyr and $[\mathrm{M/H}] = 0$ and was used for the calculations in Table 3.5. The orange-red curve is an isochrone where the stellar age is 10 Gyr, $[\mathrm{M/H}] = 0$, and the source I-band extinction is 1 sigma weaker than estimated. The dark-red curve is an isochrone where the stellar age is 10 Gyr, $[\mathrm{M/H}] = 0$, and the source I-band extinction is 1 sigma stronger than estimated. The dark-blue curve is an isochrone where the stellar age is 10 Gyr, $[\mathrm{M/H}] = 0$, and the source $V - I$ color reddening is 1 sigma weaker than estimated. The dark-green curve is an isochrone where the stellar age is 10 Gyr, $[\mathrm{M/H}] = 0$, and the source $V - I$ color reddening is 1 sigma stronger than estimated.

the isochrones with a stellar age of 10 Gyr. In addition, the semimajor axis is slightly wider. For different metallicities, the higher the metallicity, the heavier the mass of the host and companion and the wider the semimajor axis. Figure 3.13 shows the difference in position of the isochrone models on the CMD depending on stellar age and stellar metallicity. The plotted isochrones are shifted by the amount of reddning and extinction $(E(V-I), A(I)) = (1.744\pm0.061, 2.045\pm0.046)$ from the intrinsic color and absolute magnitude, respectively. The isochrone model with a stellar age of 10 Gyr and $[\mathrm{M/H}] = 0$ is close to the apparent color magnitude of the source. Thus, the assumption of the properties of the source is found to be reasonable. In Appendix A, we performed a two-dimensional chi-square test to the color magnitude of the source with extinction $(V - I, I)_{\mathrm{S}}$ using 160 isochronous models with different combinations of stellar age t_{star} and metallicity. As a result, χ^2 is the smallest in the isochronous model where the stellar age is $t_{\mathrm{star}} = 10$ Gyr and the metallicity is $[\mathrm{M/H}] = -0.2$. The difference from χ^2 of the isochronous model with $(t_{\mathrm{star}}(\mathrm{Gyr}), [\mathrm{M/H}]) = (10, -0.2)$ is shown as $\Delta\chi^2$ in Table 3.6. Table 3.6 also includes the properties of the source system calculated using $(t_{\mathrm{star}}(\mathrm{Gyr}), [\mathrm{M/H}]) = (10, -0.2)$. Figure 3.14 shows the effect of reddening and extinction and distance uncertainties on the position of the isochrones on the CMD. If the reddening is small or the extinction is large, the isochrone will be closer to the color and magnitude of the source. Around $I_{\mathrm{S}} = 21.04 \pm 0.01$, the apparent I-band magnitude of the source, the uncertainties in the isochrone in the confirmed range due to the age and metallicity of the star are comparable to the uncertainties in the estimation of reddening or extinction, making it difficult to determine the age and metallicity of the source in more detail from the CMD. However, just to be sure, we calculated the minimum and maximum values of the properties of the source system using all isochrones within 1 sigma from the best isochrones (i.e., $(t_{\mathrm{star}}(\mathrm{Gyr}), [\mathrm{M/H}]) = (10, -0.2)$) obtained by the chi-square test to isochrons described to the isochrones described in Appendix A. The results are shown in Table A.1. Uncertainty between models within $1\ \sigma$ is about 10 times the uncertainty within each model, but does not change our conclusions. It is important to note that the properties of the source system change only slightly as the age and metallicity assumptions of the source star change, and that the source system is consistently composed of a G-type star and a brown dwarf orbiting at about 0.06 AU.

Table 3.6: Differences in source system properties of XLclose2 depending on isochronous models

Age (Gyr)	[M/H]	$M_{\rm S,H}$ ($M_\odot$)	$M_{\rm S,C}$ ($M_\odot$)	$a_{\rm S}$ (10^{-2} au)	$L_{\rm S,C}/L_{\rm S,H}$ (10^{-7})	$H_{\rm S}$ (mag)	$K_{\rm S}$ (mag)	$\Delta\chi^2$
5	-0.5	0.846 ± 0.059	0.048 ± 0.004	5.89 ± 0.05	0.98 ± 0.25	18.66 ± 0.48	18.45 ± 0.48	7.6
5	0	0.917 ± 0.062	0.050 ± 0.004	6.05 ± 0.05	1.12 ± 0.31	18.56 ± 0.47	18.33 ± 0.47	0.4
5	$+0.5$	0.971 ± 0.061	0.052 ± 0.004	6.17 ± 0.05	1.26 ± 0.36	18.48 ± 0.48	18.24 ± 0.47	17.1
10	-0.5	0.794 ± 0.041	0.046 ± 0.005	5.77 ± 0.05	0.88 ± 0.30	18.63 ± 0.49	18.41 ± 0.49	3.8
10	0	0.867 ± 0.045	0.048 ± 0.004	5.94 ± 0.05	1.02 ± 0.26	18.52 ± 0.48	18.29 ± 0.48	2.6
10	$+0.5$	0.920 ± 0.049	0.050 ± 0.004	6.06 ± 0.05	1.13 ± 0.31	18.44 ± 0.48	18.19 ± 0.48	26.9
10	-0.2	0.834 ± 0.045	0.047 ± 0.004	5.87 ± 0.05	0.95 ± 0.24	18.57 ± 0.49	18.34 ± 0.48	-

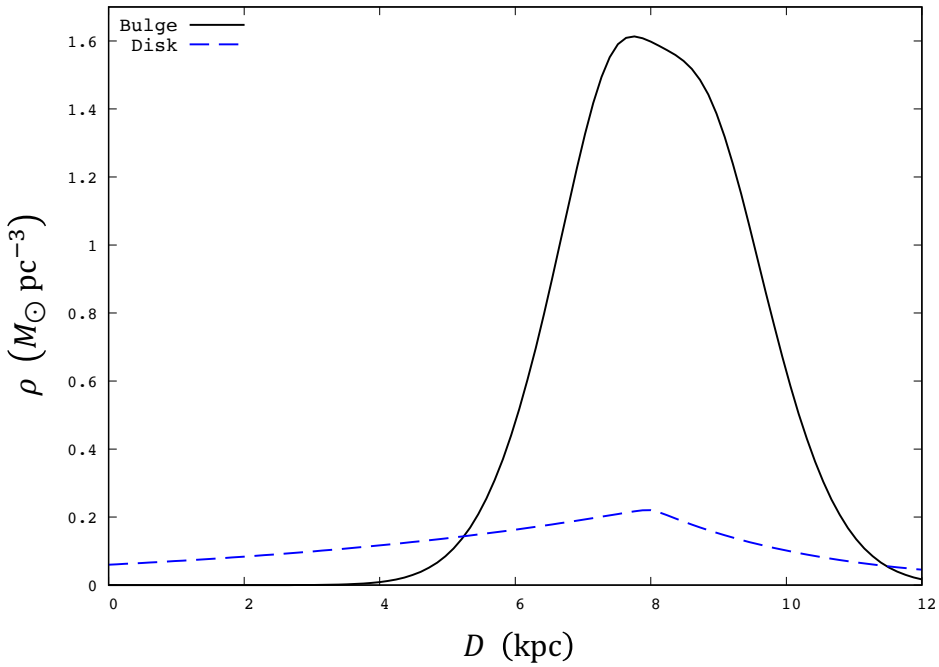

Figure 3.15: The mass density distribution in the direction of the Galactic coordinates for OGLE-2019-BLG-0825. The horizontal axis represents the distance from the earth in the direction of the event. The solid black line corresponds to the Galactic bulge and the dashed blue line to the Galactic disk.

3.6 Lens System Properties by Bayesian Analysis

The distance from the Earth to the lensing system, D_{L}, and the total mass of the host and companion in the lensing system, M_{L}, can be described by the following Equations 2.54 and 2.53 (Gaudi, 2012).

Since the parallax effect was not detected in this event, we conducted a Bayesian analysis (Beaulieu et al., 2006; Gould et al., 2006; Bennett et al., 2008) to estimate the parameters of the lens system for the 2L1S + xallarap models. We used the Galactic mass density distribution and the stellar velocity distribution and mass function as prior probabilities for Bayesian estimation.

For the mass density distribution of the galaxy, we considered the mass density distribution in the bulge region, ρ_{bulge} and the mass density distribution in the disk region, ρ_{disk}. For ρ_{bulge}, we used the model of Dwek et al. (1995), and for ρ_{disk}, we used the model of Bahcall (1986) for the mass density distribution in the disk region. Using the distance between the objects and the

Earth, D; the distance between the Galactic center and the Earth, R_0; the coordinate from the Galactic center to the Earth with the Galactic center as the origin, x; the coordinate perpendicular to the Earth direction at the Galactic plane, y; the distance from the Galactic plane, z; the scaling distances of the bar structure, (x_0, y_0, z_0); the inclination of the bar from the line between the Earth and the Galactic center theta, ϕ; the scale length of the galactic disk, $R_{\rm d}$; the scale height of the galactic disk, $h_{\rm z}$; the Galactic longitude of the event, l; and the galactic latitude of the event, b ; the respective mass density distributions can be written as follows:

$$\rho_{\rm bulge} = \rho_{\rm bulge,0} \exp\left(-\frac{r^2}{2}\right), \tag{3.19}$$

$$\rho_{\rm disk} = \rho_{\rm disk,0} \exp\left(\frac{R_0 - R}{R_{\rm d}} + \frac{z}{h_{\rm z}}\right), \tag{3.20}$$

with,

$$r = \left\{ \left[\left(\frac{x}{x_0}\right)^2 + \left(\frac{y}{y_0}\right)^2 \right]^2 + \left(\frac{z}{z_0}\right)^4 \right\}^{\frac{1}{4}}, \tag{3.21}$$

$$R = \sqrt{R_0^2 + D^2 \cos^2 b - 2R_0 D \cos b \cos l}, \tag{3.22}$$

$$x = R_0 \cos\phi - D \cos b \cos(l + \phi), \tag{3.23}$$

$$y = R_0 \sin\phi - D \cos b \sin(l + \phi), \tag{3.24}$$

$$z = D \sin b, \tag{3.25}$$

where $\rho_{\rm bulge,0}$ is the mass density at the galactic center of the bulge and $\rho_{\rm disk,0}$ is the mass density in the solar neighborhood of the disk, and from Han & Gould (1995) and Alcock et al. (1997) we assume $\rho_{\rm bulge,0} = 2.07\ M_\odot/{\rm pc}^3$ and $\rho_{\rm disk,0} = 0.06\ M_\odot/{\rm pc}^3$ are assumed. Based on Bahcall (1986), the distance between the Galactic center and the Earth was used $R_0 = 8.0\ {\rm kpc}$, the scale length of the Galactic disk was used $R_{\rm d} = 3.5\ {\rm kpc}$, and the scale height of the Galactic disk was used $h_{\rm z} = 0.325\ {\rm kpc}$. Based on the G2 model in Dwek et al. (1995) we used the scaling distance $(x_0, y_0, z_0) = (1.58{\rm kpc}, 0.62{\rm kpc}, 0.43{\rm kpc})$ for the bar structure. In addition, based on Dwek et al. (1995), we use $\phi = 20^\circ$ for the inclination theta of the bar from the line between the earth and the

galactic center. These mass density distributions in the galactic coordinates of OGLE-2019-BLG-0825 are shown in Figure 3.15.

According to Han & Gould (1995), the tangential relative velocity v of the Galaxy can be expressed as,

$$\boldsymbol{v} = \boldsymbol{v}_{\rm L} - \left[\boldsymbol{v}_{\rm S}\frac{D_{\rm L}}{D_{\rm S}} + \boldsymbol{v}_{\rm O}\frac{D_{\rm LS}}{D_{\rm S}}\right], \tag{3.26}$$

where $\boldsymbol{v}_{\rm L}$ is the lens tangential velocity to the Galaxy, $\boldsymbol{v}_{\rm S}$ is the source tangential velocity to the Galaxy, and $\boldsymbol{v}_{\rm L}$ is the observer tangential velocity to the Galaxy. By dividing the tangential velocity into two components, the velocity parallel to the Galactic plane v_y, and the velocity perpendicular to the Galactic plane v_z, the tangential velocity distribution $f(\boldsymbol{v})$ can be expressed as follows,

$$f(\boldsymbol{v}) = f(v_y, v_y) = \prod_{i=x,y}\frac{1}{\sqrt{2\pi}\sigma_i}\exp\left(-\frac{(v_i-\bar{v}_i)^2}{2\sigma_i}\right), \tag{3.27}$$

where $(\bar{v}_y, \bar{v}_z)$ is the mean velocity in each direction and (σ_y, σ_z) is the velocity dispersion in each direction. We consider this velocity distribution in two components: the disk and a barred bulge inclined 20 degrees from the line between observer and galactic center as described above. The velocity distribution of the disk is based on Alcock et al. (1997), we adopted $(\bar{v}_y, \bar{v}_z) = (220, 0)$ km s^{-1} and $(\sigma_y, \sigma_z) = (30, 30)$ km s^{-1}. The mean velocity of the barbed bulge was used $(\bar{v}_{y,\rm long}, \bar{v}_{y,\rm short}, \bar{v}_z) = (113.6, 77.4, 66.3)$ km s^{-1} based on Han & Gould (1995). The subscripts "$y, \rm long$" and "$y, \rm short$" mean the y component divided into the long and short axis directions of the bar. The velocity dispersion of the barred bulge is $(\sigma_{y,\rm long}, \sigma_{y,\rm short}, \bar{v}_z) = (113.6, 77.4, 66.3)$ km s^{-1}, which was derived by Han & Gould (1995) using the tensor virial theorem (Binney & Tremaine, 1987). We adopted $(\bar{v}_y, \bar{v}_z) = (220, 0)$ km, $(\sigma_y, \sigma_z) = (0, 0)$ km s^{-1} for the observer's velocity.

We then determined the mass function $\varphi(\log M)$ based on Sumi et al. (2011). The mass function $\varphi(\log M)$ and the prior probability distribution of the lens host mass $p(\log M)$ are as follows:

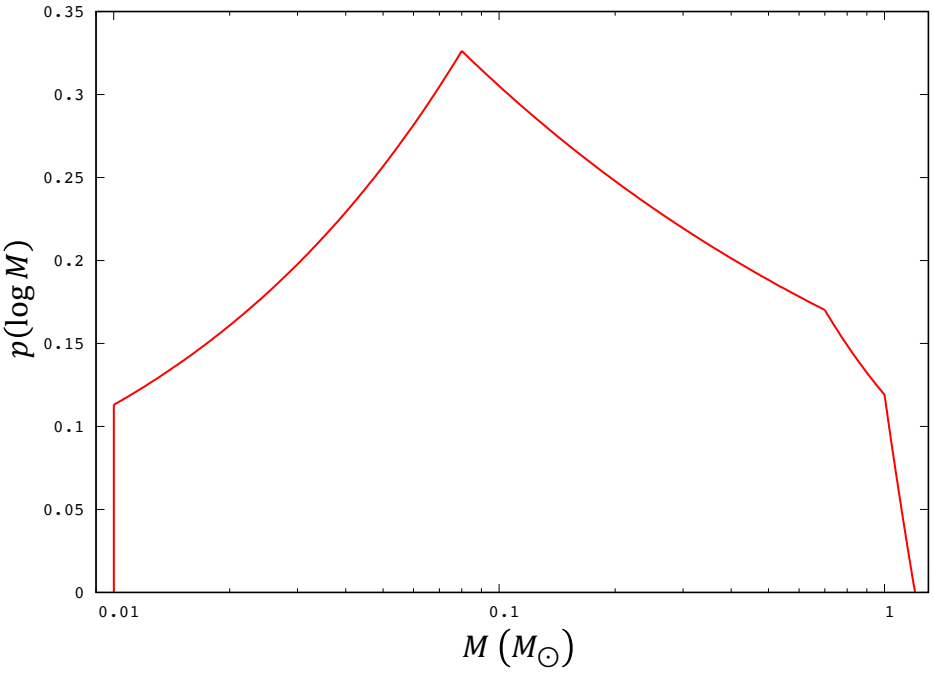

Figure 3.16: Prior probability distribution of the lens host mass.

$$\varphi(\log M) = \begin{cases} 0 & (M/M_\odot \leq 0.01) \\ \frac{0.08^{1-\upsilon_2}}{0.08^{1-\upsilon_1}} \frac{0.7^{1-\upsilon_3}}{0.7^{1-\upsilon_2}} M^{1-\upsilon_1} & (0.01 \leq M/M_\odot \leq 0.08) \\ \frac{0.7^{1-\upsilon_3}}{0.7^{1-\upsilon_2}} M^{1-\upsilon_2} & (0.08 \leq M/M_\odot \leq 0.7) \\ M^{1-\upsilon_3} & (0.7 \leq M/M_\odot \leq 1.0) \\ \frac{1.2-M}{0.2} M^{1-\upsilon_3} & (1.0 \leq M/M_\odot \leq 1.2) \\ 0 & (M/M_\odot \geq 1.2) \end{cases}, \tag{3.28}$$

$$p(\log M) = \frac{\varphi(\log M)}{\int_{-\infty}^{\infty} \varphi(\log M) d(\log M)}, \tag{3.29}$$

where $(\upsilon_1, \upsilon_2, \upsilon_3) = (0.49, 1.3, 2)$. Figure 3.16 shows the prior probability distribution $p(\log M)$ of the lens host mass.

Since the prior distribution only considers a single star, we scaled the event timescale and the Einstein radius to match those of the lens host so that the physical parameters of the lens host and

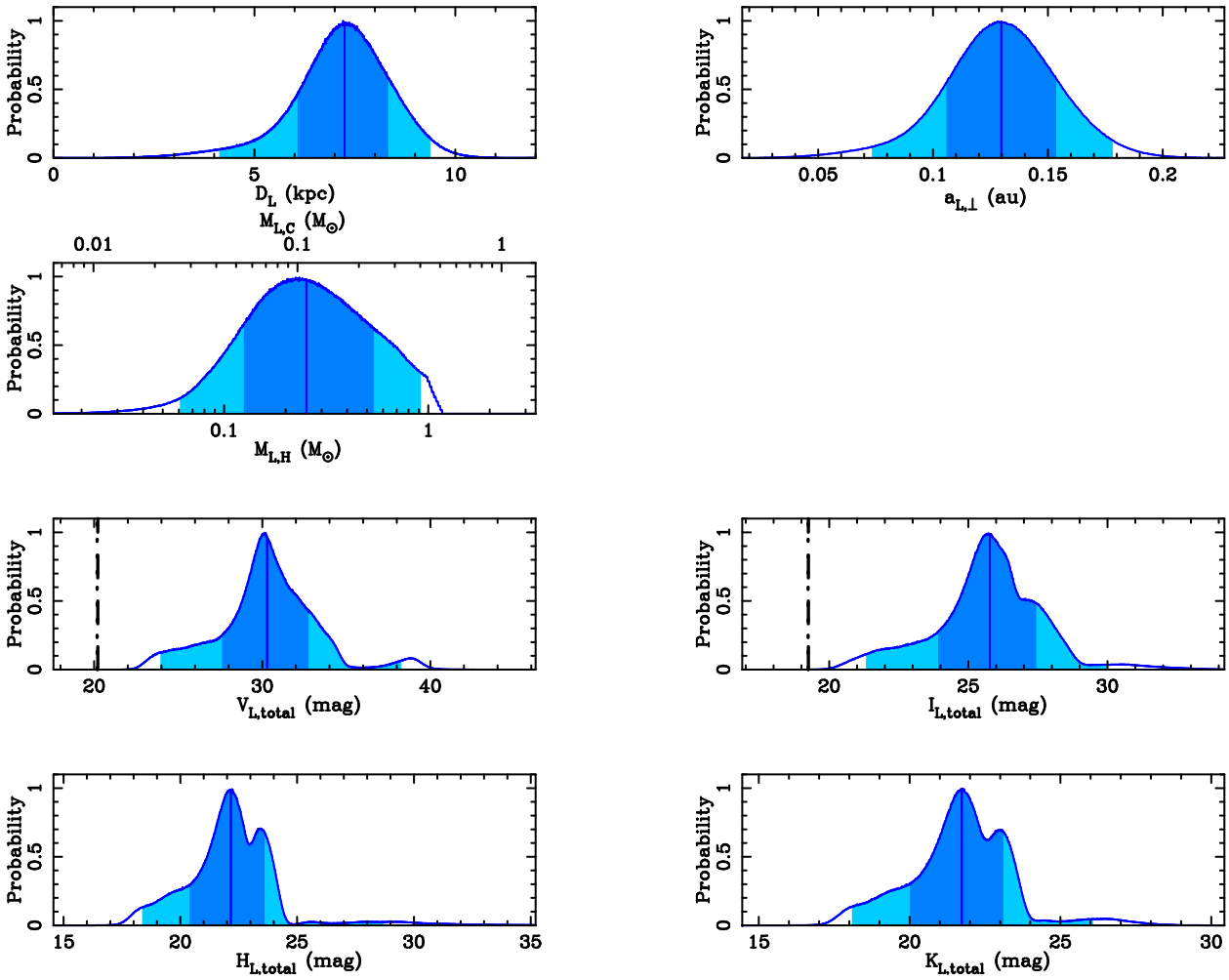

Figure 3.17: Posterior probability distribution of the properties of the lens system by Bayesian analysis for XLclose2. In each panel, the dark blue region indicates the 68.3% credible interval, light blue region indicates the 95.4% credible interval, and the blue vertical line indicates the median value. The dashed lines at the left end of the panel of apparent V- and I-band magnitudes with extinction are the blending magnitudes obtained from light curve modeling and are considered as the upper limit of brightness of the lens system.

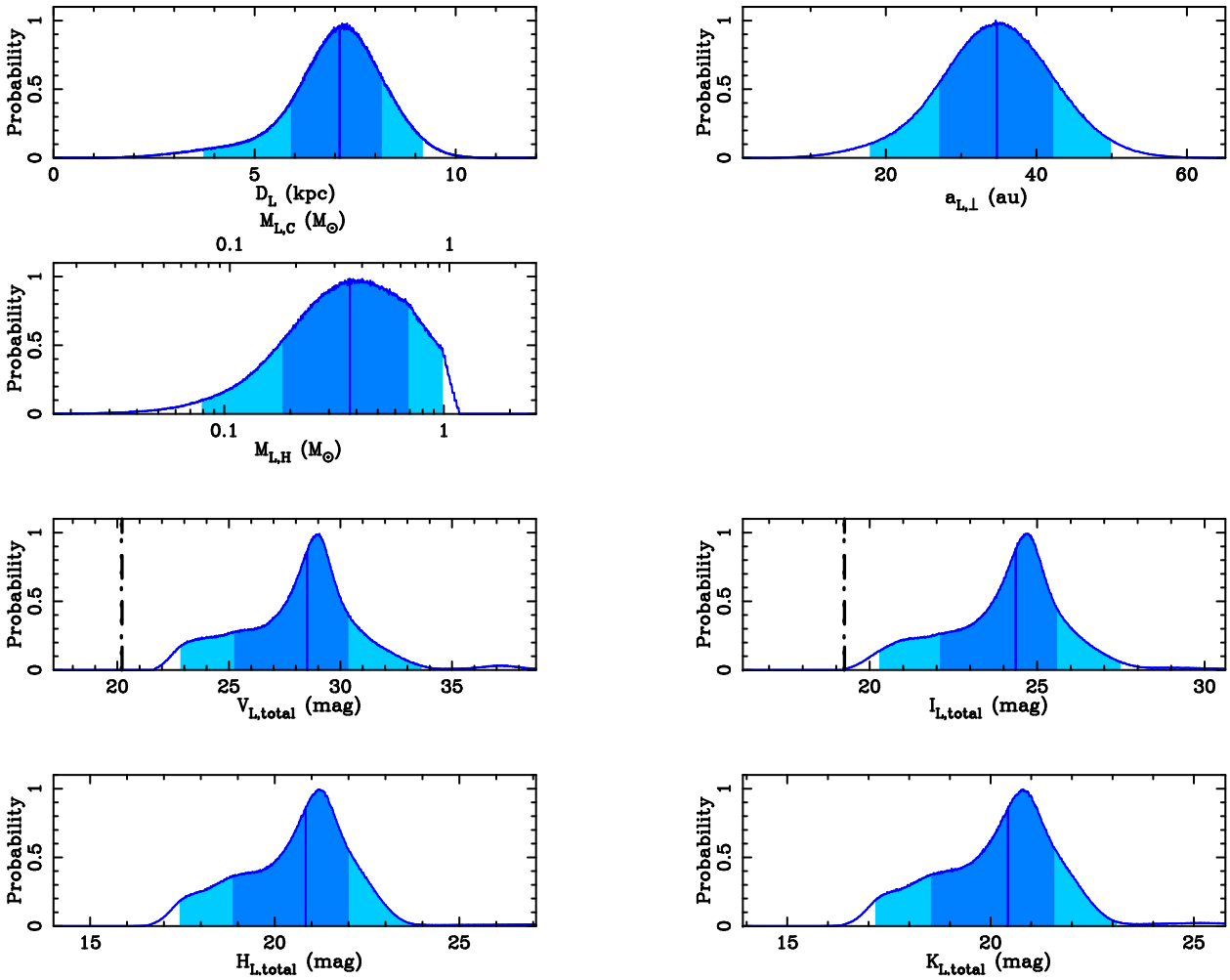

Figure 3.18: Same as Figure 3.17, but for XLwide2.

companion can be properly estimated. The event timescale of the lens host $t_{\rm E,H}$ and the Einstein radius of the lens host $\theta_{\rm E,H}$ are expressed using the mass ratio q as follows:

$$t_{\rm E,H} = \frac{t_{\rm E}}{\sqrt{1+q}}, \tag{3.30}$$

$$\theta_{\rm E,H} = \frac{\theta_{\rm E}}{\sqrt{1+q}}. \tag{3.31}$$

We also estimated the apparent magnitudes of the lens system in the V-, I-, K-, and H-bands with extinction. The magnitudes were obtained using the mass-luminosity relation for main-sequence stars (Henry & McCarthy, 1993; Kroupa & Tout, 1997) and the isochrone model for 5 Gyr old sub-stellar objects (Baraffe et al., 2003). The blending flux $f_{\rm b}$ from the light curve

Table 3.7: Lens system properties of the 2L1S + xallarap models

Model	XLclose1	XLclose2	XLwide1	XLwide2
range of q	$q \leq 0.1$	$0.1 < q \leq 1$	$q \leq 0.1$	$0.1 < q \leq 1$
$D_{\rm L}$ (kpc)	$7.27^{+1.10}_{-1.17}$	$7.24^{+1.09}_{-1.17}$	$7.24^{+1.09}_{-1.18}$	$7.11^{+1.05}_{-1.21}$
$M_{\rm L,H}$ ($M_\odot$)	$0.23^{+0.28}_{-0.12}$	$0.25^{+0.29}_{-0.13}$	$0.26^{+0.29}_{-0.13}$	$0.37^{+0.32}_{-0.19}$
$M_{\rm L,C}$ ($M_\odot$)	$0.02^{+0.03}_{-0.01}$	$0.11^{+0.13}_{-0.06}$	$0.03^{+0.03}_{-0.01}$	$0.35^{+0.30}_{-0.18}$
$a_{\rm L,\perp}$ (au)	$0.20^{+0.04}_{-0.04}$	$0.13^{+0.02}_{-0.02}$	$11.55^{+2.03}_{-2.09}$	$34.74^{+7.51}_{-7.69}$
$a_{\rm L,exp}$ (au)	$0.25^{+0.13}_{-0.06}$	$0.16^{+0.08}_{-0.04}$	$13.91^{+7.39}_{-3.15}$	$42.10^{+21.78}_{-10.92}$
$V_{\rm L,H}$ (mag)	$30.61^{+2.56}_{-2.54}$	$30.34^{+2.42}_{-2.66}$	$30.25^{+2.31}_{-2.71}$	$29.17^{+1.83}_{-3.38}$
$I_{\rm L,H}$ (mag)	$26.09^{+1.66}_{-1.75}$	$25.90^{+1.57}_{-1.83}$	$25.84^{+1.51}_{-1.86}$	$25.05^{+1.22}_{-2.35}$
$H_{\rm L,H}$ (mag)	$22.53^{+1.27}_{-1.73}$	$22.35^{+1.26}_{-1.80}$	$22.30^{+1.23}_{-1.82}$	$21.53^{+1.17}_{-2.02}$
$K_{\rm L,H}$ (mag)	$22.11^{+1.21}_{-1.70}$	$21.93^{+1.20}_{-1.75}$	$21.87^{+1.18}_{-1.77}$	$21.12^{+1.14}_{-1.94}$
$V_{\rm L,C}$ (mag)	$41.53^{+0.98}_{-1.76}$	$33.68^{+6.20}_{-2.97}$	$41.42^{+1.03}_{-2.13}$	$29.35^{+1.88}_{-3.13}$
$I_{\rm L,C}$ (mag)	$35.24^{+1.75}_{-3.05}$	$28.13^{+3.32}_{-1.94}$	$34.85^{+1.88}_{-3.13}$	$25.18^{+1.25}_{-2.16}$
$H_{\rm L,C}$ (mag)	$33.74^{+3.00}_{-3.99}$	$24.12^{+5.98}_{-1.50}$	$33.42^{+3.12}_{-4.24}$	$21.66^{+1.16}_{-1.92}$
$K_{\rm L,C}$ (mag)	$30.45^{+1.47}_{-2.24}$	$23.63^{+3.68}_{-1.44}$	$30.00^{+1.54}_{-2.24}$	$21.25^{+1.14}_{-1.85}$
$V_{\rm L,total}$ (mag)	$30.60^{+2.55}_{-2.54}$	$30.29^{+2.46}_{-2.68}$	$30.25^{+2.31}_{-2.71}$	$28.50^{+1.85}_{-3.27}$
$I_{\rm L,total}$ (mag)	$26.08^{+1.65}_{-1.75}$	$25.77^{+1.67}_{-1.86}$	$25.83^{+1.51}_{-1.86}$	$24.36^{+1.24}_{-2.26}$
$H_{\rm L,total}$ (mag)	$22.53^{+1.27}_{-1.73}$	$22.16^{+1.44}_{-1.76}$	$22.30^{+1.22}_{-1.82}$	$20.84^{+1.16}_{-1.98}$
$K_{\rm L,total}$ (mag)	$22.10^{+1.21}_{-1.70}$	$21.73^{+1.38}_{-1.71}$	$21.87^{+1.18}_{-1.77}$	$20.43^{+1.14}_{-1.89}$
$V_{\rm Blend}$ (mag)	20.21 ± 0.03	20.21 ± 0.03	20.21 ± 0.03	20.21 ± 0.03
$I_{\rm Blend}$ (mag)	19.25 ± 0.01	19.25 ± 0.01	19.25 ± 0.01	19.25 ± 0.01
χ^2	10856.4	10840.9	10861.2	10842.7
$\Delta\chi^2$	15.5	-	20.3	1.8

modeling was used as the upper limit of the lens brightness. Following Bennett et al. (2015), we estimated the extinction in front of the lens using the following equation:

$$A_{i,\rm L} = \frac{1 - \exp\left[-D_{\rm L}/h_{\rm dust}\right]}{1 - \exp\left[-D_{\rm S}/h_{\rm dust}\right]} A_{i,\rm S}, \tag{3.32}$$

where i corresponds to the observed wavelength band, $A_{i,\rm L}$ is the total extinction in the i-band of the lens, $A_{i,\rm S}$ is the total extinction in the i-band of the source, $h_{\rm dust}$ is the scale length of dust in the event direction, given by $h_{\rm dust} = (0.1\ {\rm kpc})/\sin|b|$ as a function of the Galactic latitude b of the event. We estimated $A_{\rm H}$ and $A_{\rm K}$ from $A_{\rm V}$ using the wavelength dependence of extinction law in the direction of the Galactic center from Nishiyama et al. (2008).

Table 3.7 lists the estimated parameters: the distance from the Earth to the lens, $D_{\rm L}$; the lens host mass, $M_{\rm L,H}$; the lens companion mass, $M_{\rm L,C}$; the orbital radius projected to the observation

plane, $a_{\mathrm{L},\perp}$; the expected orbital radius, $a_{\mathrm{L,exp}}$; the magnitudes with the extinction in the four wavelength bands $V_{\mathrm{L},j}$, $I_{\mathrm{L},j}$, $H_{\mathrm{L},j}$ and $K_{\mathrm{L},j}$ where j consists of "H" for the lens host, "C" for the lens companion and 'total" for the host and companion combined; the magnitudes of the blends in the V- and I-bands which are the upper limits of brightness in the lens system, V_{blend}, I_{blend}. Figures 3.17 and 3.18 show the posterior probability distributions for XLclose2 and XLwide2, respectively. The distribution of XLclose2 indicates a M-type or K-type stellar binary with a projected orbital radius $a_{\mathrm{L},\perp} = 0.13^{+0.02}_{-0.02}$ au located $7.2^{+1.1}_{-1.2}$ kpc from the Earth. The distribution of XLwide2 also indicates a M-type or K-type stellar binary with a projected orbital radius $a_{\mathrm{L},\perp} = 34.74^{+7.51}_{-7.69}$ au located $7.1^{+1.0}_{-1.2}$ kpc from the Earth. Comparing the properties of the lens systems of the four models listed in Table 3.7, while the parameters related to the companion differ significantly among the models, they are consistent in that the stellar type and the distance from the Earth. In Appendix B, we performed a Bayesian analysis using the mass function based on Mróz et al. (2017) to estimate the properties of the lensing system. However, there is little difference from the results described in this section using the mass function presented in Sumi et al. (2011), and our conclusions remain the same.

As described in Section 3.5, the apparent magnitude of the source for XLclose2 is $(H_{\mathrm{S}}, K_{\mathrm{S}}) = (18.52 \pm 0.49, 18.29 \pm 0.48)$. The apparent magnitude for the lens host and lens companion combined is $(H_{\mathrm{L,total}}, K_{\mathrm{L,total}}) = (22.16 \pm 1.16, 21.73 \pm 1.55)$. Therefore, XLclose2 has a contrast between the apparent lens brightness and the apparent source brightness where 3.6 ± 1.7 mag in the H-band and 3.4 ± 1.6 mag in the K-band. The XLclose1 and XLwode1 models also have similar contrast to XLclose2, respectively. On the other hand, the contrast between the apparent lens brightness and the apparent source brightness in the XLwide2 model is 2.3 ± 1.6 in the H-band and 2.1 ± 1.6 in the K-band, slightly lower contrast than that in XLclose2.

Chapter 4

Discussion and Conclusion

We performed a detailed analysis of the planetary microlensing candidate, OGLE-2019-BLG-0825. We first found that there are systematic residuals with the best fit standard binary model with planetary mass ratio $q \sim 10^{-3}$. Therefore, we examined various combinations of possible higher-order effects. As a result, we found that models which include the xallarap effect can fit the residuals significantly better than models which do not.

Our Bayesian analysis for the best model XLclose2 estimated the lens host mass to be $0.25^{+0.29}_{-0.13}$ $M_{\odot}$ and the lens system to be located $7.24^{+1.09}_{-1.17}$ kpc from Earth. For XLwide2, which is the best solution at $s > 1$, the lensing host is $0.37^{+0.32}_{-0.19}$ $M_{\odot}$, and the lens system is estimated to be located $7.12^{+1.05}_{-1.22}$ kpc from Earth. Owing to degenerate solutions with various combinations of (q, s) values, the uncertainties in the mass and orbital radius of the lens companion are large. Since the relative proper motion between the lens and the source is about 1 mas yr^{-1} and the apparent magnitude contrast is large, it will be more than 30 years before the source and lens can be observed separately with the current high-resolution imaging instruments. In adaptive optics (AO) observations by The European Extremely Large Telescope (ELT), the FWHM is expected to reach 10 mas in the H-band and 14 mas in the K-band (Ryu et al., 2022). Therefore, it may be possible to observe the source and lens separately by mid-2030. It is unlikely that the degeneracy of the models will be resolved by follow-up observations because the proper motion and brightness of the

lens system are comparable across models, but it may constrain the uncertainty in the lens system properties somewhat.

Calculations applying the $D_{\rm S} = 8.0 \pm 1.4$ kpc assumption and the isochrone model with age 10 Gyr in solar metallicity to the source show that the source companion OGLE-2019-BLG-0825Sb in the best 2L1S + xallarap model has a semi major axis of 0.0594 ± 0.0005 au and an orbital period of 5.53 ± 0.05 days with mass $0.048 \pm 0.004\ M_\odot$ orbiting the host source star OGLE-2019-BLG-0825S. The mass of the source companion is about that of a brown dwarf. The I-band luminosity ratio of the companion to the host is $L_{\rm S,C}/L_{\rm S,H} = (1.0 \pm 0.3) \times 10^{-7}$, which is faint and consistent with this analysis where the magnified flux of the second source is too weak to be detected. We note that these properties of the source system are almost the same among the various models considered, even though the parameters of the lens system change.

We considered whether a variable source star could also explain the ~ 5 day luminosity variations of this event, without using the xallarap effect. Most of Classical Cepheids have a pulsation periods ranging from about 1 to 100 days, and the longest period ones being rare, with a pulsation amplitude in I-band of $0.05 - 1$ mag (Klagyivik & Szabados, 2009), and the following period-luminosity relations (Gaia Collaboration et al., 2017):

$$M_I = -2.98 \log P – (1.28 \pm 0.08); \quad \sigma_{\rm rms} = 0.78, \tag{4.1}$$

where $\sigma_{\rm rms}$ is the variance around the periodic luminosity relation. At a pulsation period $P = 5.50 \pm 0.05$ days, the absolute magnitude of a type I Cepheid would be $M_I = -3.48 \pm 0.08$ mag. However our estimated absolute magnitude is $M_I = 4.5 \pm 0.4$ mag, which is too faint for a classical Cepheid (see Table 3.5). Type II Cepheids have a pulsation period of about 1 to 50 days, with a pulsation amplitude of $0.3 - 1.2$ mag, and the following period-luminosity relationships (Ngeow et al., 2022):

$$M_I = -(2.09 \pm 0.08) \log P – (0.39 \pm 0.08); \quad \sigma_{\rm rms} = 0.24. \tag{4.2}$$

For a pulsation period $P = 5.50 \pm 0.05$ days, the absolute magnitude of a type II Cepheid would be $M_I = -1.94 \pm 0.13$ mag, which is also not plausible. RR Lyrae variables have color magnitudes

close to main-sequence stars, but with a pulsation period of less than one day (e.g., Soszyński et al., 2009). Delta Scuti variables have a pulsation period of $0.01 - 0.2$ days, and Gamma Doradus variables have a pulsation period of 0.3-2.6 days, both shorter than the xallarap signal of 5 days, and the spectral type is $A - F$, which is blue compared to the color of the source of this event. Furthermore, as described in Section 3.4.3, we performed a fitting with a model with variable source flux, using the best standard 2L1S model (i.e., close1). However, the improvement from the best standard 2L1S model was only 139.1, $\Delta\chi^2 = 764.6$ worse than the 2L1S + xallarap model. Therefore, we conclude that it is difficult to explain the xallarap signal assuming a variable source star. Note that although the conclusion is that the source of this event is not a variable star, many variable stars in the direction of the Galactic bulge have been discovered (Soszyński et al., 2011a,b; Iwanek et al., 2019), and there is a possibility that a candidate planetary microlensing event with a variable source will be observed in the future.

For the lens system, the inclusion of the xallarap effect significantly changed the $\Delta\chi^2$-plane of the mass ratio q vs. separation s. The mass ratio of the best model was $q = (3.3 \pm 0.1) \times 10^{-3}$ without accounting for a xallarap effect, but became $q = (4.4 \pm 1.1) \times 10^{-1}$ with the xallarap effect. Furthermore, degenerate solutions with various combination of (q, s) values were found within a small range of $\Delta\chi^2 \lesssim 10$. This event is the first case that the short-period xallarap effect significantly affects the binary-lens parameters q, s. This effect is most likely to be seen in events with a caustic or cusp approach and no clear sharp caustic crossing. In events with a clear sharp caustic crossing, this effect is not significant because the mass ratio q and separation s can be constrained from the caustic shape.

Although the xallarap effect has been examined in the past (e.g., Bennett et al., 2008; Sumi et al., 2010), few events have been able to eliminate possibilities of systematic errors and clearly identify the xallarap signal. Miyazaki et al. (2020) analyzed a planetary microlensing event OGLE-2013-BLG-0911 and found a significant xallarap signal. They conclude from the fitting parameters that the source companion, OGLE-2013-BLG-0911Sb has a mass $M_{\rm S,C} = 0.14 \pm 0.02\ M_\odot$, an orbital period $P_\xi = 36.7 \pm 0.8$ days and a semi-major axis $a_{\rm S} = 0.225 \pm 0.004$ au. However, they assume $M_{\rm S,H} = 1\ M_\odot$ and $D_{\rm S} = 8$ kpc. Recently Rota et al. (2021) analyzed a candidate planetary

event MOA-2006-BLG-074 and detected a xallarap effect. They estimated the source host's mass $M_{\rm S,H} = 1.32 \pm 0.36\ M_\odot$ from the color and magnitude of the source and found that the companion with mass $M_{\rm S,C} = 0.44 \pm 0.14\ M_\odot$ is orbiting the source host with orbital period $P_\xi = 14.2 \pm 0.2$ days and semi-major axis $a_{\rm S} = 0.043 \pm 0.012$ au. The OGLE-2019-BLG-0825 event in this work is the second case after the MOA-2006-BLG-074 event (Rota et al., 2021), in which the physical properties of a source system were estimated from the color and magnitude of the source. This event will be a valuable example for future xallarap microlensing analyses.

Rahvar & Dominik (2009) suggested that planets orbiting sources in the Galactic bulge could be detected by the xallarap effect with sufficiently good photometry.

The fraction of close binaries like OGLE-2013-BLG-0911Sb is known to be anticorrelated with metallicity (Moe et al., 2019). The Galactic bulge observed in microlensing surveys suggests the presence of super-solar, solar, and low-metallicity components with [Fe/H]~ 0.32, [Fe/H] ~ 0.00, and [Fe/H] ~ -0.46, respectively (García Pérez et al., 2018). Moe et al. (2019) reported that the fraction of close binaries, $F_{\rm close}$, with separation $a < 10$ au is $F_{\rm close} = 24\% \pm 4\%$ at [Fe/H]$= -0.2$ and $F_{\rm close} = 10\% \pm 3\%$ at [Fe/H]$= 0.5$. However, the occurance ratio of a companion with an orbit even shorter than $\sim$0.5 au, to which the xallarap effect has sensitivity, is poorly understood.

Tokovinin et al. (2006) found that $\sim 68\%$ of close binary systems in the solar neighborhood with orbital period $P = 3 - 6$ days have an outer tertiary companion. Eggleton & Kisseleva-Eggleton (2006) and Fabrycky & Tremaine (2007) showed that Kozai-Lidov cycles with tidal friction (KCTF; Kiseleva et al., 1998; Eggleton & Kiseleva-Eggleton, 2001) produce such very close binaries. First, in the KCTF, the inner companion's eccentricity is pumped by perturbations from the outer tertiaries. The inner companion in the eccentric orbit undergoes tidal friction near the periastron, and the orbit of the inner companion is finally circularized. Timescale equations for tidal circularization have been studied (e.g., Adams & Laughlin, 2006; Correia et al., 2020). Because of their small radius relative to their mass the orbits of brown dwarfs are expected to take longer to circularize than those for Jupiter-like planets with the same orbital period over the Gyr scale. However this is difficult to estimate because the tidal quality factor for brown dwarfs is not well constrained (Heller et al., 2010; Beatty et al., 2018). Meanwhile, Meibom & Mathieu (2005)

demonstrated from the distribution of orbital eccentricity vs. orbital period that most of the companions are circularized when the orbital period is shorter than $\sim$15 days for the companions of halo stars and $\sim$10 days for the companions of nearby G-type primaries. Therefore, in this analysis of OGLE-2019-BLG-0825, the source orbital eccentricity was fixed to $e_\xi = 0$. We also performed an analysis with free eccentricity, but our results were almost the same, and the improvement in χ^2 was only $\Delta\chi^2 \sim 16$, despite two additional parameters, e_ξ and $T_{\rm peri}$.

Disc fragmentation and migration are also possible formation processes for close binaries. Moe & Kratter (2018) noted that the close binary fraction of solar-mass, pre-main-sequence binaries and field main-sequence binaries is almost identical (Mathieu, 1994; Melo, 2003), and concluded that majority of very close binaries with semi-major axis $a < 0.1$ au migrated when there was still gas composition in the circumstellar disc. Furthermore, Moe et al. (2019) showed that 90% of close binary stars with $a < 10$ au are the product of disc fragmentation. Tokovinin & Moe (2020) use simulations of disc fragmentation to show that the companion has difficulty migrating to $P < 100$ days without undergoing accretion that would grow it to more than 0.08 $M_\odot$, explaining brown dwarf deserts.

We favored the interpretation that the source companion OGLE-2019-BLG-0825Sb has a brown dwarf mass. In brown dwarf mass objects discovered by gravitational microlensing, this companion is the closest and most massive companion to the host. In addition, it is the least massive companion discovered in the xallarap event and the first brown dwarf discovered in the source system of gravitational microlensing events. Figure 4.1 shows the distribution of masses and semi-major axis for brown dwarf-mass objects around Sun-like stars of $0.7 - 1.4\ M_\odot$, with the dark-magenta dot being OGLE-2019-BLG-0825Sb. The occurrence rate for brown dwarfs orbiting main-sequence stars have been found to be low, less than 1% (Marcy & Butler, 2000; Grether & Lineweaver, 2006; Sahlmann et al., 2011; Santerne et al., 2016; Grieves et al., 2017). Fewer than 100 brown dwarf companions have been found in solar-type stars (e.g., Ma & Ge, 2014; Grieves et al., 2017). There is a particularly dry region at orbital period $P < 100$ days (e.g., Kiefer et al., 2019, 2021). Therefore, if OGLE-2019-BLG-0825Sb is a short-period brown dwarf, it is a resident of the driest region of the brown dwarf desert, making it a very valuable sample for studying brown dwarf for-

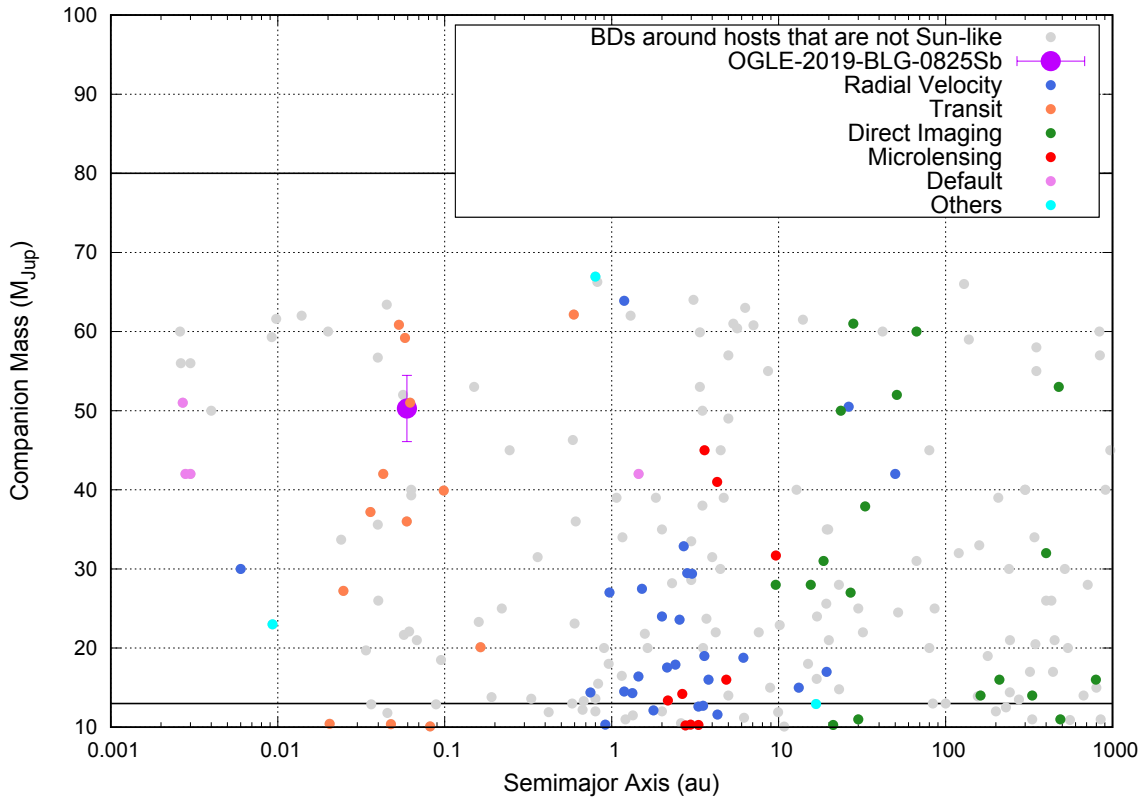

Figure 4.1: The distribution of masses and semi-major axis for brown dwarf-mass objects around Sun-like stars of $0.7 - 1.4\ M_{\odot}$. The dark-magenta dot indicates OGLE-2019-BLG-0825Sb. The other colors indicate the discovery method: blue is the radial velocity method, orange is the transit method, green is the direct imaging method, red is the microlensing method, pink is the Default (i.e., the same as a star), and cyan is other methods of detecting exoplanets. Brown dwarfs around non-Sun-like hosts ($M_{\rm h}/M_{\odot} < 0.7$ or $M_{\rm h}/M_{\odot} > 1.4$) and hosts of unknown mass are plotted as gray dots. The horizontal axis is the semi-major axis and the vertical axis is the companion mass. Solid black lines are drawn at 13 $M_{\rm Jup}$, the lower mass limit of brown dwarfs, and 80 $M_{\rm Jup}$, the upper mass limit of brown dwarfs.

mation. Miyazaki et al. (2021) estimated the planetary yield detected by the Nancy Grace Roman Space Telescope (Spergel et al., 2015, previously named WFIRST, hereafter Roman) via xallarap signals assuming a planetary distribution of masses and orbital periods of Cumming et al. (2008). They predicted that Roman will characterize tens of short-period Jupiter - brown dwarf mass companions such as OGLE-2019-BLG-0825S. By comparing the predictions with the actual results, it will be possible to verify the brown dwarf desert in the Galactic bulge.

In this study, we assumed $D_{\rm S} = 8.0 \pm 1.4$ kpc. Roman observations may be able to measure $D_{\rm S}$ by directly measuring astrometric parallax for bright source events (Gould et al., 2015). Even for non-bright source events, $D_{\rm S}$ can be determined by measuring the lensing flux $F_{\rm L}$, $\pi_{\rm E}$, and $\theta_{\rm E}$. Events with photometric accuracy ≤ 0.01 mag have been analytically shown to have the potential to measure $\theta_{\rm E}$ with $\leq 10\%$ accuracy via astrometric microlensing observations in space (Gould & Yee, 2014). Future observations of the xallarap effect may reveal the distribution of short-period binary stars in the Galactic center, which are usually difficult to observe.

Appendix A

Chi-square Test for Isochrones

To find isochrones that are close to the source color magnitude with extinction, $(V-I, I)_{\rm S}$, we performed a two-dimensional chi-square test on the isochrones. The isochrones use the PARSEC model Bressan et al. (2012) as in the main text. We first considered reasonable stellar ages. We compared isochronous models with different combinations of age-metallicity with stars in the Baade's window direction of the bulge as observed by the HST from Holtzman et al. (1998). The stars in the Baade's window direction of the bulge observed by the HST are the same as in Section 3.5, and as in Section 3.5, the color magnitudes of the RCG are shifted to match using $(V-I, I)_{\rm clump,Holz} = (1.62, 15.15)$ by Bennett et al. (2008). Figure A.1 shows isochrones with stellar ages from 1 Gyr to 4 Gyr. Figure A.2 shows isochrones with stellar ages from 5 Gyr to 8 Gyr. Figure A.3 shows isochrones with stellar ages of 9 Gyr and from 11 Gyr to 13 Gyr. Figure A.4 shows isochrones with stellar ages of 10 Gyr. Stars with ages of $1-3$ Gyr have significantly different turnoff points compared to stars in the Baade's window direction in the bulge observed by the HST. It is reasonable to assume that the source for OGLE-2019-BLG-0825 is in the direction of the Galactic bulge and has a similar age distribution to the stars in Baade's window. Therefore, we performed a two-dimensional chi-square test on isochrones with stellar ages from 4 Gyr to 13 Gyr and $[{\rm M/H}]$ from -1 to 0.5.

The interval between combinations of stellar ages and metallicities is a grid, with 1 Gyr increments for stellar ages and 0.1 increments for metallicities, for a total of 160 combinations. Since

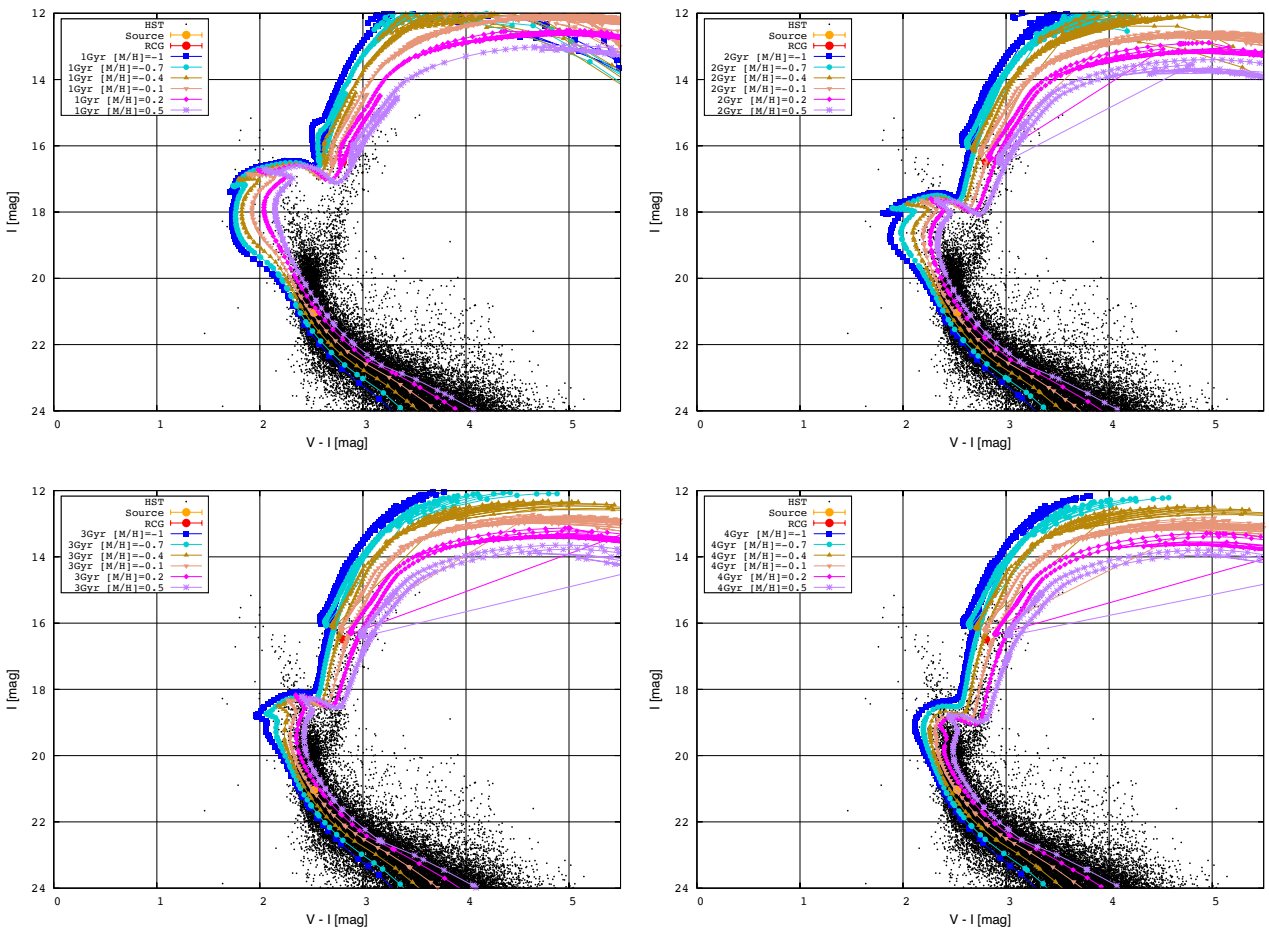

Figure A.1: CMD of isochrones with different metallicities for stellar ages from 1 Gyr to 4 Gyr. In the upper left panel, the stellar age is 1 Gyr. In the upper right panel, the stellar age is 2 Gyr. In the lower left panel, the stellar age is 3 Gyr. In the lower right panel, the stellar age is 4 Gyr. The black dots are stars in Baade's window based on HST observations (Holtzman et al., 1998), color- and magnitude-matched at the RCG position. The orange dot marked "Source" in the legend represents the position of the source with extinction. The red dot marked "RCG" in the legend represents the position of RCG centroid with extinction within $2'$ around OGLE-2019-BLG-0825. The colors of the isochrones indicate differences in metallicities: blue is $[\mathrm{M/H}] = -1$, dark-turquoise is $[\mathrm{M/H}] = -0.7$, dark-goldenrod is $[\mathrm{M/H}] = -0.4$, dark-salmon is $[\mathrm{M/H}] = -0.1$, magenta is $[\mathrm{M/H}] = 0.2$, purple is $[\mathrm{M/H}] = 0.5$.

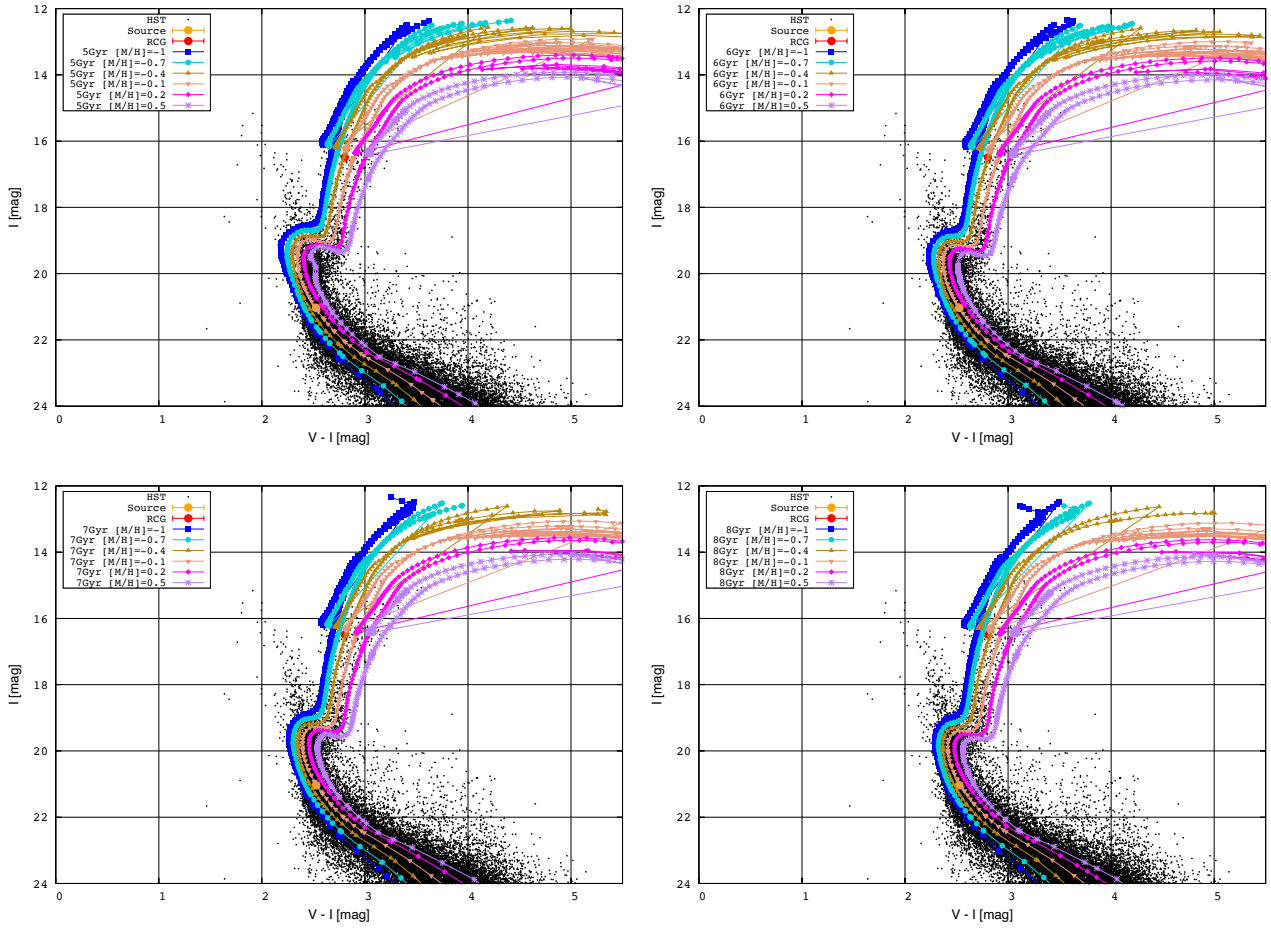

Figure A.2: Same as Figure A.1, but for stellar ages from 5 Gyr to 8 Gyr. In the upper left panel, the stellar age is 5 Gyr. In the upper right panel, the stellar age is 6 Gyr. In the lower left panel, the stellar age is 7 Gyr. In the lower right panel, the stellar age is 8 Gyr.

each of the isochrones is published as a table, adjacent data in each isochrone table are interpolated and connected. A straight line connecting adjacent data can be written as follows:

$$y = a + bx, \tag{A.1}$$

where a and b are the intercept and slope of the line connecting the two points. In this case, the following formula can be used for a two-dimensional chi-square test,

$$\chi^2(a,b) = \sum_{i=1}^{N} \frac{(y_i - a - bx_i)^2}{\sigma_{y,i}^2 + b^2\sigma_{x,i}^2}, \tag{A.2}$$

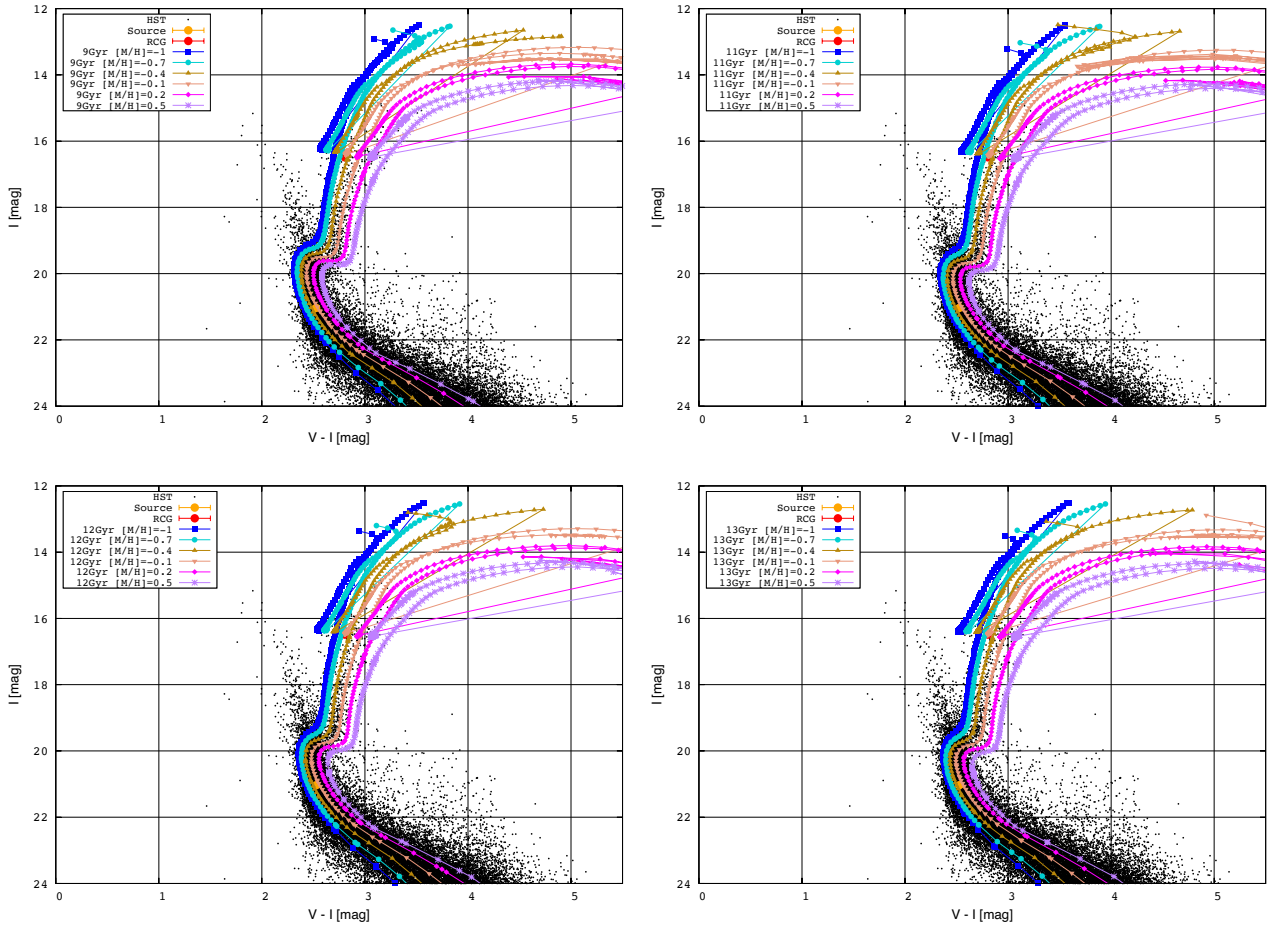

Figure A.3: Same as Figure A.1, but for stellar ages of 9 Gyr and 11 Gyr to 13 Gyr. In the upper left panel, the stellar age is 9 Gyr. In the upper right panel, the stellar age is 11 Gyr. In the lower left panel, the stellar age is 12 Gyr. In the lower right panel, the stellar age is 13 Gyr.

where $\sigma_{x,i}$ and $\sigma_{y,i}$ are the standard deviations of the i-th data along the x- and y-axes, and N is the total number of data. Our two-dimensional chi-square test is performed on the 160 isochrones using a single point, the source color magnitude with extinction, $(V-I, I)_{\rm S}$. That is, i in Equation A.2 is 1. The results are shown in Figure A.5. The best combination is $(t_{\rm star}({\rm Gyr}), [{\rm M/H}]) = (10, -0.2)$. The stellar age and metallicity $(t_{\rm star}({\rm Gyr}), [{\rm M/H}]) = (10, 0)$ assumed in the main text of the dissertation is $\Delta\chi^2 = 2.58$, which is within 2 σ. We calculated the properties of the source system for all isochrones within 1 σ of the chi-square to obtain the minimum and maximum values of the properties of the source system. The results are shown in Table A.1. As noted in the main text, uncertainty between models within 1 σ is about 10 times the uncertainty within each model,

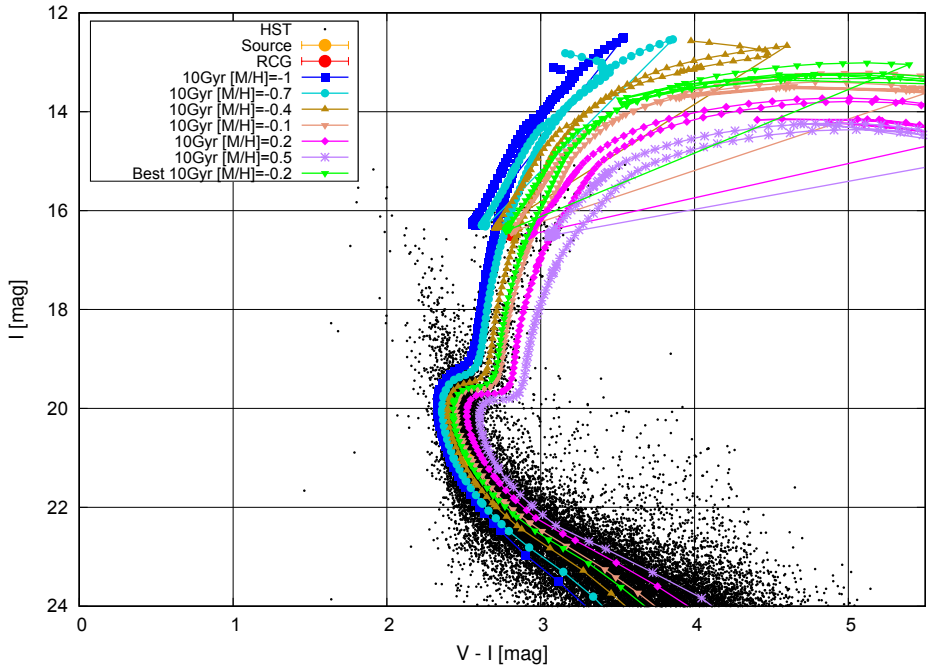

Figure A.4: Same as Figure A.1, but for stellar ages of 10 Gyr.The isochronous curve showing $[\mathrm{M/H}] = -0.2$, which was the smallest χ^2 isochrone in the two-dimensional chi-square test, is indicated by the green curve.

but this does not change our conclusions that the source system is composed of a Sun-like star and a short-period brown dwarf.

Table A.1: Minimum and maximum values of the properties of the source system calculated using all 1 σ isochrones

property	min	max
$M_{\mathrm{S,H}}$ ($M_\odot$)	0.767	0.944
$M_{\mathrm{S,C}}$ ($M_\odot$)	0.045	0.051
a_{S} (10^{-2} au)	5.71	6.11
$L_{\mathrm{S,C}}/L_{\mathrm{S,H}}$ (10^{-7})	0.99	1.00
H_{S} (mag)	18.52	18.62
K_{S} (mag)	18.29	18.40

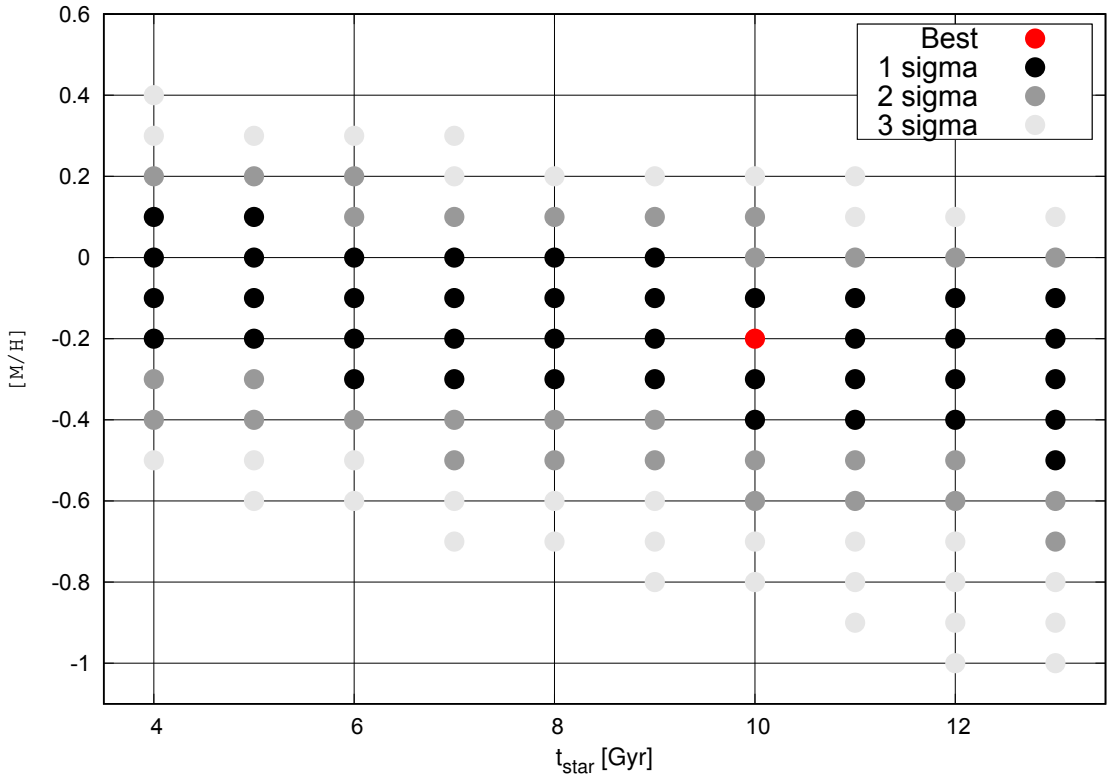

Figure A.5: Results of a two-dimensional chi-square test. The horizontal axis is the stellar age $t_{\rm star}$ and the vertical axis is the metallicity $[{\rm M/H}]$. Red dot is the best, black are isochrones within $1\ \sigma$, dark gray are isochrones within $2\ \sigma$, and light gray are isochrones within $3\ \sigma$.

Appendix B

Lens Systems Properties for Different Mass Function

To investigate the extent to which the properties of the lensing system depend on the prior probability of the mass function used in the Bayesian analysis, we performed a Bayesian analysis using a function that is based on the mass function of Mróz et al. (2017) and compared it with the results of the Bayesian analysis using the mass function presented in Sumi et al. (2011). The mass function of Sumi et al. (2011) used in the main text was derived from 464 gravitational microlensing events observed by MOA-II in 2006-2007. The mass function used in Appendix B is based on the function of Mróz et al. (2017), derived from 2617 gravitational microlensing events from 2010 to 2015 by OGLE-IV. However, it differs slightly from Mróz et al. (2017) in that it adds break to 1 $M_{\odot}$ for comparison with the main text. The function is expressed as follows:

$$\varphi(\log M) = \begin{cases} 0 & (M/M_{\odot} \leq 0.01) \\ \frac{0.08^{1-\upsilon_2}}{0.08^{1-\upsilon_1}} \frac{0.5^{1-\upsilon_3}}{0.5^{1-\upsilon_2}} M^{1-\upsilon_1} & (0.01 \leq M/M_{\odot} \leq 0.08) \\ \frac{0.5^{1-\upsilon_3}}{0.5^{1-\upsilon_2}} M^{1-\upsilon_2} & (0.08 \leq M/M_{\odot} \leq 0.5) \\ M^{1-\upsilon_3} & (0.5 \leq M/M_{\odot} \leq 1.0) \\ \frac{1.2-M}{0.2} M^{1-\upsilon_3} & (1.0 \leq M/M_{\odot} \leq 1.2) \\ 0 & (M/M_{\odot} \geq 1.2) \end{cases}, \tag{B.1}$$

where $(\upsilon_1, \upsilon_2, \upsilon_3) = (0.8, 1.3, 2)$. Figure B.1 shows the probability density distributions of the two mass functions, where the solid red line is the mass function based on Sumi et al. (2011) and the dashed blue line is the mass function based on Mróz et al. (2017). Compared to the mass function of Sumi et al. (2011), the mass of breaks in the late-type main-sequence star region goes from $M = 0.7\ M_\odot$ to $M = 0.5\ M_\odot$. Furthermore, υ_1 differs, with a larger fraction of low-mass sources in the mass function based on Mróz et al. (2017). This difference may be attributed to the detrending method of Sumi et al. (2011) (Sumi et al., 2023).

Table B.1 shows the results of the Bayesian analysis using the mass function based on Mróz et al. (2017) as prior probabilities, and the posterior distribution of the lensing system properties for the XLclose2 is shown in Figure B.2 and the posterior distribution of the lensing system properties for the XLwide2 is shown in Figure B.3. The mass density and velocity distribution of the objects in our Galaxy are identical to the model used in the Section 3.6. Compared to the results of our Bayesian analysis using the mass function based on Sumi et al. (2011) as prior probability, the masses of the main star and companion in the lensing system are smaller and therefore fainter. Since the mass density of the Galactic center is greater, the effect of the smaller mass of the lensing system is that the distance to the lensing system from the Galactic center is farther away and closer to the Earth. However, the difference is small compared to the errors of the properties of the lens system. Thus, changing the prior probabilities used in the Bayesian analysis from the mass function based on Sumi et al. (2011) to the mass function based on Mróz et al. (2017) did not affect the conclusions.

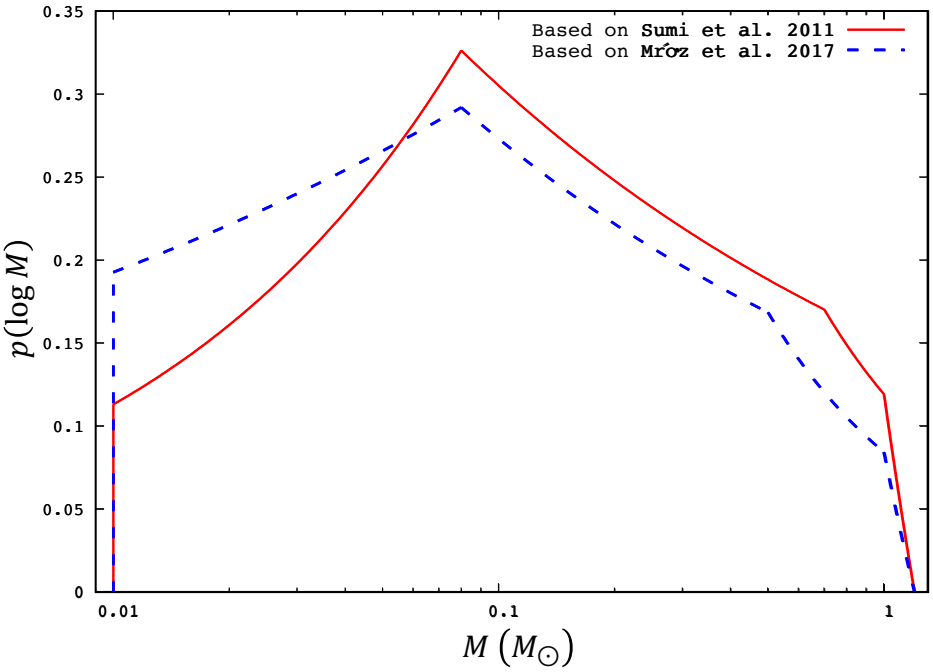

Figure B.1: Different mass functions used as prior probability distributions in Bayesian analysis for estimating lens host masses. The red line is the mass function based on Sumi et al. (2011) used in the Bayesian analysis in the Section 3.6. The blue dashed line is the mass function based on Mróz et al. (2017) used in the Appendix B.

Table B.1: Properties of the lens system of the 2L1S+xallarap model by Bayesian analysis using the mass function based on Mróz et al. (2017) as the prior probability

Model	XLclose1	XLclose2	XLwide1	XLwide2
range of q	$q \leq 0.1$	$0.1 < q \leq 1$	$q \leq 0.1$	$0.1 < q \leq 1$
$D_{\rm L}$ (kpc)	$7.25^{+1.09}_{-1.18}$	$7.21^{+1.08}_{-1.19}$	$7.21^{+1.08}_{-1.20}$	$7.08^{+1.04}_{-1.23}$
$M_{\rm L,H}$ ($M_\odot$)	$0.22^{+0.25}_{-0.11}$	$0.24^{+0.26}_{-0.12}$	$0.25^{+0.26}_{-0.13}$	$0.36^{+0.29}_{-0.18}$
$M_{\rm L,C}$ ($M_\odot$)	$0.02^{+0.02}_{-0.01}$	$0.11^{+0.11}_{-0.05}$	$0.02^{+0.03}_{-0.01}$	$0.34^{+0.28}_{-0.17}$
$a_{\rm L,\perp}$ (au)	$0.20^{+0.04}_{-0.04}$	$0.13^{+0.02}_{-0.02}$	$11.49^{+2.02}_{-2.11}$	$34.43^{+7.44}_{-7.69}$
$a_{\rm L,exp}$ (au)	$0.25^{+0.13}_{-0.06}$	$0.16^{+0.08}_{-0.04}$	$13.83^{+7.35}_{-3.15}$	$41.70^{+21.62}_{-10.87}$
$V_{\rm L,H}$ (mag)	$30.69^{+2.58}_{-2.26}$	$30.42^{+2.44}_{-2.32}$	$30.33^{+2.33}_{-2.34}$	$29.30^{+1.81}_{-3.05}$
$I_{\rm L,H}$ (mag)	$26.14^{+1.66}_{-1.56}$	$25.95^{+1.58}_{-1.60}$	$25.89^{+1.52}_{-1.62}$	$25.14^{+1.20}_{-2.10}$
$H_{\rm L,H}$ (mag)	$22.58^{+1.26}_{-1.55}$	$22.41^{+1.25}_{-1.59}$	$22.35^{+1.21}_{-1.61}$	$21.62^{+1.13}_{-1.88}$
$K_{\rm L,H}$ (mag)	$22.16^{+1.20}_{-1.53}$	$21.99^{+1.19}_{-1.56}$	$21.93^{+1.16}_{-1.57}$	$21.21^{+1.10}_{-1.80}$
$V_{\rm L,C}$ (mag)	$41.60^{+0.94}_{-1.38}$	$33.82^{+6.13}_{-2.90}$	$41.49^{+0.98}_{-1.60}$	$29.47^{+1.87}_{-2.79}$
$I_{\rm L,C}$ (mag)	$35.32^{+1.68}_{-2.81}$	$28.21^{+3.36}_{-1.88}$	$34.95^{+1.81}_{-2.88}$	$25.26^{+1.24}_{-1.91}$
$H_{\rm L,C}$ (mag)	$33.95^{+2.80}_{-3.65}$	$24.17^{+6.05}_{-1.43}$	$33.63^{+2.96}_{-3.79}$	$21.74^{+1.13}_{-1.77}$
$K_{\rm L,C}$ (mag)	$30.51^{+1.44}_{-2.09}$	$23.69^{+3.72}_{-1.37}$	$30.07^{+1.50}_{-2.08}$	$21.33^{+1.11}_{-1.70}$
$V_{\rm L,total}$ (mag)	$30.69^{+2.57}_{-2.26}$	$30.38^{+2.48}_{-2.35}$	$30.33^{+2.32}_{-2.34}$	$28.63^{+1.84}_{-2.94}$
$I_{\rm L,total}$ (mag)	$26.14^{+1.66}_{-1.56}$	$25.83^{+1.68}_{-1.64}$	$25.89^{+1.51}_{-1.62}$	$24.45^{+1.22}_{-2.01}$
$H_{\rm L,total}$ (mag)	$22.58^{+1.26}_{-1.55}$	$22.22^{+1.43}_{-1.57}$	$22.35^{+1.21}_{-1.61}$	$20.93^{+1.13}_{-1.82}$
$K_{\rm L,total}$ (mag)	$22.15^{+1.20}_{-1.53}$	$21.78^{+1.37}_{-1.53}$	$21.92^{+1.16}_{-1.57}$	$20.51^{+1.11}_{-1.75}$
$V_{\rm Blend}$ (mag)	20.21 ± 0.03	20.21 ± 0.03	20.21 ± 0.03	20.21 ± 0.03
$I_{\rm Blend}$ (mag)	19.25 ± 0.01	19.25 ± 0.01	19.25 ± 0.01	19.25 ± 0.01
χ^2	10856.4	10840.9	10861.2	10842.7
$\Delta\chi^2$	15.5	-	20.3	1.8

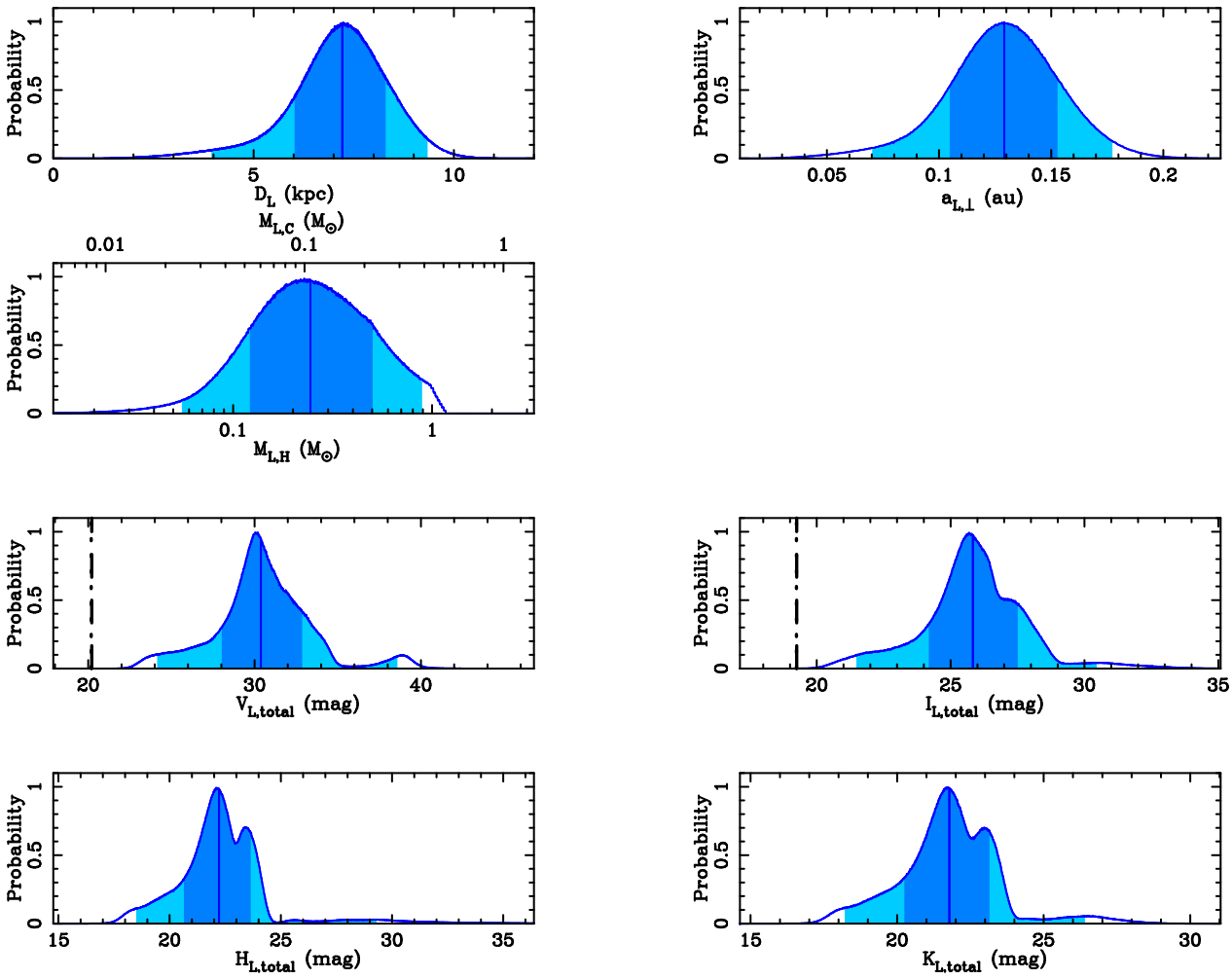

Figure B.2: Same as Figure 3.17, posterior probability distribution of lens system properties for the XLclose2, but with the mass function based on Mróz et al. (2017) as the prior probability.

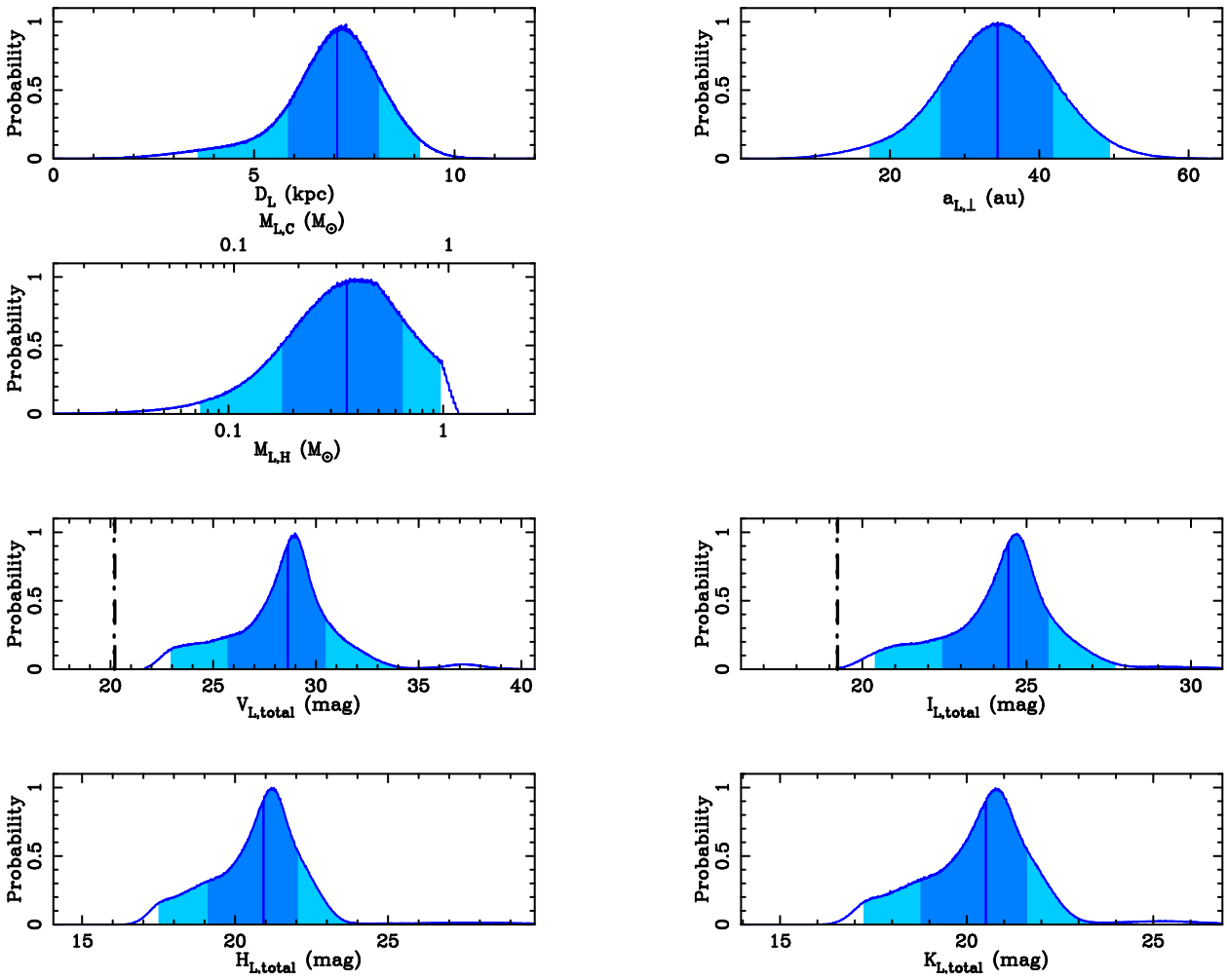

Figure B.3: Same as Figure 3.18, posterior probability distribution of lens system properties for the XLwide2, but with the mass function based on Mróz et al. (2017) as the prior probability.

Acknowledgements

I would like to express my sincere gratitude to my supervisor, Professor T. Sumi for allowing me to enroll in the doctoral program and giving me a valuable opportunity to study exploration using the gravitational microlensing method. He also gave me various very important suggestions regarding my research.

I would like to express my sincere gratitude to Assistant Professor D. Suzuki for his kindness in consulting with me about my research and for his various helpful comments. I was able to publish our paper on OGLE-2019-BLG-0825 and present it at the 25th Microlensing Conference because of his various support. I would like to express my deepest gratitude to Assistant Professor N. Koshimoto, who always gave me valuable advice, took a lot of time for my consultation, and answered my poor questions very carefully in conducting this research. I would like to express my gratitude to Assistant Professor K. Masuda, who has provided me with much important knowledge in the statistical interpretation of my research. His teachings were always eye-opening. I am grateful to Professor Emeritus H. Shibai for giving me the opportunity to do research and for teaching me so much about research attitudes.

I would like to thank all members of the MOA Collaboration for their support. I thank Dr. D. P. Bennett of NASA/GSFC for his careful guidance during the research process. I would like to thank Dr. N. J. Rattenbury of the University of Auckland for many important suggestions on writing and editing the paper. I thank Associate Professor I. A. Bond of Massey University for important contributions to the reduction of data for this paper.

I would like to express my sincere gratitude to Associate Professor M. Kajisawa of Ehime University, who taught me so many things that are irreplaceable for continuing research, such as the fun of research, the basics of analysis, and how to approach problems.

I would like to thank all the members of the Infrared Astronomy Group at Osaka University. I learned a lot from Dr. T. Ito, Dr. Y. Hirao, Dr. M. Nagakane, Mr. T. Oyama, Mr. J. Sudo, Dr. S. Miyazaki, Dr. I. Kondo, and Mr. R. Kirikawa. Their advice enabled me to write this dissertation. In particular, Dr. S. Miyazaki has been very motivating to me since I started at Osaka University by sharing various conversations with me about things other than research. I would like to express my gratitude to Mr. H. Fujii, Ms. R. Ono, Mr. M. Saeki, Ms. H. Suematsu, Mr. T. Tsuboi, Ms. H. Shoji, Mr. Y. Tanaka, Mr. T. Yamawaki, Mr. S. Kadono, Ms. M. Maruno, Mr. Y. Yamasaki, Mr. S. Matsumoto, Mr. K. Niwa, Ms. A. Okamura, Mr. T. Toda, Mr. H. Yama, Mr. K. Fujita, Mr. R. Hamada, Mr. T. Ikeno, Mr. M. Tomoyoshi, Mr. K. Yamashita, Mr. K. Bando, Mr. S. Hamada, Mr. N. Hamasaki, and Ms. X. Li for making my research life in the laboratory fulfilling and enjoyable. I would like to thank the laboratory secretaries, Ms. A. Yamamoto, Ms. H. Jo, and Ms. K. Mori, who provided various kinds of support.

I would like to thank my family and friends for their support during my student life. Without their presence, of course I would not have been able to reach this dissertation submission.

Finally, I would like to thank once again all those who have been involved in my research to date.

Bibliography

Adams, F. C. & Laughlin, G.: Long-Term Evolution of Close Planets Including the Effects of Secular Interactions, ApJ, 649, 1004–1009, https://doi.org/10.1086/506145, 2006.

Adibekyan, V., Santos, N. C., Figueira, P., Dorn, C., Sousa, S. G., Delgado-Mena, E., Israelian, G., Hakobyan, A. A., & Mordasini, C.: From stellar to planetary composition: Galactic chemical evolution of Mg/Si mineralogical ratio, A&A, 581, L2, https://doi.org/10.1051/0004-6361/201527059, 2015.

Adibekyan, V., Dorn, C., Sousa, S. G., Santos, N. C., Bitsch, B., Israelian, G., Mordasini, C., Barros, S. C. C., Delgado Mena, E., Demangeon, O. D. S., Faria, J. P., Figueira, P., Hakobyan, A. A., Oshagh, M., Soares, B. M. T. B., Kunitomo, M., Takeda, Y., Jofré, E., Petrucci, R., & Martioli, E.: A compositional link between rocky exoplanets and their host stars, Science, 374, 330–332, https://doi.org/10.1126/science.abg8794, 2021.

Adibekyan, V. Z., Santos, N. C., Sousa, S. G., Israelian, G., Delgado Mena, E., González Hernández, J. I., Mayor, M., Lovis, C., & Udry, S.: Overabundance of α-elements in exoplanet-hosting stars, A&A, 543, A89, https://doi.org/10.1051/0004-6361/201219564, 2012a.

Adibekyan, V. Z., Sousa, S. G., Santos, N. C., Delgado Mena, E., González Hernández, J. I., Israelian, G., Mayor, M., & Khachatryan, G.: Chemical abundances of 1111 FGK stars from the HARPS GTO planet search program. Galactic stellar populations and planets, A&A, 545, A32, https://doi.org/10.1051/0004-6361/201219401, 2012b.

Alard, C.: First Results Of The DUO Program, in: Astrophysical Applications of Gravitational Lensing, edited by Kochanek, C. S. & Hewitt, J. N., vol. 173, p. 215, 1996.

Alard, C.: Image subtraction using a space-varying kernel, A&AS, 144, 363–370, https://doi.org/10.1051/aas:2000214, 2000.

Alard, C. & Lupton, R. H.: A Method for Optimal Image Subtraction, ApJ, 503, 325–331, https://doi.org/10.1086/305984, 1998.

Albrow, M. D., Horne, K., Bramich, D. M., Fouqué, P., Miller, V. R., Beaulieu, J. P., Coutures, C., Menzies, J., Williams, A., Batista, V., Bennett, D. P., Brillant, S., Cassan, A., Dieters, S., Dominis Prester, D., Donatowicz, J., Greenhill, J., Kains, N., Kane, S. R., Kubas, D., Marquette, J. B., Pollard, K. R., Sahu, K. C., Tsapras, Y., Wambsganss, J., & Zub, M.: Difference imaging photometry of blended gravitational microlensing events with a numerical kernel, MNRAS, 397, 2099–2105, https://doi.org/10.1111/j.1365-2966.2009.15098.x, 2009.

Alcock, C., Akerlof, C. W., Allsman, R. A., Axelrod, T. S., Bennett, D. P., Chan, S., Cook, K. H., Freeman, K. C., Griest, K., Marshall, S. L., Park, H. S., Perlmutter, S., Peterson, B. A., Pratt, M. R., Quinn, P. J., Rodgers, A. W., Stubbs, C. W., & Sutherland, W.: Possible gravitational microlensing of a star in the Large Magellanic Cloud, Nature, 365, 621–623, https://doi.org/10.1038/365621a0, 1993.

Alcock, C., Allsman, R. A., Alves, D., Axelrod, T. S., Bennett, D. P., Cook, K. H., Freeman, K. C., Griest, K., Guern, J., Lehner, M. J., Marshall, S. L., Park, H. S., Perlmutter, S., Peterson, B. A., Pratt, M. R., Quinn, P. J., Rodgers, A. W., Stubbs, C. W., & Sutherland, W.: The Macho Project: 45 Candidate Microlensing Events from the First Year Galactic Bulge Data, ApJ, 479, 119–146, https://doi.org/10.1086/303851, 1997.

Alcock, C., Allsman, R. A., Alves, D. R., Axelrod, T. S., Becker, A. C., Bennett, D. P., Cook, K. H., Dalal, N., Drake, A. J., Freeman, K. C., Geha, M., Griest, K., Lehner, M. J., Marshall, S. L., Minniti, D., Nelson, C. A., Peterson, B. A., Popowski, P., Pratt, M. R., Quinn, P. J., Stubbs, C. W., Sutherland, W., Tomaney, A. B., Vandehei, T., & Welch, D.: The MACHO

Project: Microlensing Results from 5.7 Years of Large Magellanic Cloud Observations, ApJ, 542, 281–307, https://doi.org/10.1086/309512, 2000.

Anglada-Escudé, G., Amado, P. J., Barnes, J., Berdiñas, Z. M., Butler, R. P., Coleman, G. A. L., de La Cueva, I., Dreizler, S., Endl, M., Giesers, B., Jeffers, S. V., Jenkins, J. S., Jones, H. R. A., Kiraga, M., Kürster, M., López-González, M. J., Marvin, C. J., Morales, N., Morin, J., Nelson, R. P., Ortiz, J. L., Ofir, A., Paardekooper, S.-J., Reiners, A., Rodríguez, E., Rodríguez-López, C., Sarmiento, L. F., Strachan, J. P., Tsapras, Y., Tuomi, M., & Zechmeister, M.: A terrestrial planet candidate in a temperate orbit around Proxima Centauri, Nature, 536, 437–440, https://doi.org/10.1038/nature19106, 2016.

Armitage, P. J. & Bonnell, I. A.: The brown dwarf desert as a consequence of orbital migration, MNRAS, 330, L11–L14, https://doi.org/10.1046/j.1365-8711.2002.05213.x, 2002.

Aubourg, E., Bareyre, P., Bréhin, S., Gros, M., Lachièze-Rey, M., Laurent, B., Lesquoy, E., Magneville, C., Milsztajn, A., Moscoso, L., Queinnec, F., Rich, J., Spiro, M., Vigroux, L., Zylberajch, S., Ansari, R., Cavalier, F., Moniez, M., Beaulieu, J. P., Ferlet, R., Grison, P., Vidal-Madjar, A., Guibert, J., Moreau, O., Tajahmady, F., Maurice, E., Prévôt, L., & Gry, C.: Evidence for gravitational microlensing by dark objects in the Galactic halo, Nature, 365, 623–625, https://doi.org/10.1038/365623a0, 1993.

Bachelet, E., Shin, I. G., Han, C., Fouqué, P., Gould, A., Menzies, J. W., Beaulieu, J. P., Bennett, D. P., Bond, I. A., Dong, S., Heyrovský, D., Marquette, J. B., Marshall, J., Skowron, J., Street, R. A., Sumi, T., Udalski, A., Abe, L., Agabi, K., Albrow, M. D., Allen, W., Bertin, E., Bos, M., Bramich, D. M., Chavez, J., Christie, G. W., Cole, A. A., Crouzet, N., Dieters, S., Dominik, M., Drummond, J., Greenhill, J., Guillot, T., Henderson, C. B., Hessman, F. V., Horne, K., Hundertmark, M., Johnson, J. A., Jørgensen, U. G., Kandori, R., Liebig, C., Mékarnia, D., McCormick, J., Moorhouse, D., Nagayama, T., Nataf, D., Natusch, T., Nishiyama, S., Rivet, J. P., Sahu, K. C., Shvartzvald, Y., Thornley, G., Tomczak, A. R., Tsapras, Y., Yee, J. C., Batista, V., Bennett, C. S., Brillant, S., Caldwell, J. A. R., Cassan, A., Corrales, E., Coutures, C., Dominis

Prester, D., Donatowicz, J., Kubas, D., Martin, R., Williams, A., Zub, M., PLANET Collaboration, de Almeida, L. A., DePoy, D. L., Gaudi, B. S., Hung, L. W., Jablonski, F., Kaspi, S., Klein, N., Lee, C. U., Lee, Y., Koo, J. R., Maoz, D., Muñoz, J. A., Pogge, R. W., Polishook, D., Shporer, A., μFUN Collaboration, Abe, F., Botzler, C. S., Chote, P., Freeman, M., Fukui, A., Furusawa, K., Harris, P., Itow, Y., Kobara, S., Ling, C. H., Masuda, K., Matsubara, Y., Miyake, N., Ohmori, K., Ohnishi, K., Rattenbury, N. J., Saito, T., Sullivan, D. J., Suzuki, D., Sweatman, W. L., Tristram, P. J., Wada, K., Yock, P. C. M., MOA Collaboration, Szymański, M. K., Soszyński, I., Kubiak, M., Poleski, R., Ulaczyk, K., Pietrzyński, G., Wyrzykowski, Ł., OGLE Collaboration, Kains, N., Snodgrass, C., Steele, I. A., RoboNet Collaboration, Alsubai, K. A., Bozza, V., Browne, P., Burgdorf, M. J., Calchi Novati, S., Dodds, P., Dreizler, S., Finet, F., Gerner, T., Hardis, S., Harpsøe, K., Hinse, T. C., Kerins, E., Mancini, L., Mathiasen, M., Penny, M. T., Proft, S., Rahvar, S., Ricci, D., Scarpetta, G., Schäfer, S., Schönebeck, F., Southworth, J., Surdej, J., Wambsganss, J., & MiNDSTEp Consortium: MOA 2010-BLG-477Lb: Constraining the Mass of a Microlensing Planet from Microlensing Parallax, Orbital Motion, and Detection of Blended Light, ApJ, 754, 73, https://doi.org/10.1088/0004-637X/754/1/73, 2012.

Badenes, C., Mazzola, C., Thompson, T. A., Covey, K., Freeman, P. E., Walker, M. G., Moe, M., Troup, N., Nidever, D., Allende Prieto, C., Andrews, B., Barbá, R. H., Beers, T. C., Bovy, J., Carlberg, J. K., De Lee, N., Johnson, J., Lewis, H., Majewski, S. R., Pinsonneault, M., Sobeck, J., Stassun, K. G., Stringfellow, G. S., & Zasowski, G.: Stellar Multiplicity Meets Stellar Evolution and Metallicity: The APOGEE View, ApJ, 854, 147, https://doi.org/10.3847/1538-4357/aaa765, 2018.

Bahcall, J. N.: Star counts and galactic structure., ARA&A, 24, 577–611, https://doi.org/10.1146/annurev.aa.24.090186.003045, 1986.

Baraffe, I., Chabrier, G., Barman, T. S., Allard, F., & Hauschildt, P. H.: Evolutionary models for cool brown dwarfs and extrasolar giant planets. The case of HD 209458, A&A, 402, 701–712, https://doi.org/10.1051/0004-6361:20030252, 2003.

Bashi, D., Zucker, S., Adibekyan, V., Santos, N. C., Tal-Or, L., Trifonov, T., & Mazeh, T.: Occurrence rates of small planets from HARPS. Focus on the Galactic context, A&A, 643, A106, https://doi.org/10.1051/0004-6361/202038881, 2020.

Batista, V., Gould, A., Dieters, S., Dong, S., Bond, I., Beaulieu, J. P., Maoz, D., Monard, B., Christie, G. W., McCormick, J., Albrow, M. D., Horne, K., Tsapras, Y., Burgdorf, M. J., Calchi Novati, S., Skottfelt, J., Caldwell, J., Kozłowski, S., Kubas, D., Gaudi, B. S., Han, C., Bennett, D. P., An, J., MOA Collaboration, Abe, F., Botzler, C. S., Douchin, D., Freeman, M., Fukui, A., Furusawa, K., Hearnshaw, J. B., Hosaka, S., Itow, Y., Kamiya, K., Kilmartin, P. M., Korpela, A., Lin, W., Ling, C. H., Makita, B. S., Masuda, K., Matsubara, Y., Miyake, N., Muraki, Y., Nagaya, M., Nishimoto, K., Ohnishi, K., Okumura, T., Perrott, Y. C., Rattenbury, N., Saito, T., Sullivan, D. J., Sumi, T., Sweatman, W. L., Tristram, P. J., von Seggern, E., Yock, P. C. M., PLANET Collaboration, Brillant, S., Calitz, J. J., Cassan, A., Cole, A., Cook, K., Coutures, C., Dominis Prester, D., Donatowicz, J., Greenhill, J., Hoffman, M., Jablonski, F., Kane, S. R., Kains, N., Marquette, J. B., Martin, R., Martioli, E., Meintjes, P., Menzies, J., Pedretti, E., Pollard, K., Sahu, K. C., Vinter, C., Wambsganss, J., Watson, R., Williams, A., Zub, M., FUN Collaboration, Allen, W., Bolt, G., Bos, M., DePoy, D. L., Drummond, J., Eastman, J. D., Gal-Yam, A., Gorbikov, E., Higgins, D., Janczak, J., Kaspi, S., Lee, C. U., Mallia, F., Maury, A., Monard, L. A. G., Moorhouse, D., Morgan, N., Natusch, T., Ofek, E. O., Park, B. G., Pogge, R. W., Polishook, D., Santallo, R., Shporer, A., Spector, O., Thornley, G., Yee, J. C., MiNDSTEp Consortium, Bozza, V., Browne, P., Dominik, M., Dreizler, S., Finet, F., Glitrup, M., Grundahl, F., Harpsøe, K., Hessman, F. V., Hinse, T. C., Hundertmark, M., Jørgensen, U. G., Liebig, C., Maier, G., Mancini, L., Mathiasen, M., Rahvar, S., Ricci, D., Scarpetta, G., Southworth, J., Surdej, J., Zimmer, F., RoboNet Collaboration, Allan, A., Bramich, D. M., Snodgrass, C., Steele, I. A., & Street, R. A.: MOA-2009-BLG-387Lb: a massive planet orbiting an M dwarf, A&A, 529, A102, https://doi.org/10.1051/0004-6361/201016111, 2011.

Batista, V., Beaulieu, J. P., Gould, A., Bennett, D. P., Yee, J. C., Fukui, A., Gaudi, B. S., Sumi, T., & Udalski, A.: MOA-2011-BLG-293Lb: First Microlensing Planet Possibly in the Habitable Zone, ApJ, 780, 54, https://doi.org/10.1088/0004-637X/780/1/54, 2014.

Beatty, T. G., Morley, C. V., Curtis, J. L., Burrows, A., Davenport, J. R. A., & Montet, B. T.: A Significant Overluminosity in the Transiting Brown Dwarf CWW 89Ab, AJ, 156, 168, https://doi.org/10.3847/1538-3881/aad697, 2018.

Beaugé, C. & Nesvorný, D.: Emerging Trends in a Period-Radius Distribution of Close-in Planets, ApJ, 763, 12, https://doi.org/10.1088/0004-637X/763/1/12, 2013.

Beaulieu, J. P., Bennett, D. P., Fouqué, P., Williams, A., Dominik, M., Jørgensen, U. G., Kubas, D., Cassan, A., Coutures, C., Greenhill, J., Hill, K., Menzies, J., Sackett, P. D., Albrow, M., Brillant, S., Caldwell, J. A. R., Calitz, J. J., Cook, K. H., Corrales, E., Desort, M., Dieters, S., Dominis, D., Donatowicz, J., Hoffman, M., Kane, S., Marquette, J. B., Martin, R., Meintjes, P., Pollard, K., Sahu, K., Vinter, C., Wambsganss, J., Woller, K., Horne, K., Steele, I., Bramich, D. M., Burgdorf, M., Snodgrass, C., Bode, M., Udalski, A., Szymański, M. K., Kubiak, M., Więckowski, T., Pietrzyński, G., Soszyński, I., Szewczyk, O., Wyrzykowski, Ł., Paczyński, B., Abe, F., Bond, I. A., Britton, T. R., Gilmore, A. C., Hearnshaw, J. B., Itow, Y., Kamiya, K., Kilmartin, P. M., Korpela, A. V., Masuda, K., Matsubara, Y., Motomura, M., Muraki, Y., Nakamura, S., Okada, C., Ohnishi, K., Rattenbury, N. J., Sako, T., Sato, S., Sasaki, M., Sekiguchi, T., Sullivan, D. J., Tristram, P. J., Yock, P. C. M., & Yoshioka, T.: Discovery of a cool planet of 5.5 Earth masses through gravitational microlensing, Nature, 439, 437–440, https://doi.org/10.1038/nature04441, 2006.

Benneke, B., Wong, I., Piaulet, C., Knutson, H. A., Lothringer, J., Morley, C. V., Crossfield, I. J. M., Gao, P., Greene, T. P., Dressing, C., Dragomir, D., Howard, A. W., McCullough, P. R., Kempton, E. M. R., Fortney, J. J., & Fraine, J.: Water Vapor and Clouds on the Habitable-zone Sub-Neptune Exoplanet K2-18b, ApJL, 887, L14, https://doi.org/10.3847/2041-8213/ab59dc, 2019.

Bennett, D.: Magellanic Cloud gravitational microlensing results: what do they mean?, PhR, 307, 97–106, https://doi.org/10.1016/S0370-1573(98)00077-5, 1998.

Bennett, D. P.: An Efficient Method for Modeling High-magnification Planetary Microlensing Events, ApJ, 716, 1408–1422, https://doi.org/10.1088/0004-637X/716/2/1408, 2010.

Bennett, D. P. & Rhie, S. H.: Detecting Earth-Mass Planets with Gravitational Microlensing, ApJ, 472, 660, https://doi.org/10.1086/178096, 1996.

Bennett, D. P., Bond, I. A., Udalski, A., Sumi, T., Abe, F., Fukui, A., Furusawa, K., Hearnshaw, J. B., Holderness, S., Itow, Y., Kamiya, K., Korpela, A. V., Kilmartin, P. M., Lin, W., Ling, C. H., Masuda, K., Matsubara, Y., Miyake, N., Muraki, Y., Nagaya, M., Okumura, T., Ohnishi, K., Perrott, Y. C., Rattenbury, N. J., Sako, T., Saito, T., Sato, S., Skuljan, L., Sullivan, D. J., Sweatman, W. L., Tristram, P. J., Yock, P. C. M., Kubiak, M., Szymański, M. K., Pietrzyński, G., Soszyński, I., Szewczyk, O., Wyrzykowski, Ł., Ulaczyk, K., Batista, V., Beaulieu, J. P., Brillant, S., Cassan, A., Fouqué, P., Kervella, P., Kubas, D., & Marquette, J. B.: A Low-Mass Planet with a Possible Sub-Stellar-Mass Host in Microlensing Event MOA-2007-BLG-192, ApJ, 684, 663–683, https://doi.org/10.1086/589940, 2008.

Bennett, D. P., Batista, V., Bond, I. A., Bennett, C. S., Suzuki, D., Beaulieu, J. P., Udalski, A., Donatowicz, J., Bozza, V., Abe, F., Botzler, C. S., Freeman, M., Fukunaga, D., Fukui, A., Itow, Y., Koshimoto, N., Ling, C. H., Masuda, K., Matsubara, Y., Muraki, Y., Namba, S., Ohnishi, K., Rattenbury, N. J., Saito, T., Sullivan, D. J., Sumi, T., Sweatman, W. L., Tristram, P. J., Tsurumi, N., Wada, K., Yock, P. C. M., MOA Collaboration, Albrow, M. D., Bachelet, E., Brillant, S., Caldwell, J. A. R., Cassan, A., Cole, A. A., Corrales, E., Coutures, C., Dieters, S., Dominis Prester, D., Fouqué, P., Greenhill, J., Horne, K., Koo, J. R., Kubas, D., Marquette, J. B., Martin, R., Menzies, J. W., Sahu, K. C., Wambsganss, J., Williams, A., Zub, M., PLANET Collaboration, Choi, J. Y., DePoy, D. L., Dong, S., Gaudi, B. S., Gould, A., Han, C., Henderson, C. B., McGregor, D., Lee, C. U., Pogge, R. W., Shin, I. G., Yee, J. C., μFUN Collaboration, Szymański, M. K., Skowron, J., Poleski, R., Kozłowski, S., Wyrzykowski, Ł., Kubiak, M., Pietrukowicz, P., Pietrzyński, G., Soszyński, I., Ulaczyk, K., OGLE Collaboration, Tsapras, Y., Street, R. A.,

Dominik, M., Bramich, D. M., Browne, P., Hundertmark, M., Kains, N., Snodgrass, C., Steele, I. A., RoboNet Collaboration, Dekany, I., Gonzalez, O. A., Heyrovský, D., Kandori, R., Kerins, E., Lucas, P. W., Minniti, D., Nagayama, T., Rejkuba, M., Robin, A. C., & Saito, R.: MOA-2011-BLG-262Lb: A Sub-Earth-Mass Moon Orbiting a Gas Giant Primary or a High Velocity Planetary System in the Galactic Bulge, ApJ, 785, 155, https://doi.org/10.1088/0004-637X/785/2/155, 2014.

Bennett, D. P., Bhattacharya, A., Anderson, J., Bond, I. A., Anderson, N., Barry, R., Batista, V., Beaulieu, J. P., DePoy, D. L., Dong, S., Gaudi, B. S., Gilbert, E., Gould, A., Pfeifle, R., Pogge, R. W., Suzuki, D., Terry, S., & Udalski, A.: Confirmation of the Planetary Microlensing Signal and Star and Planet Mass Determinations for Event OGLE-2005-BLG-169, ApJ, 808, 169, https://doi.org/10.1088/0004-637X/808/2/169, 2015.

Bennett, D. P., Rhie, S. H., Udalski, A., Gould, A., Tsapras, Y., Kubas, D., Bond, I. A., Greenhill, J., Cassan, A., Rattenbury, N. J., Boyajian, T. S., Luhn, J., Penny, M. T., Anderson, J., Abe, F., Bhattacharya, A., Botzler, C. S., Donachie, M., Freeman, M., Fukui, A., Hirao, Y., Itow, Y., Koshimoto, N., Li, M. C. A., Ling, C. H., Masuda, K., Matsubara, Y., Muraki, Y., Nagakane, M., Ohnishi, K., Oyokawa, H., Perrott, Y. C., Saito, T., Sharan, A., Sullivan, D. J., Sumi, T., Suzuki, D., Tristram, P. J., Yonehara, A., Yock, P. C. M., MOA Collaboration, Szymański, M. K., Soszyński, I., Ulaczyk, K., Wyrzykowski, Ł., OGLE Collaboration, Allen, W., DePoy, D., Gal-Yam, A., Gaudi, B. S., Han, C., Monard, I. A. G., Ofek, E., Pogge, R. W., μFUN Collaboration, Street, R. A., Bramich, D. M., Dominik, M., Horne, K., Snodgrass, C., Steele, I. A., Robonet Collaboration, Albrow, M. D., Bachelet, E., Batista, V., Beaulieu, J. P., Brillant, S., Caldwell, J. A. R., Cole, A., Coutures, C., Dieters, S., Dominis Prester, D., Donatowicz, J., Fouqué, P., Hundertmark, M., Jørgensen, U. G., Kains, N., Kane, S. R., Marquette, J. B., Menzies, J., Pollard, K. R., Ranc, C., Sahu, K. C., Wambsganss, J., Williams, A., Zub, M., & PLANET Collaboration: The First Circumbinary Planet Found by Microlensing: OGLE-2007-BLG-349L(AB)c, AJ, 152, 125, https://doi.org/10.3847/0004-6256/152/5/125, 2016.

Bensby, T., Yee, J. C., Feltzing, S., Johnson, J. A., Gould, A., Cohen, J. G., Asplund, M., Meléndez, J., Lucatello, S., Han, C., Thompson, I., Gal-Yam, A., Udalski, A., Bennett, D. P., Bond, I. A., Kohei, W., Sumi, T., Suzuki, D., Suzuki, K., Takino, S., Tristram, P., Yamai, N., & Yonehara, A.: Chemical evolution of the Galactic bulge as traced by microlensed dwarf and subgiant stars. V. Evidence for a wide age distribution and a complex MDF, A&A, 549, A147, https://doi.org/10.1051/0004-6361/201220678, 2013.

Bhatiani, S., Dai, X., & Guerras, E.: Confirmation of Planet-mass Objects in Extragalactic Systems, ApJ, 885, 77, https://doi.org/10.3847/1538-4357/ab46ac, 2019.

Binney, J. & Tremaine, S.: Galactic dynamics, 1987.

Bolatto, A. D. & Falco, E. E.: The Detectability of Planetary Companions of Compact Galactic Objects from Their Effects on Microlensed Light Curves of Distant Stars, ApJ, 436, 112, https://doi.org/10.1086/174885, 1994.

Bond, I. A., Abe, F., Dodd, R. J., Hearnshaw, J. B., Honda, M., Jugaku, J., Kilmartin, P. M., Marles, A., Masuda, K., Matsubara, Y., Muraki, Y., Nakamura, T., Nankivell, G., Noda, S., Noguchi, C., Ohnishi, K., Rattenbury, N. J., Reid, M., Saito, T., Sato, H., Sekiguchi, M., Skuljan, J., Sullivan, D. J., Sumi, T., Takeuti, M., Watase, Y., Wilkinson, S., Yamada, R., Yanagisawa, T., & Yock, P. C. M.: Real-time difference imaging analysis of MOA Galactic bulge observations during 2000, MNRAS, 327, 868–880, https://doi.org/10.1046/j.1365-8711.2001.04776.x, 2001.

Bond, I. A., Udalski, A., Jaroszyński, M., Rattenbury, N. J., Paczyński, B., Soszyński, I., Wyrzykowski, L., Szymański, M. K., Kubiak, M., Szewczyk, O., Żebruń, K., Pietrzyński, G., Abe, F., Bennett, D. P., Eguchi, S., Furuta, Y., Hearnshaw, J. B., Kamiya, K., Kilmartin, P. M., Kurata, Y., Masuda, K., Matsubara, Y., Muraki, Y., Noda, S., Okajima, K., Sako, T., Sekiguchi, T., Sullivan, D. J., Sumi, T., Tristram, P. J., Yanagisawa, T., Yock, P. C. M., & OGLE Collaboration: OGLE 2003-BLG-235/MOA 2003-BLG-53: A Planetary Microlensing Event, ApJL, 606, L155–L158, https://doi.org/10.1086/420928, 2004.

Borgniet, S., Lagrange, A. M., Meunier, N., & Galland, F.: Extrasolar planets and brown dwarfs around AF-type stars. IX. The HARPS southern sample, A&A, 599, A57, https://doi.org/10.1051/0004-6361/201628805, 2017.

Borucki, W. J., Koch, D., Basri, G., Batalha, N., Brown, T., Caldwell, D., Caldwell, J., Christensen-Dalsgaard, J., Cochran, W. D., DeVore, E., Dunham, E. W., Dupree, A. K., Gautier, T. N., Geary, J. C., Gilliland, R., Gould, A., Howell, S. B., Jenkins, J. M., Kondo, Y., Latham, D. W., Marcy, G. W., Meibom, S., Kjeldsen, H., Lissauer, J. J., Monet, D. G., Morrison, D., Sasselov, D., Tarter, J., Boss, A., Brownlee, D., Owen, T., Buzasi, D., Charbonneau, D., Doyle, L., Fortney, J., Ford, E. B., Holman, M. J., Seager, S., Steffen, J. H., Welsh, W. F., Rowe, J., Anderson, H., Buchhave, L., Ciardi, D., Walkowicz, L., Sherry, W., Horch, E., Isaacson, H., Everett, M. E., Fischer, D., Torres, G., Johnson, J. A., Endl, M., MacQueen, P., Bryson, S. T., Dotson, J., Haas, M., Kolodziejczak, J., Van Cleve, J., Chandrasekaran, H., Twicken, J. D., Quintana, E. V., Clarke, B. D., Allen, C., Li, J., Wu, H., Tenenbaum, P., Verner, E., Bruhweiler, F., Barnes, J., & Prsa, A.: Kepler Planet-Detection Mission: Introduction and First Results, Science, 327, 977, https://doi.org/10.1126/science.1185402, 2010.

Boyajian, T. S., van Belle, G., & von Braun, K.: Stellar Diameters and Temperatures. IV. Predicting Stellar Angular Diameters, AJ, 147, 47, https://doi.org/10.1088/0004-6256/147/3/47, 2014.

Bramich, D. M.: A new algorithm for difference image analysis, MNRAS, 386, L77–L81, https://doi.org/10.1111/j.1745-3933.2008.00464.x, 2008.

Bramich, D. M., Horne, K., Albrow, M. D., Tsapras, Y., Snodgrass, C., Street, R. A., Hundertmark, M., Kains, N., Arellano Ferro, A., Figuera, J. R., & Giridhar, S.: Difference image analysis: extension to a spatially varying photometric scale factor and other considerations, MNRAS, 428, 2275–2289, https://doi.org/10.1093/mnras/sts184, 2013.

Bressan, A., Marigo, P., Girardi, L., Salasnich, B., Dal Cero, C., Rubele, S., & Nanni, A.: PARSEC: stellar tracks and isochrones with the PAdova and TRieste Stellar Evolution Code, MNRAS, 427, 127–145, https://doi.org/10.1111/j.1365-2966.2012.21948.x, 2012.

Buchhave, L. A., Bitsch, B., Johansen, A., Latham, D. W., Bizzarro, M., Bieryla, A., & Kipping, D. M.: Jupiter Analogs Orbit Stars with an Average Metallicity Close to That of the Sun, ApJ, 856, 37, https://doi.org/10.3847/1538-4357/aaafca, 2018.

Butler, R. P. & Marcy, G. W.: A Planet Orbiting 47 Ursae Majoris, ApJL, 464, L153, https://doi.org/10.1086/310102, 1996.

Cassan, A.: An alternative parameterisation for binary-lens caustic-crossing events, A&A, 491, 587–595, https://doi.org/10.1051/0004-6361:200809795, 2008.

Chandler, C. O., McDonald, I., & Kane, S. R.: The Catalog of Earth-Like Exoplanet Survey Targets (CELESTA): A Database of Habitable Zones Around Nearby Stars, AJ, 151, 59, https://doi.org/10.3847/0004-6256/151/3/59, 2016.

Charbonneau, D., Brown, T. M., Latham, D. W., & Mayor, M.: Detection of Planetary Transits Across a Sun-like Star, ApJL, 529, L45–L48, https://doi.org/10.1086/312457, 2000.

Chartas, G., Krawczynski, H., Zalesky, L., Kochanek, C. S., Dai, X., Morgan, C. W., & Mosquera, A.: Measuring the Innermost Stable Circular Orbits of Supermassive Black Holes, ApJ, 837, 26, https://doi.org/10.3847/1538-4357/aa5d50, 2017.

Choudhury, S., Subramaniam, A., & Cole, A. A.: Photometric metallicity map of the Large Magellanic Cloud, MNRAS, 455, 1855–1880, https://doi.org/10.1093/mnras/stv2414, 2016.

Choudhury, S., Subramaniam, A., Cole, A. A., & Sohn, Y. J.: Photometric metallicity map of the Small Magellanic Cloud, MNRAS, 475, 4279–4297, https://doi.org/10.1093/mnras/sty087, 2018.

Chung, S.-J.: Characterization of the Resonant Caustic Perturbation, ApJ, 705, 386–390, https://doi.org/10.1088/0004-637X/705/1/386, 2009.

Claret, A. & Bloemen, S.: Gravity and limb-darkening coefficients for the Kepler, CoRoT, Spitzer, uvby, UBVRIJHK, and Sloan photometric systems, A&A, 529, A75, https://doi.org/10.1051/0004-6361/201116451, 2011.

Correia, A. C. M., Bourrier, V., & Delisle, J. B.: Why do warm Neptunes present nonzero eccentricity?, A&A, 635, A37, https://doi.org/10.1051/0004-6361/201936967, 2020.

Cumming, A., Butler, R. P., Marcy, G. W., Vogt, S. S., Wright, J. T., & Fischer, D. A.: The Keck Planet Search: Detectability and the Minimum Mass and Orbital Period Distribution of Extrasolar Planets, PASP, 120, 531, https://doi.org/10.1086/588487, 2008.

Dai, X. & Guerras, E.: Probing Extragalactic Planets Using Quasar Microlensing, ApJL, 853, L27, https://doi.org/10.3847/2041-8213/aaa5fb, 2018.

Dawson, R. I. & Murray-Clay, R. A.: Giant Planets Orbiting Metal-rich Stars Show Signatures of Planet-Planet Interactions, ApJL, 767, L24, https://doi.org/10.1088/2041-8205/767/2/L24, 2013.

Delfosse, X., Forveille, T., Ségransan, D., Beuzit, J. L., Udry, S., Perrier, C., & Mayor, M.: Accurate masses of very low mass stars. IV. Improved mass-luminosity relations, A&A, 364, 217–224, 2000.

Dominik, M.: The binary gravitational lens and its extreme cases, A&A, 349, 108–125, 1999.

Dominik, M. & Sahu, K. C.: Astrometric Microlensing of Stars, ApJ, 534, 213–226, https://doi.org/10.1086/308716, 2000.

Dominik, M., Jørgensen, U. G., Rattenbury, N. J., Mathiasen, M., Hinse, T. C., Calchi Novati, S., Harpsøe, K., Bozza, V., Anguita, T., Burgdorf, M. J., Horne, K., Hundertmark, M., Kerins, E., Kjærgaard, P., Liebig, C., Mancini, L., Masi, G., Rahvar, S., Ricci, D., Scarpetta, G., Snodgrass, C., Southworth, J., Street, R. A., Surdej, J., Thöne, C. C., Tsapras, Y., Wambsganss, J., & Zub, M.: Realisation of a fully-deterministic microlensing observing strategy for inferring planet populations, Astronomische Nachrichten, 331, 671, https://doi.org/10.1002/asna.201011400, 2010.

Dong, S., Gould, A., Udalski, A., Anderson, J., Christie, G. W., Gaudi, B. S., OGLE Collaboration, Jaroszyński, M., Kubiak, M., Szymański, M. K., Pietrzyński, G., Soszyński, I., Szewczyk, O., Ulaczyk, K., Wyrzykowski, Ł., μFUN Collaboration, DePoy, D. L., Fox, D. B., Gal-Yam,

A., Han, C., Lépine, S., McCormick, J., Ofek, E., Park, B. G., Pogge, R. W., MOA Collaboration, Abe, F., Bennett, D. P., Bond, I. A., Britton, T. R., Gilmore, A. C., Hearnshaw, J. B., Itow, Y., Kamiya, K., Kilmartin, P. M., Korpela, A., Masuda, K., Matsubara, Y., Motomura, M., Muraki, Y., Nakamura, S., Ohnishi, K., Okada, C., Rattenbury, N., Saito, T., Sako, T., Sasaki, M., Sullivan, D., Sumi, T., Tristram, P. J., Yanagisawa, T., Yock, P. C. M., Yoshoika, T., PLANET/RoboNet Collaborations, Albrow, M. D., Beaulieu, J. P., Brillant, S., Calitz, H., Cassan, A., Cook, K. H., Coutures, C., Dieters, S., Dominis Prester, D., Donatowicz, J., Fouqué, P., Greenhill, J., Hill, K., Hoffman, M., Horne, K., Jørgensen, U. G., Kane, S., Kubas, D., Marquette, J. B., Martin, R., Meintjes, P., Menzies, J., Pollard, K. R., Sahu, K. C., Vinter, C., Wambsganss, J., Williams, A., Bode, M., Bramich, D. M., Burgdorf, M., Snodgrass, C., Steele, I., Doublier, V., & Foellmi, C.: OGLE-2005-BLG-071Lb, the Most Massive M Dwarf Planetary Companion?, ApJ, 695, 970–987, https://doi.org/10.1088/0004-637X/695/2/970, 2009.

Doyle, L. R., Carter, J. A., Fabrycky, D. C., Slawson, R. W., Howell, S. B., Winn, J. N., Orosz, J. A., Přsa, A., Welsh, W. F., Quinn, S. N., Latham, D., Torres, G., Buchhave, L. A., Marcy, G. W., Fortney, J. J., Shporer, A., Ford, E. B., Lissauer, J. J., Ragozzine, D., Rucker, M., Batalha, N., Jenkins, J. M., Borucki, W. J., Koch, D., Middour, C. K., Hall, J. R., McCauliff, S., Fanelli, M. N., Quintana, E. V., Holman, M. J., Caldwell, D. A., Still, M., Stefanik, R. P., Brown, W. R., Esquerdo, G. A., Tang, S., Furesz, G., Geary, J. C., Berlind, P., Calkins, M. L., Short, D. R., Steffen, J. H., Sasselov, D., Dunham, E. W., Cochran, W. D., Boss, A., Haas, M. R., Buzasi, D., & Fischer, D.: Kepler-16: A Transiting Circumbinary Planet, Science, 333, 1602, https://doi.org/10.1126/science.1210923, 2011.

Duchêne, G. & Kraus, A.: Stellar Multiplicity, ARA&A, 51, 269–310, https://doi.org/10.1146/annurev-astro-081710-102602, 2013.

Dwek, E., Arendt, R. G., Hauser, M. G., Kelsall, T., Lisse, C. M., Moseley, S. H., Silverberg, R. F., Sodroski, T. J., & Weiland, J. L.: Morphology, Near-Infrared Luminosity, and Mass of the Galactic Bulge from COBE DIRBE Observations, ApJ, 445, 716, https://doi.org/10.1086/175734, 1995.

Eggleton, P. P. & Kiseleva-Eggleton, L.: Orbital Evolution in Binary and Triple Stars, with an Application to SS Lacertae, ApJ, 562, 1012–1030, https://doi.org/10.1086/323843, 2001.

Eggleton, P. P. & Kisseleva-Eggleton, L.: A Mechanism for Producing Short-Period Binaries, Ap&SS, 304, 75–79, https://doi.org/10.1007/s10509-006-9078-z, 2006.

Einstein, A.: Lens-Like Action of a Star by the Deviation of Light in the Gravitational Field, Science, 84, 506–507, https://doi.org/10.1126/science.84.2188.506, 1936.

Fabrycky, D. & Tremaine, S.: Shrinking Binary and Planetary Orbits by Kozai Cycles with Tidal Friction, ApJ, 669, 1298–1315, https://doi.org/10.1086/521702, 2007.

Fischer, D. A. & Valenti, J.: The Planet-Metallicity Correlation, ApJ, 622, 1102–1117, https://doi.org/10.1086/428383, 2005.

Fressin, F., Torres, G., Charbonneau, D., Bryson, S. T., Christiansen, J., Dressing, C. D., Jenkins, J. M., Walkowicz, L. M., & Batalha, N. M.: The False Positive Rate of Kepler and the Occurrence of Planets, ApJ, 766, 81, https://doi.org/10.1088/0004-637X/766/2/81, 2013.

Fukui, A., Gould, A., Sumi, T., Bennett, D. P., Bond, I. A., Han, C., Suzuki, D., Beaulieu, J. P., Batista, V., Udalski, A., Street, R. A., Tsapras, Y., Hundertmark, M., Abe, F., Bhattacharya, A., Freeman, M., Itow, Y., Ling, C. H., Koshimoto, N., Masuda, K., Matsubara, Y., Muraki, Y., Ohnishi, K., Philpott, L. C., Rattenbury, N., Saito, T., Sullivan, D. J., Tristram, P. J., Yonehara, A., MOA Collaboration, Choi, J. Y., Christie, G. W., DePoy, D. L., Dong, S., Drummond, J., Gaudi, B. S., Hwang, K. H., Kavka, A., Lee, C. U., McCormick, J., Natusch, T., Ngan, H., Park, H., Pogge, R. W., Shin, I. G., Tan, T. G., Yee, J. C., μFUN Collaboration, Szymański, M. K., Pietrzyński, G., Soszyński, I., Poleski, R., Kozłowski, S., Pietrukowicz, P., Ulaczyk, K., Wyrzykowski, Ł., OGLE Collaboration, Bramich, D. M., Browne, P., Dominik, M., Horne, K., Ipatov, S., Kains, N., Snodgrass, C., Steele, I. A., & RoboNet Collaboration: OGLE-2012-BLG-0563Lb: A Saturn-mass Planet around an M Dwarf with the Mass Constrained by Subaru AO Imaging, ApJ, 809, 74, https://doi.org/10.1088/0004-637X/809/1/74, 2015.

Fulbright, J. P., McWilliam, A., & Rich, R. M.: Abundances of Baade's Window Giants from Keck HIRES Spectra. I. Stellar Parameters and [Fe/H] Values, ApJ, 636, 821–841, https://doi.org/10.1086/498205, 2006.

Fulton, B. J., Petigura, E. A., Howard, A. W., Isaacson, H., Marcy, G. W., Cargile, P. A., Hebb, L., Weiss, L. M., Johnson, J. A., Morton, T. D., Sinukoff, E., Crossfield, I. J. M., & Hirsch, L. A.: The California-Kepler Survey. III. A Gap in the Radius Distribution of Small Planets, AJ, 154, 109, https://doi.org/10.3847/1538-3881/aa80eb, 2017.

Gaia Collaboration, Clementini, G., Eyer, L., Ripepi, V., Marconi, M., Muraveva, T., Garofalo, A., Sarro, L. M., Palmer, M., Luri, X., Molinaro, R., Rimoldini, L., Szabados, L., Musella, I., Anderson, R. I., Prusti, T., de Bruijne, J. H. J., Brown, A. G. A., Vallenari, A., Babusiaux, C., Bailer-Jones, C. A. L., Bastian, U., Biermann, M., Evans, D. W., Jansen, F., Jordi, C., Klioner, S. A., Lammers, U., Lindegren, L., Mignard, F., Panem, C., Pourbaix, D., Randich, S., Sartoretti, P., Siddiqui, H. I., Soubiran, C., Valette, V., van Leeuwen, F., Walton, N. A., Aerts, C., Arenou, F., Cropper, M., Drimmel, R., Høg, E., Katz, D., Lattanzi, M. G., O'Mullane, W., Grebel, E. K., Holland, A. D., Huc, C., Passot, X., Perryman, M., Bramante, L., Cacciari, C., Castañeda, J., Chaoul, L., Cheek, N., De Angeli, F., Fabricius, C., Guerra, R., Hernández, J., Jean-Antoine-Piccolo, A., Masana, E., Messineo, R., Mowlavi, N., Nienartowicz, K., Ordóñez-Blanco, D., Panuzzo, P., Portell, J., Richards, P. J., Riello, M., Seabroke, G. M., Tanga, P., Thévenin, F., Torra, J., Els, S. G., Gracia-Abril, G., Comoretto, G., Garcia-Reinaldos, M., Lock, T., Mercier, E., Altmann, M., Andrae, R., Astraatmadja, T. L., Bellas-Velidis, I., Benson, K., Berthier, J., Blomme, R., Busso, G., Carry, B., Cellino, A., Cowell, S., Creevey, O., Cuypers, J., Davidson, M., De Ridder, J., de Torres, A., Delchambre, L., Dell'Oro, A., Ducourant, C., Frémat, Y., García-Torres, M., Gosset, E., Halbwachs, J. L., Hambly, N. C., Harrison, D. L., Hauser, M., Hestroffer, D., Hodgkin, S. T., Huckle, H. E., Hutton, A., Jasniewicz, G., Jordan, S., Kontizas, M., Korn, A. J., Lanzafame, A. C., Manteiga, M., Moitinho, A., Muinonen, K., Osinde, J., Pancino, E., Pauwels, T., Petit, J. M., Recio-Blanco, A., Robin, A. C., Siopis, C., Smith, M., Smith, K. W., Sozzetti, A., Thuillot, W., van Reeven, W., Viala, Y., Abbas, U.,

Abreu Aramburu, A., Accart, S., Aguado, J. J., Allan, P. M., Allasia, W., Altavilla, G., Álvarez, M. A., Alves, J., Andrei, A. H., Anglada Varela, E., Antiche, E., Antoja, T., Antón, S., Arcay, B., Bach, N., Baker, S. G., Balaguer-Núñez, L., Barache, C., Barata, C., Barbier, A., Barblan, F., Barrado y Navascués, D., Barros, M., Barstow, M. A., Becciani, U., Bellazzini, M., Bello García, A., Belokurov, V., Bendjoya, P., Berihuete, A., Bianchi, L., Bienaymé, O., Billebaud, F., Blagorodnova, N., Blanco-Cuaresma, S., Boch, T., Bombrun, A., Borrachero, R., Bouquillon, S., Bourda, G., Bragaglia, A., Breddels, M. A., Brouillet, N., Brüsemeister, T., Bucciarelli, B., Burgess, P., Burgon, R., Burlacu, A., Busonero, D., Buzzi, R., Caffau, E., Cambras, J., Campbell, H., Cancelliere, R., Cantat-Gaudin, T., Carlucci, T., Carrasco, J. M., Castellani, M., Charlot, P., Charnas, J., Chiavassa, A., Clotet, M., Cocozza, G., Collins, R. S., Costigan, G., Crifo, F., Cross, N. J. G., Crosta, M., Crowley, C., Dafonte, C., Damerdji, Y., Dapergolas, A., David, P., David, M., De Cat, P., de Felice, F., de Laverny, P., De Luise, F., De March, R., de Souza, R., Debosscher, J., del Pozo, E., Delbo, M., Delgado, A., Delgado, H. E., Di Matteo, P., Diakite, S., Distefano, E., Dolding, C., Dos Anjos, S., Drazinos, P., Durán, J., Dzigan, Y., Edvardsson, B., Enke, H., Evans, N. W., Eynard Bontemps, G., Fabre, C., Fabrizio, M., Falcão, A. J., Farràs Casas, M., Federici, L., Fedorets, G., Fernández-Hernández, J., Fernique, P., Fienga, A., Figueras, F., Filippi, F., Findeisen, K., Fonti, A., Fouesneau, M., Fraile, E., Fraser, M., Fuchs, J., Gai, M., Galleti, S., Galluccio, L., Garabato, D., García-Sedano, F., Garralda, N., Gavras, P., Gerssen, J., Geyer, R., Gilmore, G., Girona, S., Giuffrida, G., Gomes, M., González-Marcos, A., González-Núñez, J., González-Vidal, J. J., Granvik, M., Guerrier, A., Guillout, P., Guiraud, J., Gúrpide, A., Gutiérrez-Sánchez, R., Guy, L. P., Haigron, R., Hatzidimitriou, D., Haywood, M., Heiter, U., Helmi, A., Hobbs, D., Hofmann, W., Holl, B., Holland, G., Hunt, J. A. S., Hypki, A., Icardi, V., Irwin, M., Jevardat de Fombelle, G., Jofré, P., Jonker, P. G., Jorissen, A., Julbe, F., Karampelas, A., Kochoska, A., Kohley, R., Kolenberg, K., Kontizas, E., Koposov, S. E., Kordopatis, G., Koubsky, P., Krone-Martins, A., Kudryashova, M., Bachchan, R. K., Lacoste-Seris, F., Lanza, A. F., Lavigne, J. B., Le Poncin-Lafitte, C., Lebreton, Y., Lebzelter, T., Leccia, S., Leclerc, N., Lecoeur-Taibi, I., Lemaitre, V., Lenhardt, H., Leroux, F., Liao, S., Licata, E., Lindstrøm, H. E. P., Lister, T. A., Livanou, E., Lobel, A., Löffler, W., López, M.,

Lorenz, D., MacDonald, I., Magalhães Fernandes, T., Managau, S., Mann, R. G., Mantelet, G., Marchal, O., Marchant, J. M., Marinoni, S., Marrese, P. M., Marschalkó, G., Marshall, D. J., Martín-Fleitas, J. M., Martino, M., Mary, N., Matijevič, G., McMillan, P. J., Messina, S., Michalik, D., Millar, N. R., Miranda, B. M. H., Molina, D., Molinaro, M., Molnár, L., Moniez, M., Montegriffo, P., Mor, R., Mora, A., Morbidelli, R., Morel, T., Morgenthaler, S., Morris, D., Mulone, A. F., Narbonne, J., Nelemans, G., Nicastro, L., Noval, L., Ordénovic, C., Ordieres-Meré, J., Osborne, P., Pagani, C., Pagano, I., Pailler, F., Palacin, H., Palaversa, L., Parsons, P., Pecoraro, M., Pedrosa, R., Pentikäinen, H., Pichon, B., Piersimoni, A. M., Pineau, F. X., Plachy, E., Plum, G., Poujoulet, E., Prša, A., Pulone, L., Ragaini, S., Rago, S., Rambaux, N., Ramos-Lerate, M., Ranalli, P., Rauw, G., Read, A., Regibo, S., Reylé, C., Ribeiro, R. A., Riva, A., Rixon, G., Roelens, M., Romero-Gómez, M., Rowell, N., Royer, F., Ruiz-Dern, L., Sadowski, G., Sagristà Sellés, T., Sahlmann, J., Salgado, J., Salguero, E., Sarasso, M., Savietto, H., Schultheis, M., Sciacca, E., Segol, M., Segovia, J. C., Segransan, D., Shih, I. C., Smareglia, R., Smart, R. L., Solano, E., Solitro, F., Sordo, R., Soria Nieto, S., Souchay, J., Spagna, A., Spoto, F., Stampa, U., Steele, I. A., Steidelmüller, H., Stephenson, C. A., Stoev, H., Suess, F. F., Süveges, M., Surdej, J., Szegedi-Elek, E., Tapiador, D., Taris, F., Tauran, G., Taylor, M. B., Teixeira, R., Terrett, D., Tingley, B., Trager, S. C., Turon, C., Ulla, A., Utrilla, E., Valentini, G., van Elteren, A., Van Hemelryck, E., van Leeuwen, M., Varadi, M., Vecchiato, A., Veljanoski, J., Via, T., Vicente, D., Vogt, S., Voss, H., Votruba, V., Voutsinas, S., Walmsley, G., Weiler, M., Weingrill, K., Wevers, T., Wyrzykowski, Ł., Yoldas, A., Žerjal, M., Zucker, S., Zurbach, C., Zwitter, T., Alecu, A., Allen, M., Allende Prieto, C., Amorim, A., Anglada-Escudé, G., Arsenijevic, V., Azaz, S., Balm, P., Beck, M., Bernstein, H. H., Bigot, L., Bijaoui, A., Blasco, C., Bonfigli, M., Bono, G., Boudreault, S., Bressan, A., Brown, S., Brunet, P. M., Bunclark, P., Buonanno, R., Butkevich, A. G., Carret, C., Carrion, C., Chemin, L., Chéreau, F., Corcione, L., Darmigny, E., de Boer, K. S., de Teodoro, P., de Zeeuw, P. T., Delle Luche, C., Domingues, C. D., Dubath, P., Fodor, F., Frézouls, B., Fries, A., Fustes, D., Fyfe, D., Gallardo, E., Gallegos, J., Gardiol, D., Gebran, M., Gomboc, A., Gómez, A., Grux, E., Gueguen, A., Heyrovsky, A., Hoar, J., Iannicola, G., Isasi Parache, Y., Janotto, A. M., Joliet, E., Jonckheere, A., Keil, R., Kim,

D. W., Klagyivik, P., Klar, J., Knude, J., Kochukhov, O., Kolka, I., Kos, J., Kutka, A., Lainey, V., LeBouquin, D., Liu, C., Loreggia, D., Makarov, V. V., Marseille, M. G., Martayan, C., Martinez-Rubi, O., Massart, B., Meynadier, F., Mignot, S., Munari, U., Nguyen, A. T., Nordlander, T., O'Flaherty, K. S., Ocvirk, P., Olias Sanz, A., Ortiz, P., Osorio, J., Oszkiewicz, D., Ouzounis, A., Park, P., Pasquato, E., Peltzer, C., Peralta, J., Péturaud, F., Pieniluoma, T., Pigozzi, E., Poels, J., Prat, G., Prod'homme, T., Raison, F., Rebordao, J. M., Risquez, D., Rocca-Volmerange, B., Rosen, S., Ruiz-Fuertes, M. I., Russo, F., Serraller Vizcaino, I., Short, A., Siebert, A., Silva, H., Sinachopoulos, D., Slezak, E., Soffel, M., Sosnowska, D., Straižys, V., ter Linden, M., Terrell, D., Theil, S., Tiede, C., Troisi, L., Tsalmantza, P., Tur, D., Vaccari, M., Vachier, F., Valles, P., Van Hamme, W., Veltz, L., Virtanen, J., Wallut, J. M., Wichmann, R., Wilkinson, M. I., Ziaeepour, H., & Zschocke, S.: Gaia Data Release 1. Testing parallaxes with local Cepheids and RR Lyrae stars, A&A, 605, A79, https://doi.org/10.1051/0004-6361/201629925, 2017.

García Pérez, A. E., Ness, M., Robin, A. C., Martinez-Valpuesta, I., Sobeck, J., Zasowski, G., Majewski, S. R., Bovy, J., Allende Prieto, C., Cunha, K., Girardi, L., Mészáros, S., Nidever, D., Schiavon, R. P., Schultheis, M., Shetrone, M., & Smith, V. V.: The Bulge Metallicity Distribution from the APOGEE Survey, ApJ, 852, 91, https://doi.org/10.3847/1538-4357/aa9d88, 2018.

Gaudi, B. S.: Distinguishing Between Binary-Source and Planetary Microlensing Perturbations, ApJ, 506, 533–539, https://doi.org/10.1086/306256, 1998.

Gaudi, B. S.: Microlensing Surveys for Exoplanets, ARA&A, 50, 411–453, https://doi.org/10.1146/annurev-astro-081811-125518, 2012.

Gaudi, B. S. & Gould, A.: Planet Parameters in Microlensing Events, ApJ, 486, 85–99, https://doi.org/10.1086/304491, 1997.

Gaudi, B. S. & Sackett, P. D.: Detection Efficiencies of Microlensing Data Sets to Stellar and Planetary Companions, ApJ, 528, 56–73, https://doi.org/10.1086/308161, 2000.

Gaudi, B. S., Bennett, D. P., Udalski, A., Gould, A., Christie, G. W., Maoz, D., Dong, S., McCormick, J., Szymański, M. K., Tristram, P. J., Nikolaev, S., Paczyński, B., Kubiak, M.,

Pietrzyński, G., Soszyński, I., Szewczyk, O., Ulaczyk, K., Wyrzykowski, Ł., OGLE Collaboration, DePoy, D. L., Han, C., Kaspi, S., Lee, C. U., Mallia, F., Natusch, T., Pogge, R. W., Park, B. G., μ-Fun Collabortion, Abe, F., Bond, I. A., Botzler, C. S., Fukui, A., Hearnshaw, J. B., Itow, Y., Kamiya, K., Korpela, A. V., Kilmartin, P. M., Lin, W., Masuda, K., Matsubara, Y., Motomura, M., Muraki, Y., Nakamura, S., Okumura, T., Ohnishi, K., Rattenbury, N. J., Sako, T., Saito, T., Sato, S., Skuljan, L., Sullivan, D. J., Sumi, T., Sweatman, W. L., Yock, P. C. M., MOA Collaboration, Albrow, M. D., Allan, A., Beaulieu, J. P., Burgdorf, M. J., Cook, K. H., Coutures, C., Dominik, M., Dieters, S., Fouqué, P., Greenhill, J., Horne, K., Steele, I., Tsapras, Y., Planet Collaboration, RoboNet Collaborations, Chaboyer, B., Crocker, A., Frank, S., & Macintosh, B.: Discovery of a Jupiter/Saturn Analog with Gravitational Microlensing, Science, 319, 927, https://doi.org/10.1126/science.1151947, 2008.

Gizis, J. E., Kirkpatrick, J. D., Burgasser, A., Reid, I. N., Monet, D. G., Liebert, J., & Wilson, J. C.: Substellar Companions to Main-Sequence Stars: No Brown Dwarf Desert at Wide Separations, ApJL, 551, L163–L166, https://doi.org/10.1086/320017, 2001.

Gizis, J. E., Reid, I. N., & Hawley, S. L.: The Palomar/MSU Nearby Star Spectroscopic Survey. III. Chromospheric Activity, M Dwarf Ages, and the Local Star Formation History, AJ, 123, 3356–3369, https://doi.org/10.1086/340465, 2002.

Goldman, B.: The microlensing searches for Galactic dark matter., PhR, 307, 107–115, https://doi.org/10.1016/S0370-1573(98)00072-6, 1998.

Gomes, R., Levison, H. F., Tsiganis, K., & Morbidelli, A.: Origin of the cataclysmic Late Heavy Bombardment period of the terrestrial planets, Nature, 435, 466–469, https://doi.org/10.1038/nature03676, 2005.

Gonzalez, G., Brownlee, D., & Ward, P.: The Galactic Habitable Zone: Galactic Chemical Evolution, Icarus, 152, 185–200, https://doi.org/10.1006/icar.2001.6617, 2001.

González Hernández, J. I. & Bonifacio, P.: A new implementation of the infrared flux method using the 2MASS catalogue, A&A, 497, 497–509, https://doi.org/10.1051/0004-6361/200810904, 2009.

Gott, J. R., I.: Are heavy halos made of low mass stars - A gravitational lens test, ApJ, 243, 140–146, https://doi.org/10.1086/158576, 1981.

Gould, A.: Extending the MACHO Search to approximately 10 6 M sub sun, ApJ, 392, 442, https://doi.org/10.1086/171443, 1992.

Gould, A.: A Natural Formalism for Microlensing, ApJ, 542, 785–788, https://doi.org/10.1086/317037, 2000.

Gould, A.: Resolution of the MACHO-LMC-5 Puzzle: The Jerk-Parallax Microlens Degeneracy, ApJ, 606, 319–325, https://doi.org/10.1086/382782, 2004.

Gould, A. & Loeb, A.: Discovering Planetary Systems through Gravitational Microlenses, ApJ, 396, 104, https://doi.org/10.1086/171700, 1992.

Gould, A. & Yee, J. C.: Microlens Masses from Astrometry and Parallax in Space-based Surveys: From Planets to Black Holes, ApJ, 784, 64, https://doi.org/10.1088/0004-637X/784/1/64, 2014.

Gould, A., Udalski, A., An, D., Bennett, D. P., Zhou, A. Y., Dong, S., Rattenbury, N. J., Gaudi, B. S., Yock, P. C. M., Bond, I. A., Christie, G. W., Horne, K., Anderson, J., Stanek, K. Z., DePoy, D. L., Han, C., McCormick, J., Park, B. G., Pogge, R. W., Poindexter, S. D., Soszyński, I., Szymański, M. K., Kubiak, M., Pietrzyński, G., Szewczyk, O., Wyrzykowski, Ł., Ulaczyk, K., Paczyński, B., Bramich, D. M., Snodgrass, C., Steele, I. A., Burgdorf, M. J., Bode, M. F., Botzler, C. S., Mao, S., & Swaving, S. C.: Microlens OGLE-2005-BLG-169 Implies That Cool Neptune-like Planets Are Common, ApJL, 644, L37–L40, https://doi.org/10.1086/505421, 2006.

Gould, A., Huber, D., Penny, M., & Stello, D.: WFIRST Ultra-Precise Astrometry II: Asteroseismology, Journal of Korean Astronomical Society, 48, 93–104, https://doi.org/10.5303/JKAS.2015.48.2.93, 2015.

Grether, D. & Lineweaver, C. H.: How Dry is the Brown Dwarf Desert? Quantifying the Relative Number of Planets, Brown Dwarfs, and Stellar Companions around Nearby Sun-like Stars, ApJ, 640, 1051–1062, https://doi.org/10.1086/500161, 2006.

Griest, K. & Hu, W.: Effect of Binary Sources on the Search for Massive Astrophysical Compact Halo Objects via Microlensing, ApJ, 397, 362, https://doi.org/10.1086/171793, 1992.

Griest, K. & Safizadeh, N.: The Use of High-Magnification Microlensing Events in Discovering Extrasolar Planets, ApJ, 500, 37–50, https://doi.org/10.1086/305729, 1998.

Grieves, N., Ge, J., Thomas, N., Ma, B., Sithajan, S., Ghezzi, L., Kimock, B., Willis, K., De Lee, N., Lee, B., Fleming, S. W., Agol, E., Troup, N., Paegert, M., Schneider, D. P., Stassun, K., Varosi, F., Zhao, B., Jian, L., Li, R., Porto de Mello, G. F., Bizyaev, D., Pan, K., Dutra-Ferreira, L., Lorenzo-Oliveira, D., Santiago, B. X., da Costa, L. N., Maia, M. A. G., Ogando, R. L. C., & del Peloso, E. F.: Exploring the brown dwarf desert: new substellar companions from the SDSS-III MARVELS survey, MNRAS, 467, 4264–4281, https://doi.org/10.1093/mnras/stx334, 2017.

Guillot, T., Lin, D. N. C., Morel, P., Havel, M., & Parmentier, V.: Evolution of exoplanets and their parent stars, in: EAS Publications Series, vol. 65 of EAS Publications Series, pp. 327–336, https://doi.org/10.1051/eas/1465009, 2014.

Gummersbach, C. A., Kaufer, A., Schaefer, D. R., Szeifert, T., & Wolf, B.: B stars and the chemical evolution of the Galactic disk, A&A, 338, 881–896, 1998.

Han, C.: Analysis of Microlensing Light Curves Induced by Multiple-Planet Systems, ApJ, 629, 1102–1109, https://doi.org/10.1086/431143, 2005.

Han, C. & Gould, A.: The Mass Spectrum of MACHOs from Parallax Measurements, ApJ, 447, 53, https://doi.org/10.1086/175856, 1995.

Han, C. & Gould, A.: Einstein Radii from Binary-Source Lensing Events, ApJ, 480, 196–202, https://doi.org/10.1086/303944, 1997.

Han, C. & Kang, Y. W.: Probing the Spatial Distribution of Extrasolar Planets with Gravitational Microlensing, ApJ, 596, 1320–1326, https://doi.org/10.1086/378191, 2003.

Han, C. & Lee, C.: Properties of planet-induced deviations in the astrometric microlensing centroid shift trajectory, MNRAS, 329, 163–174, https://doi.org/10.1046/j.1365-8711.2002.04976.x, 2002.

Han, C., Gaudi, B. S., An, J. H., & Gould, A.: Microlensing Detection and Characterization of Wide-Separation Planets, ApJ, 618, 962–972, https://doi.org/10.1086/426115, 2005.

Hayashi, C., Nakazawa, K., & Nakagawa, Y.: Formation of the solar system., in: Protostars and Planets II, edited by Black, D. C. & Matthews, M. S., pp. 1100–1153, 1985.

Haywood, M.: A peculiarity of metal-poor stars with planets?, A&A, 482, 673–676, https://doi.org/10.1051/0004-6361:20079141, 2008.

Haywood, M.: On the Correlation Between Metallicity and the Presence of Giant Planets, ApJL, 698, L1–L5, https://doi.org/10.1088/0004-637X/698/1/L1, 2009.

Haywood, M., Di Matteo, P., Lehnert, M. D., Katz, D., & Gómez, A.: The age structure of stellar populations in the solar vicinity. Clues of a two-phase formation history of the Milky Way disk, A&A, 560, A109, https://doi.org/10.1051/0004-6361/201321397, 2013.

Heller, R., Jackson, B., Barnes, R., Greenberg, R., & Homeier, D.: Tidal effects on brown dwarfs: application to the eclipsing binary 2MASS J05352184-0546085. The anomalous temperature reversal in the context of tidal heating, A&A, 514, A22, https://doi.org/10.1051/0004-6361/200912826, 2010.

Henry, T. J. & McCarthy, Donald W., J.: The Mass-Luminosity Relation for Stars of Mass 1.0 to 0.08M(solar), AJ, 106, 773, https://doi.org/10.1086/116685, 1993.

Hirsch, L. A., Rosenthal, L., Fulton, B. J., Howard, A. W., Ciardi, D. R., Marcy, G. W., Nielsen, E., Petigura, E. A., de Rosa, R. J., Isaacson, H., Weiss, L. M., Sinukoff, E., & Macintosh, B.: Understanding the Impacts of Stellar Companions on Planet Formation and Evolution: A Survey of Stellar and Planetary Companions within 25 pc, AJ, 161, 134, https://doi.org/10.3847/1538-3881/abd639, 2021.

Hog, E., Novikov, I. D., & Polnarev, A. G.: MACHO photometry and astrometry., A&A, 294, 287–294, 1995.

Holtzman, J. A., Watson, A. M., Baum, W. A., Grillmair, C. J., Groth, E. J., Light, R. M., Lynds, R., & O'Neil, Earl J., J.: The Luminosity Function and Initial Mass Function in the Galactic Bulge, AJ, 115, 1946–1957, https://doi.org/10.1086/300336, 1998.

Howard, A. W., Marcy, G. W., Bryson, S. T., Jenkins, J. M., Rowe, J. F., Batalha, N. M., Borucki, W. J., Koch, D. G., Dunham, E. W., Gautier, Thomas N., I., Van Cleve, J., Cochran, W. D., Latham, D. W., Lissauer, J. J., Torres, G., Brown, T. M., Gilliland, R. L., Buchhave, L. A., Caldwell, D. A., Christensen-Dalsgaard, J., Ciardi, D., Fressin, F., Haas, M. R., Howell, S. B., Kjeldsen, H., Seager, S., Rogers, L., Sasselov, D. D., Steffen, J. H., Basri, G. S., Charbonneau, D., Christiansen, J., Clarke, B., Dupree, A., Fabrycky, D. C., Fischer, D. A., Ford, E. B., Fortney, J. J., Tarter, J., Girouard, F. R., Holman, M. J., Johnson, J. A., Klaus, T. C., Machalek, P., Moorhead, A. V., Morehead, R. C., Ragozzine, D., Tenenbaum, P., Twicken, J. D., Quinn, S. N., Isaacson, H., Shporer, A., Lucas, P. W., Walkowicz, L. M., Welsh, W. F., Boss, A., Devore, E., Gould, A., Smith, J. C., Morris, R. L., Prsa, A., Morton, T. D., Still, M., Thompson, S. E., Mullally, F., Endl, M., & MacQueen, P. J.: Planet Occurrence within 0.25 AU of Solar-type Stars from Kepler, ApJS, 201, 15, https://doi.org/10.1088/0067-0049/201/2/15, 2012.

Ida, S. & Lin, D. N. C.: Toward a Deterministic Model of Planetary Formation. II. The Formation and Retention of Gas Giant Planets around Stars with a Range of Metallicities, ApJ, 616, 567–572, https://doi.org/10.1086/424830, 2004.

Iwanek, P., Soszyński, I., Skowron, J., Udalski, A., Stępień, K., Kozłowski, S., Mróz, P., Poleski, R., Skowron, D., Szymański, M. K., Pietrukowicz, P., Ulaczyk, K., Wyrzykowski, Ł., Kruszyńska, K., & Rybicki, K.: 12,660 Spotted Stars toward the OGLE Galactic Bulge Fields, ApJ, 879, 114, https://doi.org/10.3847/1538-4357/ab23f6, 2019.

Jung, Y. K., Udalski, A., Yee, J. C., Sumi, T., Gould, A., Han, C., Albrow, M. D., Lee, C. U., Kim, S. L., Chung, S. J., Hwang, K. H., Ryu, Y. H., Shin, I. G., Zhu, W., Cha, S. M., Kim, D. J., Lee, Y., Park, B. G., Pogge, R. W., KMTNet Collaboration, Pietrukowicz, P., Kozłowski, S., Poleski, R., Skowron, J., Mróz, P., Szymański, M. K., Soszyński, I., Pawlak, M., Ulaczyk, K., OGLE Collaboration, Abe, F., Bennett, D. P., Barry, R., Bond, I. A., Asakura, Y., Bhattacharya, A., Donachie, M., Freeman, M., Fukui, A., Hirao, Y., Itow, Y., Koshimoto, N., Li, M. C. A., Ling, C. H., Masuda, K., Matsubara, Y., Muraki, Y., Nagakane, M., Oyokawa, H., Rattenbury, N. J., Sharan, A., Sullivan, D. J., Suzuki, D., Tristram, P. J., Yamada, T., Yamada, T., Yonehara, A., & MOA Collaboration: Binary Source Microlensing Event OGLE-2016-BLG-0733: Interpretation of a Long-term Asymmetric Perturbation, AJ, 153, 129, https://doi.org/10.3847/1538-3881/aa5d07, 2017.

Kennedy, G. M., Kenyon, S. J., & Bromley, B. C.: Planet Formation around Low-Mass Stars: The Moving Snow Line and Super-Earths, ApJL, 650, L139–L142, https://doi.org/10.1086/508882, 2006.

Kiefer, F., Hébrard, G., Sahlmann, J., Sousa, S. G., Forveille, T., Santos, N., Mayor, M., Deleuil, M., Wilson, P. A., Dalal, S., Díaz, R. F., Henry, G. W., Hagelberg, J., Hobson, M. J., Demangeon, O., Bourrier, V., Delfosse, X., Arnold, L., Astudillo-Defru, N., Beuzit, J. L., Boisse, I., Bonfils, X., Borgniet, S., Bouchy, F., Courcol, B., Ehrenreich, D., Hara, N., Lagrange, A. M., Lovis, C., Montagnier, G., Moutou, C., Pepe, F., Perrier, C., Rey, J., Santerne, A., Ségransan, D., Udry, S., & Vidal-Madjar, A.: Detection and characterisation of 54 massive companions with the SOPHIE

spectrograph. Seven new brown dwarfs and constraints on the brown dwarf desert, A&A, 631, A125, https://doi.org/10.1051/0004-6361/201935113, 2019.

Kiefer, F., Hébrard, G., Lecavelier des Etangs, A., Martioli, E., Dalal, S., & Vidal-Madjar, A.: Determining the true mass of radial-velocity exoplanets with Gaia. Nine planet candidates in the brown dwarf or stellar regime and 27 confirmed planets, A&A, 645, A7, https://doi.org/10.1051/0004-6361/202039168, 2021.

Kim, D. J., Kim, H. W., Hwang, K. H., Albrow, M. D., Chung, S. J., Gould, A., Han, C., Jung, Y. K., Ryu, Y. H., Shin, I. G., Yee, J. C., Zhu, W., Cha, S. M., Kim, S. L., Lee, C. U., Lee, D. J., Lee, Y., Park, B. G., Pogge, R. W., & KMTNet Collaboration: Korea Microlensing Telescope Network Microlensing Events from 2015: Event-finding Algorithm, Vetting, and Photometry, AJ, 155, 76, https://doi.org/10.3847/1538-3881/aaa47b, 2018.

Kim, S.-L., Lee, C.-U., Park, B.-G., Kim, D.-J., Cha, S.-M., Lee, Y., Han, C., Chun, M.-Y., & Yuk, I.: KMTNET: A Network of 1.6 m Wide-Field Optical Telescopes Installed at Three Southern Observatories, Journal of Korean Astronomical Society, 49, 37–44, https://doi.org/10.5303/JKAS.2016.49.1.37, 2016.

Kiseleva, L. G., Eggleton, P. P., & Mikkola, S.: Tidal friction in triple stars, MNRAS, 300, 292–302, https://doi.org/10.1046/j.1365-8711.1998.01903.x, 1998.

Klagyivik, P. & Szabados, L.: Observational studies of Cepheid amplitudes. I. Period-amplitude relationships for Galactic Cepheids and interrelation of amplitudes, A&A, 504, 959–972, https://doi.org/10.1051/0004-6361/200811464, 2009.

Kopparapu, R. K.: A Revised Estimate of the Occurrence Rate of Terrestrial Planets in the Habitable Zones around Kepler M-dwarfs, ApJL, 767, L8, https://doi.org/10.1088/2041-8205/767/1/L8, 2013.

Kopparapu, R. K., Ramirez, R., Kasting, J. F., Eymet, V., Robinson, T. D., Mahadevan, S., Terrien, R. C., Domagal-Goldman, S., Meadows, V., & Deshpande, R.: Habitable Zones around Main-

sequence Stars: New Estimates, ApJ, 765, 131, https://doi.org/10.1088/0004-637X/765/2/131, 2013.

Kopparapu, R. K., Ramirez, R. M., SchottelKotte, J., Kasting, J. F., Domagal-Goldman, S., & Eymet, V.: Habitable Zones around Main-sequence Stars: Dependence on Planetary Mass, ApJL, 787, L29, https://doi.org/10.1088/2041-8205/787/2/L29, 2014.

Koshimoto, N., Bennett, D. P., Suzuki, D., & Bond, I. A.: No Large Dependence of Planet Frequency on Galactocentric Distance, ApJL, 918, L8, https://doi.org/10.3847/2041-8213/ac17ec, 2021.

Kotani, T., Tamura, M., Suto, H., Nishikawa, J., Sato, B., Aoki, W., Usuda, T., Kurokawa, T., Kashiwagi, K., Nishiyama, S., Ikeda, Y., Hall, D. B., Hodapp, K. W., Hashimoto, J., Morino, J.-I., Okuyama, Y., Tanaka, Y., Suzuki, S., Inoue, S., Kwon, J., Suenaga, T., Oh, D., Baba, H., Narita, N., Kokubo, E., Hayano, Y., Izumiura, H., Kambe, E., Kudo, T., Kusakabe, N., Ikoma, M., Hori, Y., Omiya, M., Genda, H., Fukui, A., Fujii, Y., Guyon, O., Harakawa, H., Hayashi, M., Hidai, M., Hirano, T., Kuzuhara, M., Machida, M., Matsuo, T., Nagata, T., Onuki, H., Ogihara, M., Takami, H., Takato, N., Takahashi, Y. H., Tachinami, C., Terada, H., Kawahara, H., & Yamamuro, T.: Infrared Doppler instrument (IRD) for the Subaru telescope to search for Earth-like planets around nearby M-dwarfs, in: Ground-based and Airborne Instrumentation for Astronomy V, edited by Ramsay, S. K., McLean, I. S., & Takami, H., vol. 9147 of Society of Photo-Optical Instrumentation Engineers (SPIE) Conference Series, p. 914714, https://doi.org/10.1117/12.2055075, 2014.

Kroupa, P. & Tout, C. A.: The theoretical mass-magnitude relation of low mass stars and its metallicity dependence, MNRAS, 287, 402–414, https://doi.org/10.1093/mnras/287.2.402, 1997.

Kumar, S. S.: The Structure of Stars of Very Low Mass., ApJ, 137, 1121, https://doi.org/10.1086/147589, 1963.

Lada, C. J.: Stellar Multiplicity and the Initial Mass Function: Most Stars Are Single, ApJL, 640, L63–L66, https://doi.org/10.1086/503158, 2006.

Lam, C. Y., Lu, J. R., Udalski, A., Bond, I., Bennett, D. P., Skowron, J., Mróz, P., Poleski, R., Sumi, T., Szymański, M. K., Kozłowski, S., Pietrukowicz, P., Soszyński, I., Ulaczyk, K., Wyrzykowski, Ł., Miyazaki, S., Suzuki, D., Koshimoto, N., Rattenbury, N. J., Hosek, M. W., Abe, F., Barry, R., Bhattacharya, A., Fukui, A., Fujii, H., Hirao, Y., Itow, Y., Kirikawa, R., Kondo, I., Matsubara, Y., Matsumoto, S., Muraki, Y., Olmschenk, G., Ranc, C., Okamura, A., Satoh, Y., Silva, S. I., Toda, T., Tristram, P. J., Vandorou, A., Yama, H., Abrams, N. S., Agarwal, S., Rose, S., & Terry, S. K.: An Isolated Mass-gap Black Hole or Neutron Star Detected with Astrometric Microlensing, ApJL, 933, L23, https://doi.org/10.3847/2041-8213/ac7442, 2022.

Laughlin, G., Bodenheimer, P., & Adams, F. C.: The Core Accretion Model Predicts Few Jovian-Mass Planets Orbiting Red Dwarfs, ApJL, 612, L73–L76, https://doi.org/10.1086/424384, 2004.

Liebes, S.: Gravitational Lenses, Physical Review, 133, 835–844, https://doi.org/10.1103/PhysRev.133.B835, 1964.

Lineweaver, C. H., Fenner, Y., & Gibson, B. K.: The Galactic Habitable Zone and the Age Distribution of Complex Life in the Milky Way, Science, 303, 59–62, https://doi.org/10.1126/science.1092322, 2004.

Ma, B. & Ge, J.: Statistical properties of brown dwarf companions: implications for different formation mechanisms, MNRAS, 439, 2781–2789, https://doi.org/10.1093/mnras/stu134, 2014.

Mao, S. & Paczynski, B.: Gravitational Microlensing by Double Stars and Planetary Systems, ApJL, 374, L37, https://doi.org/10.1086/186066, 1991.

Marcy, G. W. & Butler, R. P.: Planets Orbiting Other Suns, PASP, 112, 137–140, https://doi.org/10.1086/316516, 2000.

Mathieu, R. D.: Pre-Main-Sequence Binary Stars, ARA&A, 32, 465–530, https://doi.org/10.1146/annurev.aa.32.090194.002341, 1994.

Matsumura, S., Ida, S., & Nagasawa, M.: Effects of Dynamical Evolution of Giant Planets on Survival of Terrestrial Planets, ApJ, 767, 129, https://doi.org/10.1088/0004-637X/767/2/129, 2013.

Matzner, C. D. & Levin, Y.: Protostellar Disks: Formation, Fragmentation, and the Brown Dwarf Desert, ApJ, 628, 817–831, https://doi.org/10.1086/430813, 2005.

Mayor, M. & Queloz, D.: A Jupiter-mass companion to a solar-type star, Nature, 378, 355–359, https://doi.org/10.1038/378355a0, 1995.

Mayor, M., Pepe, F., Queloz, D., Bouchy, F., Rupprecht, G., Lo Curto, G., Avila, G., Benz, W., Bertaux, J. L., Bonfils, X., Dall, T., Dekker, H., Delabre, B., Eckert, W., Fleury, M., Gilliotte, A., Gojak, D., Guzman, J. C., Kohler, D., Lizon, J. L., Longinotti, A., Lovis, C., Megevand, D., Pasquini, L., Reyes, J., Sivan, J. P., Sosnowska, D., Soto, R., Udry, S., van Kesteren, A., Weber, L., & Weilenmann, U.: Setting New Standards with HARPS, The Messenger, 114, 20–24, 2003.

Meibom, S. & Mathieu, R. D.: A Robust Measure of Tidal Circularization in Coeval Binary Populations: the Solar-Type Spectroscopic Binary Population in the Open Cluster M35, in: Tidal Evolution and Oscillations in Binary Stars, edited by Claret, A., Giménez, A., & Zahn, J. P., vol. 333 of Astronomical Society of the Pacific Conference Series, p. 95, 2005.

Melo, C. H. F.: The short period multiplicity among T Tauri stars, A&A, 410, 269–282, https://doi.org/10.1051/0004-6361:20031242, 2003.

Miyamoto, M. & Yoshii, Y.: Astrometry for Determining the MACHO Mass and Trajectory, AJ, 110, 1427, https://doi.org/10.1086/117616, 1995.

Miyazaki, S., Sumi, T., Bennett, D. P., Udalski, A., Shvartzvald, Y., Street, R., Bozza, V., Yee, J. C., Bond, I. A., Rattenbury, N., Koshimoto, N., Suzuki, D., Fukui, A., Abe, F., Bhattacharya, A., Barry, R., Donachie, M., Fujii, H., Hirao, Y., Itow, Y., Kamei, Y., Kondo, I., Li, M. C. A., Ling, C. H., Matsubara, Y., Matsuo, T., Muraki, Y., Nagakane, M., Ohnishi, K., Ranc, C., Saito, T., Sharan, A., Shibai, H., Suematsu, H., Sullivan, D. J., Tristram, P. J., Yamakawa, T., Yonehara, A., MOA Collaboration, Skowron, J., Poleski, R., Mróz, P., Szymański, M. K., Soszyński,

I., Pietrukowicz, P., KozŁowski, S., Ulaczyk, K., Wyrzykowski, Ł., OGLE Collaboration, Friedmann, M., Kaspi, S., Maoz, D., Wise Team, Albrow, M., Christie, G., DePoy, D. L., Gal-Yam, A., Gould, A., Lee, C. U., Manulis, I., McCormick, J., Natusch, T., Ngan, H., Pogge, R. W., Porritt, I., μFUN Collaboration, Tsapras, Y., Bachelet, E., Hundertmark, M. P. G., Dominik, M., Bramich, D. M., Cassan, A., Jaimes, R. F., Horne, K., Schmidt, R., Snodgrass, C., Wambsganss, J., Steele, I. A., Menzies, J., Mao, S., RoboNet Collabofratino, Jørgensen, U. G., Burgdorf, M. J., Ciceri, S., Novati, S. C., D'Ago, G., Evans, D. F., Hinse, T. C., Kains, N., Kerins, E., Korhonen, H., Mancini, L., Popovas, A., Rabus, M., Rahvar, S., Scarpetta, G., Skottfelt, J., Southworth, J., D'Ago, G., Peixinho, N., Verma, P., & MiNDSTEp Collaboration: OGLE-2013-BLG-0911Lb: A Secondary on the Brown-dwarf Planet Boundary around an M Dwarf, AJ, 159, 76, https://doi.org/10.3847/1538-3881/ab64de, 2020.

Miyazaki, S., Johnson, S. A., Sumi, T., Penny, M. T., Koshimoto, N., & Yamawaki, T.: Revealing Short-period Exoplanets and Brown Dwarfs in the Galactic Bulge Using the Microlensing Xallarap Effect with the Nancy Grace Roman Space Telescope, AJ, 161, 84, https://doi.org/10.3847/1538-3881/abcec2, 2021.

Moe, M. & Kratter, K. M.: Dynamical Formation of Close Binaries during the Pre-main-sequence Phase, ApJ, 854, 44, https://doi.org/10.3847/1538-4357/aaa6d2, 2018.

Moe, M., Kratter, K. M., & Badenes, C.: The Close Binary Fraction of Solar-type Stars Is Strongly Anticorrelated with Metallicity, ApJ, 875, 61, https://doi.org/10.3847/1538-4357/ab0d88, 2019.

Morbidelli, A., Levison, H. F., Tsiganis, K., & Gomes, R.: Chaotic capture of Jupiter's Trojan asteroids in the early Solar System, Nature, 435, 462–465, https://doi.org/10.1038/nature03540, 2005.

Morgan, C. W., Kochanek, C. S., Dai, X., Morgan, N. D., & Falco, E. E.: X-Ray and Optical Microlensing in the Lensed Quasar PG 1115+080, ApJ, 689, 755–761, https://doi.org/10.1086/592767, 2008.

Mróz, P., Udalski, A., Skowron, J., Poleski, R., Kozłowski, S., Szymański, M. K., Soszyński, I., Wyrzykowski, Ł., Pietrukowicz, P., Ulaczyk, K., Skowron, D., & Pawlak, M.: No large population of unbound or wide-orbit Jupiter-mass planets, Nature, 548, 183–186, https://doi.org/10.1038/nature23276, 2017.

Mróz, P., Udalski, A., Skowron, J., Szymański, M. K., Soszyński, I., Wyrzykowski, Ł., Pietrukowicz, P., Kozłowski, S., Poleski, R., Ulaczyk, K., Rybicki, K., & Iwanek, P.: Microlensing Optical Depth and Event Rate toward the Galactic Bulge from 8 yr of OGLE-IV Observations, ApJS, 244, 29, https://doi.org/10.3847/1538-4365/ab426b, 2019.

Mróz, P., Udalski, A., & Gould, A.: Systematic Errors as a Source of Mass Discrepancy in Black Hole Microlensing Event OGLE-2011-BLG-0462, ApJL, 937, L24, https://doi.org/10.3847/2041-8213/ac90bb, 2022.

Muirhead, P. S., Vanderburg, A., Shporer, A., Becker, J., Swift, J. J., Lloyd, J. P., Fuller, J., Zhao, M., Hinkley, S., Pineda, J. S., Bottom, M., Howard, A. W., von Braun, K., Boyajian, T. S., Law, N., Baranec, C., Riddle, R., Ramaprakash, A. N., Tendulkar, S. P., Bui, K., Burse, M., Chordia, P., Das, H., Dekany, R., Punnadi, S., & Johnson, J. A.: Characterizing the Cool KOIs. V. KOI-256: A Mutually Eclipsing Post-common Envelope Binary, ApJ, 767, 111, https://doi.org/10.1088/0004-637X/767/2/111, 2013.

Muraki, Y., Sumi, T., Abe, F., Bond, I., Carter, B., Dodd, R., Fujimoto, M., Hearnshaw, J., Honda, M., Jugaku, J., Kabe, S., Kato, Y., Kobayashi, M., Koribalski, B., Kilmartin, P., Masuda, K., Matsubara, Y., Nakamura, T., Noda, S., Pennycook, G., Rattenbury, N., Reid, M., Saito, T., Sato, H., Sato, S., Sekiguchi, M., Sullivan, D., Takeuti, M., Watase, Y., Yanagisawa, T., Yock, P., & Yoshizawa, M.: Search for Machos by the MOA Collaboration, Progress of Theoretical Physics Supplement, 133, 233–246, https://doi.org/10.1143/PTPS.133.233, 1999.

Nakajima, T., Oppenheimer, B. R., Kulkarni, S. R., Golimowski, D. A., Matthews, K., & Durrance, S. T.: Discovery of a cool brown dwarf, Nature, 378, 463–465, https://doi.org/10.1038/378463a0, 1995.

Nataf, D. M., Gould, A., Fouqué, P., Gonzalez, O. A., Johnson, J. A., Skowron, J., Udalski, A., Szymański, M. K., Kubiak, M., Pietrzyński, G., Soszyński, I., Ulaczyk, K., Wyrzykowski, Ł., & Poleski, R.: Reddening and Extinction toward the Galactic Bulge from OGLE-III: The Inner Milky Way's R_V ~2.5 Extinction Curve, ApJ, 769, 88, https://doi.org/10.1088/0004-637X/769/2/88, 2013a.

Nataf, D. M., Gould, A. P., Pinsonneault, M. H., & Udalski, A.: Red Giant Branch Bump Brightness and Number Counts in 72 Galactic Globular Clusters Observed with the Hubble Space Telescope, ApJ, 766, 77, https://doi.org/10.1088/0004-637X/766/2/77, 2013b.

Neuhäuser, R. & Guenther, E. W.: Infrared spectroscopy of a brown dwarf companion candidate near the young star GSC 08047-00232 in Horologium, A&A, 420, 647–653, https://doi.org/10.1051/0004-6361:20035713, 2004.

Ngeow, C.-C., Bhardwaj, A., Henderson, J.-Y., Graham, M. J., Laher, R. R., Medford, M. S., Purdum, J., & Rusholme, B.: Zwicky Transient Facility and Globular Clusters: The Period-Luminosity and Period-Wesenheit Relations for Type II Cepheids, AJ, 164, 154, https://doi.org/10.3847/1538-3881/ac87a4, 2022.

Nishiyama, S., Nagata, T., Tamura, M., Kandori, R., Hatano, H., Sato, S., & Sugitani, K.: The Interstellar Extinction Law toward the Galactic Center. II. V, J, H, and K_s Bands, ApJ, 680, 1174–1179, https://doi.org/10.1086/587791, 2008.

Nucita, A. A., de Paolis, F., Ingrosso, G., Giordano, M., & Manni, L.: Astrometric microlensing, International Journal of Modern Physics D, 26, 1741015, https://doi.org/10.1142/S0218271817410152, 2017.

Oppenheimer, B. R., Kulkarni, S. R., Matthews, K., & Nakajima, T.: Infrared Spectrum of the Cool Brown Dwarf Gl 229B, Science, 270, 1478–1479, https://doi.org/10.1126/science.270.5241.1478, 1995.

Paczynski, B.: Gravitational Microlensing at Large Optical Depth, ApJ, 301, 503, https://doi.org/10.1086/163919, 1986a.

Paczynski, B.: Gravitational Microlensing by the Galactic Halo, ApJ, 304, 1, https://doi.org/10.1086/164140, 1986b.

Paczynski, B.: Gravitational Microlensing of the Galactic Bulge Stars, ApJL, 371, L63, https://doi.org/10.1086/186003, 1991.

Paczynski, B.: Binary Source Parallactic Effect in Gravitational Micro-lensing, arXiv e-prints, astro-ph/9711007, 1997.

Park, H., Udalski, A., Han, C., Gould, A., Beaulieu, J. P., Tsapras, Y., Szymański, M. K., Kubiak, M., Soszyński, I., Pietrzyński, G., Poleski, R., Ulaczyk, K., Pietrukowicz, P., Kozłowski, S., Skowron, J., Wyrzykowski, Ł., OGLE Collaboration, Choi, J. Y., Depoy, D. L., Dong, S., Gaudi, B. S., Hwang, K. H., Jung, Y. K., Kavka, A., Lee, C. U., Monard, L. A. G., Park, B. G., Pogge, R. W., Porritt, I., Shin, I. G., Yee, J. C., μFUN Collaboration, Albrow, M. D., Bennett, D. P., Caldwell, J. A. R., Cassan, A., Coutures, C., Dominis, D., Donatowicz, J., Fouqué, P., Greenhill, J., Huber, M., Jørgensen, U. G., Kane, S., Kubas, D., Marquette, J. B., Menzies, J., Pitrou, C., Pollard, K. R., Sahu, K. C., Wambsganss, J., Williams, A., Zub, M., PLANET Collaboration, Allan, A., Bramich, D. M., Browne, P., Dominik, M., Horne, K., Hundertmark, M., Kains, N., Snodgrass, C., Steele, I. A., Street, R. A., & RoboNet Collaboration: Gravitational Binary-lens Events with Prominent Effects of Lens Orbital Motion, ApJ, 778, 134, https://doi.org/10.1088/0004-637X/778/2/134, 2013.

Peale, S. J.: Expectations from a Microlensing Search for Planets, Icarus, 127, 269–289, https://doi.org/10.1006/icar.1997.5711, 1997.

Pejcha, O. & Heyrovský, D.: Extended-Source Effect and Chromaticity in Two-Point-Mass Microlensing, ApJ, 690, 1772–1796, https://doi.org/10.1088/0004-637X/690/2/1772, 2009.

Penny, M. T., Gaudi, B. S., Kerins, E., Rattenbury, N. J., Mao, S., Robin, A. C., & Calchi Novati, S.: Predictions of the WFIRST Microlensing Survey. I. Bound Planet Detection Rates, ApJS, 241, 3, https://doi.org/10.3847/1538-4365/aafb69, 2019.

Perryman, M.: The Exoplanet Handbook, Cambridge University Press, 2018.

Petigura, E. A., Howard, A. W., & Marcy, G. W.: Prevalence of Earth-size planets orbiting Sun-like stars, Proceedings of the National Academy of Science, 110, 19 273–19 278, https://doi.org/10.1073/pnas.1319909110, 2013.

Petigura, E. A., Marcy, G. W., Winn, J. N., Weiss, L. M., Fulton, B. J., Howard, A. W., Sinukoff, E., Isaacson, H., Morton, T. D., & Johnson, J. A.: The California-Kepler Survey. IV. Metal-rich Stars Host a Greater Diversity of Planets, AJ, 155, 89, https://doi.org/10.3847/1538-3881/aaa54c, 2018.

Poindexter, S., Afonso, C., Bennett, D. P., Glicenstein, J.-F., Gould, A., Szymański, M. K., & Udalski, A.: Systematic Analysis of 22 Microlensing Parallax Candidates, ApJ, 633, 914–930, https://doi.org/10.1086/468182, 2005.

Pollack, J. B., Hubickyj, O., Bodenheimer, P., Lissauer, J. J., Podolak, M., & Greenzweig, Y.: Formation of the Giant Planets by Concurrent Accretion of Solids and Gas, Icarus, 124, 62–85, https://doi.org/10.1006/icar.1996.0190, 1996.

Pooley, D., Blackburne, J. A., Rappaport, S., & Schechter, P. L.: X-Ray and Optical Flux Ratio Anomalies in Quadruply Lensed Quasars. I. Zooming in on Quasar Emission Regions, ApJ, 661, 19–29, https://doi.org/10.1086/512115, 2007.

Rahvar, S. & Dominik, M.: Planetary microlensing signals from the orbital motion of the source star around the common barycentre, MNRAS, 392, 1193–1204, https://doi.org/10.1111/j.1365-2966.2008.14120.x, 2009.

Ranc, C., Bennett, D. P., Hirao, Y., Udalski, A., Han, C., Bond, I. A., Yee, J. C., and, Albrow, M. D., Chung, S.-J., Gould, A., Hwang, K.-H., Jung, Y.-K., Ryu, Y.-H., Shin, I.-G., Shvartzvald, Y., Zang, W., Zhu, W., Cha, S.-M., Kim, D.-J., Kim, H.-W., Kim, S.-L., Lee, C.-U., Lee, D.-J., Lee, Y.-S., Park, B.-G., Pogge, R. W., KMTNet Collaboration, Abe, F., Barry, R. K., Bhattacharya, A., Donachie, M., Fukui, A., Itow, Y., Kawasaki, K., Kondo, I., Koshimoto,

N., Li, M. C. A., Matsubara, Y., Miyazaki, S., Muraki, Y., Nagakane, M., Rattenbury, N. J., Suematsu, H., Sullivan, D. J., Sumi, T., Suzuki, D., Tristram, P. J., Yonehara, A., MOA Collaboration, Poleski, R., Mróz, P., Skowron, J., Szymański, M. K., Soszyński, I., Kozłowski, S., Pietrukowicz, P., Ulaczyk, K., & OGLE Collaboration: OGLE-2015-BLG-1670Lb: A Cold Neptune beyond the Snow Line in the Provisional WFIRST Microlensing Survey Field, AJ, 157, 232, https://doi.org/10.3847/1538-3881/ab141b, 2019.

Rattenbury, N. J., Bond, I. A., Skuljan, J., & Yock, P. C. M.: Planetary microlensing at high magnification, MNRAS, 335, 159–169, https://doi.org/10.1046/j.1365-8711.2002.05607.x, 2002.

Refsdal, S.: The gravitational lens effect, MNRAS, 128, 295, https://doi.org/10.1093/mnras/128.4.295, 1964.

Rhie, S. H., Becker, A. C., Bennett, D. P., Fragile, P. C., Johnson, B. R., King, L. J., Peterson, B. A., & Quinn, J.: Observations of the Binary Microlens Event MACHO 98-SMC-1 by the Microlensing Planet Search Collaboration, ApJ, 522, 1037–1045, https://doi.org/10.1086/307697, 1999.

Ricker, G. R., Winn, J. N., Vanderspek, R., Latham, D. W., Bakos, G. Á., Bean, J. L., Berta-Thompson, Z. K., Brown, T. M., Buchhave, L., Butler, N. R., Butler, R. P., Chaplin, W. J., Charbonneau, D., Christensen-Dalsgaard, J., Clampin, M., Deming, D., Doty, J., De Lee, N., Dressing, C., Dunham, E. W., Endl, M., Fressin, F., Ge, J., Henning, T., Holman, M. J., Howard, A. W., Ida, S., Jenkins, J. M., Jernigan, G., Johnson, J. A., Kaltenegger, L., Kawai, N., Kjeldsen, H., Laughlin, G., Levine, A. M., Lin, D., Lissauer, J. J., MacQueen, P., Marcy, G., McCullough, P. R., Morton, T. D., Narita, N., Paegert, M., Palle, E., Pepe, F., Pepper, J., Quirrenbach, A., Rinehart, S. A., Sasselov, D., Sato, B., Seager, S., Sozzetti, A., Stassun, K. G., Sullivan, P., Szentgyorgyi, A., Torres, G., Udry, S., & Villasenor, J.: Transiting Exoplanet Survey Satellite (TESS), Journal of Astronomical Telescopes, Instruments, and Systems, 1, 014003, https://doi.org/10.1117/1.JATIS.1.1.014003, 2015.

Rota, P., Hirao, Y., Bozza, V., Abe, F., Barry, R., Bennett, D. P., Bhattacharya, A., Bond, I. A., Donachie, M., Fukui, A., Fujii, H., Silva, S. I., Itow, Y., Kirikawa, R., Koshimoto, N., Li, M. C. A., Matsubara, Y., Miyazaki, S., Muraki, Y., Olmschenk, G., Ranc, C., Satoh, Y., Sumi, T., Suzuki, D., Tristram, P. J., & Yonehara, A.: MOA-2006-BLG-074: Recognizing Xallarap Contaminants in Planetary Microlensing, AJ, 162, 59, https://doi.org/10.3847/1538-3881/ac0155, 2021.

Ryan, S. G. & Norris, J. E.: Subdwarf Studies. III. The Halo Metallicity Distribution, AJ, 101, 1865–1878, https://doi.org/10.1086/115812, 1991.

Ryu, Y.-H., Kil Jung, Y., Yang, H., Gould, A., Albrow, M. D., Chung, S.-J., Han, C., Hwang, K.-H., Shin, I.-G., Shvartzvald, Y., Yee, J. C., Zang, W., Cha, S.-M., Kim, D.-J., Kim, S.-L., Lee, C.-U., Lee, D.-J., Lee, Y., Park, B.-G., & Pogge, R. W.: Mass Production of 2021 KMTNet Microlensing Planets. I, AJ, 164, 180, https://doi.org/10.3847/1538-3881/ac8d6c, 2022.

Safronov, V. S.: Evolution of the protoplanetary cloud and formation of the earth and planets., Keter Publishing House, 1972.

Sahlmann, J., Ségransan, D., Queloz, D., Udry, S., Santos, N. C., Marmier, M., Mayor, M., Naef, D., Pepe, F., & Zucker, S.: Search for brown-dwarf companions of stars, A&A, 525, A95, https://doi.org/10.1051/0004-6361/201015427, 2011.

Sahu, K. C., Anderson, J., Casertano, S., Bond, H. E., Udalski, A., Dominik, M., Calamida, A., Bellini, A., Brown, T. M., Rejkuba, M., Bajaj, V., Kains, N., Ferguson, H. C., Fryer, C. L., Yock, P., Mróz, P., Kozłowski, S., Pietrukowicz, P., Poleski, R., Skowron, J., Soszyński, I., Szymański, M. K., Ulaczyk, K., Wyrzykowski, Ł., Barry, R. K., Bennett, D. P., Bond, I. A., Hirao, Y., Silva, S. I., Kondo, I., Koshimoto, N., Ranc, C., Rattenbury, N. J., Sumi, T., Suzuki, D., Tristram, P. J., Vandorou, A., Beaulieu, J.-P., Marquette, J.-B., Cole, A., Fouqué, P., Hill, K., Dieters, S., Coutures, C., Dominis-Prester, D., Bennett, C., Bachelet, E., Menzies, J., Albrow, M., Pollard, K., Gould, A., Yee, J. C., Allen, W., Almeida, L. A., Christie, G., Drummond, J., Gal-Yam, A., Gorbikov, E., Jablonski, F., Lee, C.-U., Maoz, D., Manulis, I., McCormick, J., Natusch, T., Pogge,

R. W., Shvartzvald, Y., Jørgensen, U. G., Alsubai, K. A., Andersen, M. I., Bozza, V., Novati, S. C., Burgdorf, M., Hinse, T. C., Hundertmark, M., Husser, T.-O., Kerins, E., Longa-Peña, P., Mancini, L., Penny, M., Rahvar, S., Ricci, D., Sajadian, S., Skottfelt, J., Snodgrass, C., Southworth, J., Tregloan-Reed, J., Wambsganss, J., Wertz, O., Tsapras, Y., Street, R. A., Bramich, D. M., Horne, K., Steele, I. A., & RoboNet Collaboration: An Isolated Stellar-mass Black Hole Detected through Astrometric Microlensing, ApJ, 933, 83, https://doi.org/10.3847/1538-4357/ac739e, 2022.

Sajadian, S.: Sensitivity to habitable planets in the Roman microlensing survey, MNRAS, 508, 5991–6000, https://doi.org/10.1093/mnras/stab2942, 2021.

Sako, T., Sekiguchi, T., Sasaki, M., Okajima, K., Abe, F., Bond, I. A., Hearnshaw, J. B., Itow, Y., Kamiya, K., Kilmartin, P. M., Masuda, K., Matsubara, Y., Muraki, Y., Rattenbury, N. J., Sullivan, D. J., Sumi, T., Tristram, P., Yanagisawa, T., & Yock, P. C. M.: MOA-cam3: a wide-field mosaic CCD camera for a gravitational microlensing survey in New Zealand, Experimental Astronomy, 22, 51–66, https://doi.org/10.1007/s10686-007-9082-5, 2008.

Santerne, A., Díaz, R. F., Moutou, C., Bouchy, F., Hébrard, G., Almenara, J. M., Bonomo, A. S., Deleuil, M., & Santos, N. C.: SOPHIE velocimetry of Kepler transit candidates. VII. A false-positive rate of 35% for Kepler close-in giant candidates, A&A, 545, A76, https://doi.org/10.1051/0004-6361/201219608, 2012.

Santerne, A., Moutou, C., Tsantaki, M., Bouchy, F., Hébrard, G., Adibekyan, V., Almenara, J. M., Amard, L., Barros, S. C. C., Boisse, I., Bonomo, A. S., Bruno, G., Courcol, B., Deleuil, M., Demangeon, O., Díaz, R. F., Guillot, T., Havel, M., Montagnier, G., Rajpurohit, A. S., Rey, J., & Santos, N. C.: SOPHIE velocimetry of Kepler transit candidates. XVII. The physical properties of giant exoplanets within 400 days of period, A&A, 587, A64, https://doi.org/10.1051/0004-6361/201527329, 2016.

Santos, N. C., Israelian, G., & Mayor, M.: Spectroscopic [Fe/H] for 98 extra-solar planet-host stars. Exploring the probability of planet formation, A&A, 415, 1153–1166, https://doi.org/10.1051/0004-6361:20034469, 2004.

Santos, N. C., Adibekyan, V., Dorn, C., Mordasini, C., Noack, L., Barros, S. C. C., Delgado-Mena, E., Demangeon, O., Faria, J. P., Israelian, G., & Sousa, S. G.: Constraining planet structure and composition from stellar chemistry: trends in different stellar populations, A&A, 608, A94, https://doi.org/10.1051/0004-6361/201731359, 2017.

Satoh, Y. K., Koshimoto, N., Bennett, D. P., Sumi, T., Rattenbury, N. J., Suzuki, D., Miyazaki, S., Bond, I. A., Udalski, A., Gould, A., Bozza, V., Dominik, M., Hirao, Y., Kondo, I., Kirikawa, R., Hamada, R., Abe, F., Barry, R., Bhattacharya, A., Fujii, H., Fukui, A., Fujita, K., Ikeno, T., Ishitani Silva, S., Itow, Y., Matsubara, Y., Matsumoto, S., Muraki, Y., Niwa, K., Okamura, A., Olmschenk, G., Ranc, C., Toda, T., Tomoyoshi, M., Tristram, P. J., Vandorou, A., Yama, H., Yamashita, K., Moa Collaboration, Mróz, P., Poleski, R., Skowron, J., Szymański, M. K., Poleski, R., Soszyński, I., Pietrukowicz, P., Kozłowski, S., Ulaczyk, K., Rybicki, K. A., Iwanek, P., Wrona, M., Gromadzki, M., Ogle Collaboration, Albrow, M. D., Chung, S.-J., Han, C., Hwang, K.-H., Kim, D., Jung, Y. K., Kim, H. W., Ryu, Y.-H., Shin, I.-G., Shvartzvald, Y., Yang, H., Yee, J. C., Zang, W., Cha, S.-M., Kim, D.-J., Kim, S.-L., Lee, C.-U., Lee, D.-J., Lee, Y., Park, B.-G., Pogge, R. W., Kmtnet Collaboration, Jørgensen, U. G., Longa-Peña, P., Sajadian, S., Skottfelt, J., Snodgrass, C., Tregloan-Reed, J., Bach-Møller, N., Burgdorf, M., D'Ago, G., Haikala, L., Hitchcock, J., Hundertmark, M., Khalouei, E., Peixinho, N., Rahvar, S., Southworth, J., Spyratos, P., & Mindstep Collaboration: OGLE-2019-BLG-0825: Constraints on the Source System and Effect on Binary-lens Parameters Arising from a Five-day Xallarap Effect in a Candidate Planetary Microlensing Event, AJ, 166, 116, https://doi.org/10.3847/1538-3881/ace908, 2023.

Schneider, P. & Weiss, A.: The two-point-mass lens - Detailed investigation of a special asymmetric gravitational lens, A&A, 164, 237–259, 1986.

Sit, T. & Ness, M. K.: The Age Distribution of Stars in the Milky Way Bulge, ApJ, 900, 4, https://doi.org/10.3847/1538-4357/ab9ff6, 2020.

Skowron, J., Udalski, A., Gould, A., Dong, S., Monard, L. A. G., Han, C., Nelson, C. R., McCormick, J., Moorhouse, D., Thornley, G., Maury, A., Bramich, D. M., Greenhill, J., Kozłowski, S., Bond, I., Poleski, R., Wyrzykowski, Ł., Ulaczyk, K., Kubiak, M., Szymański, M. K., Pietrzyński, G., Soszyński, I., OGLE Collaboration, Gaudi, B. S., Yee, J. C., Hung, L. W., Pogge, R. W., DePoy, D. L., Lee, C. U., Park, B. G., Allen, W., Mallia, F., Drummond, J., Bolt, G., μFUN Collaboration, Allan, A., Browne, P., Clay, N., Dominik, M., Fraser, S., Horne, K., Kains, N., Mottram, C., Snodgrass, C., Steele, I., Street, R. A., Tsapras, Y., RoboNet Collaboration, Abe, F., Bennett, D. P., Botzler, C. S., Douchin, D., Freeman, M., Fukui, A., Furusawa, K., Hayashi, F., Hearnshaw, J. B., Hosaka, S., Itow, Y., Kamiya, K., Kilmartin, P. M., Korpela, A., Lin, W., Ling, C. H., Makita, S., Masuda, K., Matsubara, Y., Muraki, Y., Nagayama, T., Miyake, N., Nishimoto, K., Ohnishi, K., Perrott, Y. C., Rattenbury, N., Saito, T., Skuljan, L., Sullivan, D. J., Sumi, T., Suzuki, D., Sweatman, W. L., Tristram, P. J., Wada, K., Yock, P. C. M., MOA Collaboration, Beaulieu, J. P., Fouqué, P., Albrow, M. D., Batista, V., Brillant, S., Caldwell, J. A. R., Cassan, A., Cole, A., Cook, K. H., Coutures, C., Dieters, S., Dominis Prester, D., Donatowicz, J., Kane, S. R., Kubas, D., Marquette, J. B., Martin, R., Menzies, J., Sahu, K. C., Wambsganss, J., Williams, A., Zub, M., & PLANET Collaboration: Binary Microlensing Event OGLE-2009-BLG-020 Gives Verifiable Mass, Distance, and Orbit Predictions, ApJ, 738, 87, https://doi.org/10.1088/0004-637X/738/1/87, 2011.

Smith, M. C., Mao, S., & Paczyński, B.: Acceleration and parallax effects in gravitational microlensing, MNRAS, 339, 925–936, https://doi.org/10.1046/j.1365-8711.2003.06183.x, 2003.

Song, Y.-Y., Mao, S., & An, J. H.: Degeneracies in triple gravitational microlensing, MNRAS, 437, 4006–4018, https://doi.org/10.1093/mnras/stt2222, 2014.

Soszyński, I., Udalski, A., Szymański, M. K., Kubiak, M., Pietrzyński, G., Wyrzykowski, Ł., Szewczyk, O., Ulaczyk, K., & Poleski, R.: The Optical Gravitational Lensing Experiment. The

OGLE-III Catalog of Variable Stars. III. RR Lyrae Stars in the Large Magellanic Cloud, AcA, 59, 1–18, https://doi.org/10.48550/arXiv.0903.2482, 2009.

Soszyński, I., Dziembowski, W. A., Udalski, A., Poleski, R., Szymański, M. K., Kubiak, M., Pietrzyński, G., Wyrzykowski, Ł., Ulaczyk, K., Kozłowski, S., & Pietrukowicz, P.: The Optical Gravitational Lensing Experiment. The OGLE-III Catalog of Variable Stars. XI. RR Lyrae Stars in the Galactic Bulge, AcA, 61, 1–23, https://doi.org/10.48550/arXiv.1105.6126, 2011a.

Soszyński, I., Udalski, A., Pietrukowicz, P., Szymański, M. K., Kubiak, M., Pietrzyński, G., Wyrzykowski, Ł., Ulaczyk, K., Poleski, R., & Kozłowski, S.: The Optical Gravitational Lensing Experiment. The OGLE-III Catalog of Variable Stars. XIV. Classical and TypeII Cepheids in the Galactic Bulge, AcA, 61, 285–301, https://doi.org/10.48550/arXiv.1112.1406, 2011b.

Sousa, S. G., Adibekyan, V., Santos, N. C., Mortier, A., Barros, S. C. C., Delgado-Mena, E., Demangeon, O., Israelian, G., Faria, J. P., Figueira, P., Rojas-Ayala, B., Tsantaki, M., Andreasen, D. T., Brandão, I., Ferreira, A. C. S., Montalto, M., & Santerne, A.: The metallicity-period-mass diagram of low-mass exoplanets, MNRAS, 485, 3981–3990, https://doi.org/10.1093/mnras/stz664, 2019.

Spergel, D., Gehrels, N., Baltay, C., Bennett, D., Breckinridge, J., Donahue, M., Dressler, A., Gaudi, B. S., Greene, T., Guyon, O., Hirata, C., Kalirai, J., Kasdin, N. J., Macintosh, B., Moos, W., Perlmutter, S., Postman, M., Rauscher, B., Rhodes, J., Wang, Y., Weinberg, D., Benford, D., Hudson, M., Jeong, W. S., Mellier, Y., Traub, W., Yamada, T., Capak, P., Colbert, J., Masters, D., Penny, M., Savransky, D., Stern, D., Zimmerman, N., Barry, R., Bartusek, L., Carpenter, K., Cheng, E., Content, D., Dekens, F., Demers, R., Grady, K., Jackson, C., Kuan, G., Kruk, J., Melton, M., Nemati, B., Parvin, B., Poberezhskiy, I., Peddie, C., Ruffa, J., Wallace, J. K., Whipple, A., Wollack, E., & Zhao, F.: Wide-Field InfrarRed Survey Telescope-Astrophysics Focused Telescope Assets WFIRST-AFTA 2015 Report, arXiv e-prints, arXiv:1503.03757, 2015.

Spiegel, D. S. & Burrows, A.: Spectral and Photometric Diagnostics of Giant Planet Formation Scenarios, ApJ, 745, 174, https://doi.org/10.1088/0004-637X/745/2/174, 2012.

Spinelli, R., Ghirlanda, G., Haardt, F., Ghisellini, G., & Scuderi, G.: The best place and time to live in the Milky Way, A&A, 647, A41, https://doi.org/10.1051/0004-6361/202039507, 2021.

Stassun, K. G., Mathieu, R. D., & Valenti, J. A.: Discovery of two young brown dwarfs in an eclipsing binary system, Nature, 440, 311–314, https://doi.org/10.1038/nature04570, 2006.

Sumi, T., Abe, F., Bond, I. A., Dodd, R. J., Hearnshaw, J. B., Honda, M., Honma, M., Kan-ya, Y., Kilmartin, P. M., Masuda, K., Matsubara, Y., Muraki, Y., Nakamura, T., Nishi, R., Noda, S., Ohnishi, K., Petterson, O. K. L., Rattenbury, N. J., Reid, M., Saito, T., Saito, Y., Sato, H., Sekiguchi, M., Skuljan, J., Sullivan, D. J., Takeuti, M., Tristram, P. J., Wilkinson, S., Yanagisawa, T., & Yock, P. C. M.: Microlensing Optical Depth toward the Galactic Bulge from Microlensing Observations in Astrophysics Group Observations during 2000 with Difference Image Analysis, ApJ, 591, 204–227, https://doi.org/10.1086/375212, 2003.

Sumi, T., Bennett, D. P., Bond, I. A., Udalski, A., Batista, V., Dominik, M., Fouqué, P., Kubas, D., Gould, A., Macintosh, B., Cook, K., Dong, S., Skuljan, L., Cassan, A., Abe, F., Botzler, C. S., Fukui, A., Furusawa, K., Hearnshaw, J. B., Itow, Y., Kamiya, K., Kilmartin, P. M., Korpela, A., Lin, W., Ling, C. H., Masuda, K., Matsubara, Y., Miyake, N., Muraki, Y., Nagaya, M., Nagayama, T., Ohnishi, K., Okumura, T., Perrott, Y. C., Rattenbury, N., Saito, T., Sako, T., Sullivan, D. J., Sweatman, W. L., Tristram, P. J., Yock, P. C. M., MOA Collaboration, Beaulieu, J. P., Cole, A., Coutures, C., Duran, M. F., Greenhill, J., Jablonski, F., Marboeuf, U., Martioli, E., Pedretti, E., Pejcha, O., Rojo, P., Albrow, M. D., Brillant, S., Bode, M., Bramich, D. M., Burgdorf, M. J., Caldwell, J. A. R., Calitz, H., Corrales, E., Dieters, S., Dominis Prester, D., Donatowicz, J., Hill, K., Hoffman, M., Horne, K., Jørgensen, U. G., Kains, N., Kane, S., Marquette, J. B., Martin, R., Meintjes, P., Menzies, J., Pollard, K. R., Sahu, K. C., Snodgrass, C., Steele, I., Street, R., Tsapras, Y., Wambsganss, J., Williams, A., Zub, M., PLANET Collaboration, Szymański, M. K., Kubiak, M., Pietrzyński, G., Soszyński, I., Szewczyk, O., Wyrzykowski, Ł., Ulaczyk, K., OGLE Collaboration, Allen, W., Christie, G. W., DePoy, D. L., Gaudi, B. S., Han, C., Janczak, J., Lee, C. U., McCormick, J., Mallia, F., Monard, B., Natusch, T., Park, B. G., Pogge, R. W., Santallo, R., & μFUN Collaboration: A Cold Neptune-Mass Planet OGLE-2007-BLG-368Lb: Cold

Neptunes Are Common, ApJ, 710, 1641–1653, https://doi.org/10.1088/0004-637X/710/2/1641, 2010.

Sumi, T., Kamiya, K., Bennett, D. P., Bond, I. A., Abe, F., Botzler, C. S., Fukui, A., Furusawa, K., Hearnshaw, J. B., Itow, Y., Kilmartin, P. M., Korpela, A., Lin, W., Ling, C. H., Masuda, K., Matsubara, Y., Miyake, N., Motomura, M., Muraki, Y., Nagaya, M., Nakamura, S., Ohnishi, K., Okumura, T., Perrott, Y. C., Rattenbury, N., Saito, T., Sako, T., Sullivan, D. J., Sweatman, W. L., Tristram, P. J., Udalski, A., Szymański, M. K., Kubiak, M., Pietrzyński, G., Poleski, R., Soszyński, I., Wyrzykowski, Ł., Ulaczyk, K., & Microlensing Observations in Astrophysics (MOA) Collaboration: Unbound or distant planetary mass population detected by gravitational microlensing, Nature, 473, 349–352, https://doi.org/10.1038/nature10092, 2011.

Sumi, T., Koshimoto, N., Bennett, D. P., Rattenbury, N. J., Abe, F., Barry, R., Bhattacharya, A., Bond, I. A., Fujii, H., Fukui, A., Hamada, R., Hirao, Y., Silva, S. I., Itow, Y., Kirikawa, R., Kondo, I., Matsubara, Y., Miyazaki, S., Muraki, Y., Olmschenk, G., Ranc, C., Satoh, Y., Suzuki, D., Tomoyoshi, M., Tristram, P. J., Vandorou, A., Yama, H., & Yamashita, K.: Free-floating Planet Mass Function from MOA-II 9 yr Survey toward the Galactic Bulge, AJ, 166, 108, https://doi.org/10.3847/1538-3881/ace688, 2023.

Szymański, M. K., Udalski, A., Soszyński, I., Kubiak, M., Pietrzyński, G., Poleski, R., Wyrzykowski, Ł., & Ulaczyk, K.: The Optical Gravitational Lensing Experiment. OGLE-III Photometric Maps of the Galactic Bulge Fields, AcA, 61, 83–102, 2011.

Tamura, M., Suto, H., Nishikawa, J., Kotani, T., Sato, B., Aoki, W., Usuda, T., Kurokawa, T., Kashiwagi, K., Nishiyama, S., Ikeda, Y., Hall, D., Hodapp, K., Hashimoto, J., Morino, J., Inoue, S., Mizuno, Y., Washizaki, Y., Tanaka, Y., Suzuki, S., Kwon, J., Suenaga, T., Oh, D., Narita, N., Kokubo, E., Hayano, Y., Izumiura, H., Kambe, E., Kudo, T., Kusakabe, N., Ikoma, M., Hori, Y., Omiya, M., Genda, H., Fukui, A., Fujii, Y., Guyon, O., Harakawa, H., Hayashi, M., Hidai, M., Hirano, T., Kuzuhara, M., Machida, M., Matsuo, T., Nagata, T., Ohnuki, H., Ogihara, M., Oshino, S., Suzuki, R., Takami, H., Takato, N., Takahashi, Y., Tachinami, C., & Terada, H.: Infrared Doppler instrument for the Subaru Telescope (IRD), in: Ground-based and Airborne

Instrumentation for Astronomy IV, edited by McLean, I. S., Ramsay, S. K., & Takami, H., vol. 8446 of Society of Photo-Optical Instrumentation Engineers (SPIE) Conference Series, p. 84461T, https://doi.org/10.1117/12.925885, 2012.

Tisserand, P., Le Guillou, L., Afonso, C., Albert, J. N., Andersen, J., Ansari, R., Aubourg, É., Bareyre, P., Beaulieu, J. P., Charlot, X., Coutures, C., Ferlet, R., Fouqué, P., Glicenstein, J. F., Goldman, B., Gould, A., Graff, D., Gros, M., Haissinski, J., Hamadache, C., de Kat, J., Lasserre, T., Lesquoy, É., Loup, C., Magneville, C., Marquette, J. B., Maurice, É., Maury, A., Milsztajn, A., Moniez, M., Palanque-Delabrouille, N., Perdereau, O., Rahal, Y. R., Rich, J., Spiro, M., Vidal-Madjar, A., Vigroux, L., Zylberajch, S., & EROS-2 Collaboration: Limits on the Macho content of the Galactic Halo from the EROS-2 Survey of the Magellanic Clouds, A&A, 469, 387–404, https://doi.org/10.1051/0004-6361:20066017, 2007.

Tokovinin, A. & Moe, M.: Formation of close binaries by disc fragmentation and migration, and its statistical modelling, MNRAS, 491, 5158–5171, https://doi.org/10.1093/mnras/stz3299, 2020.

Tokovinin, A., Thomas, S., Sterzik, M., & Udry, S.: Tertiary companions to close spectroscopic binaries, A&A, 450, 681–693, https://doi.org/10.1051/0004-6361:20054427, 2006.

Tomaney, A. B. & Crotts, A. P. S.: Expanding the Realm of Microlensing Surveys with Difference Image Photometry, AJ, 112, 2872, https://doi.org/10.1086/118228, 1996.

Toomre, A.: On the gravitational stability of a disk of stars., ApJ, 139, 1217–1238, https://doi.org/10.1086/147861, 1964.

Troup, N. W., Nidever, D. L., De Lee, N., Carlberg, J., Majewski, S. R., Fernandez, M., Covey, K., Chojnowski, S. D., Pepper, J., Nguyen, D. T., Stassun, K., Nguyen, D. C., Wisniewski, J. P., Fleming, S. W., Bizyaev, D., Frinchaboy, P. M., García-Hernández, D. A., Ge, J., Hearty, F., Meszaros, S., Pan, K., Allende Prieto, C., Schneider, D. P., Shetrone, M. D., Skrutskie, M. F., Wilson, J., & Zamora, O.: Companions to APOGEE Stars. I. A Milky Way-spanning Catalog of Stellar and Substellar Companion Candidates and Their Diverse Hosts, AJ, 151, 85, https://doi.org/10.3847/0004-6256/151/3/85, 2016.

Tsapras, Y., Hundertmark, M., Wyrzykowski, Ł., Horne, K., Udalski, A., Snodgrass, C., Street, R., Bramich, D. M., Dominik, M., Bozza, V., Figuera Jaimes, R., Kains, N., Skowron, J., Szymański, M. K., Pietrzyński, G., Soszyński, I., Ulaczyk, K., Kozłowski, S., Pietrukowicz, P., & Poleski, R.: The OGLE-III planet detection efficiency from six years of microlensing observations (2003-2008), MNRAS, 457, 1320–1331, https://doi.org/10.1093/mnras/stw023, 2016.

Tsiaras, A., Waldmann, I. P., Tinetti, G., Tennyson, J., & Yurchenko, S. N.: Water vapour in the atmosphere of the habitable-zone eight-Earth-mass planet K2-18 b, Nature Astronomy, 3, 1086–1091, https://doi.org/10.1038/s41550-019-0878-9, 2019.

Tsiganis, K., Gomes, R., Morbidelli, A., & Levison, H. F.: Origin of the orbital architecture of the giant planets of the Solar System, Nature, 435, 459–461, https://doi.org/10.1038/nature03539, 2005.

Tsujimoto, T. & Shigeyama, T.: Enrichment history of r-process elements shaped by a merger of neutron star pairs, A&A, 565, L5, https://doi.org/10.1051/0004-6361/201423751, 2014.

Udalski, A.: The Optical Gravitational Lensing Experiment. Real Time Data Analysis Systems in the OGLE-III Survey, AcA, 53, 291–305, 2003.

Udalski, A., Szymanski, M., Kaluzny, J., Kubiak, M., Krzeminski, W., Mateo, M., Preston, G. W., & Paczynski, B.: The Optical Gravitational Lensing Experiment. Discovery of the First Candidate Microlensing Event in the Direction of the Galactic Bulge, AcA, 43, 289–294, 1993.

Udalski, A., Szymanski, M., Stanek, K. Z., Kaluzny, J., Kubiak, M., Mateo, M., Krzeminski, W., Paczynski, B., & Venkat, R.: The Optical Gravitational Lensing Experiment. The Optical Depth to Gravitational Microlensing in the Direction of the Galactic Bulge, AcA, 44, 165–189, 1994.

Udalski, A., Szymański, M. K., & Szymański, G.: OGLE-IV: Fourth Phase of the Optical Gravitational Lensing Experiment, AcA, 65, 1–38, 2015.

Vickers, J. J., Shen, J., & Li, Z.-Y.: The Flattening Metallicity Gradient in the Milky Way's Thin Disk, ApJ, 922, 189, https://doi.org/10.3847/1538-4357/ac27a9, 2021.

Walsh, D., Carswell, R. F., & Weymann, R. J.: 0957+561 A, B: twin quasistellar objects or gravitational lens?, Nature, 279, 381–384, https://doi.org/10.1038/279381a0, 1979.

Walsh, K. J., Morbidelli, A., Raymond, S. N., O'Brien, D. P., & Mandell, A. M.: A low mass for Mars from Jupiter's early gas-driven migration, Nature, 475, 206–209, https://doi.org/10.1038/nature10201, 2011.

Wambsganss, J.: Discovering Galactic planets by gravitational microlensing: magnification patterns and light curves, MNRAS, 284, 172–188, https://doi.org/10.1093/mnras/284.1.172, 1997.

Weiss, L. M. & Marcy, G. W.: The Mass-Radius Relation for 65 Exoplanets Smaller than 4 Earth Radii, ApJL, 783, L6, https://doi.org/10.1088/2041-8205/783/1/L6, 2014.

Will, C. M.: Theory and Experiment in Gravitational Physics, Cambridge University Press, 1993.

Witt, H. J.: Investigation of high amplification events in light curves of gravitationally lensed quasars., A&A, 236, 311, 1990.

Wozniak, P. R.: Difference Image Analysis of the OGLE-II Bulge Data. I. The Method, AcA, 50, 421–450, 2000.

Wyse, R. F. G. & Gilmore, G.: Chemistry and Kinematics in the Solar Neighborhood: Implications for Stellar Populations and for Galaxy Evolution, AJ, 110, 2771, https://doi.org/10.1086/117729, 1995.

Yee, J. C., Shvartzvald, Y., Gal-Yam, A., Bond, I. A., Udalski, A., Kozłowski, S., Han, C., Gould, A., Skowron, J., Suzuki, D., Abe, F., Bennett, D. P., Botzler, C. S., Chote, P., Freeman, M., Fukui, A., Furusawa, K., Itow, Y., Kobara, S., Ling, C. H., Masuda, K., Matsubara, Y., Miyake, N., Muraki, Y., Ohmori, K., Ohnishi, K., Rattenbury, N. J., Saito, T., Sullivan, D. J., Sumi, T., Suzuki, K., Sweatman, W. L., Takino, S., Tristram, P. J., Wada, K., MOA Collaboration, Szymański, M. K., Kubiak, M., Pietrzyński, G., Soszyński, I., Poleski, R., Ulaczyk, K., Wyrzykowski, Ł., Pietrukowicz, P., OGLE Collaboration, Allen, W., Almeida, L. A., Batista, V., Bos, M., Christie, G., DePoy, D. L., Dong, S., Drummond, J., Finkelman, I., Gaudi, B. S.,

Gorbikov, E., Henderson, C., Higgins, D., Jablonski, F., Kaspi, S., Manulis, I., Maoz, D., McCormick, J., McGregor, D., Monard, L. A. G., Moorhouse, D., Muñoz, J. A., Natusch, T., Ngan, H., Ofek, E., Pogge, R. W., Santallo, R., Tan, T. G., Thornley, G., Shin, I. G., Choi, J. Y., Park, S. Y., Lee, C. U., Koo, J. R., & μFUN Collaboration: MOA-2011-BLG-293Lb: A Test of Pure Survey Microlensing Planet Detections, ApJ, 755, 102, https://doi.org/10.1088/0004-637X/755/2/102, 2012.

Yee, J. C., Gould, A., Beichman, C., Calchi Novati, S., Carey, S., Gaudi, B. S., Henderson, C. B., Nataf, D., Penny, M., Shvartzvald, Y., & Zhu, W.: Criteria for Sample Selection to Maximize Planet Sensitivity and Yield from Space-Based Microlens Parallax Surveys, ApJ, 810, 155, https://doi.org/10.1088/0004-637X/810/2/155, 2015.

Yee, J. C., Zang, W., Udalski, A., Ryu, Y.-H., Green, J., Hennerley, S., Marmont, A., Sumi, T., Mao, S., Gromadzki, M., Mróz, P., Skowron, J., Poleski, R., Szymański, M. K., Soszyński, I., Pietrukowicz, P., Kozłowski, S., Ulaczyk, K., Rybicki, K. A., Iwanek, P., Wrona, M., Albrow, M. D., Chung, S.-J., Gould, A., Han, C., Hwang, K.-H., Jung, Y. K., Kim, H.-W., Shin, I.-G., Shvartzvald, Y., Cha, S.-M., Kim, D.-J., Kim, S.-L., Lee, C.-U., Lee, D.-J., Lee, Y., Park, B.-G., Pogge, R. W., Bachelet, E., Christie, G., Hundertmark, M. P. G., Maoz, D., McCormick, J., Natusch, T., Penny, M. T., Street, R. A., Tsapras, Y., Beichman, C. A., Bryden, G., Novati, S. C., Carey, S., Gaudi, B. S., Henderson, C. B., Johnson, S., Zhu, W., Bond, I. A., Abe, F., Barry, R., Bennett, D. P., Bhattacharya, A., Donachie, M., Fujii, H., Fukui, A., Hirao, Y., Silva, S. I., Itow, Y., Kirikawa, R., Kondo, I., Koshimoto, N., Alex Li, M. C., Matsubara, Y., Muraki, Y., Miyazaki, S., Olmschenk, G., Ranc, C., Rattenbury, N. J., Satoh, Y., Shoji, H., Suzuki, D., Tanaka, Y., Tristram, P. J., Yamawaki, T., Yonehara, A., & MOA Collaboration: OGLE-2019-BLG-0960 Lb: the Smallest Microlensing Planet, AJ, 162, 180, https://doi.org/10.3847/1538-3881/ac1582, 2021.

Zakharov, A. F.: The duration of astrometric (weak) microlensing events, Astronomy Reports, 59, 823–828, https://doi.org/10.1134/S1063772915090097, 2015.

Zhu, W.: Influence of Stellar Metallicity on Occurrence Rates of Planets and Planetary Systems, ApJ, 873, 8, https://doi.org/10.3847/1538-4357/ab0205, 2019.

Zhu, W., Udalski, A., Novati, S. C., Chung, S. J., Jung, Y. K., Ryu, Y. H., Shin, I. G., Gould, A., Lee, C. U., Albrow, M. D., Yee, J. C., Han, C., Hwang, K. H., Cha, S. M., Kim, D. J., Kim, H. W., Kim, S. L., Kim, Y. H., Lee, Y., Park, B. G., Pogge, R. W., KMTNet Collaboration, Poleski, R., Mróz, P., Pietrukowicz, P., Skowron, J., Szymański, M. K., KozLowski, S., Ulaczyk, K., Pawlak, M., OGLE Collaboration, Beichman, C., Bryden, G., Carey, S., Fausnaugh, M., Gaudi, B. S., Henderson, C. B., Shvartzvald, Y., Wibking, B., & Spitzer Team: Toward a Galactic Distribution of Planets. I. Methodology and Planet Sensitivities of the 2015 High-cadence Spitzer Microlens Sample, AJ, 154, 210, https://doi.org/10.3847/1538-3881/aa8ef1, 2017.